

DTIC FILE COPY

01

GL-TR-89-0293

AD-A223 908

IONOSPHERIC IRREGULARITIES: SOURCE, STRUCTURE, PLASMA PROCESSES
AND EFFECTS ON SENSOR SYSTEMS

Sunanda Basu
Cesar Valladares
Eileen MacKenzie
Clifford Bryant
Patricia Doherty
M.P. Hagan

The Trustees of Emmanuel College
400 The Fenway
Boston MA 02115

Final Report
2 October 1986 - 1 October 1989

31 October 1989

DTIC
ELECTE
JUL 10 1990
S E D

Approved for public release; distribution unlimited

GEOPHYSICS LABORATORY
AIR FORCE SYSTEMS COMMAND
UNITED STATES AIR FORCE
RANDCOM AFB MA 01731-5000

90 07 10 026

"This technical report has been reviewed and is approved for publication"


WILLIAM K. VICKERY
Contract Manager


WILLIAM K. VICKERY
Branch Chief

FOR THE COMMANDER


ROBERT A. SKRIVANEK
Division Director

This report has been reviewed by the ESD Public Affairs Office (PA) and is releasable to the National Technical Information Service (NTIS).

Qualified requestors may obtain additional copies from Defense Technical Information Center. All others should apply to the National Technical Information Service.

If your address has changed, or if you wish to be removed from the mailing list, or if the addressee is no longer employed by your organization, please notify GL/IMA Hanscom AFB, MA 01731. This will assist us in maintaining a current mailing list.

Do not return copies of this report unless contractual obligations or notice on a specific document requires that it be returned.

Unclassified

SECURITY CLASSIFICATION OF THIS PAGE

REPORT DOCUMENTATION PAGE				
1a. REPORT SECURITY CLASSIFICATION Unclassified		1b. RESTRICTIVE MARKINGS None		
2a. SECURITY CLASSIFICATION AUTHORITY N/A		3. DISTRIBUTION/AVAILABILITY OF REPORT Approved for public release; distribution unlimited		
2b. DECLASSIFICATION/DOWNGRADING SCHEDULE N/A		4. PERFORMING ORGANIZATION REPORT NUMBER(S) Technical Report - Final		
6a. NAME OF PERFORMING ORGANIZATION Emmanuel College	6b. OFFICE SYMBOL PRD	5. MONITORING ORGANIZATION REPORT NUMBER(S) GL-TR-89-0293		
6c. ADDRESS (City, State and ZIP Code) 400 The Fenway Boston MA 02115		7a. NAME OF MONITORING ORGANIZATION Geophysics Laboratory		
8a. NAME OF FUNDING/SPONSORING ORGANIZATION		8b. OFFICE SYMBOL 199628-86-K-0038		
8c. ADDRESS (City, State and ZIP Code)		9. PROCUREMENT INSTRUMENT IDENTIFICATION NUMBER		
11. TITLE (Include Security Classification) see 16.		10. SOURCE OF FUNDING NOS.		
12. PERSONAL AUTHOR(S) Sunanda Basu, Cesar Valladares, Eileen Mackenzie, Clifford Bryant, (cont. on reverse)		PROGRAM ELEMENT NO.	PROJECT NO.	TASK NO.
13a. TYPE OF REPORT Final	13b. TIME COVERED FROM 10/2/86 TO 10/1/89	14. DATE OF REPORT (Yr., Mo. Day) 89 OCT 31		15. PAGE COUNT 228
16. SUPPLEMENTARY NOTATION Title: Ionospheric Irregularities: Source, Structure, Plasma Processes and Effects on Sensor Systems				
17. COSATI CODES		18. SUBJECT TERMS (Continue on reverse if necessary and identify by block number) Phase and amplitude scintillations, spaced-receiver measurements, polar cusp, polar cap patches, sun-aligned arcs, auroral blobs, in-situ data, (Cont. on reverse)		
19. ABSTRACT (Continue on reverse if necessary and identify by block number) A multi-technique approach has been used at a number of geophysically interesting locations to determine various sources of high-latitude irregularities, their occurrence characteristics and effects on sensor systems. Auroral scintillation morphology and irregularity anisotropy were determined using HiLat satellite data obtained at Tromso. Global scintillation characteristics were determined as a function of the sunspot cycle and a high latitude scintillation review was prepared reflecting our improved understanding of different sources of irregularity generation. A high latitude campaign mounted under the auspices of the CEDAR initiative provided multiple diagnostic studies of the polar cusp, polar cap patches and sun-aligned arcs. Multiple sensor data on the DE-2 satellite have been utilized to isolate two different classes of plasma instabilities responsible for structuring plasmas at high latitudes. Finally, an active experiment was performed with the high power HF heater at Tromso, Norway to study the characteristics of the artificially generated irregularities in the daytime sub-auroral ionosphere. (10/2)				
20. DISTRIBUTION/AVAILABILITY OF ABSTRACT UNCLASSIFIED/UNLIMITED <input checked="" type="checkbox"/> SAME AS RPT. <input type="checkbox"/> DTIC USERS <input type="checkbox"/>		21. ABSTRACT SECURITY CLASSIFICATION Unclassified		
22a. NAME OF RESPONSIBLE INDIVIDUAL William K. Vickery		22b. TELEPHONE NUMBER (Include Area Code) (617) 377-2458	22c. OFFICE SYMBOL GL/LIS	

Unclassified

SECURITY CLASSIFICATION OF THIS PAGE

12. (Cont.) Patricia Doherty, M. P. Hagan

16. (Cont.) velocity shears, power spectra, energetic particle precipitation,
E-region conductivity, ionospheric modification, artificial
irregularities

Unclassified

SECURITY CLASSIFICATION OF THIS PAGE

PREFACE

We wish to acknowledge AFOSR support of the work presented in this report under Project 2310, Task G9.

We are indebted to many of our colleagues both at GL and elsewhere for their cooperation. They are acknowledged individually in some of the publications that form a part of this report.

Accession For	
NTIS	GRA&I
DTIC TAB	<input type="checkbox"/>
Unannounced	<input type="checkbox"/>
Justification	
By	
Distribution/	
Availability Codes	
Avail and/or	
Dist	Special
A-1	



TABLE OF CONTENTS

	<u>Page</u>
SUMMARY	1
Attachment 1 - Scintillation technique for probing ionospheric irregularities	4
Attachment 2 - Ionospheric scintillations and in-situ measurements at an auroral location in the European sector	13
Attachment 3 - Cross-correlation analysis and interpretation of spaced-receiver measurements	26
Attachment 4 - Cross-spectral analysis of spaced-receiver measurements	48
Attachment 5 - Ionospheric constraints on VHF/UHF communications links during solar maximum and minimum periods	59
Attachment 6 - High latitude scintillations	75
Attachment 7 - Simultaneous radar and satellite observations of the polar cusp/cleft at Sondre Stromfjord	85
Attachment 8 - Coordinated observations of high latitude ionospheric turbulence	99
Attachment 9 - Simultaneous density and electric field fluctuation spectra associated with velocity shears in the auroral oval	115
Attachment 10 - Plasma structuring by the gradient-drift instability at high latitudes and comparison with velocity-shear driven processes	137
Attachment 11 - Daytime scintillations induced by high-power HF waves at Tromso, Norway	216

SUMMARY

A large number of studies have been performed using a variety of ground-based and satellite in-situ techniques to determine various sources of high-latitude irregularities, their morphology and structure and their effects on sensor systems.

The scintillation technique is extensively used to determine morphology of irregularities at interesting geophysical locations and to estimate the effects of these irregularities on various Air Force communication and radar systems. Different methods for measuring phase and amplitude scintillations are described and the application of this technique, particularly when used in conjunction with other radio and optical diagnostics, in determining plasma processes is enumerated (Attachment 1).

Extensive scintillation and in-situ measurements made with the DNA HiLat satellite at Tromso are utilized to determine morphology and anisotropy of auroral irregularities. The dynamics of the spatial and temporal extent of this region are illustrated and the dependence of ionospheric structure parameters on short-term variability of solar activity during the sunspot minimum are pointed out (Attachment 2). The geometrical enhancement of scintillations observed during the alignment of the propagation path with the local magnetic L-shell is shown to be the most consistent and conspicuous feature of scintillations in the nighttime auroral oval. Particular attention was given to the geometrical enhancement region by utilizing the spaced-receiver scintillation technique to determine the anisotropy of the ground diffraction pattern in this region (Attachment 3). Further, an algorithm was obtained to estimate the anisotropy of the ground diffraction pattern directly from the cross-spectra of the received signals (Attachment 4).

The large scintillation data base archived at the Geophysics Laboratory has been utilized to estimate the ionospheric effects on VHF/UHF communication links between geostationary satellites and

stations on the magnetic equator, at the anomaly peak and in auroral and polar cap locations as a function of sunspot cycle. The "worst case" scenario was encountered at the crest of the anomaly at sunspot maximum when 20 dB fades at 1.5 GHz were observed for 30 percent of the time in pre-midnight hours during the equinoxes. The highest scintillation at high latitudes was encountered deep within the polar cap where median fades of 20 dB at 250 MHz were observed at equinoxes during sunspot maximum (Appendix 5).

A review of high latitude scintillation was prepared to summarize the new insights gained by combining quasi-geostationary satellite measurements of scintillations together with HiLat and Polar Bear observations of scintillations, in-situ and ultraviolet imager data. New classes of E-region and F-region irregularities were isolated with these co-ordinated measurements (Attachment 6) and the technique of modeling of scintillations caused by polar cap patches from in-situ data could be demonstrated (Scientific Report 2 - Basu et al., Radio Science, 23, 545, 1988).

A multi-diagnostic experiment was mounted in February, 1988 under the auspices of the National Science Foundation's CEDAR initiative to study plasma structuring in the polar cusp. The energy input and dynamics were estimated by the in-situ instruments on HiLat whereas total electron content (TEC) and scintillation measurements provided information regarding large and small scale structures. Preliminary modeling studies were conducted to determine the consistency of the particle precipitation and incoherent scatter radar measured densities and temperatures at Sondrestrom (Attachment 7).

Convecting polar cap patches and sun-aligned polar cap arcs were also detected during the February, 1988 CEDAR High Latitude Plasma Structure (HLPS) campaign. A description of high-latitude turbulence associated with patches and arcs during low sunspot conditions was presented (Attachment 8).

The next couple of papers provide comprehensive studies of two different classes of plasma instabilities responsible for plasma structuring at high latitudes. Multiple Sensor Dynamics Explorer - 2

(DE-2) data were used to determine simultaneous density and electric field spectra under conditions of velocity shear near auroral arcs and also in conjunction with convecting patches and blobs. It is shown that it is imperative to consider both the magnitudes of the density and electric field perturbations as well as their spectral shapes in determining the type of plasma instability operating in the high latitude ionosphere (Attachments 9 and 10).

Finally, an active experiment was performed with the high power HF heater at Tromso, Norway to modify the daytime sub-auroral ionosphere. Using scintillations and the EISCAT radar as diagnostics, it was found that the HF heating caused narrow band spectral enhancements corresponding to an irregularity scale length of approximately 750 m. Such scale-sizes were generally consistent with those expected from the self-focusing instability at the power densities employed in the experiment (Attachment 11).

ATTACHMENT 1

To appear in WITS Handbook, 1989

SCINTILLATION TECHNIQUE FOR PROBING IONOSPHERIC IRREGULARITIES

Santimay Basu
Geophysics Laboratory (LIS)
Hanscom AFB, MA 01731

Sunanda Basu
Physics Research Division
Emmanuel College
Boston, MA 02115

ABSTRACT

The phenomenon of radio wave scintillation caused by ionospheric irregularities of electron density are described. The different indices of scintillation that provide a measure of intensity and phase scintillation have been defined. Both simple and sophisticated receiving systems used for recording scintillations are briefly described. The use of scintillation experiments in exploring the physical mechanisms of irregularity formation and in defining the constraints of practical communication systems are outlined.

INTRODUCTION

Radio waves from satellites or radio stars during their passage through the ionospheric irregularities of electron density develop random phase fluctuations across the wavefront. As the wavefront travels towards the ground, phase mixing occurs and, as a result, not only phase but amplitude fluctuations as well, develop on the ground. Due to the relative motion between the satellite, the ionosphere and the receiver on ground, the spatial pattern of amplitude and phase variation sweeps past the receiver and temporal variations of phase and amplitude known as scintillations are recorded by the receiver. In the case of radio stars or geostationary satellites, the temporal variation is caused by the ionospheric drift whereas in the case of low altitude (~1000 km) orbiting satellites, the satellite motion projected on to the ionosphere dictates the temporal structure.

SCINTILLATION PARAMETERS

The amplitude and phase fluctuations of the recorded signal are statistically characterized by two major parameters, amplitude and phase scintillation indices, denoted respectively by S_4 and σ_4 . Additional parameters such as the signal decorrelation time and spectral shape of signal fluctuations are also of importance for specifying effects on systems.

Scintillation Index, S_4

The amplitude scintillation index, S_4 , is defined as the ratio of the standard deviation of signal intensity and the average signal intensity and defined as

$$S_4 = \frac{(\langle I^2 \rangle - \langle I \rangle^2)}{\langle I \rangle^2} \quad (1)$$

The time interval over which this parameter is computed depends on the time period over

which the signal fluctuations are observed to be stationary. For geostationary satellite observations, a 3-minute to 15-minute data segment has been considered to be optimum whereas for orbiting satellites a data segment varying between 10-30 seconds has been used.

RMS Phase Deviation, σ_ϕ

The phase scintillation index is defined as the standard deviation of a linearly detrended phase data segment. The linear detrending over the appropriate data segment discussed in the previous paragraph removes the background phase variation caused by smooth changes of ionization density. Thus the phase scintillation index is defined as

$$\sigma_\phi = (\langle \phi^2 \rangle - \langle \phi \rangle^2)^{1/2} \quad (2)$$

Intensity Decorrelation Time, τ_I

In addition to the above two parameters the intensity decorrelation time, τ_I , defined as the time shift required to obtain signal correlation of 0.5 is also important. The decorrelation time, τ_I , is defined as

$$\frac{\langle I(t) I(t + \tau_I) \rangle}{\langle I(t) \rangle^2} = 0.5 \quad (3)$$

In the case of receiving systems capable of acquiring both signal amplitude and phase from a satellite source, the complex decorrelation time can be obtained by replacing the intensity terms in Eq. (3) by the complex amplitude.

Scintillation Spectrum

The time series of intensity and phase scintillation can be analyzed by the standard Fast Fourier Transform (FFT) or Maximum Entropy Method (MEM) to derive a plot of the variation of the power spectral density of amplitude or phase as a function of fluctuation frequency. The length of the data sample chosen for such spectral analysis needs to be stationary. For geostationary satellite observations a 3-minute scintillation data sample is, in general, found to be optimum. In such applications, the data digitization rate is required to be in the range of 30-50 Hz. The frequency range of the spectral analysis is dictated at the low frequency end by the inverse of the data sample duration and at the high frequency end by the Nyquist frequency which is half of the digitization rate. Thus for a 180-sec data segment from a geostationary satellite and 50-Hz sampling frequency, the frequency interval over which the spectrum is obtained corresponds to .0056 Hz to 25 Hz. For an average ionospheric drift of 50 ms^{-1} , the above frequency interval corresponds to spatial irregularity wavelength range of 8.9 km to 2 m. In the equatorial region, when strong to moderate levels of scintillations are observed, the ionospheric drift typically varies smoothly between 200 ms^{-1} to 50 ms^{-1} in the course of an evening which changes the coverage of irregularity wavelengths by a factor of 4. At high latitudes, the ionospheric drift variations are more severe with drifts changing from 50 ms^{-1} to 2000 ms^{-1} in a matter of minutes. Thus the irregularity wavelengths covered by the spectral analysis can vary greatly at high latitudes.

For orbiting satellites, at an altitude of 1000 km, the scan velocity of the propagation path through the F-region height of 300 km corresponds to 2.2 km/sec. The temporal structure of scintillation is, therefore, dictated by the scan velocity except at high latitudes where the ionospheric drift may not, on occasions, be negligible. In the case of orbiting satellites, data length of 10 sec and digitization rate of 125 Hz is found to be optimum. Considering only the ionospheric scan

velocity, the above parameters provide an irregularity wavelength coverage of 22 km to 18 m.

The scintillation parameters, defined above, can be readily computed from digital recordings. Many scintillation recording systems still employ chart recorders instead of digital recorders. For such systems, Whitney et al. [1969] defined the amplitude scintillation magnitude, SI_{dB} , in terms of dB excursions between the third peak up from the minimum and third peak down from the maximum signal levels. By providing calibrations with a signal source applied to the antenna input terminals of the receiver in terms of dB and using relatively fast chart speed so that the individual fadings and signal enhancements can be delineated, the third peak method is a useful way to quantify the analog recordings. Comparing digital and analog recordings Whitney et al. [1969] showed that the third peak method provides the dB excursions between the 2nd and 98th percentiles of signal fluctuations. In addition, he provided a useful graph that can be used to convert SI (dB) indices to S_4 indices. Attempts have also been made to manually digitize fast chart recordings to derive scintillation spectra. Reliability of such spectra is, however, limited because the response time of chart recorders does not exceed a few Hz thereby limiting the Nyquist frequency to 1 Hz or less. Since strong scintillations often contain fluctuation frequencies that exceed 10 Hz, manually derived spectra often provides misleading results.

SCINTILLATION RECORDING SYSTEMS

Total Power Recording System

The total power or systems recording intensity scintillations from geostationary satellites transmitting circularly polarized signals in the VHF range (typically at 136, 137, 244 and 257 MHz) can be achieved by a simple system. It consists of a ten element Yagi antenna, a commercial converter (noise figure of 3 dB, conversion gain of 10 dB) that converts VHF frequencies to a radio frequency (typically 28 MHz or 10.7 MHz) followed by a communications receiver tuned to accept the converted frequency, and operated with an IF bandwidth of 4 or 8 KHz. The above IF bandwidth is found to be wide enough to be unaffected by the frequency drift of the local oscillator. The communication receiver is operated in the fast AGC mode providing a time constant of .01 sec. The AGC voltage is fed to a chart recorder. In order to protect the pen from jitter, an external RC circuit with a time constant of 0.1 to .05 sec is often inserted between the AGC port and the pen recorder. The pen recorder is usually equipped with a d.c. buckout facility. The signals from geostationary satellites received with a ten-element Yagi antenna usually develop 110 dBm at the converter input. In order to calibrate the system, the antenna is disconnected from the converter and a calibrating signal source (providing 100-120 dBm at VHF followed by attenuators capable of varying the attenuation over a 100-dB range in 1-dB steps) is connected to the converter input. This is used to obtain calibration levels in the chart recorder at 1 to 3-dB intervals over the full scale deflection range. The system is so adjusted that the satellite signal level runs at a level 6 dB below the full-scale deflection. It should be noted that for scintillations arising from a diffraction process, the positive excursions do not exceed a 6-dB level although the associated negative excursions may approach 25 dB.

Recording of amplitude scintillations of L-band signals from stationary satellites can be achieved with a similar system by replacing the Yagi antenna with an 8-ft paraboloidal antenna and a low noise L-band converter.

With the advent of desktop computers, the AGC signal after d.c. buckout can be digitally recorded on a disk and processed to obtain the full range of statistical parameters, such as, S_4 index, decorrelation time, and scintillation spectrum, on a real-time basis.

Phase and Amplitude Scintillation Recording from Stationary Satellites

Stationary satellites transmitting single frequency phase coherent signals have been used to re-

cord both amplitude and phase scintillations by using a sophisticated computer-controlled receiver.

For such measurements an extended dynamic range receiver with an extremely stable local oscillator is employed. The receiver operates under computer control and once tuned to within a few hertz of a signal detected in a 10-Hz bandwidth, self-tunes to within ± 1 millihertz of the mean frequency as determined by the zero crossings averaged over a 20-sec period. Subsequent changes in frequency, either due to changes in ionospheric or geometrical doppler, are sensed by the system, which then retunes. At each retune, the local oscillator frequency information is recorded to allow reconstruction of the long-term phase in subsequent processing. In this way the system can measure signal phase variations with precision as would a coherent system except for any long-term relative frequency drifts between the satellite and receiver references.

Once a signal is properly acquired by the receiver, its quadrature components are sampled at 10 Hz and are digitally recorded along with time and pertinent system information. During initial off-line processing, these data are converted to signal intensity and continuous phase. While simple in concept the generation of continuous phase over long observation periods is prone to numerical difficulties. Since this is a single frequency measurement, the accumulation of phase over a period of several hours can result in extremely large values. These problems have been avoided by calculation and removal of the largest scale (for example, few hours) dispersive doppler changes during pre-processing.

Following initial processing, only phase variations with periods shorter than some tens of minutes remain. The data can then be treated using methods similar to those designed for, and proven, during the Wideband experiment [Fremouw et al., 1978]. Basically, this consists of separation of rapidly varying scintillation components of the signal from the longer term trends. The spectral components are separated by passing the phase data through a sharp cutoff high pass digital filter ($f_c = 0.0067$ Hz); there is generally no need to filter signal intensity, which has no low frequency component in the constant signal level, geostationary case.

PHASE AND AMPLITUDE SCINTILLATION MEASUREMENTS WITH MULTIFREQUENCY BEACON TRANSMISSIONS

DNA Wideband Satellite

Complex signal scintillation measurements have been performed by using multifrequency coherent radio beacon transmissions from an orbiting satellite. In 1976, the U.S. Defense Nuclear Agency launched the DNA Wideband satellite in a 1000-km orbit which radiated ten coherent radio spectral lines between the VHF and S bands [Fremouw et al., 1978]. The ten spectral lines were derived from a fundamental frequency of 11.4729 MHz and corresponded to one VHF, seven UHF, one L-band and one S-band transmission. The receiving system consisted of a tracking antenna and a receiver which was designed to maintain the coherence of the transmitted signals. The receiver incorporated a frequency synthesizer which generated a replica of the transmitted signal spectrum which were offset by the intermediate frequencies to generate the local oscillator signals.

The synthesizer was phase-locked by a loop operating on the output of the S-band reference receiver. Except for the first mixer, the reference receiver was identical to the measurement receiver channels at various frequencies. Nine measurement receiver channels were employed; one for VHF, one each for seven UHF channels, and one for L band. Remote receiving antennas comprised of identical measurement channels were used to perform spaced receiver scintillation observations.

The signals in each receiver channel were finally translated to an essentially zero frequency baseband by means of two quadrature detectors. The receiving system thus provided coherently

detected in-phase and quadrature components at VHF, seven UHF, and one L-band channel. Thus phase and intensity scintillation indices at all these frequencies, as well as, the second order statistics of complex signal scintillation in the temporal, spatial and spectral domains could be obtained. In addition to scintillation measurements, the second difference of phase measurement at the three UHF comb frequencies provided the total electron content (TEC) of the ionosphere.

The second difference of phase, $\Delta_2\phi$, is obtained by first forming the phase difference between a carrier and its upper sideband (413 MHz and 435 MHz) and the same carrier and its lower sideband (390 MHz and 413 MHz) and then taking the difference of the two differences. It can be shown [Fremouw et al., 1978] that

$$\Delta_2\phi = \frac{e^2}{2\pi\epsilon_0 mc} \frac{f_m^2}{f^3} N_T$$

where,
 e - electronic charge,
 m - mass of an electron,
 ϵ_0 - permittivity of free space,
 c - speed of light,
 f_m - the frequency separation between the UHF triad,
 f - center UHF frequency of the triad,
 N_T - total electron content up to satellite height.

The full complement of Wideband satellite signals were monitored from the auroral location of Poker Flat, Alaska, and the equatorial locations of Ancon, Peru and Kwajalein, Marshall Island. A brief period of Wideband satellite measurement was initially performed at Stanford, California through the relatively undisturbed ionosphere. The satellite was placed in a sun-synchronous orbit so that equatorward crossings were obtained around 1120 and 2320 local time and the auroral ionosphere was intercepted in the post-midnight time frame. The nighttime equator crossings could have been a couple of hours earlier for the interception of most intense early evening irregularities.

DNA HiLat Satellite

The DNA HiLat satellite was launched on June 27, 1983 in a near circular 800-km orbit with an inclination of 82°. The satellite carried a beacon transmitter package similar to the Wideband satellite, but, in addition, performed satellite in-situ measurements which were telemetered to ground using the L-band transmission of the beacon. The objective of the mission was to characterize the physical environment of the upper atmosphere through in-situ measurements, establish their relationship with the generation of plasma density irregularities and measure the effects of the irregularities on radio wave propagation. The beacon transmitter provided coherent transmission at L-band (1239 MHz), three UHF frequencies (447, 413 and 378 MHz), and one at VHF (138 MHz). The L-band signal while serving as a phase reference for phase scintillation measurement was also modulated by the telemetry signal. At the receiver, an L-band carrier recovery loop has been used to generate the reference signal for the demodulation of the telemetry data and synchronous demodulation of the UHF and VHF frequencies.

The HiLat satellite in-situ instrument package consisted of a J-sensor for the measurement of the local flux of electrons over the energy range of 20 eV to 20 keV in 16 channels, a magnetometer for the measurement of field-aligned 'Birkeland' currents, an ion drift meter for the measurement of thermal ion density and cross track ion drift, a retarding potential analyzer for the measurement of the ram component of ion drift, ion composition and ion temperature and an electron Langmuir probe. In addition, a vacuum ultraviolet (UV) imager was included to obtain auroral UV images in full daylight in selectable spectral windows over the range of 1100 Å to

2078 Å. The in-situ package provided an excellent array of instruments that characterized the currents, particles and fields in the high latitude ionosphere.

The data from the HiLat satellite were acquired at Sondrestrom, Greenland located in the dayside cusp region and at Fort Churchill, Canada and Tromso, Norway corresponding to two auroral locations in the American and European sectors. In addition, a portable Rover receiving system normally located at Bellevue, Washington could be deployed anywhere at high latitudes to perform campaign observations.

The Polar Bear Satellite

This satellite carrying a beacon package identical to that of the HiLat satellite but more limited in-situ instrumentation providing UV imaging and magnetometer measurements only was launched in 1986. Both HiLat and Polar Bear satellites were monitored with identical receiving systems at the four high latitude locations mentioned above.

APPLICATION OF SCINTILLATION MEASUREMENTS

Scintillation measurements have been used as a key diagnostic for the presence of the irregularities of electron density in the ionosphere. This knowledge is important, on one hand, to determine the spatial and temporal distribution of the ionospheric irregularities and to understand the physical processes that lead to the formation of such irregularities. On the other hand, the characteristics of the scintillating signal structure determines how the performance of a communication link or a radar system can be degraded. The key scintillation characteristics that contribute to our knowledge of geophysics and the parameters that dictate the degradation of system performance are briefly summarized in the following paragraphs.

The key irregularity parameter, namely the integrated electron density deviation (ΔN) of the ionospheric irregularities, can be derived from intensity and phase scintillation measurements. In the framework of weak scatter theory the intensity and phase scintillation indices, S_4 and σ_4 , have been related [Rino, 1979] to ΔN and the geometrical term accounting for both the geometry of the propagation path and the irregularity anisotropy. Of the two scintillation indices, the phase scintillation index, σ_4 , is more useful as it is related, in a straightforward manner, to the irregularity parameters.

The other irregularity parameter of great importance to our understanding of the generation of irregularities is related to the form and shape of the irregularity spectrum. The scintillation spectrum reflects the form of the irregularity spectrum and the spectral index of scintillation has been simply related to the 3-dimensional irregularity spectral index. As such, the spectral studies of both intensity and phase scintillations have been performed and important conclusions regarding the irregularity spectral shapes, spectral indices and drifts have been derived [Basu et al., 1985].

Scintillation measurements, because of their relative simplicity, have been most useful in determining global morphology of irregularities. Earlier reviews were presented by Aarons [1982] and Yeh and Liu [1982]. Figure 1 taken from S. Basu et al. [1988] provides a synopsis of the global distribution of scintillation occurring regions during the solar maximum and minimum periods.

Since the maximum scintillation amplitude occurs in the equatorial region, specialized reviews have appeared which deal only with this region [Aarons, 1977; Basu and Basu, 1981; 1985]. The latter two reviews discuss the impact of equatorial plasma density depletions or "bubbles" caused by the Rayleigh Taylor instability [Ossakow, 1981] on scintillation magnitude and longitudinal variability in this region. Further, data from the equatorial anomaly region have been used to study

the effects of scintillations on communications and radar systems through the variability of spectral shape, decorrelation time, cumulative distribution functions of signal amplitude, fade durations, the distribution of phase and intensity rates, and depolarization effects caused by diffractive scattering [Su. Basu et al., 1983; S. Basu et al., 1987; Lee et al., 1982; Franke and Liu, 1983].

At high latitudes the scintillation technique was the first to establish that the polar cap was the seat of large amplitude irregularities during solar maximum [Aarons et al., 1981; Su. Basu et al., 1985] which could be caused by the gradient-drift instability occurring at the edges of convecting plasma density enhancements known as patches [Weber et al., 1984; Tsunoda, 1988] or by F-layer sun-aligned arcs [Weber and Buchau, 1981]. The DNA Wideband satellite did much to elucidate the sheet-like anisotropy of auroral irregularities and their morphology [Fremouw et al., 1977; Rino et al., 1978; Rino and Matthews, 1980], while the DNA HiLat satellite with its complement of scintillations and in-situ package was instrumental in identifying velocity shears as a viable source of small-scale irregularities in the ionosphere [Su. Basu et al., 1986].

Thus we find that scintillation measurements, particularly in conjunction with other diagnostics, have contributed greatly to our understanding of plasma processes in the coupled magnetosphere-ionosphere-thermosphere system. Multi-frequency scintillation studies have provided guidelines for the design of communication systems.

ACKNOWLEDGEMENT

The work at Emmanuel College was supported by AFGL Contract F19628-86-K-0038.

REFERENCES

Aarons, J., Equatorial scintillations: A review, IEEE Trans. Antennas Propagat., **AP-25**, 729, 1977.

Aarons, J., Global morphology of ionospheric scintillations, Proc. IEEE, **70**, 360, 1982.

Aarons, J., J.P. Mullen, H.E. Whitney, A. Johnson, and E. Weber, VHF scintillation activity over polar latitudes, Geophys. Res. Lett., **8**, 277, 1981.

Basu, S. and Su. Basu, Equatorial scintillations - a review, J. Atmos. Terr. Phys., **43**, 473, 1981.

Basu, Su. and S. Basu, Equatorial scintillations: Advances since ISEA-6, J. Atmos. Terr. Phys., **47**, 753, 1985.

Basu, S., E.M. MacKenzie, Su. Basu, E. Costa, P.F. Fougere, H.C. Carlson, Jr., and H.E. Whitney, 250 MHz/GHz scintillation parameters in the equatorial, polar and auroral environments, IEEE J. Selec. Areas Commun., **SAC-5**, 102, 1987.

Basu, S., E. MacKenzie, and Su. Basu, Ionospheric constraints on VHF/UHF communications links during solar maximum and minimum periods, Radio Sci., **33**, 1988.

Basu, Su., S. Basu, J.P. McClure, W.B. Hanson, and H.E. Whitney, High-resolution topside in-situ data of electron densities and VHF/GHz scintillations in the equatorial region, J. Geophys. Res., **88**, 403, 1983.

Basu, Su., S. Basu, E. MacKenzie, and H.E. Whitney, Morphology of phase and intensity scintillations in the auroral oval and polar cap, Radio Sci., **20**, 347, 1985.

Basu, Su., S. Basu, C. Senior, D. Weimer, E. Nielsen, and P.F. Fougere, Velocity shears and sub-km scale irregularities in the nighttime auroral F-region, Geophys. Res. Lett., **13**, 101, 1986.

Franke, S.J. and C.H. Liu, Observations and modeling of multi-frequency VHF and GHz scintillations in the equatorial region, J. Geophys. Res., **88**, 7075, 1983.

Fremouw, E.J., C.L. Rino, R.C. Livingston, and M.D. Cousins, A persistent subauroral scintillation enhancement observed in Alaska, Geophys. Res. Lett., **4**, 539, 1977.

Fremouw, E.J., R.L. Leadabrand, R.C. Livingston, M.D. Cousins, C.L. Rino, B.C. Fair, and R.A. Long, Early results from the DNA Wideband satellite experiment - complex-signal scintillation, Radio Sci., **13**, 167, 1978.

Lee, M.C., A. DasGupta, J.A. Klobuchar, S. Basu, and Su. Basu, Depolarization of VHF geostationary satellite signals near the equatorial anomaly crest, Radio Sci., **17**, 399, 1982.

Ossakow, S.L., Spread-F theories - a review, J. Atmos. Terr. Phys., **43**, 437, 1981.

Rino, C.L., A power-law phase screen model for ionospheric scintillation, 1, Weak scatter, Radio Sci., **14**, 1135, 1979.

Rino, C.L. and S.J. Matthews, On the morphology of auroral zone radio wave scintillation, J. Geophys. Res., **85**, 4139, 1980.

Rino, C.L., R.C. Livingston, and S.J. Matthews, Evidence for sheet-like auroral ionospheric irregularities, Geophys. Res. Lett., **5**, 1039, 1978.

Tsunoda, R.T., High-latitude F-region irregularities: a review and synthesis, Revs. Geophysics, **26**, 719, 1988.

Weber, E.J. and J. Buchau, Polar cap F layer auroras, Geophys. Res. Lett., **8**, 125, 1981.

Weber, E.J., J. Buchau, J.G. Moore, J.R. Sharber, R.C. Livingston, J.D. Winningham, and B.W. Reinisch, F layer ionization patches in the polar cap, J. Geophys. Res., **89**, 1683, 1984.

Whitney, H.E., J. Aarons, and C. Malik, A. proposed index for measuring ionospheric scintillations, Planet. Space Sci., **17**, 1069, 1969.

Yeh, K.C. and C.H. Liu, Radiowave scintillations in the ionosphere, Proc. IEEE, **70**, 324, 1982.

"WORST CASE" FADING DEPTHS AT L-BAND

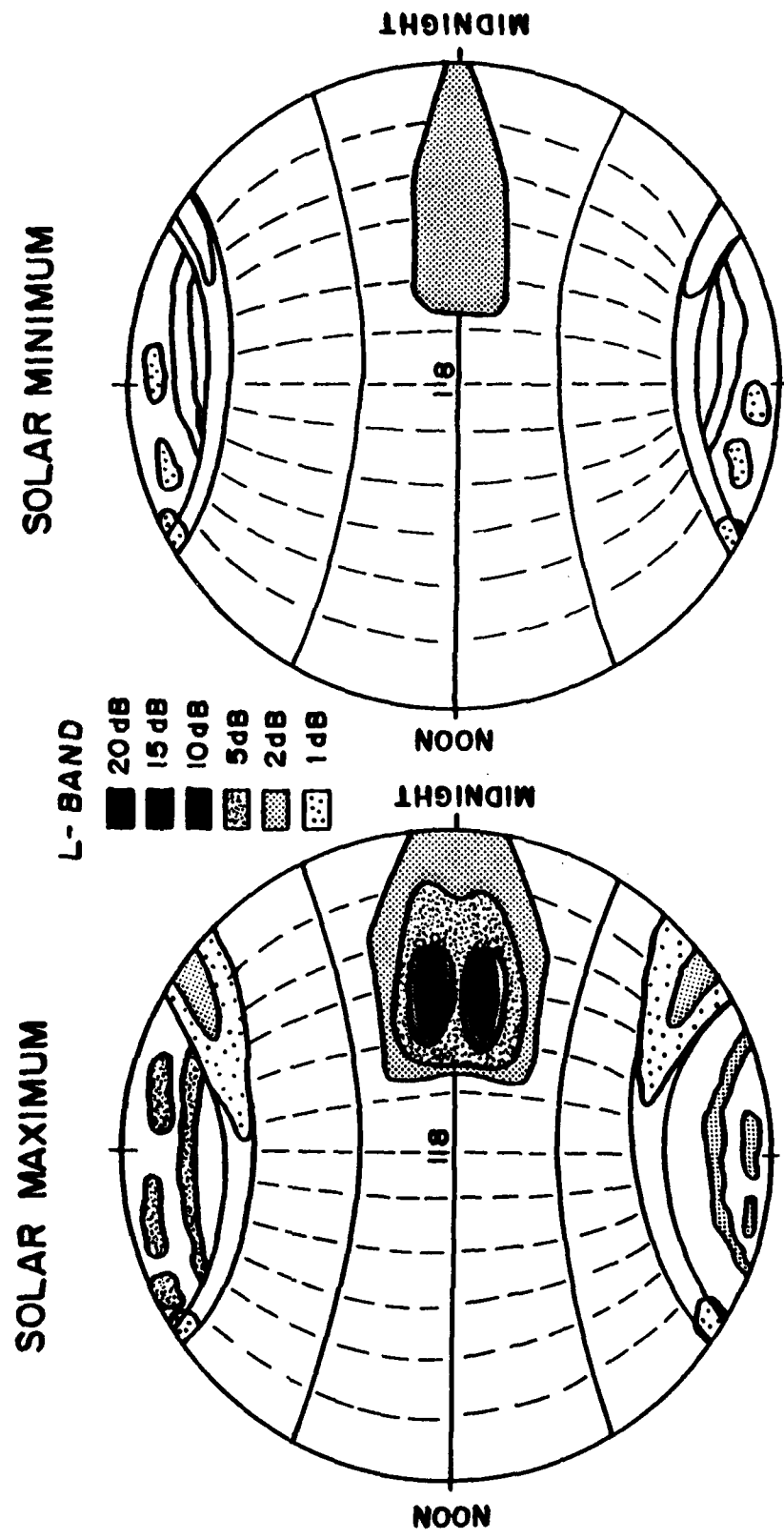


Figure 1. Global variation of scintillation fades during solar maximum and solar minimum.

AGARD

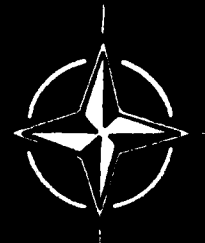
ADVISORY GROUP FOR AEROSPACE RESEARCH & DEVELOPMENT

7 RUE ANCELLE 92200 NEUILLY SUR SEINE FRANCE

**Paper Reprinted from
Conference Proceedings No.419**

SCATTERING AND PROPAGATION IN RANDOM MEDIA

NORTH ATLANTIC TREATY ORGANIZATION



IONOSPHERIC SCINTILLATIONS AND IN-SITU MEASUREMENTS AT AN AURORAL LOCATION IN THE
EUROPEAN SECTOR

Santimay Basu
Air Force Geophysics Laboratory
Hanscom AFB MA 01731

Sunanda Basu and Eileen MacKenzie
Emmanuel College
Boston MA 02115

Dan Weimer
Regis College
Weston MA 02193

SUMMARY

The orbiting HiLat satellite launched by the Defense Nuclear Agency in 1983 offered a unique opportunity for studying the ionospheric scintillation parameters in relation to the in-situ measurements of ionization density, drift velocity, field-aligned current, and particle precipitation during the sunspot minimum period. This paper discusses the results of such a morphological study performed by the Air Force Geophysics Laboratory based on their observations at the auroral oval station of Tromso, Norway. The dynamics of the spatial and temporal extent of this region are illustrated in the invariant latitude/magnetic local time grid. The geometrical enhancement of scintillations observed during the alignment of the propagation path with the local magnetic L-shell is shown to be the most consistent and conspicuous feature of scintillations in the nighttime auroral oval. The steepening of phase spectral slope in this region is indicative of the presence of L-shell aligned sheet-like irregularities at long scale lengths. The seasonal variation of total electron content (TEC) determined from the differential Doppler measurements of HiLat transmissions is discussed in relation to the in-situ density measurements at 830 km. The results are also utilized to illustrate the dependence of ionospheric structure parameters on short-term variability of solar activity during the sunspot minimum period. Special effort is made to illustrate that the joint study of scintillation/TEC and in-situ parameters provides an insight into the nature of magnetospheric coupling with the high latitude ionosphere.

INTRODUCTION

A wide variety of C³I systems suffers degradation in performance due to phase and intensity scintillations imposed by the ionospheric irregularities of electron density. There is a great deal of interest in understanding the development of such irregularities at high latitudes where the ionosphere is often strongly coupled with the magnetosphere. In such an environment the distant magnetosphere serves to activate different sources of free energy, e.g., electron precipitation, field aligned currents, electric fields, etc., that control the formation of ionospheric irregularities. No longer is it possible to pursue a study of the irregularity development in the local ionospheric environment without considering the coupling between the ionosphere and the magnetosphere. This approach is particularly useful in extrapolating our knowledge of the natural ionospheric irregularity structures to problems related to the structuring of artificially injected plasma clouds in the high latitude ionosphere.

In an effort to pursue a study of plasma structuring in the above context, the Defense Nuclear Agency (DNA) launched, on 27 June 1983, the HiLat satellite in a circular 830-km orbit at 82° inclination (Fremouw et al., 1985). The satellite transmits coherent signals at 137, 390, 413, and 436 MHz and the phase reference signal at 1239 MHz to measure complex signal scintillation and total electron content (TEC). It also carries a variety of in-situ probes providing measurements of ion density, ion drift, energetic electron precipitation, field aligned currents, and emissions at two visible wavelengths. All instruments except the Langmuir probe, the vacuum-ultraviolet imager and a part of the magnetometer continue to operate reliably. The major objective of the HiLat satellite program is to provide a quantitative specification of high latitude scintillation strength and, in particular, the temporal and spatial spectra of intensity and phase fluctuations and the shape of the irregularity structures. These parameters provided by the radio beacon experiments are supported by the simultaneous in-situ data that define the background ionospheric processes. The morphology of ionospheric structures and magnetospheric control thereof derived primarily from HiLat observations at Sondrestrom, Greenland have been enumerated by Vickrey et al. (1985).

In this paper we shall concentrate on the HiLat satellite observations performed by the Air Force Geophysics Laboratory at Tromso, Norway during the 1984-1985 period. The station is located in the central part of the auroral oval during the nighttime under magnetically quiet conditions as defined by the planetary magnetic index $K_p < 3.5$. We shall study the strength and the structure specifications of complex signal scintillations in the spatial and temporal frames of invariant latitude and magnetic local time. These distributions will then be examined in the context of in-situ plasma structures observed by the HiLat satellite in this environment and the

theoretical predictions of structures that characteristically develop in this region through gradient drift and Kelvin Helmholtz instability processes.

RESULTS

In this section we shall first illustrate the space time variations of the statistical parameters that define the complex scintillation magnitudes and their structure. In order to avoid the effects of multipath propagation, the data acquired above a satellite elevation angle of 20° were used in the study. This provided a maximum latitude coverage of about 17° at an ionospheric height of 350 km around the station. Due to precession of the Hilat orbit to earlier times each day, a full coverage in local time is also obtained over a season (i.e., 3 months) when the ascending and descending node passes are combined.

The top and bottom panels of Figure 1(a) illustrate the rms phase deviation of 137 MHz scintillation for winter 1983 (start of observations in December 1983 to January 1984) and summer 1984 (May-July, 1984) respectively for $K_p < 3.5$. The rms phase deviation is computed over a 30-second data interval. Since the projected scan velocity of the satellite is 3 km/sec at 350 km, the data interval covers irregularity scale sizes as large as 90 km. The data are binned in 2.5° latitude and 1 hour time intervals and the median values for each bin are indicated in the diagram. Each bin contains at least ten data points. The tic marks along the noon-midnight and the dawn-dusk meridians indicate 10° intervals between 50° - 90° invariant latitudes (to be denoted as Λ). The sharp increase in rms phase deviation exceeding 5 radians over a narrow latitude swath (65° - $67.5^{\circ}\Lambda$) between the pre-midnight and dawn periods is the most conspicuous feature of both diagrams. This region of enhancement corresponds to the location where the alignment of the ray path with the magnetic L-shell occurs (Rino et al., 1978). This region also coincides with the location of the diffuse aurora which is the seat of density irregularities. As we shall show later the region has enhanced total electron content (TEC) on a statistical basis due to the occurrence of plasma density blobs. Thus a combination of high irregularity amplitude, increased TEC and geometrical factors contribute to the pronounced increase of phase scintillations. Comparing the top and bottom panels of Figure 1(a) the magnitude of phase scintillations during winter is found to be larger than summer. This may appear to be somewhat intriguing because the TEC (to be shown later) was higher in summer. This leads us to conclude that the irregularities are probably less preponderant during summer in the presence of enhanced ionization of the underlying E-region.

The top and bottom panels of Figure 1(b) show the behavior of rms phase deviation at 137 MHz during February-April and August-October, 1984. The nighttime enhancement of phase deviation between 65° - $67.5^{\circ}\Lambda$ is again observed. The larger phase deviation observed during the vernal equinox can be related to increased solar activity during this period as will be shown in a subsequent diagram.

The remaining results will be presented in a different format and will indicate the variations of the statistical parameters with invariant latitude in the midnight and noon time periods only. These are basically obtained from a noon-midnight cut through the dial plots shown in Figures 1(a) and 1(b). When the number of data points in a particular bin over the noon-midnight sector fall below ten, the values are extrapolated from an adjacent time sector. Figure 2 shows such a plot for rms phase deviation obtained during 1984 and 1985. This figure illustrates an overall decrease of scintillations in 1985 due to decreased solar activity.

The intensity scintillation magnitudes have been expressed in terms of the standard S_4 index, defined as the normalized variance of signal intensity (Briggs and Parkin, 1963). Figure 3 shows the variation of S_4 index at 137 MHz with invariant latitude during noon and midnight observed during 1984 and 1985. The nighttime enhancements of S_4 index in the region of alignment of the ray path with the magnetic L-shell (65° - $67.5^{\circ}\Lambda$) is observed to be much less pronounced when it is compared to σ_{ϕ} enhancements shown in Figure 2. This indicates that the L-shell alignment of km-scale irregularities causing intensity scintillations is considerably less than the irregularities in the tens of kilometers scale that control the σ_{ϕ} values. The nighttime scintillation magnitudes during February-April, 1984 are again higher than that during August-October, 1984 due to enhanced solar activity.

In Figure 4, we show the behavior of power law spectral index, p_{ϕ} , for phase scintillations at 137 MHz during 1984 and 1985. A linear least square fit to the phase spectrum indicating the variation of the logarithm of power spectral density (psd) with the logarithm of frequency is obtained over the frequency interval of 0.2 Hz to 10 Hz. The best-fit line provides p_{ϕ} as it defines the dependence of psd on frequency f as $psd \propto f^{p_{\phi}}$. Considering the scan velocity of the ray path through the F-region, the fit range 0.2 Hz to 10 Hz corresponds to the scale size regime of about 15 km to 300 m. This regime encompasses the dominant structures that cause phase and intensity scintillations at VHF and UHF over the observing data interval. From Figure 4, it may be noted that the phase spectral index is least affected by the propagation geometry and does not show significant variations with season and solar activity in contrast to the behavior of S_4 and σ_{ϕ} . There exists, however, a tendency for p_{ϕ} to increase around $65^{\circ}\Lambda$, during the nighttime. Since this location corresponds to the average location of the diffuse aurora, the associated E-region conductivity may account for damping the short scale irregularities and causing the phase spectrum to steepen (Vickrey and Kelley, 1982). This steepening may also arise from increased psd at larger scales in the geometrical enhancement region due to better L-shell alignment of large scale irregularities as noted in connection with the increased σ_{ϕ} in comparison with S_4 . The enhancements of p_{ϕ} are, however, smooth and distributed in contrast to the sharp geometrical enhancements of σ_{ϕ} . Probably, the spectral steepening arises from an interplay of both geophysical and geometrical effects.

The comb of three UHF transmissions from HiLat is used to derive the total electron content of the ionosphere up to the satellite altitude of 830 km by the differential Doppler technique (Fremouw et al., 1978). Figure 5 shows the latitude variation of median TEC values during the noon and midnight for different seasons. The next diagram, Figure 6, shows the observed variation of noontime TEC in relation to the sunspot number. The effects of the solar activity and season on TEC appear to be coupled. At high latitudes, owing to the near vertical orientation of the earth's magnetic field, the ionospheric irregularities of electron density at F-region height are usually extended in altitude. The integrated effect of the irregularities on radio wave propagation, such as scintillation, is therefore, weighted by the total electron content of the ionosphere. Thus measurements of irregularity amplitude, $\Delta N/N$ (ΔN being the rms electron density fluctuation and N the background density), and total electron content may form the basis for a modeling of scintillation magnitudes.

Among the various in-situ parameters probed by the satellite borne sensors, the in-situ ion-density measurement is an important parameter. In the F-region, due to charge neutrality, the electron and ion densities are equal. Figure 7 shows the variation of this parameter with latitude in the noon-midnight time frame as a function of season in 1984 and 1985 during magnetically quiet conditions. The ion density at 830 km is observed to follow closely the pattern of TEC variations shown earlier in Figure 5. The ion density variations are also controlled by both solar activity and season.

Although we did not illustrate the variation of scintillations and background ionospheric parameters with magnetic activity, it should be emphasized that the magnetic activity in addition to sunspot number exerts overwhelming control of scintillations at high latitudes (Basu and Aarons, 1980; Basu et al., 1985). Our HiLat observations indicate that during magnetically active conditions scintillation magnitudes are enhanced during the nighttime and the region of enhanced activity extends both in the poleward and the equatorward directions. Irrespective of the level of solar activity, scintillations are enhanced during magnetic disturbances.

DISCUSSIONS

We have shown that the most notable feature in the observed scintillation morphology at this auroral station even under magnetically quiet to moderate conditions is the enhancement of scintillations over a narrow latitude interval centered at 65°A in the nighttime sector. This narrow band increase of scintillations coincides with the expected region of geometrical enhancement due to the alignment of the ray path with the magnetic L-shell oriented irregularities. It is interesting to note that the boundary blobs which signify plasma density enhancements also occur in this region (Rino et al., 1983). The spatial configuration of the blobs is controlled by the high latitude convection pattern which is mostly E-W in the auroral region (Heelis et al., 1982). Robinson et al. (1985) have shown with the help of simulation studies that even a primarily circular patch of ionization being convected in from the polar cap would assume a narrow in latitude and elongated in longitude shape. These blobs can also develop small scale irregularities on their trailing edges through $E \times B$ instability mechanisms. In general, the plasma blobs transported from distant regions get continually structured in the convection field and contribute a major source of nighttime auroral scintillations.

The other notable finding related to the scintillation structure is the steep phase spectral slopes observed in the region of geometrical enhancement. This region coincides with the central part of the diffuse aurora under magnetically quiet conditions as has been recently shown by Hardy et al., (1985) from DMSP satellite observations. Unlike the limited HiLat satellite data base of particle precipitation the DMSP satellites have provided a very large amount of data which have been organized by Hardy et al. to show the characteristic variations of particle precipitation with magnetic activity. The average energy of the particle precipitation in the diffuse auroral region is on the order of a few keV which is sufficient to produce a conducting E-region. This could reduce the lifetime of small scale irregularities (~ 100 m) and contribute to the observed steepening of the phase spectral indices. Basu et al. (1984) have illustrated such steepening of in-situ density spectra in regions of energetic auroral particle precipitation.

The structures present in the in-situ ion density probed by the HiLat satellite have recently been investigated (Weimer 1987). This study indicates that plasma density blobs at 830 km are concentrated over a fairly narrow latitude interval. This region when mapped down the magnetic field line corresponds approximately with the region of enhanced scintillations. These results indicate that, on a statistical basis, the blobs in addition to their E-W extent are also extended along the magnetic field lines to the topside ionosphere. The altitude profiles of the blobs have been published earlier using incoherent scatter radar measurements (Vickrey et al., 1980).

The extension of blobs to altitudes as high as 830 km indicates that magnetospheric coupling effects need to be included in the analysis of high latitude F-layer instabilities. The inclusion of ion-inertia in the $E \times B$ instability theories results in a reduction of growth rates and generation of irregularities with spectral isotropy (Mitchell et al., 1985). In the non-inertial domain the irregularity spectra become anisotropic in the north-south and the east-west directions. Thus, the irregularity spectral indices are expected to be different in the north-south and east-west directions in the non-inertial case and identical for the inertial case. At Tromsø, in addition to making HiLat observations that provide a north-south scan through the ionosphere, we have performed scintillation observations with near-stationary polar beacon satellites which provide an east-west scan controlled by ionospheric motion. The spectral indices of both sets of measurements are found to be.

approximately equal indicating that the inertial effects are important in the generation of kilometer scale irregularities at high latitudes which cause VHF scintillations.

Another type of auroral irregularity not associated with large scale organized density gradients (such as to be found on the edges of blobs) but associated with velocity shears with shear gradient scale lengths ~ 10 km has been identified from HiLat observations (Basu et al., 1986). These irregularities, having considerable psd at the shorter scales, can cause intense VHF scintillations at the edges of auroral arcs in association with upward field aligned currents. In view of the well-known temporal and spatial variability of auroral arcs, the signature of such velocity shears will be difficult to identify in a statistical study of auroral scintillations.

REFERENCES

Basu, Su. and J. Aarons, The morphology of high-latitude VHF scintillation near 70° W, Radio Sci., 15, 59, 1980.

Basu, Su., S. Basu, E. MacKenzie, W.R. Coley, W.B. Hanson, and C.S. Lin, F-region electron density irregularity spectra near auroral acceleration and shear regions, J. Geophys. Res., 89, 5554, 1984.

Basu, Su., S. Basu, E. MacKenzie, and H.E. Whitney, Morphology of phase and intensity scintillations in the auroral oval and polar cap, Radio. Sci., 20, 347, 1985.

Basu, Su., S. Basu, C. Senior, D. Weimer, E. Nielsen, and P.F. Fouger, Velocity shears and sub-km scale irregularities in the nighttime auroral F-region, Geophys. Res. Lett., 13, 101, 1986.

Briggs, B.H. and I.A. Parkin, On the variation of radio star and satellite scintillation with zenith angle, J. Atmos. Terr. Phys., 25, 339, 1963.

Fremouw, E.J., R.L. Leadsbrand, R.C. Livingston, M.D. Cousins, C.L. Rino, B.C. Fair, and R.A. Long, Early results from the DNA Wideband satellite experiment: Complex-signal scintillation, Radio Sci., 13, 167, 1978.

Fremouw, E.J., H.C. Carlson, T.A. Potemra, P.F. Bythrow, C.L. Rino, J.F. Vickrey, R.C. Livingston, R.E. Huffman, C.-I. Meng, D.A. Hardy, F.J. Rich, R.A. Heelis, W.B. Hanson, and L.A. Wittwer, The HiLat mission, Radio Sci., 20, 416, 1985.

Hardy, D.A., M.S. Gussenhoven, and E. Holeman, A statistical model of auroral electron precipitation, J. Geophys. Res., 90, 4229, 1985.

Heelis, R.A., J.K. Lowell, and R.W. Spiro, A model of the high-latitude ionospheric convection pattern, J. Geophys. Res., 87, 6339, 1982.

Mitchell, H.G., Jr., J.A. Fedder, M.J. Keskinen, and S.T. Zalesak, A simulation of high latitude F-layer instabilities in the presence of magnetosphere-ionosphere coupling, Geophys. Res. Lett., 12, 283, 1985.

Rino, C.L., R.C. Livingston, and S.J. Matthews, Evidence for sheet-like auroral ionospheric irregularities, Geophys. Res. Lett., 5, 1039, 1978.

Rino, C.L., R.C. Livingston, R.T. Tsunoda, R.M. Robinson, J.F. Vickrey, C. Senior, M.D. Cousins, J. Owen, and J.A. Klobuchar, Recent studies of the structure and morphology of auroral zone F-region irregularities, Radio Sci., 18, 1167, 1983.

Robinson, R.M., R.T. Tsunoda, J.F. Vickrey, and L. Guerin, Source of F-region ionization enhancements in the nighttime auroral zone, J. Geophys. Res., 90, 7533, 1985.

Vickrey, J.F. and M.C. Kelley, The effects of a conducting E-layer on classical F-region cross-field plasma diffusion, J. Geophys. Res., 87, 4461, 1982.

Vickrey, J.F., C.L. Rino, and T.A. Potemra, Chantanika/TRIAD observations of unstable ionization enhancements in the auroral F-region, Geophys. Res. Lett., 7, 789, 1980.

Vickrey, J.F., R.C. Livingston, R.T. Tsunoda, C.L. Rino, N.B. Walker, T.M. Dabbs, R.M. Robinson, and R.A. Heelis, The SRI ionospheric plasma structure and dynamics program - 1985 results, Final Technical Report, SRI International, June 1985.

Weimer, D.R., Large-scale plasma density fluctuations measured with the HiLat satellite at 830 km altitude, AFGL Technical Rpt., Hanscom AFB, MA, 1987.

ACKNOWLEDGMENT

This work was supported by AFGL Contract F19628-86-K-0038 with Emmanuel College and by the Defense Nuclear Agency. The authors thank L. Wittwer, H.C. Carlson, and F.J. Rich for their interest and support.

TROMSO HILAT
 137 MHz $K_p < 3.5$
 MEDIAN RMS PHASE DEVIATION σ_ϕ (radians)

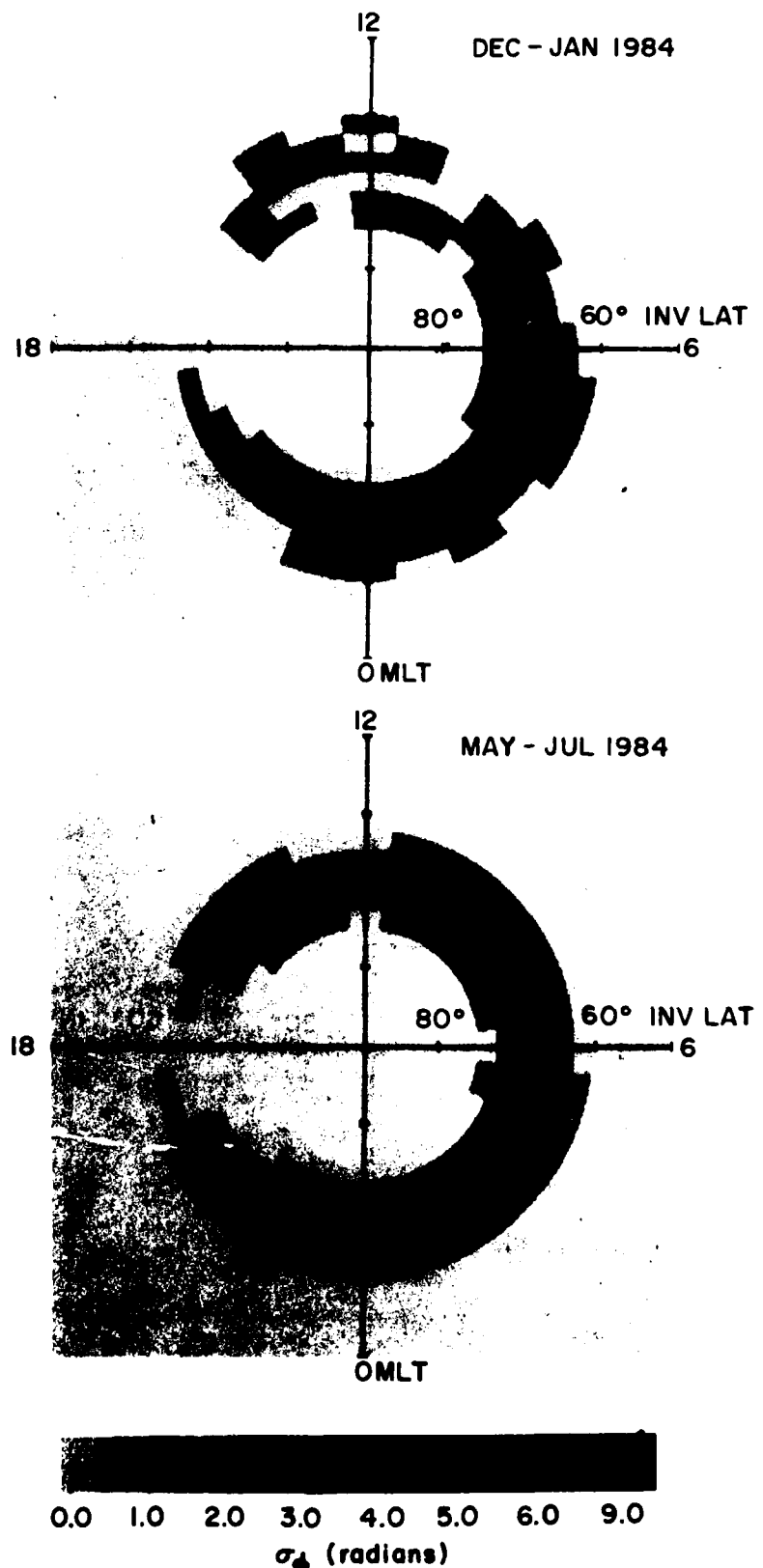


Figure 1a. Variations of rms phase deviation at 137 MHz with invariant latitude and magnetic local time during winter and summer.

TROMSO HILAT
 137 MHz $K_p < 3.5$
 MEDIAN RMS PHASE DEVIATION σ_ϕ (radians)

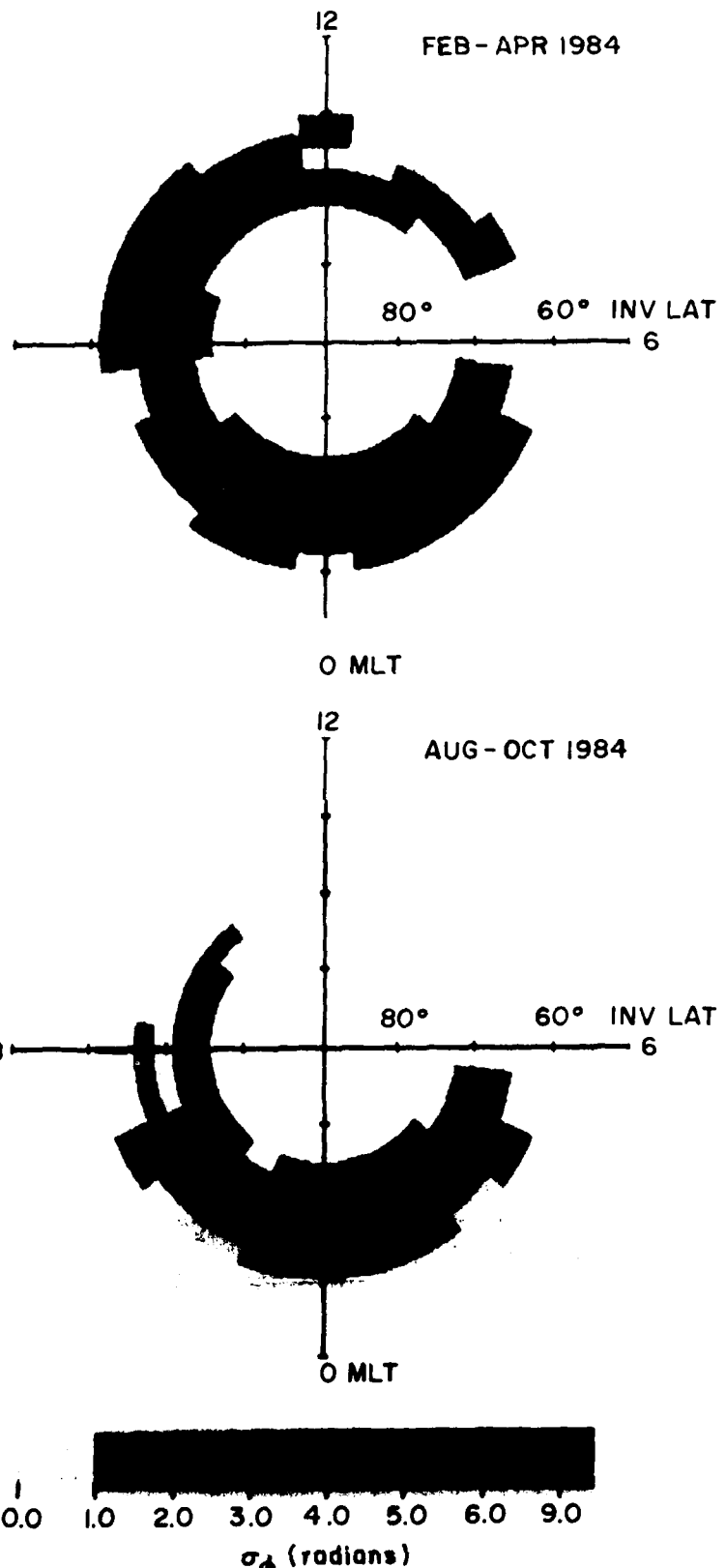


Figure 1b. Equinoctial variations of 137 MHz phase deviation with invariant latitude and magnetic local time.

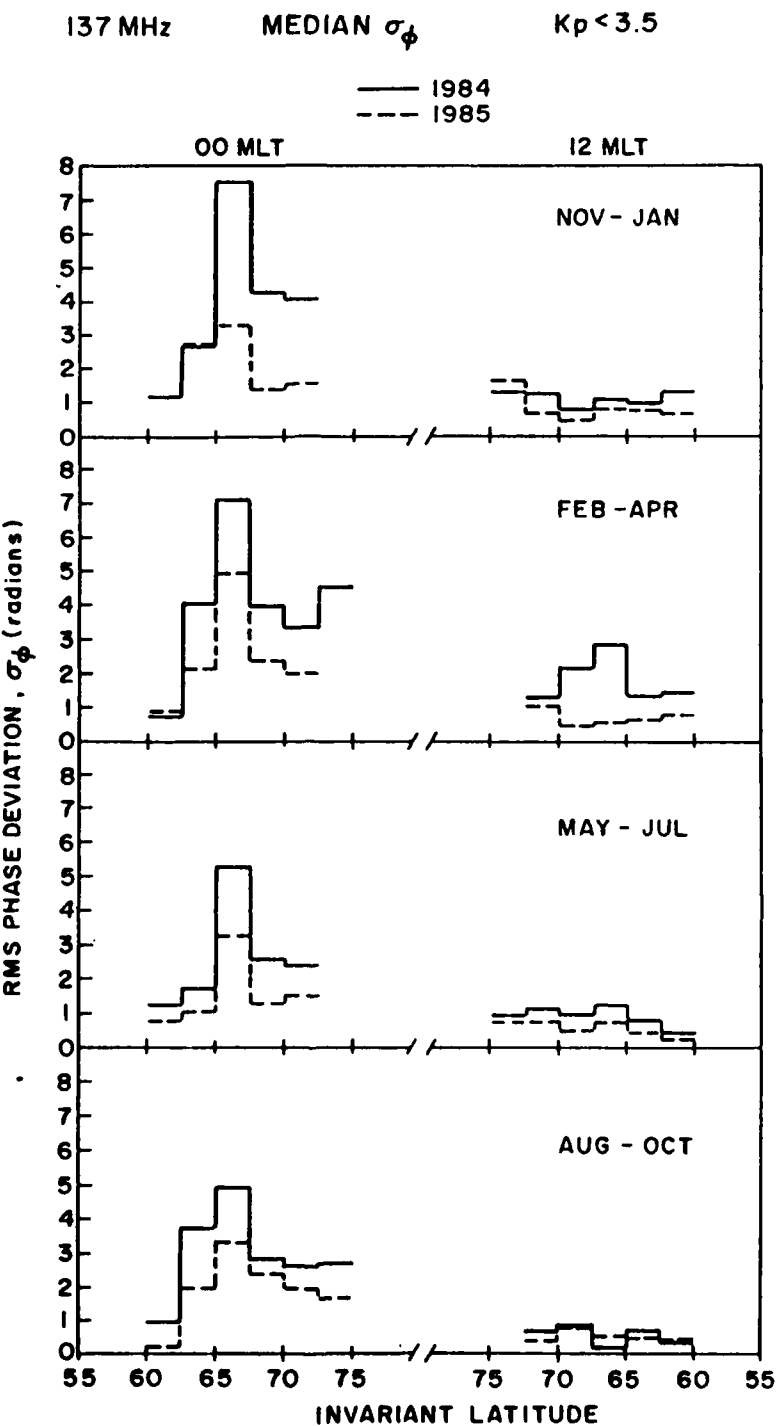


Figure 2. Seasonal variations of rms phase deviation at 137 MHz with invariant latitude along the noon-midnight meridian in 1984 and 1985.

137 MHz MEDIAN S_4

$K_p < 3.5$

— 1984
- - - 1985

00 MLT

12 MLT

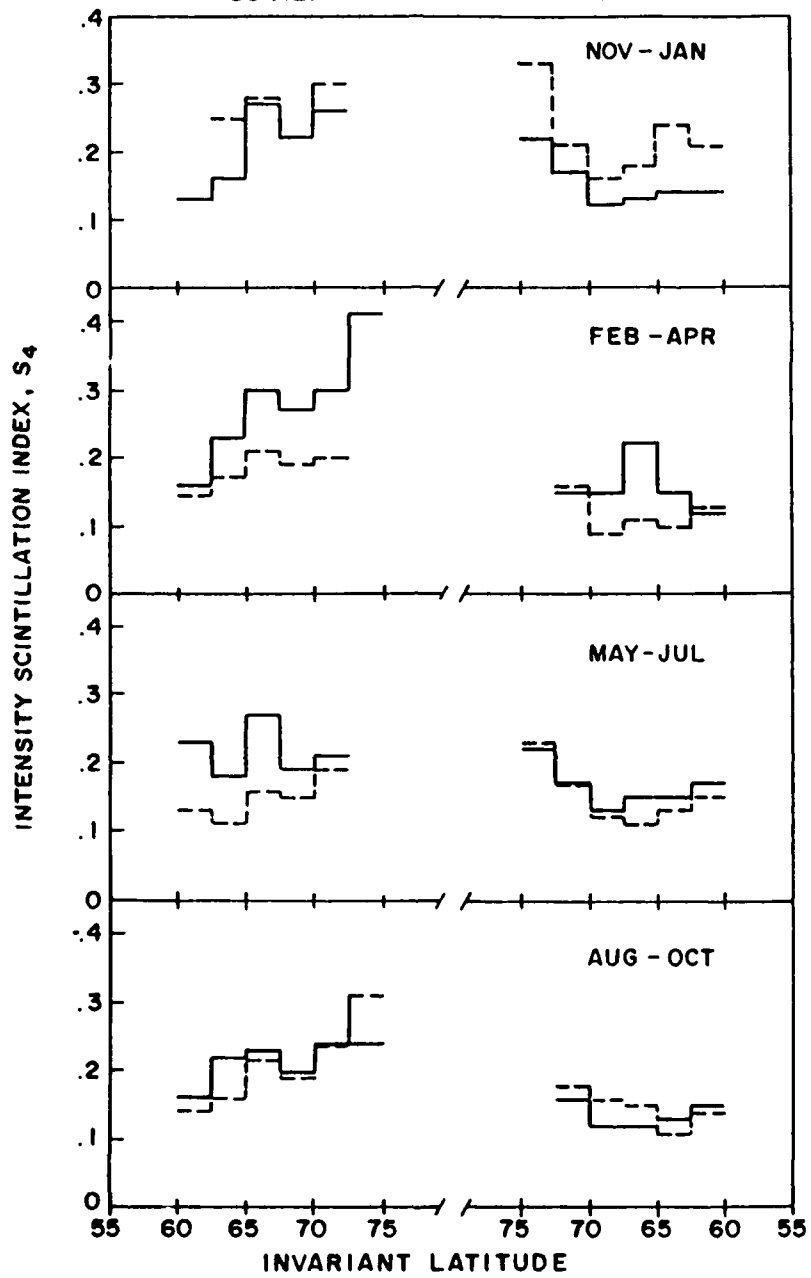


Figure 3. Seasonal variations of intensity scintillation index at 137 MHz along the noon-midnight meridian in 1984 and 1985.

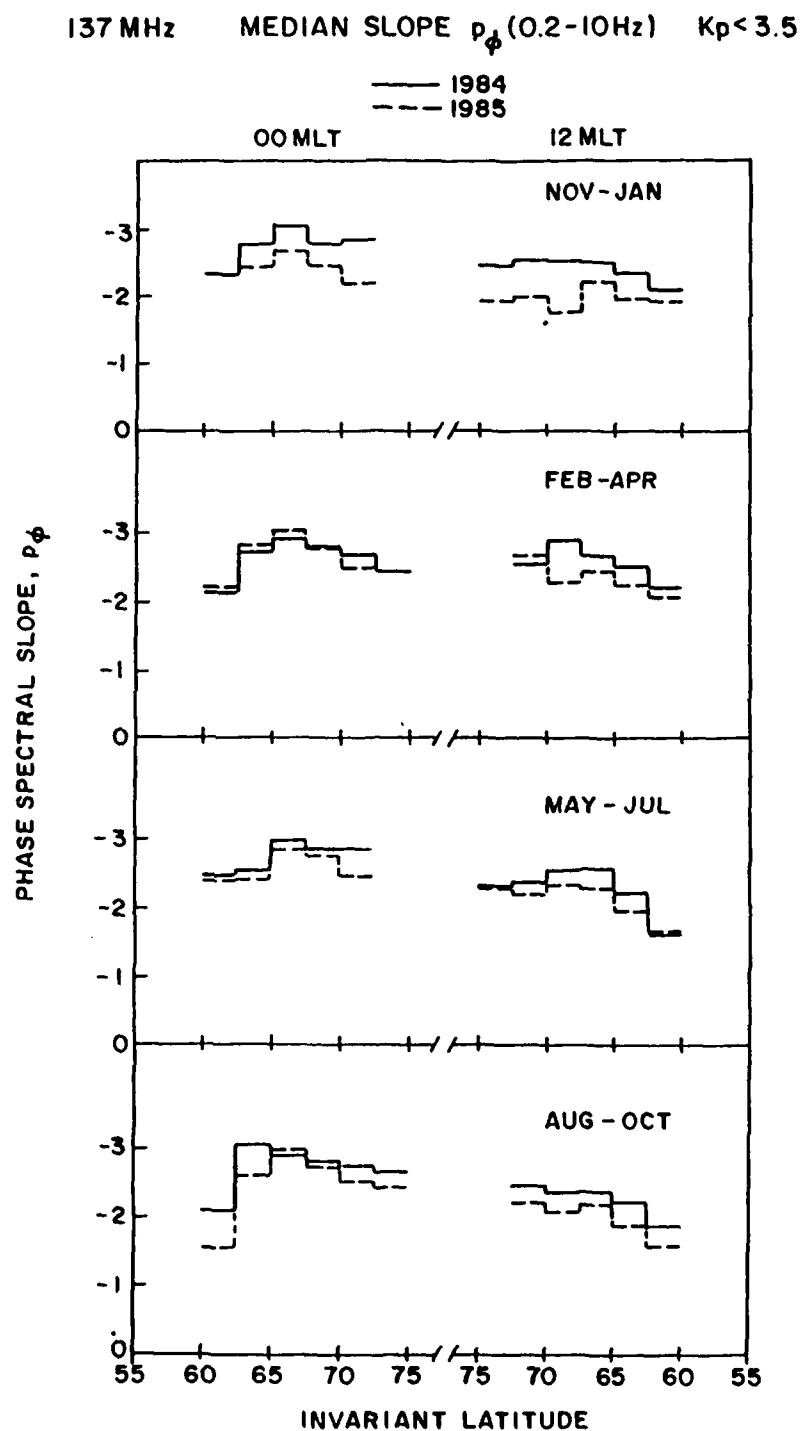


Figure 4. Seasonal variations of the slope of 137 MHz phase scintillation spectra along the interval of 0.2-10 Hz along the noon-midnight meridian in 1984 and 1985.

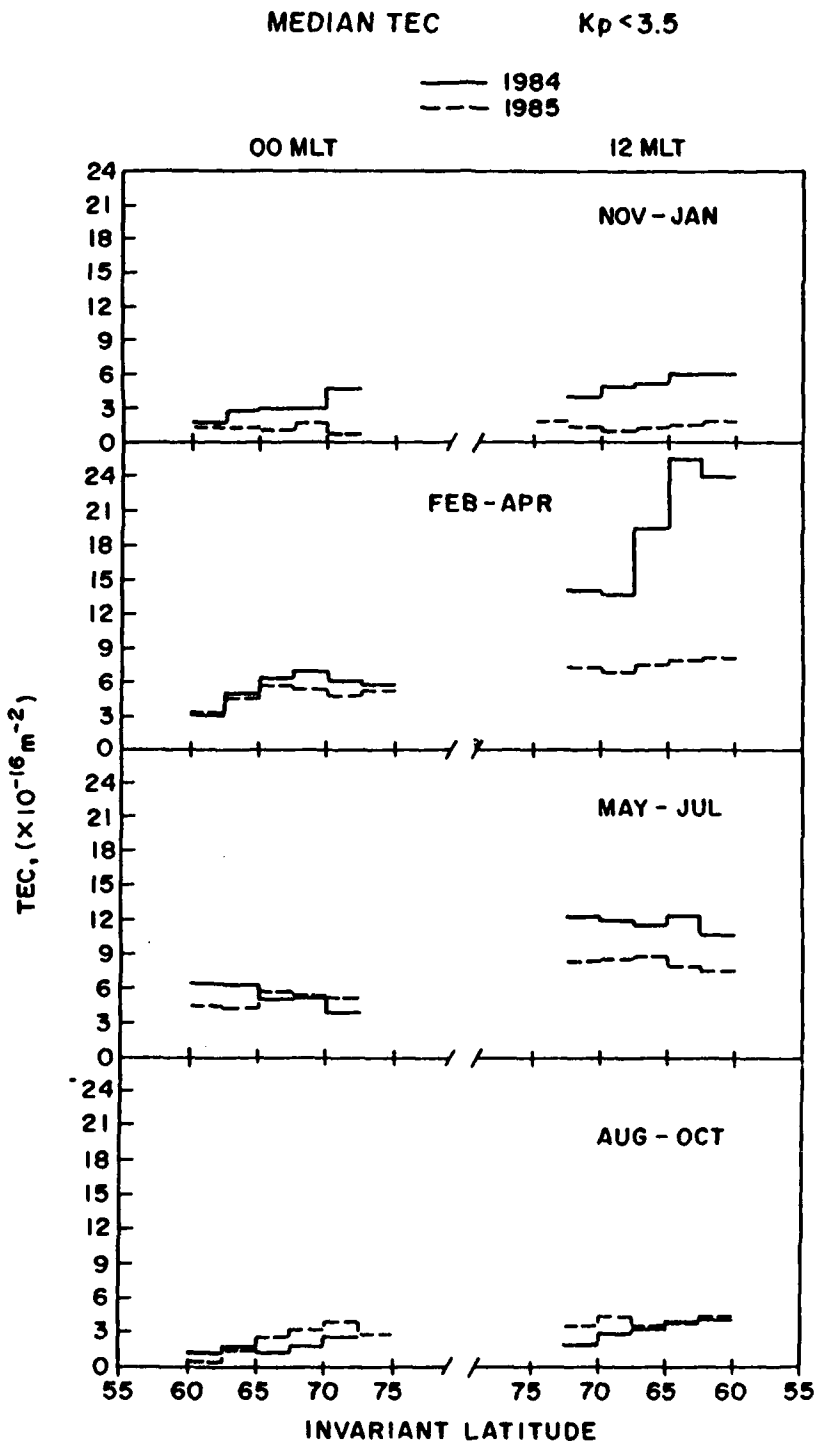


Figure 5. Seasonal variations of total electron content variations along the noon-midnight meridian in 1984 and 1985.

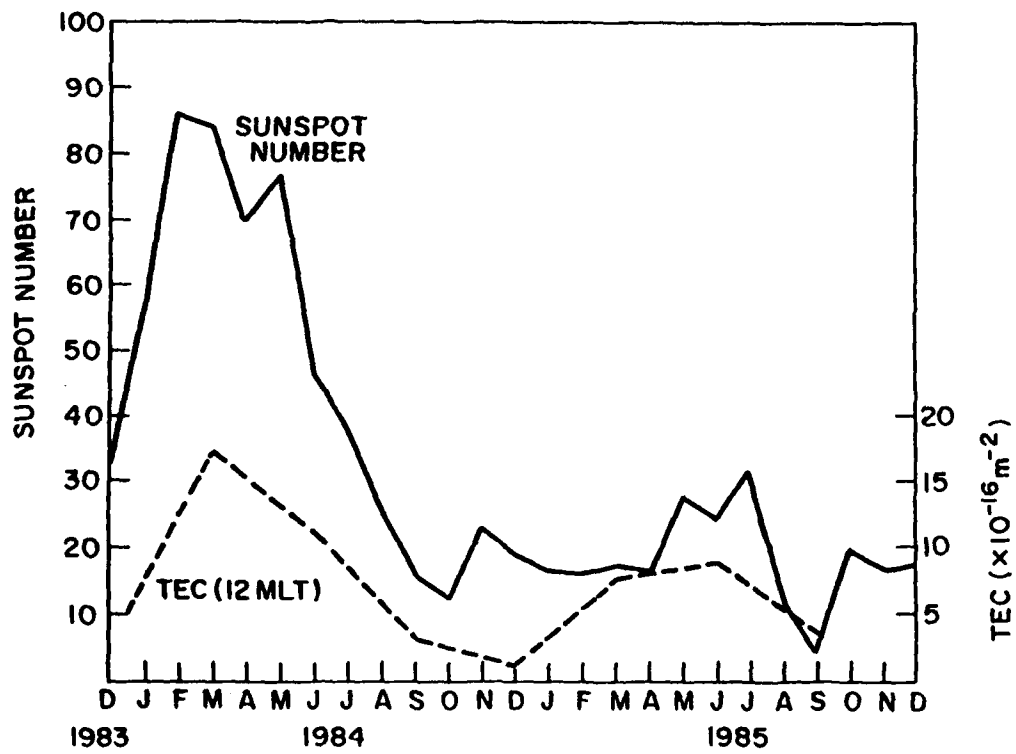


Figure 6. Illustrates the correspondence between the variations of total electron content and sunspot number.

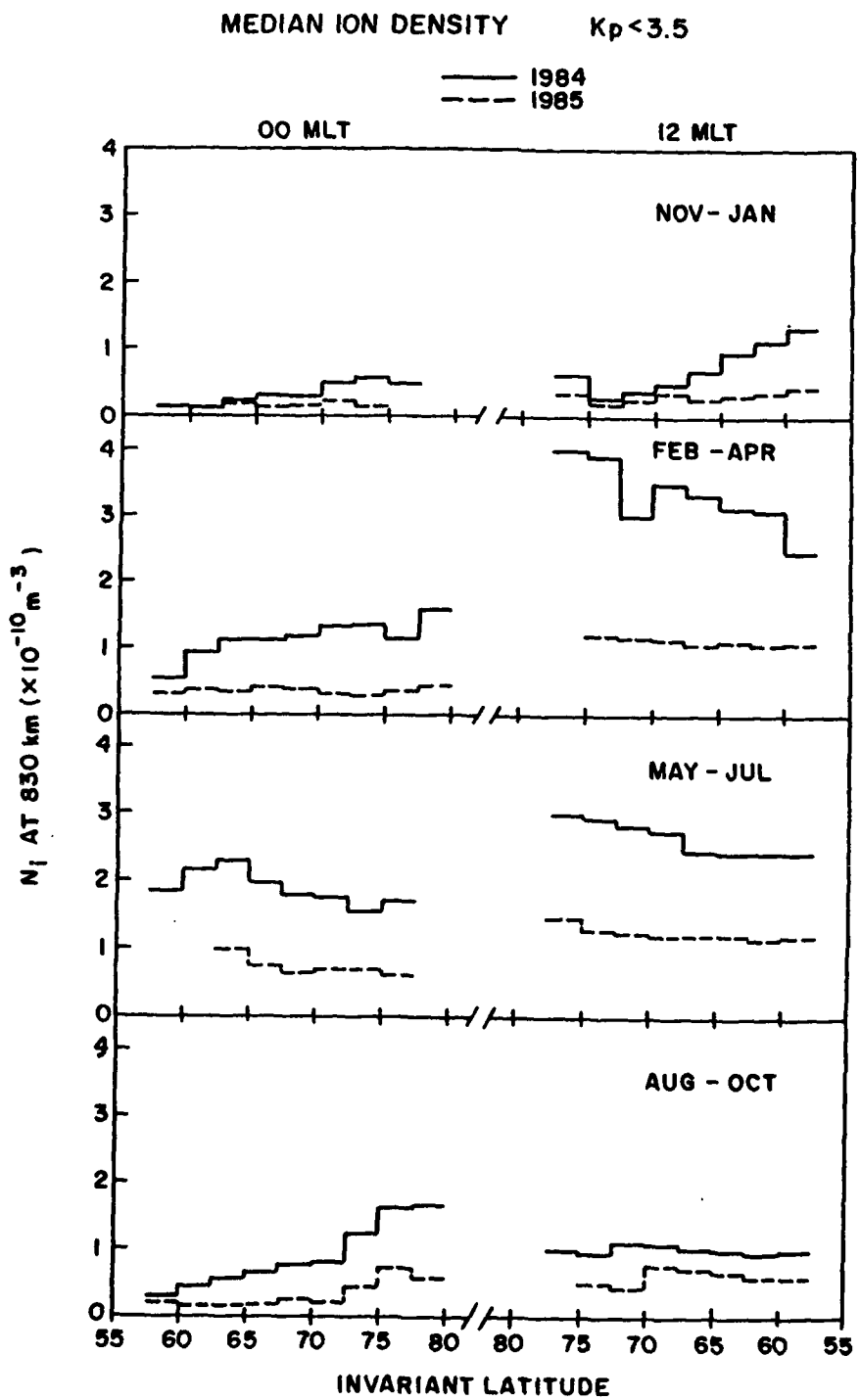


Figure 7. Seasonal variations of ion density at the satellite altitude of 830 km along the noon-midnight meridian in 1984 and 1985.

ATTACHMENT 3

Radio Science, Volume 23, Number 2, Pages 141-162, March-April 1988

Cross-correlation analysis and interpretation of spaced-receiver measurements

Emanoel Costa¹

Physics Research Division, Emmanuel College, Boston, Massachusetts

Paul F. Fougere and Santimay Basu

Ionospheric Physics Division, Air Force Geophysics Laboratory, Hanscom Air Force Base, Massachusetts

(Received May 11, 1987; revised November 16, 1987; accepted December 8, 1987.)

Two algorithms which provide a statistical treatment to the estimation of the parameters of the cross-correlation analysis of spaced-receiver data are reviewed. Their results are compared using signals: (1) transmitted by a quasi-stationary polar beacon and received at Goose Bay, Labrador (53.3°N, 60.3°W); and (2) transmitted by the orbiting Hilat satellite and received at Tromsø, Norway (69.7°N, 18.9°E). A good general agreement is displayed in this comparison. The former experiment indicates the possibility of extreme daily variations in the anisotropy of the ground diffraction pattern and in the true drift velocity of the in situ irregularities. The latter experiment displays geometrical enhancements in the intensity scintillation index S_4 , in the rms phase fluctuation σ_ϕ , and in the axial ratio of the ellipse which characterizes the anisotropy of the ground diffraction pattern, around the region of local L shell alignment of the ray paths. Increases of these parameters also are observed northward of Tromsø. These observations are thus consistent with a morphological model for anisotropy of high-latitude nighttime F region irregularities proposed in the literature. Next, a possible dependence of the results of the spaced-receiver measurements on the receiver baselines is discussed. It is argued that this mechanism could be responsible for the relatively small values of the anisotropy of the diffraction pattern obtained from the Hilat measurements at Tromsø. Finally, a procedure which combines a simple propagation model of the spaced-receiver experiment with a nonlinear minimization algorithm is proposed to estimate the anisotropy of the in situ irregularities from that of the diffraction pattern.

1. INTRODUCTION

The cross-correlation analysis of spaced-receiver data has been developed from the original idea that signals received on the ground by spaced probes after an interaction with the ionosphere display similar structures displaced in time. Dividing the separations between the probes by the respective average time delays between the similar structures, an initial estimate for an apparent drift velocity of the diffraction pattern defined on the ground can be obtained. A refinement of this idea uses the autocorrelation and the cross-correlation functions of the received signals to also estimate the anisotropy and the true drift velocity of this diffraction pattern. This radio technique is relatively well established [Mitra, 1949;

Briggs *et al.*, 1950; Phillips and Spencer, 1955; Kent and Koster, 1966; Rino and Livingston, 1982] and has been applied to ionospheric studies at the equatorial region [Basu *et al.*, 1986], in mid-latitudes [Moorecroft and Arima, 1972] and at high latitudes [Livingston *et al.*, 1982].

Several algorithms have been proposed in the literature to perform the cross-correlation analysis of spaced-receiver data. Two of these, which not only recognize the statistical nature of the present problem but also are well suited for implementation in digital computers, are reviewed here. The first algorithm is a slightly generalized version of that proposed by Fedor [1967]. The second has been suggested by Rino and Livingston [1982], based on a previous work by Armstrong and Coles [1972], devoted to interplanetary scintillation studies. Results from the two algorithms are compared, using signals: (1) transmitted by a quasi-geostationary polar beacon and received at Goose Bay, Labrador (53.3°N, 60.3°W); and (2) transmitted by the orbiting Hilat satellite and received at Tromsø, Norway (69.7°N,

¹Now at Centro de Estudos em Telecomunicações, Pontifícia Universidade Católica do Rio de Janeiro, Brazil.

Copyright 1988 by the American Geophysical Union.

Paper number 7S0931.
0048-6604/88/007S-0931\$08.00

18.9°E). In spite of the different features of the two algorithms, a good general agreement between their results is observed. Possible sources of occasionally observed differences also are discussed. The results of experiment 1 display extreme daily variations of the anisotropy and the true drift velocity of the ground diffraction pattern. Temporal variations of these parameters occurring on short time scales also are observed. Experiment 2 seems to reproduce, at Tromsø, the morphological results from the Poker Flat/Wideband spaced-receiver measurements [Fremouw *et al.*, 1978; Rino *et al.*, 1978; Livingston *et al.*, 1982]. It is observed, however, that the anisotropy of the ground diffraction pattern resulting from the Tromsø/Hilat measurements seems to be less significant than the similar result from the Goose Bay/polar beacon or the Poker Flat/Wideband experiments. There is theoretical (and not entirely conclusive) evidence that this difference may be due to a scale size dependence of the anisotropy of the in situ irregularities. This evidence is briefly reviewed. Another possible explanation for the above observation, also discussed here, is the dependence of the results from the spaced-receiver analysis on the distance between the probes [Golley and Rossiter, 1970].

To interpret the measurements in terms of the anisotropy and the drift velocity of the in situ irregularities, a propagation model of the spaced-receiver experiment is presented. This model assumes (1) a "space-time" correlation function for the random fluctuations in the electron density of the ionosphere whose surfaces of constant correlation levels are characterized by concentric ellipsoids, and (2) a relationship between the fluctuations in the phase of the received signal and the irregularities in the electron density in the F region given by geometrical optics. A simple equation is then obtained for the drift velocity of the ground diffraction pattern as a function of the drift velocity of the in situ irregularities and the satellite velocity. When the satellite velocity is negligible (such as in the case of geostationary or quasi-geostationary satellites), it is easy to estimate the drift velocity of the ionosphere from that of the diffraction pattern. Further, it is shown that the ellipses which characterize the anisotropy of the diffraction pattern are geometrical projections along the ray path onto the ground of the anisotropy ellipsoids of the in situ irregularities. Since there is a continuum of ellipsoids which could be projected onto the same ellipse, the estimation of the anisotropy of the in situ irregularities from that of the diffraction

pattern is not so straightforward as in the case of the drift velocity. It is suggested, however, that, under a few assumptions, it is possible to estimate an average anisotropy of a certain volume of the ionosphere from the observation of multiple and reasonably different anisotropy ellipses of the ground diffraction pattern. This is accomplished by an "inversion" of the propagation model, performed by a nonlinear minimization of the rms error between measured and calculated values of the anisotropy of the diffraction pattern.

2. ALGORITHMS FOR THE CORRELATION ANALYSIS OF SPACED-RECEIVER DATA

Assume the existence of n_r receivers on the ground, located at $\mathbf{x}_i = (x_i, y_i)$, $i = 1, 2, \dots, n_r$, which simultaneously receive transionospheric signals $s_i(t)$. It is also assumed that these signals are stationary, with zero mean and unit standard deviation, and are sampled at the frequency f_s . Further, it is assumed that the correlation functions $\rho_{ij}(\tau_k) = \langle s_i(t)s_j(t + \tau_k) \rangle$, where $\tau_k = (k - 1)/f_s$, with $k = 1, 2, \dots, N$, have been calculated for all possible combinations of indices i and j .

Apparently, the most general characterization for these correlation functions assumes that they are special cases of a single function of three variables. Of these three variables, two represent the vector spacing between receivers and the other time delay between different observations. These variables are combined into a single argument, in such a way that surfaces of constant argument define, in this three-dimensional space, ellipsoids of different sizes but of constant shape. That is,

$$\rho_{ij}(\tau_k) = R\{[\Delta\mathbf{x}^T \cdot \mathbf{Q} \cdot \Delta\mathbf{x}]^{1/2}\} \quad (1)$$

where

$$\mathbf{Q} = \begin{pmatrix} a & h & f \\ h & b & g \\ f & g & c \end{pmatrix} \quad (2)$$

$\Delta\mathbf{x}^T = (\Delta x_{ij}, \Delta y_{ij}, \tau_k)$, $\Delta x_{ij} = x_j - x_i$, $\Delta y_{ij} = y_j - y_i$ and the superscript T will always represent the transpose of a matrix. The parameters a, b, c, f, g and h are constants to be estimated by the analysis. It is sufficiently general for the present purposes to assume that R is a decreasing function of its argument, normalized in such a way that $R(0) = 1$. The original justification for this characterization of the correlation functions can be found in Briggs *et al.* [1950]. It will be seen in a later section that it also is consis-

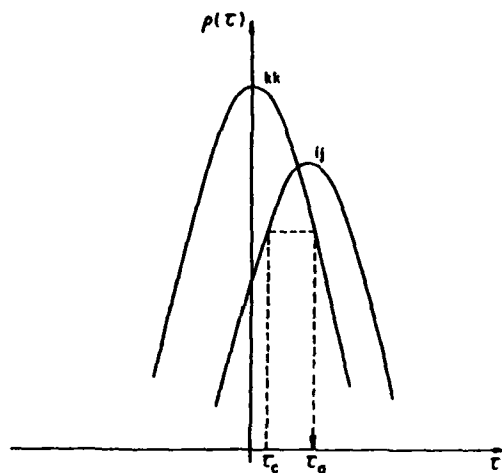


Fig. 1. Sketch of auto- and cross-correlation functions of spaced receiver signals, showing the time delays used by the modified Fedor (MF) algorithm.

tent with an analogous characterization of the random electron density fluctuations in the ionosphere, combined with a simple thin phase-screen scintillation model.

Two algorithms which have been proposed to determine the constants of the ellipsoids will be compared. Besides being well suited for implementation in digital computers, both use the redundant information available in the correlation functions to create generally overdetermined systems of linear equations, which are then solved using the least squares method. This approach thus recognizes the statistical nature of the problem. Therefore, in principle, the solutions so obtained would be more accurate than those resulting from any algorithm using only the minimum amount of information.

The first algorithm is a slightly modified version of that suggested by Fedor [1967], which originally assumed a Gaussian form for the function R . As it will be seen, the autocorrelation function ($i = j$ in (1)) provides all the information on R which is necessary for the estimation of the parameters. The Gaussian assumption can thus be avoided.

Let R_c be the value of the cross-correlation function $\rho_{ij}(\tau_c)$ at the time delay τ_c . One can calculate, using a reasonable interpolation method, the time delay τ_a such that $R_c = \rho_{kk}(\tau_a)$, as illustrated in Figure 1. From the equality $\rho_{ij}(\tau_c) = \rho_{kk}(\tau_a)$ and the assumption that R is a decreasing function, it follows that

$$(1/c)[\Delta x^T \cdot Q \cdot \Delta x - c T_c^2] = \tau_a^2 - \tau_c^2 \quad (3)$$

This expression can be used as a building block for a $n_F \times S$ system of linear equations $D_S \cdot U_S = T_S$, where $U_S^T = (a, h, b, f, g)/c$. The n_F rows in this system are obtained by selecting different combinations of cross-correlation, autocorrelation functions and time delays τ_c in (3), from which the values of the elements of the matrices $D_S (n_F \times S)$ and $T_S (n_F \times 1)$ are easily inferred.

The second algorithm has been proposed by Rino and Livingston [1982], based on a previous work by Armstrong and Coles [1972]. This algorithm, which is fully described in the previous references, uses the maxima and the crossings of the correlation functions to determine, in a two-step procedure, the unknown coefficients in (2). That is, after all maxima and crossings of correlation functions have been estimated, an analogous $n_{RL} \times 3$ linear system $D_3 \cdot U_3 = T_3$, where $U_3^T = (a, h, b)/c$, is obtained. Once this system of equations is solved, the values for a/c , h/c and b/c can be substituted into another $n_{RL} \times 2$ linear system $D_2 \cdot U_2 = T_2$. Here, $U_2^T = (V_x, V_y)$ coincides with the drift velocity V of the diffraction pattern defined on the ground.

The linear systems obtained, all of the form $D \cdot U = T$, are generally overdetermined and should be solved by the least squares method. Assuming the observations T are uncorrelated, it follows that the general solution to those systems is of the form

$$U = (D^T \cdot D)^{-1} \cdot D^T \cdot T \quad (4)$$

As pointed out by Fedor [1967] and Bauerji [1960], the observations T actually are correlated. The available solution to this more general situation is relatively cumbersome, since it involves the calculation and inversion of the covariance matrix of the observations, a formidable task even for the most powerful computers. Fortunately, as indicated by Scheffé [1959], the estimate represented by (4) will still converge to the desired solution as the number of observations increases.

Once the parameters of the ellipsoids are determined, those characterizing the anisotropy, the true drift velocity and the characteristic velocity of the diffraction pattern are calculated as prescribed by Kent and Koster [1966]. The anisotropy is characterized by the common axial ratio AR and orientation Ψ_a of the major axes of the similar ellipses along which the ellipsoids in (1) intersect the plane $\tau = 0$. The true drift velocity of the diffraction pattern is defined in terms of its amplitude V and its direction Ψ_v . The characteristic velocity V_c , defined

by Briggs *et al.* [1950], provides a measure of the amount of internal motion taking place in the diffraction pattern.

It should be realized that the fact that normalized (with respect to c) coefficients have been obtained by the two algorithms imposes no limitation on the calculation of the parameters AR , Ψ_x , V , Ψ_y , and V_c . That is, due to assumptions associated with (1), it has been found that these parameters depend on the common shape of the ellipsoids, but not on their sizes.

Omitting the indices, the argument within square brackets in (1) can be rewritten in the form

$$\Delta x^T \cdot Q \cdot \Delta x = \begin{pmatrix} \Delta x - V_x \tau \\ \Delta y - V_y \tau \end{pmatrix}^T \begin{pmatrix} a & h \\ h & b \end{pmatrix} \begin{pmatrix} \Delta x - V_x \tau \\ \Delta y - V_y \tau \end{pmatrix} + k\tau^2 \quad (5)$$

where $c = k + (aV_x^2 + 2hV_x V_y + bV_y^2)$. As discussed by Briggs [1968], the first term in the right-hand side of (5) represents the "frozen-in" motion contribution to the correlation functions. The term $k\tau^2$ represents the random motion contribution to the same functions. There is then an implicit assumption in (1) that these two motions additively contribute to the correlation functions through the same (quadratic) functional form. Also, it can be shown that $k = 0$ is equivalent to $V_c/V = 0$. Results show that V_c sometimes is a nonnegligible fraction of V , indicating that a pure "frozen-in" motion is not always in good agreement with the observations. However, it is seen that assuming $k = 0$, besides artificially imposing the condition $V_c = 0$, will only affect the value of c . Since, as seen in the previous paragraph, this has no effect on the common shape of the ellipsoids, one concludes that, within the scope of the present theory, the pure "frozen-in" assumption will provide anisotropies and drift velocities of the diffraction pattern which are no different from those calculated by the general equation (1).

Another implicit assumption is that (5) characterizes an ellipsoid. Obviously, this is only true when the same equation defines a positive-definite quadratic form. That is, one should have $a > 0$, $ab - h^2 > 0$ and $k > 0$. Imposing these nonlinear constraints upon the solution of the system $D \cdot U = T$ by the least squares method would certainly increase the level of difficulty of the present problem, as well as the computer time needed to solve it. Instead, it has been preferred to let those conditions result from the "good behavior" of the experimental data.

Before commenting on some possible consequences of this approach, it will be useful to summa-

rize some aspects of the algorithms already described. As previously indicated, the main feature of the Rino-Livingston algorithm is its use of only the time delays for maxima of the cross-correlation functions or the crossings between pairs of (auto- or cross) correlation functions. On the other hand, as indicated by (3), the modified Fedor algorithm uses time delays for all available observations of the cross correlation functions. Thus at least in principle, the modified Fedor algorithm will operate over a larger range of time delays than that of the Rino-Livingston algorithm.

Further, it should be mentioned that skewness is usually observed around the maxima of the measured cross-correlation functions. Skewness has been explained in terms of random velocity fluctuations in the ionosphere or regular velocity variations along the ray path [McGee, 1966; Briggs and Golley, 1968; Wernik *et al.*, 1983]. This feature has been neglected in (1). Occasionally, this disagreement becomes a serious source of difficulty, causing at least one of the algorithms to estimate a set of parameters which does not satisfy the inequalities characterizing a positive-definite quadratic form. When this happens, it has been chosen to reject the whole set. Fortunately, as the results to be discussed in a later section will show, the discrepancy between modeled (through (1)) and measured correlation functions is not severe enough to prevent the algorithms to calculate a consistent set of parameters in a large fraction of the cases analyzed.

On the other hand, moderate to small skewness of the cross-correlation functions, combined with the difference in the ranges of time delays over which the two algorithms operate or even with the different ways through which they process the data, could be translated into differences between their estimates. Again, the results to be presented later will show that, although there occasionally are significant differences, the agreement between the two algorithms is generally good.

3. A MODEL OF THE SPACED-RECEIVER EXPERIMENT

Let the region of the ionosphere where electron density irregularities exist be represented by a plane horizontal slab situated between the heights z_i and $z_i + \Delta L$ (ΔL representing its thickness), as shown in Figure 2. The random fluctuation $\delta N(R, t)$ in the electron density within the layer is assumed to have

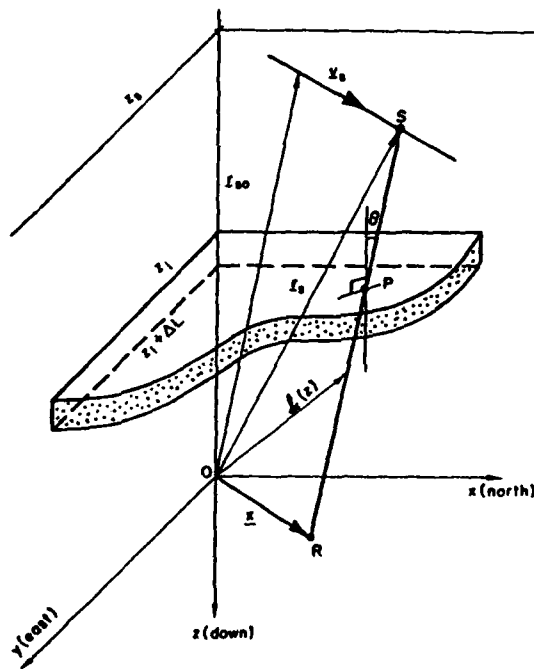


Fig. 2. Geometry assumed by the model of the spaced-receiver experiment.

zero mean, total power equal to $\langle \delta N^2 \rangle$ and to be homogeneous and anisotropic, with its "space-time" correlation function being characterized by

$$\rho_n(\Delta R, \Delta t) = R_n \{ [\Delta r^2 + (\Delta t/B)^2 + (\Delta s/A)^2 + (\Delta \tau/C)^2]^{1/2} \} = R_n(p) \quad (6)$$

in the reference frame *nts* aligned with the geomagnetic field, as shown in Figure 3, and moving with the drift of the irregularities (which drift is assumed to remain constant throughout the slab). The parameters *A*, *B*, and *C* are constants and it is assumed that $R_N(p)$ is a decreasing function of its argument, normalized by the condition $R_N(0) = 1$. Here, in the remainder of this paper, as well as in the companion paper [Costa and Fougere, this issue], three-dimensional position vectors or their increments will be represented by upper case variables, to distinguish themselves from two-dimensional position vectors, their increments (generally defined on the plane $z = 0$ shown in Figure 2) or the components of any vector, which will be represented by lower case variables.

It is seen that the components of the space-lag vector $\Delta R = (\Delta r, \Delta \theta, \Delta \phi)$ are combined in such a way that surfaces of constant correlation levels are ellip-

soids with axes in the ratio $1:B:A$. In this reference frame, the term involving Δt represents the contribution to the correlation function of random density changes with time, while the remaining terms in the argument represent contributions due to density fluctuations in space. Implicit in (6), and important to the spaced-receiver analysis [Briggs, 1968], is the assumption that spatial and temporal correlation functions have the same form.

Taking the Fourier transform of the previous equation, it is found that the corresponding power spectral density of the irregularities can be expressed in the general form

$$P_K(\mathbf{K}, \omega) = \langle \delta N^2 \rangle \int_{-\infty}^{+\infty} \rho_N(\Delta \mathbf{R}, \Delta \tau) e^{-(i(\omega \Delta \tau - \mathbf{K} \cdot \Delta \mathbf{R}))} d\Delta \mathbf{R} d\Delta \tau$$

$$= 4\pi^2 ABC \langle \delta N^2 \rangle \int_0^{\infty} p^3 \frac{J_1(pq)}{(pq)} R_N(p) dp = Q_N(q) \quad (7)$$

where $J_1(p)$ is the Bessel function of first kind and first order and $q = (K_x^2 + B^2 K_y^2 + A^2 K_z^2 + C^2 \omega^2)^{1/2}$. Similarly, it is seen that (7) defines ellipsoids of constant power spectral density levels. Their axes, however, are in the ratio $1:(1/B):(1/A)$. The inverse Fourier transform associated with (7) gives

$$\begin{aligned}
 \rho_K(\Delta R, \Delta \tau) &= \frac{1}{(2\pi)^2} \cdot \frac{1}{\langle \delta N^2 \rangle} \int_{-1}^{+\infty} P_K(K, \omega) e^{i(\omega \Delta \tau - K \Delta R)} dK d\omega \\
 &= \frac{1}{4\pi^2 ABC \langle \delta N^2 \rangle} \int_0^\infty q^3 \frac{J_1(pq)}{(pq)} Q_K(q) dq = R_K(p) \quad (8)
 \end{aligned}$$

where p has been defined in (6).

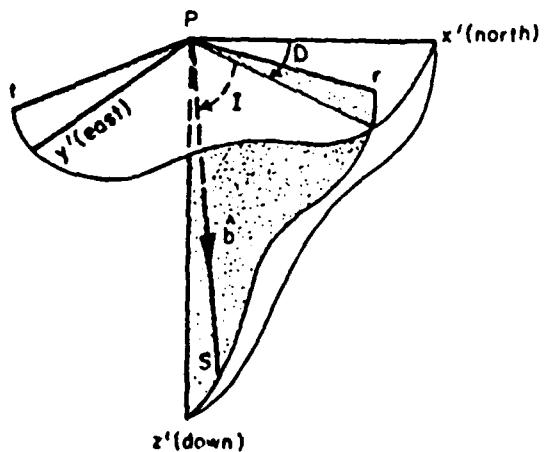


Fig. 3 Geometry for the geomagnetic field at the penetration point P .

To evaluate the effects of the medium on a signal transmitted by a satellite S and received on the ground, it is convenient to characterize the correlation function of the density fluctuations in a different reference frame. This will be done by initially applying two successive rotations $\Delta X' = R_1 \cdot \Delta R$ and $\Delta X'' = R_2 \cdot \Delta X'$. The former is performed around the penetration point P (where the ray path intersects the plane at the center of the irregularity layer), being characterized in Figure 3. On the other hand, the reference frame $x''y''z''$ has its axes respectively aligned with the northward, eastward and downward directions defined at the origin O shown in Figure 2 (that is, they are parallel to the axes x , y and z). The latter rotation thus takes the sphericity of the earth into account. It is assumed, however, that both reference frames $x'y'z'$ and $x''y''z''$ are also moving with the drift velocity of the irregularities. Performing the indicated transformations, the correlation function of the density fluctuation can be written in the reference frame $x''y''z''$ as

$$\rho_N(\Delta X'', \Delta t) = R_N \{ [(\Delta X'')^T \cdot A^T \cdot C A \cdot \Delta X'' + (\Delta t/C)^2]^{1/2} \} \quad (9a)$$

where

$$(\Delta X'')^T = (\Delta x'', \Delta y'', \Delta z'')$$

$$C_{xx} = \cos^2 D \sin^2 I + \cos^2 D \cos^2 I/A^2 + \sin^2 D/B^2 \quad (9b)$$

$$C_{yy} = \sin^2 D \sin^2 I + \sin^2 D \cos^2 I/A^2 + \cos^2 D/B^2 \quad (9c)$$

$$C_{zz} = \cos^2 I + \sin^2 I/A^2 \quad (9d)$$

$$C_{xy} = C_{yx} = \cos D \sin D (\sin^2 I + \cos^2 I/A^2 - 1/B^2) \quad (9e)$$

$$C_{xz} = C_{zx} = -\cos D \cos I \sin I (1 - 1/A^2) \quad (9f)$$

$$C_{yz} = C_{zy} = -\sin D \cos I \sin I (1 - 1/A^2) \quad (9g)$$

and

$$A = \begin{pmatrix} \cos \theta_p \cos \theta_R \cos (\lambda_p - \lambda_R) & -\cos \theta_p \sin (\lambda_p - \lambda_R) & \cos \theta_p \sin \theta_R \cos (\lambda_p - \lambda_R) \\ \sin \theta_p \sin \theta_R & \cos (\lambda_p - \lambda_R) & -\sin \theta_p \cos \theta_R \\ \cos \theta_R \sin (\lambda_p - \lambda_R) & \sin \theta_p \sin (\lambda_p - \lambda_R) & \sin \theta_R \sin (\lambda_p - \lambda_R) \\ \sin \theta_p \cos \theta_R \cos (\lambda_p - \lambda_R) & -\sin \theta_p \sin (\lambda_p - \lambda_R) & \sin \theta_p \sin \theta_R \cos (\lambda_p - \lambda_R) \\ -\cos \theta_p \sin \theta_R & \cos \theta_p \cos \theta_R & +\cos \theta_p \cos \theta_R \end{pmatrix} \quad (9h)$$

In the above equations, D and I are, respectively, the declination and the dip angle of the geomagnetic field. $\theta_{p,R}$ represent colatitudes. $\lambda_{p,R}$ represent longitudes. the subscripts P and R indicate the penetration point and the receiver, respectively, and the superscript T again indicates the transpose of a matrix.

Finally, it is important to observe that the density irregularities $\delta \cdot \mathbf{1}'(\mathbf{X}, t)$, defined in the reference frame xyz (fixed with respect to the receivers) shown in Figure 2, are related to $\delta N(\mathbf{X}'', t)$ through

$$\delta \cdot \mathbf{1}'(\mathbf{X}, t) = \delta N(\mathbf{X} - \mathbf{X}_0 - \mathbf{v}_D t, t) \quad (10)$$

where $\mathbf{X}_0 = (x_0, y_0, z_0)$ defines the position of the origin of the reference frame $x''y''z''$ with respect to the reference frame xyz at $t = 0$ and \mathbf{v}_D is the drift velocity of the irregularities.

There is a vast literature describing the propagation of radio waves through continuous random media [Tatarskii, 1971; Yeh and Liu, 1982, and references therein]. It is immediately evident that more elaborate models lead to extremely complex mathematical equations, which generally are solved numerically. Although it may be important to model the spaced-receiver experiment more accurately in the future, this will make it considerably more difficult to interpret the measurements or to explore the possibility of unambiguously estimating the anisotropy of the ionospheric irregularities from the measured anisotropy of the ground diffraction pattern. On the other hand, it has been shown [Rino, 1982; Rino and Livingston, 1982] that, in spite of its limitations, the geometrical optics relationship between $\delta \cdot \mathbf{1}'(\mathbf{x}, t)$ and the phase fluctuations $\delta \phi(\mathbf{x}, t)$ of the transionospheric signals received on the ground is able to provide useful insight into ionospheric scintillation and the spaced-receiver experiment. This relationship is given by

$$\delta \phi(\mathbf{x}, t) = -r_e \lambda_0 \int_{\text{ray path}} \delta \cdot \mathbf{1}' dl \quad (11)$$

where $r_e (= 2.82 \times 10^{-15} \text{ m})$ is the classical electron radius and λ_0 is the free space wavelength of the transmitted signal.

Assuming that a satellite is the source of the transmitted signals, there are two typical situations in the spaced-receiver experiment. The first involves a vehicle with near circular, low-altitude orbit, such as the Hilat satellite (830-km-high orbit, with an 82° inclination and orbital velocity of 7.4 km/s). The second involves signals transmitted from geostation-

ary or quasi-stationary satellites. In both cases, the source can be assumed to be moving with a constant horizontal velocity in the plane $z = z_s$, shown in Figure 2, for the short period of time involved in the analysis of each sample of data. Thus in both cases the position $\mathbf{l}(z, t)$ of the point of the ray path situated at the height z at time t can be characterized by the general equation

$$\mathbf{l}(z, t) = \mathbf{r}_s(t) + [\mathbf{x} - \mathbf{r}_s(t)](z_s - z)/z_s \quad (12)$$

where, as shown in Figure 2, $\mathbf{r}_s(t) = \mathbf{r}_{s0} + \mathbf{v}_s t$ is the satellite position vector (assumed to be always contained in the plane $z = z_s$), $\mathbf{r}_{s0} = \mathbf{r}_s(0)$, \mathbf{v}_s is the (horizontal) satellite velocity and \mathbf{x} is the receiver position (on the plane $z = 0$).

Combining (10)–(12) and using the relationship $dl = \sec \theta dz$ (where θ is the angle between the ray path and the vertical at the penetration point P), followed by a change of variables, it is found that

$$\begin{aligned} \delta\phi(\mathbf{x}, t) = & -r_s \lambda \sec \theta \int_0^{\Delta L} \delta N \{[(z_s - z_i - z')/z_s] \mathbf{x} \\ & + [(z_i + z')/z_s] (\mathbf{r}_{s0H} + \mathbf{v}_s t) \\ & - \mathbf{v}_{DH} t - \mathbf{X}_{s0H}, z' + z_i - \mathbf{r}_{DH} t - z_{s0}, t\} dz' \end{aligned} \quad (13)$$

where the subscripts H and z indicate components of a vector in the horizontal plane or in the z direction, respectively. Using this basic result to calculate the "space-time" correlation function of the phase fluctuations of the received signals, one gets

$$\begin{aligned} \phi_0^2 \rho_\phi(\Delta x, \Delta t) = & \langle \delta\phi(\mathbf{x} + \Delta x, t + \Delta t) \delta\phi(\mathbf{x}, t) \rangle \\ \approx & r_s^2 \lambda_0^2 \langle \delta N^2 \rangle \Delta L \sec^2 \theta \\ & \int_{-\Delta L}^{\Delta L} (1 - |z'|/\Delta L) \rho_N \{[(z_s - z_i - z')/z_s] \Delta x \\ & - [\mathbf{v}_{DH} - (z_i/z_s) \mathbf{v}_s] \Delta t + \tan \theta \mathbf{k}_H z' \\ & - \mathbf{r}_{DH} \Delta t, \Delta t\} dz' \approx r_s^2 \lambda_0^2 \langle \delta N^2 \rangle \Delta L \sec^2 \theta \\ & \int_{-\Delta L}^{\Delta L} \rho_N \{[(z_s - z_i)/z_s] (\Delta x - \mathbf{V} \Delta t) \\ & + \tan \theta \mathbf{k}_H z', \Delta t\} dz' \end{aligned} \quad (14)$$

where ϕ_0 is the rms phase fluctuation, \mathbf{k}_H is the unit vector resulting from the projection of SR (vector defining the ray path) onto the horizontal plane $z = 0$ and

$$\mathbf{V} = [z_i/(z_s - z_i)] (\mathbf{v}_{DH} - \tan \theta \mathbf{k}_H \mathbf{v}_{DH} - (z_i/z_s) \mathbf{v}_s) \quad (15)$$

In the last step of (14), it has been assumed that ΔL is large in comparison with the decorrelation distance of the density fluctuation in the z direction.

In (14) and (15), the effects of the oblique propagation on $\rho_\phi(\Delta x, \Delta t)$ are considered through the terms involving $\tan \theta \mathbf{k}_H$ [Rino and Fremouw, 1977]. Further comments on the meaning of one of these terms will be represented at the end of this section. Equation (14) clearly shows that the spatial and temporal behavior of $\rho_\phi(\Delta x, \Delta t)$ can be fully described by a general function of both $\Delta u = (\Delta x - \mathbf{V} \Delta t)$ and Δt , regardless of the functional form taken by $\rho_N(\Delta R, \Delta t)$. Comparing this result with the right-hand side of (5), it is immediately concluded that (15) relates the drift velocity \mathbf{V} of the ground diffraction pattern to the drift velocity of the irregularities in the ionosphere and the satellite velocity. For stationary or quasi-stationary satellites, \mathbf{v}_s tends to zero and \mathbf{V} is essentially a function of the ionospheric drift. On the other hand, (15) is dominated by \mathbf{v}_s for low-altitude, near-circular orbit satellites (such as Hilat). It is also seen that \mathbf{V} simultaneously depends on both the horizontal and the vertical components of the ionospheric drift. That is, it is theoretically impossible to separate the two components from a single measurement of \mathbf{V} .

Substituting the horizontal space lags indicated in the integrand of (14) for $\Delta x''$ and $\Delta y''$ in (9), one gets

$$\phi_0^2 \rho_\phi(\Delta x, \Delta t) = \phi_{00}^2 \sec^2 \theta \int_{-\Delta L}^{\Delta L} \begin{aligned} & R_N \{[C_{xx} \Delta u_s^2 + 2C_{xy} \Delta u_x \Delta u_y + C_{yy} \Delta u_y^2 \\ & + (\Delta t/C)^2 + 2(C_{xz} \Delta u_x + C_{yz} \Delta u_y) z + C_{zz} z^2]^{1/2}\} dz' \end{aligned} \quad (16)$$

where $\phi_{00}^2 = r_s^2 \lambda_0^2 \langle \delta N^2 \rangle \Delta L$. The coefficients C_{xx} to C_{zz} in this equation result from the substitution indicated above in a straightforward manner. Applying a linear change of variables to the integrand in (16), one immediately identifies

$$\phi_0^2 = r_s^2 \lambda_0^2 \langle \delta N^2 \rangle \Delta L \sec^2 \theta \int_{-z_0}^{z_0} R_N(|z'|) dz' / \sqrt{C_{zz}} \quad (17a)$$

and

$$\begin{aligned} \rho_\phi(\Delta x, \Delta t) = & \frac{\int_{-z_0}^{z_0} R_N \{[z'^2 + (C_{zz} Z_0 - Z_0^2) C_{zz}]\}^{1/2} dz'}{\int_{-z_0}^{z_0} R_N(|z'|) dz'} \\ = & R_\phi \{[(C_{zz} Z_0 - Z_0^2) C_{zz}]^{1/2}\} \end{aligned} \quad (17b)$$

where Z_0 is the term independent from z' and $2Z_1$ is

the coefficient of the linear term in z' , both obtained from the argument within square brackets in that equation. The last step in (17b) holds regardless of the functional form for $R_N(p)$. From the assumed properties for this function, it follows that $R_\phi(p)$ also is a decreasing function of its argument, such that $R_\phi(0) = 1$. The argument within parentheses in (17b) can be rewritten in the form

$$\begin{aligned} & C_{zz} Z_0^2 - Z_1^2 \\ &= \begin{pmatrix} \Delta u_z \\ \Delta u_y \end{pmatrix}^T \begin{pmatrix} C_{zz} C_{xx} - C_{xx}^2 & C_{zz} C_{xy} - C_{xx} C_{yy} \\ C_{yy} C_{xy} - C_{xx} C_{yy} & C_{yy} C_{yy} - C_{yy}^2 \end{pmatrix} \begin{pmatrix} \Delta u_z \\ \Delta u_y \end{pmatrix} \\ &+ \left(\frac{\Delta t}{C} \right)^2 \end{aligned} \quad (18)$$

A comparison between (5) and (18) immediately shows that (17b) has the same form as (1), thus lending full support to the assumptions in the previous section. As explained in the companion paper [Costa and Fougere, this issue], (17a), (17b) and (18) would have to be extended if it were important to explain some fine details in the observed cross-correlation functions (namely, the skewness around their respective maxima).

Assume strictly "frozen-in" irregularities (that is, neglect the terms involving $(\Delta t/C)^2$), as well as a reference frame moving with the drift of the ground diffraction pattern. To further simplify the discussion, let $z_s \gg z_i$, in (14). Under these assumptions, the arguments within brackets in (9a), (16), and (18) become completely independent of Δt . It can then be shown analytically that the ellipse characterized by equating the argument of $R_\phi(p)$ in (17b) to a constant (say, C_0) is the geometrical projection along the ray path onto the plane containing the receivers ($z = 0$ in Figure 2) of the ellipsoid

$$(\Delta X'')^T \cdot C' \cdot \Delta X'' = (\Delta X'')^T \cdot A^T \cdot C \cdot A \cdot \Delta X = C_0^2 \quad (19)$$

characterized by the term within square brackets in (9a). This result is identical to the one previously derived by Moorcroft and Arima [1972], except for these authors' assumption of a vertical ray path. To see that it is also valid in the present general geometry, consider the equation, parametric in w , for the ray path

$$x = x_0 + w \sin \theta \cos \phi \quad (20a)$$

$$y = y_0 + w \sin \theta \sin \phi \quad (20b)$$

$$z = w \cos \theta \quad (20c)$$

Here, it is assumed that the ray path intersects the

ground plane at $(x_0, y_0, 0)$ and that its direction in space is defined by the angles θ and ϕ . Solving the third equation for w and substituting the result into the other two, the new equation, parametric in z , for the ray path becomes

$$x = x_0 + z \tan \theta \cos \phi = x_0 + \tan \theta k_{Hx} z \quad (21a)$$

$$y = y_0 + z \tan \theta \sin \phi = y_0 + \tan \theta k_{Hy} z \quad (21b)$$

where $k_H = (k_{Hx}, k_{Hy}) = (\cos \phi, \sin \phi)$. This equation is identical to the relationship shown to exist in (14) between the horizontal argument and the variable of integration z' , after the ground space lag Δx is appropriately scaled by the ratio $(z_s - z_i)/z_s$.

The result represented by (18) and (19), which has been confirmed by the present authors with necessary calculations, is expected, on physical grounds, from the relationship between the phase fluctuations and the irregularities in the ionospheric density given by the geometrical optics.

4. RESULTS FROM AURORAL-REGION MEASUREMENTS

In this and the following sections, spaced-receiver measurements carried out at two auroral-region stations will be described. Results provided by the two previously described algorithms will be compared and interpreted in terms of the corresponding parameters of the electron density irregularities in the ionosphere.

Motivated by the proven success of the maximum entropy method (MEM) of power spectrum analysis as applied to ionospheric scintillation data [Fougere, 1985], it was decided to use multichannel MEM for the present correlation analysis. Throughout this paper all estimates from the time series data, of the autocorrelation function (ACF) in three channels and of the cross-correlation function (CCF) between all pairs of channels were obtained using the multichannel maximum entropy method. The Burg technique [Burg, 1975, 1981] was generalized independently and nearly simultaneously by four different authors: Jones [1978], Nutall [1976], Strand [1977], and Morf et al. [1978]. The program used in the present research was put together by R. G. Currie (private communication, 1980) using parts of Jones' program and parts of Strand's program modified by using some of Morf et al.'s ideas. Fougere [1981] added a set of subroutines which find for each channel, the accurate location and height of all spectral peaks and the integral under the spectrum. The integral under

the spectrum is used in conjunction with Parseval's theorem to check the accuracy of the computed spectrum. The present authors modified the program further to make it yield conveniently the estimated ACFs and CCFs. The first $M + 1$ correlation coefficients (where M is the order of the autoregression) are directly estimated by the recursive algorithm described by Jones [1978]. Higher order coefficients also are directly estimated, by the generalization of the Yule-Walker equations described by Strand [1977]. Thus, it is not necessary to apply the fast Fourier transform to the maximum entropy spectrum to obtain the desired correlation coefficients. Indeed, it is not even necessary to estimate this spectrum for the present application.

4.1. Quasi-stationary satellite observations at Goose Bay, Labrador

In the first experiment to be discussed, the intensity of the signal transmitted at apparently 250 MHz from a quasi-geostationary polar beacon and received by three spaced receivers at Goose Bay, Labrador (53.3°N , 60.3°W), on March 7 and 8, 1982, was recorded between 0400 UT and 0530 UT. On both days, the elevations of the ray paths were approximately equal to 45° , the corrected geomagnetic latitude (CGL) of their 350-km penetration points remained closest to 65°N and the vehicle was due northeast of the receiving station. The three receivers defined an isosceles right triangle on the ground, with smaller sides equal to 500 m. These sides were rotated clockwise by 18° from the westward and northward directions, respectively. The received signals were sampled at 50 Hz. The satellite frequency was updated every 168 s, thus creating a loss of lock during a fraction of this time, in the beginning. As a result, and also due to some preprocessing of the received information, data blocks of 72-s length (corresponding to 3600 observations of the signal intensity per channel) approximately centered at the middle of each cycle were used in the correlation analysis. A more detailed description of the receiving system and preprocessing of the data was presented by Basu *et al.* [1985].

These authors also discussed the time history of the scintillation index S_4 , the rms phase fluctuation σ_ϕ and the decorrelation time observed on the 2 days. On March 7, they obtained 0.5-decorrelation times of the intensity signal of the order of a few

seconds and average values of σ_ϕ approximately equal to 2 radians. On March 8, however, the 0.5-decorrelation time was of the order of a few tenths of a second only and σ_ϕ was generally greater than 4 radians, sometimes exhibiting peaks which surpassed the 10-radian level. On the other hand, the average values of the observed scintillation index S_4 remained virtually at the same level on both days ($S_{4,\text{ave}} \approx 0.7$).

In their discussion of these observations, Basu *et al.* [1985] emphasized the great impact of irregularity drift variations on intensity decorrelation times and magnitudes of phase scintillation. Indeed, it has been crudely estimated from the raw data that the average time delay between similar structures observed on different channels was relatively high (of the order of 10 s, and sometimes even larger) on March 7 and much smaller (1 s to 2 s) on March 8. Very different apparent velocities would then result from the ratios of the distance between two receivers and the corresponding time delays obtained on the 2 days. The data also indicate that as these time delays increase, the signal structures in different channels become increasingly different. The above feature reflects the effects of temporal variations of the in situ irregularities, and, as a result, the largest time delays are generally associated with the lowest correlation coefficients between the corresponding signals. This situation, which occurred principally on March 7, frequently yielded correlation functions whose main and secondary lobes were approximately of the same magnitude, a less than ideal condition for the correlation analysis of spaced receiver data.

The anisotropies of the diffraction pattern obtained on March 7 and 8 are represented in Figures 4a and 4b, respectively. Each figure shows two sectors of a circle covering corrected geomagnetic latitudes (CGL) from 60° to 90° and corrected geomagnetic local times (CGLT) from 0000 to 0600. These sectors separately exhibit the results obtained using the modified-Fedor (MF) and the Rino-Livingston (RL) algorithms. Axial ratios are represented by the length of a line segment centered at the vertical projection on the ground of the 350-km ionospheric penetration point of the ray path. On the upper right-hand corners of both figures, line segments corresponding to an axial ratio of 20 are shown. The orientations of the major axes of the anisotropy ellipses are measured by the angle between the radial direction through each penetration point (indicating the local northward direction in the polar CGL \times CGLT coordinate system) and the corre-

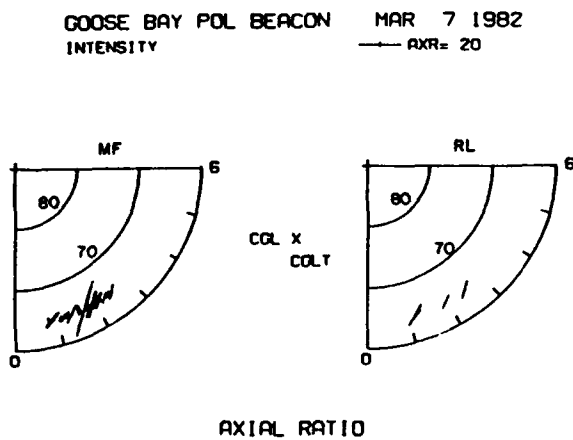


Fig. 4a. Axial ratios and orientations of the major axes of the anisotropy ellipses of the diffraction pattern, obtained by the modified Fedor (MF) and the Rino-Livingston (RL) algorithms. Goose Bay/polar beacon spaced-receiver intensity data recorded on March 7, 1982, have been used. The scale for the axial ratios is shown in the upper right-hand corner. Orientations are represented in this CGL \times CGLT reference frame by the angles between the line segments and the radial directions through their respective centers.

sponding line segment (aligned with the major axis of the ellipse).

Figures 4a and 4b show a good general agreement between the two algorithms for estimated axial ratios and orientations. Both also have been able to detect a considerable increase in the elongation of the diffraction pattern from March 7 to March 8, as well as an increase in the axial ratio in the later hours on March 8. This example indicates that the anisotropy of in situ irregularities can also display considerable temporal structuring (even for the short time scales observed in Figures 4a and 4b). Such structuring is analogous to the behavior of other parameters of the medium. The anisotropy also has a patterned behavior as a function of the invariant latitude and the corrected geomagnetic local time [Livingston *et al.*, 1982].

A variation in the total number of results respectively obtained during March 7 and March 8 is evident from a comparison between the two Figures. This difference should really be expected, due to the critical geophysical conditions (small velocities and cross-correlation levels) which prevailed on March 7. The RL algorithm seemed to be particularly sensitive to these conditions, possibly due to its features (discussed in the second section) or to the authors' approach to its implementation.

Without further investigation, it is difficult to provide a quantitative interpretation for the present measurements in terms of the parameters characterizing the anisotropy of ionospheric irregularities, due to problems to be discussed in the next section. There are, however, indications that the present results could have been caused by rodlike irregularities [Livingston *et al.*, 1982] on both days. The orientations of the major axes of the anisotropy ellipse are in good agreement with the projection of highly field-aligned in situ irregularities onto the ground along the ray path. This information alone is not always able to determine the most likely shape of the ellipsoid characterizing the anisotropy of the in situ irregularities. Indeed, it has been pointed out [Rino *et al.*, 1978; Livingston *et al.*, 1982] that the orientation of the major axis of the anisotropy ellipse becomes essentially independent of that shape when the elevation of the ray path decreases. On the other hand, it should be remembered that the penetration point is due northeast of the station, being well outside the region of local *L* shell alignment. This is the only region where sheetlike irregularities produce a significant enhancement in the axial ratio. This shape (sheetlike) thus would not easily explain the present results. Rodlike structures, however, cause the opposite behavior, yielding minimum axial ratios for

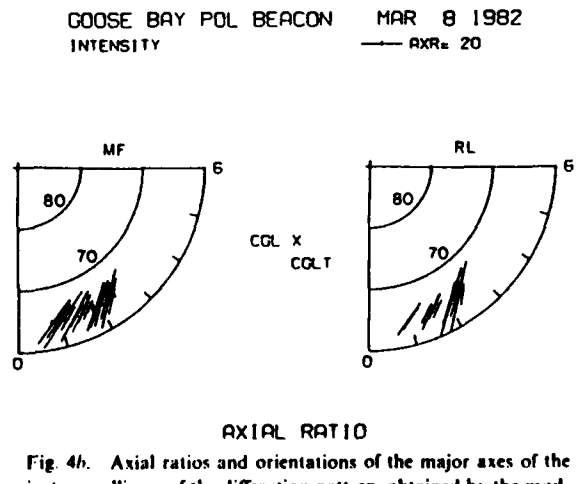


Fig. 4b. Axial ratios and orientations of the major axes of the anisotropy ellipses of the diffraction pattern, obtained by the modified Fedor (MF) and the Rino-Livingston (RL) algorithms. Goose Bay/polar beacon spaced-receiver intensity data recorded on March 8, 1982, have been used. The scale for the axial ratios is shown in the upper right-hand corner. Orientations are represented in this CGL \times CGLT reference frame by the angles between the line segments and the radial directions through their respective centers.

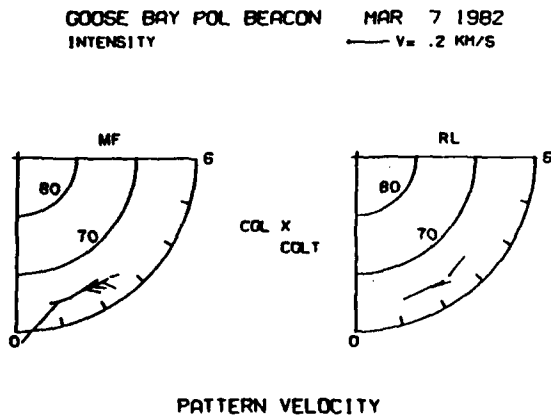


Fig. 5a. Magnitudes and directions of the true drift velocity of the diffraction pattern, obtained by the modified Fedor (MF) and the Rino-Livingston (RL) algorithms. Goose Bay/polar beacon spaced-receiver intensity data recorded on March 7, 1982, have been used. The scale for the magnitudes is shown in the upper right-hand corner. Directions are represented in this CGL \times CGLT reference frame by the angle between the line segments and the radial directions through their respective initial points.

the highest elevations of the ray path and higher axial ratios, such as those observed in Figures 4a and 4b, as the elevation decreases.

The drift velocities of the diffraction pattern measured on the same days are displayed in Figures 5a and 5b, using identical polar CGL versus CGLT coordinate systems. The magnitude of the velocity vector is represented by the length of a line segment starting at the vertical projection on the ground of the 350-km ionospheric penetration point. The scales for the magnitude, shown on the upper right-hand corners of these figures, differ from March 7 to March 8. The orientation of the velocity, on the other hand, is measured exactly as before.

A good general agreement between the results by the two algorithms is again observed, despite the numerical difficulties (the discussion on the geophysical conditions on March 7 and the greater sensitivity of the RL algorithm also applies here). A dramatic increase in the drift velocity of the diffraction pattern between the two consecutive days has been detected by the spaced-receiver measurements, confirming the calculations by Basu *et al.* [1985] from observations of the frequency of the Fresnel maxima in the spectra of the signal intensity. Using appropriate parameters for a quasi-stationary satellite ($z_s \gg z_i$, $v_s \approx 0$) and neglecting r_{pi} in (25), it is seen that, in such cases, the drift velocity of the diffraction pattern can be con-

sidered as an acceptable representation of the drift velocity in the high-latitude ionospheric *F* region. The eastward convection in the postmidnight time frame follows the simple two-cell model of the high-latitude ionospheric convection pattern *Heelis and Hanson, 1980; Heelis *et al.*, 1982*.

4.2. *Hilat observations at Tromsø, Norway*

In the second experiment to be discussed, signals transmitted at 413 MHz by the polar-orbiting Hilat satellite and recorded by three receivers at Tromsø, Norway (69.7°N, 18.9°E) on a routine basis have been analyzed. The receivers define a right triangle in the local NW quadrant, with sides equal to 331 m (east-west), 314 m (north-south) and 464 m, respectively. The north-south baseline is tilted eastward by approximately 8°. For more information on the Hilat scientific program, a special issue of the *Johns Hopkins APL Technical Digest* (April/June, 1984) can be consulted. Data recorded during the Hilat orbits over Tromsø beginning at 2330:00 UT on Dec. 5, 1983, at 2235:00 UT on Dec. 11, 1983, and at 0016:30 UT on Dec. 12, 1983, have been selected for discussion in this report. The projections on the ground of the 350-km ionospheric penetration point of the ray paths corresponding to these passes are sketched in Figure 6. The maximum elevation angles reached

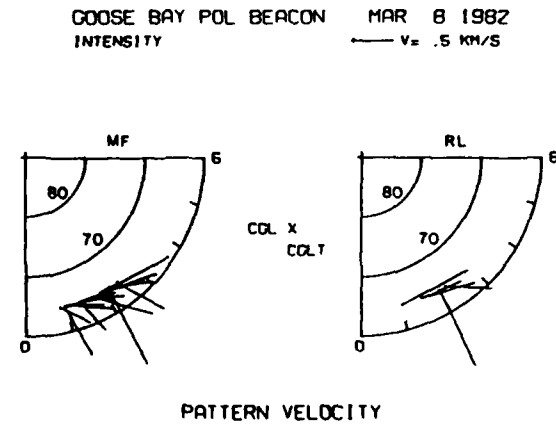


Fig. 5b. Magnitudes and directions of the true drift velocity of the diffraction pattern, obtained by the modified Fedor (MF) and the Rino-Livingston (RL) algorithms. Goose Bay/polar beacon spaced-receiver intensity data recorded on March 8, 1982, have been used. The scale for the magnitudes is shown in the upper right-hand corner. Directions are represented in this CGL \times CGLT reference frame by the angle between the line segments and the radial directions through their respective initial points.

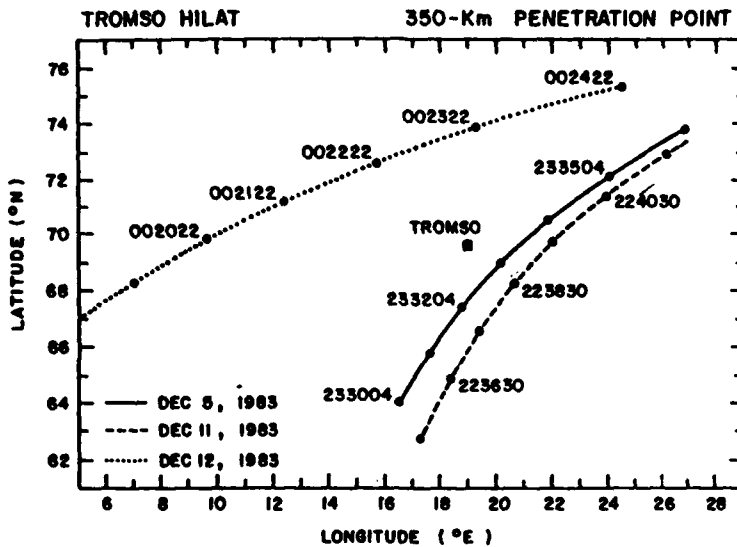


Fig. 6. Projections on the ground of the 350-km ionospheric penetration points of the ray paths for the three selected Hiliat passes over Tromsø.

during these passes were equal to 85°, 71°, and 47°, respectively. The effect of elevation angle on spaced receiver analysis will be illustrated from this set.

Scintillation enhancements frequently have been observed [Martin and Aarons, 1977; Fremouw *et al.*, 1978; Rino *et al.*, 1978; Livingston *et al.*, 1982] at auroral latitudes when the ray path lies within the local *L* shell. These enhancements can be clearly observed in Figure 7, which presents the values of the intensity scintillation index S_4 and the rms phase fluctuation σ_ϕ (in radians) at 137 MHz measured during the three passes as functions of the corrected geomagnetic latitude (CGL). The S_4 and σ_ϕ values are computed over 30 s of data with a 15 s overlap. The universal time for the three transits can also be obtained from the abscissa by considering that the successive tic marks signify 1-min intervals and the origin corresponds to 2329:01 UT, 2235:03 UT, and 0016:30 UT for Dec. 5, 11, and 12, 1983, respectively. It is seen that, regardless of the different geometries of the three passes, the geometrical enhancements are observed around $CGL \approx 66^\circ$ near midnight CGLT.

In the Hiliat experiment at Tromsø, the measured drift velocity of the ground diffraction pattern is dominated by the contribution of the satellite motion. This is clearly observed when the appropriate values for the satellite velocity and altitude ($v_s \approx 7.4$ km/s and $z_s \approx 830$ km) and typical ionospheric

drift velocities are substituted into (25). This equation also suggests that, as a result of uncertainties in z_s (height of the irregularity layer), the term $(z_s/z_i) v_s$ could introduce errors in the value of V which are comparable to the ionospheric drift v_d . Due to these difficulties, only results describing the anisotropy of the diffraction pattern will be further discussed.

For the spaced-receiver analysis, the signals have been sampled at 125 Hz, corresponding to a decimation of the original data by a factor of 2. Blocks with 10 s of data (corresponding to 1250 consecutive observations of the signal per channel) have been used to calculate each value of axial ratio and the orientation of the major axis of the anisotropy ellipse. Consecutive data blocks have been overlapped by 5 s.

Figures 8 and 9 show the results obtained on Dec. 5 and 11, respectively, using both the modified-Fedor (MF, triangles) and the Rino-Livingston (RL, pluses) algorithms. In Figure 10, results obtained on Dec. 12 using only the RL algorithm (pluses) can be seen. Although rectangular plots are presented here, angles (describing the orientations of the major axes) are measured in the CGL \times CGLT reference frame, exactly as before. That is, a 0° angle indicates a major axis aligned with the corrected geomagnetic north-south direction and a +90° (or -90°) angle represents a major axis aligned with the corrected geo-

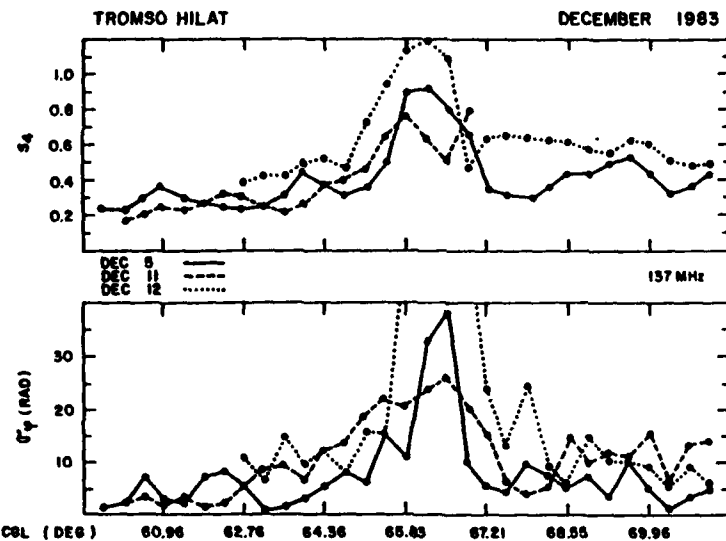


Fig. 7. Scintillation index S_4 and root mean square (rms) phase fluctuation σ_ϕ as functions of the corrected geomagnetic latitude (CGL), observed during the three selected Hilat passes over Tromsø. Tic marks on the horizontal axis are separated by 1 min in universal time. The respective origins for this scale are 2329:01 UT (Dec. 5), 2235:03 UT (Dec. 11) and 0016:30 UT (Dec. 12).

magnetic east-west direction. Large jumps in the angles sometimes observed in the lower panels are artificially caused by the existing 180° ambiguity in the orientation of the major axes.

The good agreement between the results obtained by the two algorithms is immediately evident from Figures 8 and 9. Although a similar agreement has been obtained on Dec. 12, 1983, we have illustrated

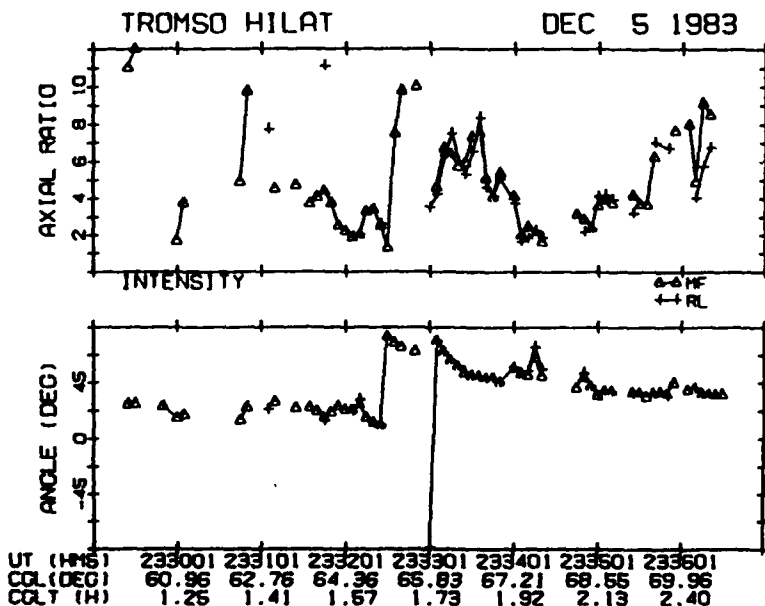


Fig. 8. Axial ratios and orientations of the major axes of the anisotropy ellipses of the diffraction patterns, obtained by applying the modified Fedor (MF, triangles) and the Rino-Livingston (RL, pluses) algorithms to Tromsø/Hilat spaced-receiver intensity data recorded on Dec. 5, 1983. Orientation angles are measured with respect to the northward direction in the CGL \times CGLT reference frame, being positive in the NE quadrant.

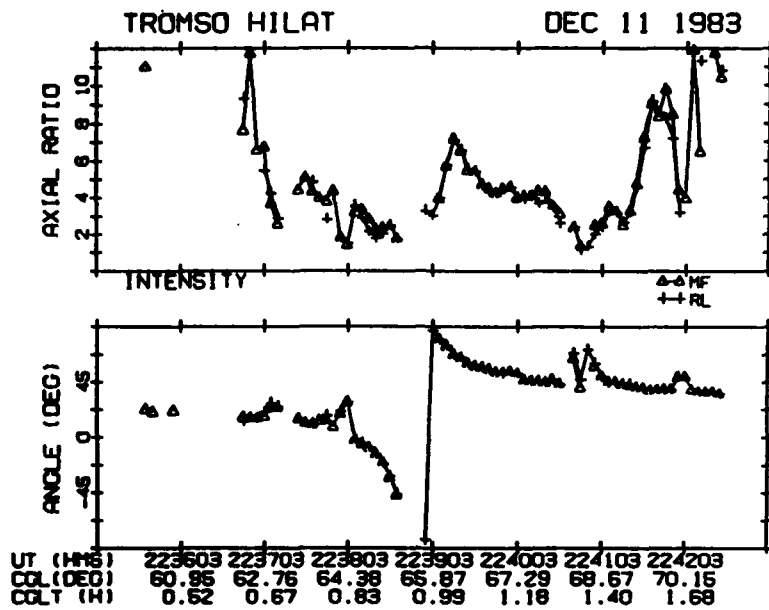


Fig. 9. Axial ratios and orientations of the major axes of the anisotropy ellipses of the diffraction patterns, obtained by applying the modified Fedor (MF, triangles) and the Rino-Livingston (RL, pluses) algorithms to Tromsø/Hilat spaced-receiver intensity data recorded on December 11, 1983. Orientation angles are measured with respect to the northward direction in the CGL \times CGLT reference frame, being positive in the NE quadrant.

in Figure 10 only the RL results to retain clarity of the diagram. The dashed lines in Figure 10 show the results of propagation model calculations for assumed anisotropy of in situ irregularities. The observational results will be compared with the model calculations in the next section.

It is interesting to note that the increased values of the axial ratio around 2333:15 UT on Dec. 5, 2239:10 UT on Dec. 11, and 001845 UT on Dec. 12 in Figures 8, 9 and 10, respectively, correspond to the regions where the ray paths were aligned with the local L shell. As a consequence, enhancements in S_4 and σ_s occurred and are shown in Figure 7 for the respective passes. On the three days, the peaks of these enhancements occurred around $CGL \approx 66^\circ$.

There is another feature to be noted. The axial ratios resulting from the Tromsø/Hilat measurements (even in the geometric enhancement region) are generally smaller than the typical Goose Bay/polar beacon axial ratios displayed in Figure 4. The same is true when the axial ratios at the geometric enhancement region shown here are compared with those previously obtained from the Poker Flat/Wideband measurements [Rino *et al.*, 1978; Livingston *et al.*, 1982]. Possible contributing factors to these differences will also be discussed in the next section.

4. DRIFT AND ANISOTROPY OF IONOSPHERIC IRREGULARITIES

The relationship between the measured drift of the ground diffraction pattern, the satellite velocity, and the ionospheric drift, summarized by (15), has been discussed in the previous sections. It is apparent that in the case of a low orbiting satellite, such as Hilat, the drift of the diffraction pattern is dominated by v_s . In such cases, it is very difficult to estimate v_d from a measurement of the drift of the diffraction pattern. In the case of a quasi-geostationary satellite, such as the polar beacon, however, a good estimate of the horizontal component of ionospheric drift can be obtained when the vertical component of drift becomes negligible.

The objective of the anisotropy measurements is to estimate the parameters A and B in (6) which characterizes the anisotropy of the in situ irregularities. In order to determine these parameters from the axial ratio and orientation of the major axis of the anisotropy ellipse of the diffraction pattern on the ground, an appropriate inverse propagation model has to be used. In keeping with the nomenclature used by Livingston *et al.* [1982] and others, the irregularities with $B \approx 1$ will be called rods, those with

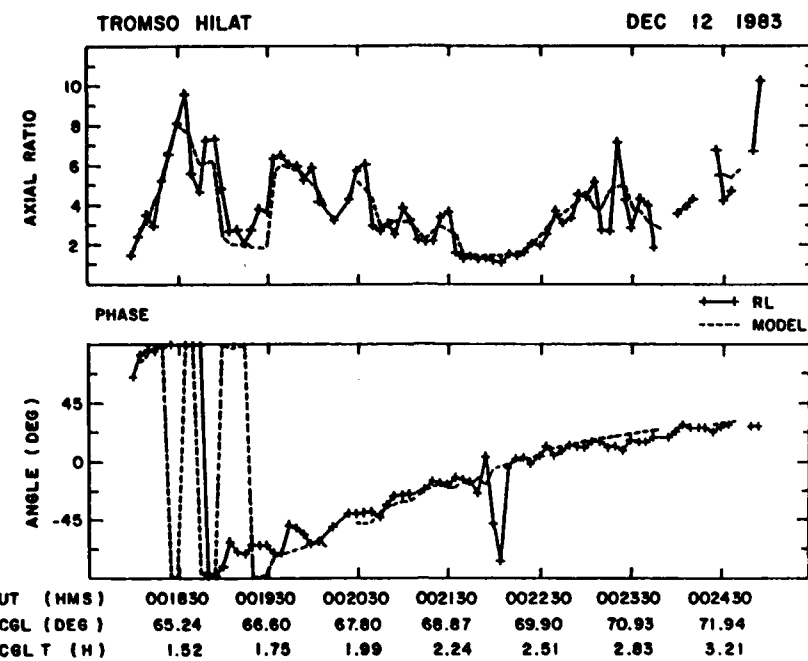


Fig. 10. Axial ratios and orientations of the major axes of the anisotropy ellipses of the diffraction pattern, obtained by applying the Rino-Livingston (RL, pluses) algorithm in Tromsø/Hilat spaced-receiver phase data recorded on December 12, 1983. Orientation angles are measured with respect to the northward direction in the CGL \times CGLT reference frame, being positive in the NE quadrant. Dashed lines show results of calculations by the propagation model, using the values for A and B displayed in Figure 11.

$A \approx B > 1$ will be referred as sheets and those with $A > B > 1$ as wings. The isotropic irregularities will be described by $A \approx B \approx 1$.

It has been shown in the discussion on (18) and (19) that the anisotropy ellipse of the diffraction pattern is the geometrical projection along the ray path onto the ground of the ellipsoid defining the anisotropy of the in situ irregularities. Since different ellipsoids could project onto the same ellipse, it is not possible to associate a unique pair (A , B) to each single observation of the axial ratio and orientation of the major axis of the anisotropy ellipse. However, it should be possible, under a few obvious conditions, to reconstruct a single ellipsoid from multiple projections on the ground. First, the projections should all correspond to the same ellipsoid. Further, it is necessary that these projections be reasonably different from each other. That is, they should correspond to reasonably different ray paths.

These conditions are not easily met in the case of a quasi-geostationary satellite where the ray path moves very slowly, penetrating the ionosphere at approximately constant aspect angles. In view of this,

we shall not attempt to derive a more quantitative estimate of the anisotropy of the in situ irregularities for the Goose Bay/polar beacon experiment.

In the case of a low-orbiting satellite, the ray path experiences fast variations in azimuth and elevation. This is one of the desired conditions which has been established above. However, the underlying constraint to preserve the anisotropy of the in situ irregularities requires the measurement set to encompass a small spatial scan of the ionosphere.

Consistent with these conflicting requirements, an average ionospheric anisotropy can be estimated from the minimum adequate number of observations of the anisotropy ellipse of the diffraction pattern by an inversion of the propagation model.

5.1. Irregularity anisotropy by error minimization procedure

In this section, we shall attempt to determine the anisotropy coefficients A and B through the minimization of the rms errors between measured and calculated (by the model) values of the axial ratio

and the orientation of the major axis of the anisotropy ellipse of the diffraction pattern. More precisely, given a set of consecutive observations (R_n, Ψ_n) , $n = 1, \dots, N_0$, it is desired to find (A, B) in the region $A \geq B \geq 1$ (since the irregularities are supposed to be preferentially elongated along the geomagnetic field lines) which minimizes

$$\begin{aligned} \epsilon &= \sum_{n=1}^{N_0} \{ [R_n \cos 2\Psi_n - r(A, B; \mathbf{p}_n) \cos 2\psi(A, B; \mathbf{p}_n)]^2 \\ &\quad + [R_n \sin 2\Psi_n - r(A, B; \mathbf{p}_n) \sin 2\psi(A, B; \mathbf{p}_n)]^2 \} \\ &= \sum_{n=1}^{N_0} \{ [R_n - r(A, B; \mathbf{p}_n)]^2 + 4R_n r(A, B; \mathbf{p}_n) \\ &\quad \cdot \sin^2 [\Psi_n - \psi(A, B; \mathbf{p}_n)] \} \end{aligned} \quad (22)$$

where $r(A, B; \mathbf{p}_n)$ and $\psi(A, B; \mathbf{p}_n)$ are the respective values of the axial ratio and the orientation of the diffraction pattern calculated by the model as functions of A , B and \mathbf{p}_n . The vector \mathbf{p}_n gathers all the remaining parameters of the model (such as the height of the penetration point, azimuth and elevation of the ray path, geomagnetic field declination and dip angle, and so on), assumed to be known at the instant of time t_n that the pair (R_n, Ψ_n) has been observed ($n = 1, \dots, N_0$). The angles in the first part of (22) are multiplied by 2 to account for the 180° ambiguity in the orientation of the major axis of the anisotropy ellipse. It is seen that the final expression for ϵ displays the intuitively desired properties: the rms error tends to zero when, simultaneously, measured and calculated axial ratios are equal and measured and calculated orientations differ by an arbitrary integer multiple of 180° . It should also be observed that the value found for ϵ at the solution (A, B) can be considered as an indicator of its quality: the higher the error is, the less reliable the solution is.

A computer code to minimize (22) has been implemented by combining the propagation model already described with subroutine ZXSSQ, available from the International Mathematical Subroutine Library (IMSL). This subroutine is based on a derivative-free analogue of the Levenberg-Marquardt algorithm for nonlinear least squares approximation [Brown and Dennis, 1972]. To guarantee that the solutions are constrained to the region $A \geq B \geq 1$, the following transformation has been used

$$A = 1 + (A_0 - 1) \sin^2 t \quad (23a)$$

$$B = 1 + (A_0 - 1) \sin^2 u \quad (23b)$$

where A_0 is an arbitrarily large constant. The minimization is initially performed over the unconstrained two-dimensional space (t, u) , the solution being then substituted back into (23) to calculate the desired anisotropy of the in situ irregularities.

This procedure has been tested initially using artificial data. In order to generate this data set, irregularities with known anisotropy (A, B) were uniformly distributed through the ionosphere. Next an artificial satellite mimicking a Hilat orbit was allowed to scan through the ionosphere. By the use of the propagation model, the ground diffraction pattern was artificially generated and the axial ratio and orientation of the diffraction pattern determined. The error minimization procedure, outlined above, was next used in conjunction with the inverse propagation model to recover the assumed values of A and B . The tests were successful in all three types of assumed anisotropies.

The minimization procedure has been applied to results obtained by the Rino-Livingston algorithm operating on Tromsø Hilat data and shown in Figure 10. Here, three consecutive observations (R_m, Ψ_m) , $m = M - 1, M, M + 1$ have been used to estimate the values for A and B at the instant of time corresponding to the central observation ($m = M$). M has then been incremented by 1 and the process has been successively repeated until the data have been exhausted. The estimated values for these parameters are shown in Figure 11. These values have also been applied to the model to calculate the corresponding parameters of the anisotropy ellipse of the diffraction pattern. The calculated axial ratios and orientations are shown in Figure 10 (dashed curve). The good agreement between measured and calculated anisotropies of the diffraction pattern is evident.

There are reasons to believe that the most outstanding features in Figure 11 (a 20:16:1 sheet at 0018:30 UT and a winglike structure immediately after 0022:30 UT) are not real, but are artificially generated when the inversion of the model becomes unstable. The examples in Livingston et al. [1982] also indicate that there are regions along the passes (where the elevation angles of the ray paths are generally low) in which the model predicts very similar values of axial ratios (and orientations) from very different combinations of A and B .

Apart from these regions, Figure 11 shows a complex structuring of the F region irregularities, with moderate to small sheets (particularly in the geometrical enhancement region, around 0018:45 UT)

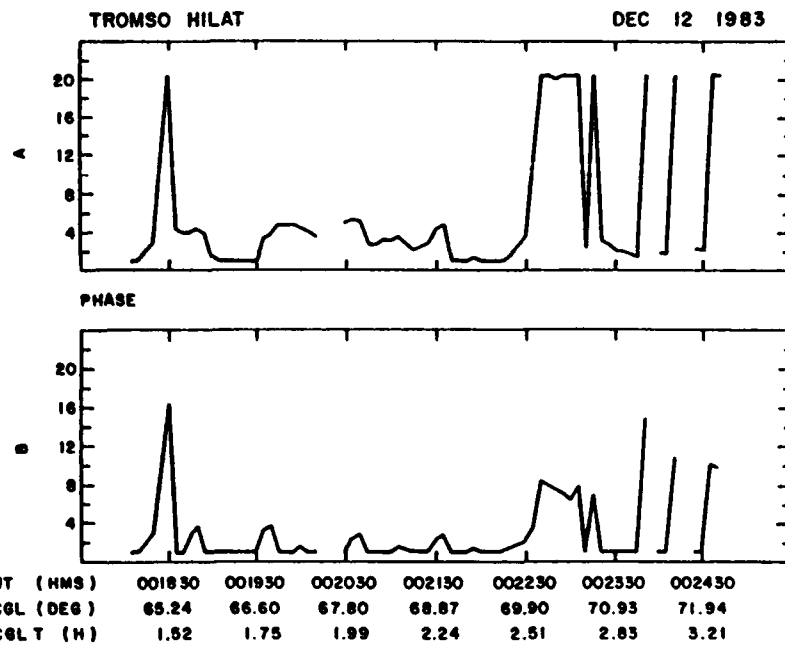


Fig. 11. Values for the parameters A and B characterizing the anisotropy of the in situ irregularities, obtained from the application of the minimization procedure to the Rino-Livingston (RL, pluses) results shown in Figure 10.

giving way to moderate to small rods or isotropic irregularities at later times (northward of Tromsø). Further, from a comparison between the axial ratios in Figures 8–10, one would expect a similar behavior of the irregularities on the other 2 days. High axial ratios are obtained in the region of local L shell alignment due to the presence of sheetlike irregularities. In addition, there is a clear indication of the presence of rodlike irregularities northward of Tromsø on these days (later than 2335:30 UT on December 5, 1983, and 2241:03 UT on December 11, 1983). These results thus seem to reproduce at Tromsø those results which emerged from the Poker Flat/Wideband experiment [Livingston et al., 1982].

The present example thus shows encouraging results of a numerical technique to estimate the anisotropy of in situ irregularities from the measurements of analogous parameters of the ground diffraction pattern. A study is being initiated to better characterize its sensitivity to perturbations in the input data and its ability to converge to correct solutions for a large set of practical conditions.

Comparing each of the time histories of the rms phase fluctuation σ_ϕ or the scintillation index S_4 (shown in Figure 7) with that of the axial ratio mea-

sured on the same day (respectively shown in Figures 8–10), one can observe the importance of the anisotropy in relation to the scintillation magnitudes. Since the axial ratio does not depend on the strength of the irregularities, the observed enhancements of S_4 and σ_ϕ result from the geometrical factors that are sensitively controlled by the anisotropy parameters.

The elongations of the irregularities inferred from Figures 8–10 are considerably smaller than those detected by the Goose Bay/polar beacon measurements previously discussed (particularly those obtained on March 8, 1982). They also seem to be typically smaller than the elongations resulting from the Wideband program [Livingston et al., 1982].

An explanation for smaller-than-expected values of the axial ratio of the ground diffraction pattern involves effects of the distances between the receivers on the measurements. Golley and Rossiter [1970] have used an array of 89 dipoles filling a circle of diameter 1 km (with the dipoles located at the nodes of a 91.4-m² grid) to (1) compare results from the spatial correlation analysis [Briggs, 1968] with those from the temporal correlation analysis of spaced-receiver data, and (2) compare results from the temporal correlation analysis, using different receiver

layouts. Some of their findings on the behaviors of the parameters of the ground diffraction pattern can be summarized as follows: (1) the drift velocities resulting from the temporal correlation analysis increase with the triangle size, tending however to a limiting value which is very nearly equal to the drift velocity obtained from the spatial correlation technique; (2) the directions of the drift velocity obtained from the temporal correlation technique have not shown any systematic dependence on the triangle size, being in good agreement with the respective values calculated by the other technique; (3) the scale of the correlation ellipses, defined as their radius in the direction of the drift, varies with increasing triangle sizes, in a similar manner to that of the drift velocity; (4) the major axis of the correlation ellipse tends to be aligned along the triangle hypotenuse for small triangles, but this tendency decreases as the size of the triangle increases; (5) the size of the triangle at which the drift velocity reaches a limiting value depends on the scale of the pattern. Although variations of the measured axial ratios with the triangle size have not been explicitly studied in that reference, the above results, at least, leave the door open to this relationship. In addition, the observation of irregularity fluctuations with large scale sizes by small triangles would result in essentially equal received signals, with negligible time delays between similar structures detected in different channels. In this situation, the spaced-receiver analysis would tend to identify a larger number of isotropic diffraction patterns than it should. On the other hand, when the separations between the antennas become very large, there is an increasing possibility that structures detected by one ray path be missed by at least one of the other ray paths. There would then be very little correlation between the signals and the spaced-receiver analysis would break down. It should be noted that, in a power-law environment, the former situation is potentially more damaging, since large structures also carry more power.

In an attempt to quantify the above discussion, it will be assumed that a satellite is orbiting at a height z , above the ground, where two receivers are separated by l , as shown in Figure 12. Let the range of perpendicular scale sizes λ_1 of the in situ irregularities from which the spaced-receiver measurements provide the best results be such that $r_1 < l/\lambda_1 < r_2$, where $r_{1,2}$ are the lower and upper limits for the ratio l/λ_1 and λ is defined in the same figure. Further, let frequencies v and scale sizes λ_1 be scaled by λ_1 , $v =$

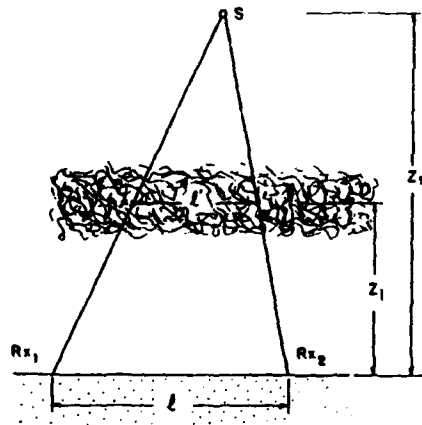


Fig. 12. Partial sketch of the spaced-receiver experiment, to support the study on the influence of the separation between the antennas and the satellite velocity on the measurements.

v_p , where v_p is the velocity of the irregularities with respect to the ionospheric penetration point of the ray paths. It then follows that the ideal frequency band for the spaced-receiver measurements is given by

$$v_1(l; r_1) = r_1 \left(\frac{z_s}{z_s - z_i} \right) \frac{v_p}{l} < v \\ < r_2 \left(\frac{z_s}{z_s - z_i} \right) \frac{v_p}{l} = v_2(l; r_2) \quad (24)$$

where the velocity v_p is equal to the ionospheric drift v_d in the case of a quasi-geostationary satellite and to $(z_s/z_i) v_s$ in the case of a low-orbiting satellite with orbital velocity v_s . The ideal frequency band thus depends on both the velocity v_p and the separation l between the receivers.

In the experiments discussed in the previous section, power spectral densities of intensity and phase scintillation have been observed in the frequency band $0.1 \text{ Hz} < v < 10 \text{ Hz}$, shown in the left-hand scales of Figures 13a and 13b. The much narrower frequency bands where the observed spectra typically reach the respective noise levels, defining frequencies v_{N} , are clearly identified in these figures. Another relevant feature of the observed intensity spectra is the Fresnel frequency v_{F} , below which the spectra flatten. As indicated by the arrows, this frequency has not remained constant during the periods of observation (approximately 90 min or 10 min for the Goose Bay/polar beacon or the Tromsø/Hilat measurements, respectively). Also shown by the dotted lines and the horizontal scales in these figures is an

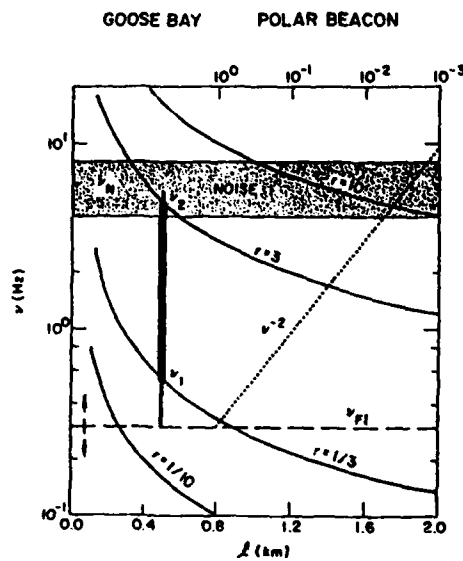


Fig. 13a. Relationships between the lower and upper limits of the frequency band (vertical scale) involved in the Goose Bay/polar beacon spaced-receiver experiment and the distance l between the antennas (lower horizontal scale), for different values of the parameter $r = r_{1,2}$. Also shown are the frequency band where the observed power spectra reach the noise level, the (variable) Fresnel frequency v_{FI} of the intensity signals, as well as a dotted curve displaying a normalized v^{-2} dependence of the power spectra of the received signals (upper horizontal scale). The thick vertical bar at $l = 500$ m (actual separation between the antennas) represents the ideal frequency band for the Goose Bay/polar beacon spaced-receiver measurements.

approximate $P(v) \propto v^{-2}$ frequency behavior for the power spectral densities, arbitrarily normalized in such a way that $P(v_{FI}) = 1$.

Curves showing variations of the frequency limits $v_{1,2}(l; r_{1,2})$ as functions of the receiver spacing (lower horizontal scales) and having $r = r_{1,2}$ as a parameter can also be seen. Curves are shown for $r_1 = 1/10, 1/3$ and for $r_2 = 3, 10$. The values $r_1 = 1/10$ and $r_2 = 10$ are generally associated with the ideas of "much smaller than" or "much greater than" in engineering calculations. The values $r_1 = 1/3$ and $r_2 = 3$ have been associated with the same respective ideas in the magnetoionic theory and, more importantly, with the characterization of the scale size interval which has provided the most reliable results in a simulation of the spaced-receiver measurements by Wright and Pitteway [1978]. Typical values for the remaining parameters have been used. For the Goose Bay/polar beacon experiment, $z_s \gg z_i$ and $v_D \approx 800$ m/s. For the Tromsø/Hilat experiment, $z_s \approx 800$ km, $z_i \approx 350$ km

and $v_s = 7.4$ km/s. While v_s is approximately constant, variations in v_D would cause the Goose Bay/polar beacon curves to proportionally shift upward or downward.

The typical receiver spacings in these experiments are 500 m and 320 m, respectively. In each figure, a thick vertical bar (parallel to the frequency axis) at the appropriate spacing defines the "ideal" frequency band for the respective spaced-receiver measurements. The lower limit for this frequency band is given by the respective curve $v_1(l; r_1 = 1/3)$. Its upper limit is given by the smaller of $v_2(l; r_2 = 3)$ and v_N . It is seen that the values for r_1 and r_2 established by Wright and Pitteway [1978] have been adopted in the present characterization of the "ideal" frequency band. Broader frequency bands, defined by thin vertical bars, can also be seen in the same figures. The lower limits for these frequency bands are the greater of $v_1(l; r_1 = 1/10)$ and v_{FI} (in the case of intensity spectra), while their upper limits are the smaller of

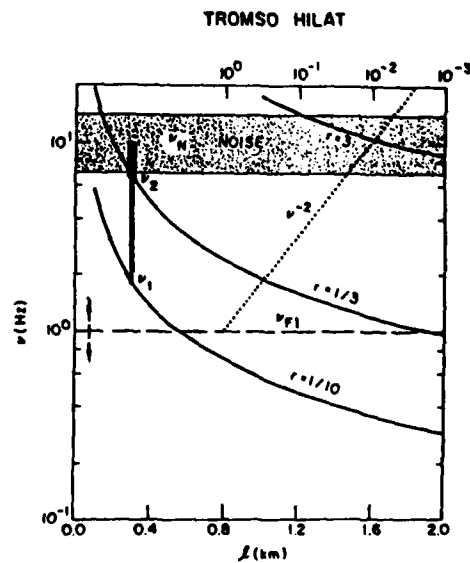


Fig. 13b. Relationships between the lower and upper limits of the frequency band (vertical scale) involved in the Tromsø/Hilat spaced-receiver experiment and the distance l between the antennas (lower horizontal scale), for different values of the parameter $r = r_{1,2}$. Also shown are the frequency band where the observed power spectra reach the noise level, the (variable) Fresnel frequency v_{FI} of the intensity signals, as well as a dotted curve displaying a normalized v^{-2} dependence of the power spectra of the received signals (upper horizontal scale). The thick vertical bar at $l = 320$ m (actual separation between the antennas) represents the ideal frequency band for the Tromsø/Hilat spaced-receiver measurements.

$v_2(l; r_2 = 10)$ and v_N . Since scale sizes reasonably larger than the respective receiver spacing are now considered, a degradation of the results from the spaced-receiver analysis applied over this broader frequency band is more likely to occur, according to the above reasoning.

Finally, note that the "ideal" frequency band for the spaced-receiver analysis is relatively well matched with the available frequency band (between v_F and v_N) for scintillation observations in the case of the Goose Bay/polar beacon experiment. The relative mismatch between these two frequency bands in the case of the Tromsø/Hilat measurements could be partially responsible for the small axial ratios obtained for the anisotropy ellipse of the diffraction pattern. One obvious way of obtaining a better match between these two frequency bands is to bandpass filter the original signals to reject the components outside the "ideal" frequency band as much as possible. One alternative to this procedure would be to apply the spectral analysis of spaced-receiver data described in the companion paper [Costa and Fougere, 1987] upon the "ideal" frequency band only. Figure 13b shows, however, that neither solution is totally effective in the present case, since both are equivalent to rejecting a very high percentage of the total available power. Nevertheless, in support of the above arguments, one of the examples (using Tromsø/Hilat data recorded on December 5, 1983) of the application of the spectral analysis upon a slightly broader frequency band than the "ideal" has shown an increase in the axial ratio around the geometrical enhancement region.

The present arguments could also explain the apparently higher axial ratios resulting from the Poker Flat/Wideband measurements. While the relevant parameters of the Wideband and Hilat satellites were similar, the typical antenna separation at Poker Flat was approximately equal to 900 m. This is a more favorable situation to spaced-receiver measurements employing such a low-orbiting satellite as the source of the signals, as a diagram analogous to that in Figure 13b would show.

6. SUMMARY

Two algorithms which provide a statistical treatment to the estimation of the parameters of the spaced-receiver analysis have been reviewed in this contribution. Both operate on the autocorrelation and cross-correlation functions of the received signals, which are modeled by a decreasing function of

two spatial variables (representing distances between receivers) and the time delay, all combined into a positive-definite quadratic form. That is, it is assumed that, for a fixed instant of time, lines of constant correlation levels define ellipses, which characterize the anisotropy of the ground diffraction pattern.

In general, a good agreement has been found between the results from the two algorithms. However, in a relatively small percentage of the observations, at least one of the algorithms has collapsed or a difference has been detected between their results. It has been shown [McGee, 1966; Briggs and Golley, 1968; Wernik et al., 1983] that random or regular velocity changes along the ray path could be translated into cross-correlation functions which are not symmetric around their maxima, thus leading to a disagreement between the data and the present model, represented by (1). Also, the algorithm suggested by Rino and Livingston [1982] uses only the time delays for the maxima and the crossings of the correlation functions to estimate the anisotropy and the drift velocity of the diffraction pattern. On the other hand, the generalized version of the Fedor [1967] algorithm presented here uses the information provided by the correlation functions more fully. This disagreement between the data and their model and the different approaches of the algorithms to the same estimation problem are the most likely explanations for the observed differences in their results.

The spaced-receiver analysis of signals transmitted from a quasi-geostationary polar beacon and received at Goose Bay has shown a great variability in the anisotropy and the drift velocity of the diffraction pattern observed on 2 consecutive days. Variations of these parameters on shorter time scales have also been detected. Relatively high axial ratios of the anisotropy ellipse of the diffraction pattern have been observed. Considering the relatively low elevation angles of the ray paths (approximately 45°), these values seem to indicate the presence of rodlike in situ irregularities northward of Goose Bay. Further, the essentially eastward drift velocities measured on both days between 0400 UT and 0530 UT follow the pattern of eastward plasma drift in the auroral zone during this time sector [Heelis and Hanson, 1980; Heelis et al., 1982].

Signals transmitted by the Hilat satellite and received at Tromsø have also been analyzed. The results seem to reproduce those observed during the Poker Flat/Wideband experiment [Fremouw et al.,

1977; Rino *et al.*, 1978; Livingston *et al.*, 1982]. That is, enhancements of the axial ratio are observed around the region of local L shell alignment of the ray path, indicating the presence of sheetlike irregularities. Further, the observed increase of the axial ratio at the later parts of the orbits selected for analysis indicates the existence of rodlike irregularities northward of Tromsø. Analogous behaviors have also been observed in the scintillation index S_4 and in the rms phase fluctuation σ_ϕ . Within the scope of the present theory, the axial ratio does not depend on the strength of the in situ irregularities. The above result thus seems to indicate that changes in the anisotropy of the irregularities may play an important role in the observed variations in S_4 and σ_ϕ .

It has also been observed that the axial ratios resulting from the Tromsø/Hilat measurements are smaller than their equivalents from the Goose Bay/polar beacon or the Poker Flat/Wideband experiments. Since different receiver separations and/or satellites with different velocities have been employed, these experiments sample irregularities with different scale sizes. Any dependence of the anisotropy of the in situ irregularities on their scale sizes (caused, for instance, by mechanisms responsible for their generation or removal) could, in principle, be translated into differences in the axial ratios. It is not clear, however, whether such a dependence would be strong enough to explain the above observations. Further, structures with scale sizes much larger than those which would be ideally sampled by the particular experiment would be detected by all the receivers almost simultaneously, thus tending to indicate the presence of more isotropic irregularities. This mechanism is reinforced by the fact that, in a power-law environment, structures with larger scale sizes also carry more power. It has been indicated that the Tromsø/Hilat experiment, due to the relatively small separations between the receivers, seems to have been particularly affected by this mechanism.

Finally, a simple propagation model of the spaced-receiver experiment has been presented. It has shown that the anisotropy ellipses of the diffraction pattern are geometrical projections along the ray path onto the ground of the assumed ellipsoids which characterize the anisotropy of the in situ irregularities. Since a continuum of ellipsoids project onto the same ellipse, it is not theoretically possible to associate a unique set of parameters specifying the anisotropy of the irregularities to each observation of

the anisotropy of the ground diffraction pattern. A numerical technique has been proposed which associates an average anisotropy of a volume in the ionospheric F region to multiple observations of the anisotropy ellipse of the diffraction pattern. A nonlinear minimization of the rms error between measured and calculated (by the propagation model) values of this parameter is used in this procedure. The importance of using observations of the anisotropy ellipse corresponding to ray paths which penetrate the ionosphere with reasonably different aspect angles has been emphasized. When this condition is not met, the procedure becomes very unstable, and small perturbations in the data could lead to large departures from the true value of the anisotropy of the F region irregularities. Thus to use this procedure more effectively in the future, it is important, as a continuation of the present work, to define its stability region more precisely.

Acknowledgments. This work has been performed while E.C. was on a sabbatical leave of absence from CETUC-PUC/RJ, Rio de Janeiro, Brazil. He would like to thank his colleagues and friends from the Physics Research Division, Emmanuel College, and the Ionospheric Effects Branch, Air Force Geophysics Laboratory, for the stimulating scientific environment and the continued demonstrations of hospitality during this period. The discussions within the Hilat scientific community have also been greatly appreciated. The authors thank Sunanda Basu for her genuine interest and many valuable suggestions, which led to improvements in the present work. They also wish to acknowledge the essential role of Elizabeth Galligan in the tedious and time-consuming preprocessing of the data. The work at Emmanuel College was partially supported by AFGL contract F1928-86-K-0038, and by an AFGL laboratory director's fund, ILIR 5B01.

REFERENCES

- Armstrong, J. W., and W. A. Coles, Analysis of three-station interplanetary scintillation, *J. Geophys. Res.*, 77, 4602-4610, 1972.
- Banerji, R. B., Radio-measurements of ionospheric drift as a problem in parameter estimation, in *Statistical Methods in Radio Wave Propagation*, edited by W. C. Hoffman, Pergamon, New York, 1960.
- Basu, S., Su. Basu, J. LaBelle, E. Kudeki, B. G. Fejer, M. C. Kelley, H. E. Whitney, and A. Bushby, Gigahertz scintillations and spaced receiver drift measurements during Project Condor equatorial F region rocket campaign in Peru, *J. Geophys. Res.*, 91, 5526-5538, 1986.
- Basu, Su., S. Basu, E. MacKenzie, and H. E. Whitney, Morphology of phase and intensity scintillations in the auroral oval and polar cap, *Radio Sci.*, 20, 347-356, 1985.
- Briggs, B. H., On the analysis of moving patterns in geophysics, I. Correlation analysis, *J. Atmos. Terr. Phys.*, 30, 1777-1788, 1968.
- Briggs, B. H., and M. G. Golley, A test for dispersion in F -region drifts observed by the radio star scintillation method, *J. Atmos. Terr. Phys.*, 30, 963-973, 1968.

Briggs, B. H., G. J. Phillips, and D. H. Shinn, The analysis of observations on spaced receivers of the fading of radio signals, *Proc. Phys. Soc. London, Sec. B*, 63, 106-121, 1950.

Brown, K. M., and J. E. Dennis, Jr., Derivative free analogues of the Levenberg-Marquardt and Gauss algorithms for nonlinear least squares approximation, *Num. Math.*, 18, 289-297, 1972.

Burg, J. P., Maximum entropy spectral analysis, Ph.D. thesis, 123 pp., Stanford Univ., Palo Alto, Calif., 1975.

Burg, J. P., A new analysis technique for time series data, in *Modern Spectrum Analysis*, edited by D. G. Childers, IEEE Press, New York, 1981.

Costa, E., and P. F. Fougere, Cross-spectral analysis of spaced-receiver measurements, *Radio Sci.*, this issue.

Fedor, L. S., A statistical approach to the determination of three-dimensional ionospheric drifts, *J. Geophys. Res.*, 72, 5401, 1967.

Fougere, P. F., Spontaneous line splitting in multichannel maximum entropy power spectra, paper presented at First Acoustics, Speech and Signal Processing Workshop on Spectral Estimation, ASSP, Hamilton, Ont., Canada, 1981.

Fougere, P. F., On the accuracy of spectrum analysis of red noise processes using maximum entropy and periodogram methods: Simulation studies and application to geophysical data, *J. Geophys. Res.*, 90, 4355-4366, 1985.

Fremouw, E. J., R. L. Leadabrand, R. C. Livingston, M. D. Cousins, C. L. Rino, B. C. Fair, and R. A. Long, Early result from the DNA Wideband satellite experiment: Complex-signal scintillations, *Radio Sci.*, 13, 167-187, 1978.

Golley, M. G., and D. E. Rossiter, Some tests of methods of analysis of ionospheric drift records using an array of 89 aerials, *J. Atmos. Terr. Phys.*, 32, 1215-1233, 1970.

Heelis, R. A., and W. B. Hanson, High-latitude ion convection in the nighttime F region, *J. Geophys. Res.*, 85, 1995-2002, 1980.

Heelis, R. A., J. K. Lowell, and R. W. Spiro, A model of the high-latitude ionospheric convection pattern, *J. Geophys. Res.*, 87, 6339-6345, 1982.

Jones, R. H., Multivariate autoregression estimation using residuals, in *Applied Time Series Analysis*, edited by D. Findley, Academic, Orlando, Fla., 1978.

Kent, G. S., and J. R. Koster, Some studies of nighttime F-layer irregularities at the equator using very high frequency signals radiated from earth satellite, *Ann. Geophys.*, 22, 405-417, 1966.

Livingston, R. C., C. L. Rino, J. Owen, and R. T. Tsunoda, The anisotropy of high-latitude nighttime F region irregularities, *J. Geophys. Res.*, 87, 10,519-10,526, 1982.

Martin, E., and J. Aarons, F layer scintillations and the aurora, *J. Geophys. Res.*, 82, 2717-2722, 1977.

McGee, C. R., On the nature of movements in the ionosphere, *J. Atmos. Terr. Phys.*, 28, 861-869, 1966.

Mitra, A. N., A radio method of measuring winds in the ionosphere, *Proc. Inst. Elec. Eng.*, 96, 441-446, 1949.

Moorcroft, D. R., and K. S. Arima, The shape of the F-region irregularities which produce satellite scintillations: Evidence for axial asymmetry, *J. Atmos. Terr. Phys.*, 34, 437-450, 1972.

Morf, M., A. Vieira, D. T. L. Lee, and T. Kailath, Recursive multi-channel maximum entropy spectral estimation, *IEEE Trans. Geosci. Electron.*, GE-16, 85-94, 1978.

Nuttall, A. H., Multivariate linear predictive spectral analysis employing weighted forward and backward averaging: A generalization of Burg's algorithm, *Tech. Rep. 5501*, Nav. Underwater Syst. Cent., New London, Conn., 1976.

Phillips, G. J., and M. Spencer, The effects of anisometric amplitude patterns in the measurements of ionospheric drifts, *Proc. Phys. Soc. London, Sec. B*, 68, 481-492, 1955.

Rino, C. L., On the application of phase screen models to the interpretation of ionospheric scintillation data, *Radio Sci.*, 17, 855-867, 1982.

Rino, C. L., and E. J. Fremouw, The angle dependence of singly scattered wavefields, *J. Atmos. Terr. Phys.*, 39, 859-868, 1977.

Rino, C. L., and R. C. Livingston, On the analysis and interpretation of spaced-receiver measurements of transionospheric radio waves, *Radio Sci.*, 17, 845-854, 1982.

Rino, C. L., R. C. Livingston, and S. J. Matthews, Evidence for sheetlike auroral ionospheric irregularities, *Geophys. Res. Lett.*, 5, 1039-1042, 1978.

Scheffé, H., *The Analysis of Variance*, John Wiley, New York, 1959.

Strand, O. N., Multichannel complex maximum entropy (autoregression) spectral analysis, *IEEE Trans. Auto. Contr.*, AC-22, 634-640, 1977.

Tatarskii, V. I., *The effects of the turbulent atmosphere on wave propagation*, Nat. Tech. Inform. Serv., Springfield, Va., 1971.

Wernik, A. W., C.-H. Liu, and K. C. Yeh, Modeling of spaced-receiver scintillation measurements, *Radio Sci.*, 18, 743-764, 1983.

Wright, J. W., and M. L. Pitteway, Computer simulation of ionospheric radio drift measurements, and their analysis by correlation methods, *Radio Sci.*, 13, 189-210, 1978.

Yeh, K. C., and C. H. Liu, Radio wave scintillations in the ionosphere, *Proc. IEEE*, 70, 324-360, 1982.

S. Basu and P. F. Fougere, Ionospheric Physics Division, Air Force Geophysics Laboratory, Hanscom Air Force Base, MA 01731.

E. Costa, CETUC-PUC, RJ, Rua Marqués de São Vicente 225, 22453 Rio de Janeiro RJ, Brazil.

ATTACHMENT 4

Radio Science, Volume 23, Number 2, Pages 129-139, March-April 1988

Cross-spectral analysis of spaced-receiver measurements

Emanoel Costa¹

Physics Research Division, Emmanuel College, Boston, Massachusetts

Paul F. Fougerre

Ionospheric Physics Division, Air Force Geophysics Laboratory, Hanscom Air Force Base, Massachusetts

(Received May 11, 1987; revised November 16, 1987; accepted December 8, 1987.)

The apparent velocity calculated by the dispersion analysis is interpreted in terms of the fundamental parameters of the cross-correlation analysis of spaced-receiver data, without any assumptions in addition to those already present in the latter technique. The dispersion analysis is then generalized, by assuming a realistic (power law) functional form for the power spectral density of the irregularities in the ionospheric *F* region. Next, an algorithm is proposed to estimate the anisotropy and the true drift velocity of the ground diffraction pattern directly from the cross spectra of the received signals. This technique is applied to HiLat spaced-receiver data recorded at Tromsø, Norway (69.7°N, 18.9°N), in two different modes. In the first, it is applied on a relatively broad frequency band and its results compared with those from the cross-correlation analysis. A good general agreement is found. In the second mode, the technique is repeatedly applied on narrow and adjacent frequency bands, to detect possible frequency variations of the anisotropy of the diffraction pattern. A behavior analogous to that of the apparent velocity, previously reported in the literature, is then observed.

1. INTRODUCTION

There are two ways to analyze data from spaced-receiver measurements.

The first is the correlation analysis technique, based on the original idea that transionospheric signals received by spaced probes on the ground display similar structures displaced in time. Dividing the distances between the receivers by the respective average time delays between these similar structures, a crude estimate for the drift velocity of the diffraction pattern defined on the ground can be obtained. A refinement of this idea uses the autocorrelation and cross-correlation functions between the received signals to estimate the anisotropy, the true drift velocity and the apparent velocity of this diffraction pattern. The correlation analysis is relatively well established [Briggs *et al.*, 1950; Kent and Koster, 1966; Rino and Livingston, 1982] and has been used in ionospheric studies at the equatorial region [Basu *et al.*, 1986], in midlatitudes [Moorcroft and Arima,

1972] and at high latitudes [Livingston *et al.*, 1982]. Two of the available algorithms for the correlation analysis of spaced-receiver data are reviewed in the companion paper [Costa *et al.*, this issue] (hereafter referred to as CFB) and their results compared and interpreted in terms of the anisotropy of the in situ irregularities.

The second is the dispersion analysis technique, based on the assumption that a given Fourier component in the records arises from the passage over the receivers of a sinusoidal waveform with its own velocity, which is then estimated at each frequency [Briggs, 1968b; Briggs and Golley, 1968]. This is done by equating the calculated phase of a cross spectrum to the phase difference between the two corresponding Fourier components. Thus this technique uses only the phases of the cross spectra to calculate an apparent velocity and provides no information on the anisotropy of the ground diffraction pattern.

These authors (see also Wernik *et al.* [1983]) stressed the differences between the correlation and the dispersion analysis. They also noted that the assumption that a given Fourier component in the records is produced by a single wave passing over the receivers is crucial. They further pointed out that in other situations (for instance, a system of waves with

¹Now at Centro de Estudos em Telecomunicações, Pontifícia Universidade Católica do Rio de Janeiro, Brazil.

Copyright 1988 by the American Geophysical Union.

Paper number 7S0930.
0048-6604/88/007S-0930\$08.00

the same wavelength but different directions) the analysis would also give a result, whose interpretation, however, would be extremely difficult. They thus suggested that the results of the dispersion analysis should be interpreted with caution.

In a diametrically opposite approach, the similarities between the two techniques will be emphasized here. By a trivial one-dimensional Fourier transform of the fundamental equation for the "space-time" correlation function of the received signals, and imposing no additional restrictions, an equation will be obtained for the phase of the cross spectra. Based on this result, the apparent velocity of the dispersion analysis will be expressed in terms of the parameters of the original correlation function. This will show that an apparent velocity can be calculated by the correlation analysis which is equivalent to that of the dispersion analysis. This interpretation is entirely free from the assumption of sinusoidal waves passing over the receiving system.

Further, autocorrelation and cross-correlation functions are Fourier transforms of auto- and cross spectra, respectively, and vice versa. The information available to the spectral analysis (in the frequency domain) is thus totally equivalent to that available to the correlation analysis (in the time domain). It should then be possible to generalize the dispersion analysis to also estimate the anisotropy and the true drift velocity from the calculated auto- and cross spectra of the received signals. This generalized technique will be called cross-spectral analysis of spaced-receiver data.

An algorithm to estimate the same parameters of the fundamental "space-time" correlation function directly from the auto, coherency and phase spectra of the received signals will be developed in the following sections. In the process, a realistic functional form for the power spectral density of the ionospheric irregularities will be assumed. It will then be possible to characterize the anisotropy and the drift velocity of the ground diffraction pattern exactly as in the correlation analysis (see, for instance, Kent and Koster [1966]). Axial ratios and orientations of the major axes of the anisotropy ellipses of the ground diffraction pattern obtained by the correlation and spectral techniques will be compared using data obtained during different HiLat orbits over Tromsø, Norway (69.7°N, 18.9°E). It will be seen that the agreement between the respective results is generally good. Localized differences will also be discussed.

In principle, it would be possible to investigate frequency variations of the anisotropy and the drift

velocity of the ground diffraction pattern by the correlation analysis. Initially, it would be necessary to design several very narrow and sharp digital bandpass filters. The received signals would then be pre-filtered before the correlation analysis. Of course, it is much easier to perform this analysis in the frequency domain, by applying the present algorithm on very narrow and adjacent frequency bands. Using such a technique, Briggs and Golley [1968] observed frequency variations of the amplitude of the apparent velocity, while its direction remained essentially constant. These results have been mainly attributed to the presence of random or regular velocity variations along the ray path (see again Wernik *et al.* [1983]). It will be shown here, also using Tromsø/HiLat spaced-receiver data, that the anisotropy of the diffraction pattern seems to display an analogous frequency behavior to that of the apparent velocity. That is, frequency variations are mainly observed in the axial ratio, and not in the orientation of the major axis of the anisotropy ellipse.

2. "SPACE-FREQUENCY" SPECTRUM OF THE PHASE FLUCTUATIONS IN THE RECEIVED SIGNALS

In this and in the following sections, the same geometry, assumptions and nomenclature established in the companion paper (CFB) will be employed.

As a partial result of the model described therein, and slightly rearranging terms, the expression previously found for the "space-time" correlation function of the phase fluctuations in the received signals can be cast in the following form

$$\begin{aligned}
 & R_p(\Delta x, \Delta t) \\
 & = \int_{-\infty}^{+\infty} R_N\{u^2 + c[E + (\Delta t + F)^2]\}^{1/2} du \\
 & \quad \left| \int_{-\infty}^{+\infty} R_N\{u\} du \right. \\
 & = R_p\{[a\Delta x^2 + 2h\Delta x\Delta y + b\Delta y^2 + 2f\Delta x\Delta t \right. \\
 & \quad \left. + 2g\Delta y\Delta t + c\Delta t^2]^{1/2}\} \quad (1)
 \end{aligned}$$

which is the basic equation for the correlation analysis of spaced-receiver data. In the above equation

$$\begin{aligned}
 E & = (a/c)\Delta x^2 + 2(h/c)\Delta x\Delta y + (b/c)\Delta y^2 \\
 & - [(f/c)\Delta x + (g/c)\Delta y]^2 \quad (2)
 \end{aligned}$$

$$F = (f/c)\Delta x + (g/c)\Delta y \quad (3)$$

and, as indicated in that paper, (1) $R_N(p)$ is a decreasing function of its (positive) argument, normalized in

such a way that $R_N(0) = 1$; (2) the parameters a, b, c, f, g and h can be expressed in terms of the geometry, the geomagnetic field, the velocity of the satellite transmitting the signals, the drift velocity of irregularities in the electron density in the ionosphere and the parameters characterizing the "space-time" correlation function of these irregularities. Since the main objective in this contribution is to introduce a technique which directly estimates the values for these coefficients from data obtained by the spaced-receiver experiment, it is not important to present these complicated relationships here.

Calculating the Fourier transform of (1) with respect to Δt alone, the following general equation is found for the "space-frequency" power spectral density of the phase fluctuations of the signals received on the ground

$$P_\phi(\Delta x, \omega) = \frac{\iint_{-\infty}^{+\infty} R_N\{(u^2 + c[E + (\Delta t + F)^2])^{1/2}\} e^{-i\omega\Delta t} du d\Delta t}{\int_{-\infty}^{+\infty} R_N(|u|) du} = \frac{\frac{\pi}{\sqrt{c}} e^{i\omega F} \int_0^\infty s R_N[(s^2 + cE)^{1/2}] J_0(\omega s / \sqrt{c}) ds}{\int_0^\infty R_N(s) ds} \quad (4)$$

where $J_0(s)$ is the Bessel function of first kind and order zero. This general model can be applied to the particular spaced-receiver layout by appropriately selecting the values for Δx to predict the cross spectrum between each particular pair of received signals. Obviously, the special case $\Delta x = 0$ would yield the autospectrum of any of the signals.

It is seen from (4) that the absolute value of $P_\phi(\Delta x, \omega)$ depends only on (cE) and $[\omega/(c)^{1/2}]$. However, it is impossible here to express $|P_\phi(\Delta x, \omega)|$ as a general function of a one-dimensional argument formed by some combination of these parameters, as resulted from (1). Thus to continue the present derivation, it is necessary to assume a special shape for $R_N(p)$ or, equivalently, for the "wave number-frequency" power spectral density $Q_N(K, \omega)$ of the electron density irregularities in the ionosphere.

To be useful, such a shape would have to be selected as a compromise between two features. Simplicity is important, to ensure that the final results are manageable enough to permit the development of a

scheme for the estimation of the desired parameters. On the other hand, the importance of achieving the best possible agreement with observations in the region of interest should be even more obvious. Extensive in situ [Dyson et al., 1974; Kelley et al., 1980, 1982] and ground-based [Fremouw et al., 1978; Aarons, 1982; Basu et al., 1985] measurements, as well as computer simulation studies [Keskinen and Ossakow, 1983], of high-latitude F region ionospheric irregularities have all indicated that their power spectral density can be well represented by a simple power law in the range of scale sizes usually observed in the spaced-receiver experiment (a few tens of kilometers to several hundred meters). That is, it will be assumed that, in a reference frame aligned with the geomagnetic field,

$$Q_N(K, \omega) = Q_N(q) = Q_0(q_0^2 + q^2)^{-\mu+1} \quad (5)$$

where Q_0 , q_0 , and μ are constants and $q = (K^2 + A^2 K_i^2 + B^2 K_i^2 + C^2 \omega^2)^{1/2}$, referring again the reader to the nomenclature of CFB. Calculating the corresponding "space-time" correlation function via the Fourier transform defined in the same reference, substituting the result into (4) and rearranging and redefining terms, the final result for the "space-frequency" power spectral density of the phase fluctuations can be written in the form

$$P_\phi(\Delta x, \omega) = P_\phi(\omega) C_\phi(\Delta x, \omega) \exp[i\Phi_\phi(\Delta x, \omega)] \quad (6)$$

$$P_\phi(\omega) = P_0(\omega_0^2 + \omega^2)^{-\mu} \quad (7)$$

$$C_\phi(\Delta x, \omega) = \left| \frac{P_\phi(\Delta x, \omega)}{P_\phi(\omega)} \right| = \frac{1}{2^{\mu-1} \Gamma(\mu)} [\sqrt{E(\omega_0^2 + \omega^2)}]^\mu K_\mu[\sqrt{E(\omega_0^2 + \omega^2)}] \quad (8)$$

$$\Phi_\phi(\Delta x, \omega) = \omega F = \omega[(f/c) \Delta x + (g/c) \Delta y] \quad (9)$$

$P_\phi(\omega)$ is the autospectrum and $C_\phi(\Delta x, \omega)$ and $\Phi_\phi(\Delta x, \omega)$ are, respectively, the "space-frequency" coherency and phase spectra of the phase fluctuations in the received signals. In the above equations, ω_0 is a constant (related to q_0) representing the roll-off frequency of the power spectrum, $\Gamma(\mu)$ is the gamma function and $K_\mu(w)$ is the modified Bessel function of the second kind and order μ . It should be observed that $F_\mu(w) = w^\mu K_\mu(w)$ is a decreasing function of its argument and that $F_\mu(w) \rightarrow 2^{\mu-1} \Gamma(\mu)$ as $w \rightarrow 0$. Equations (6)–(9) are thus "internally consistent" when $\Delta x = 0$.

It is obtained from (4) that, considering the assumptions under which it was derived, equation (9)

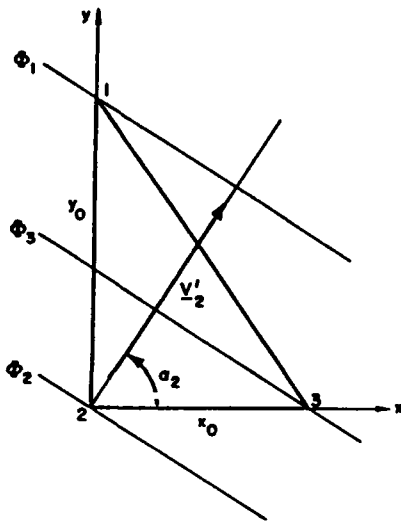


Fig. 1. Propagation of a plane wave front, represented by lines of constant phase Φ_i , and whose velocity V'_2 makes an angle α_2 with the x axis, over a system of three receivers. The receiver layout defines a right triangle with sides x_0 and y_0 .

for the phase spectrum $\Phi_4(\Delta x, \omega)$ does not depend on the shape of the function $R_N(p)$. This equation can be used to calculate the velocity V'_2 defined in the dispersion analysis in terms of the basic parameters of the correlation analysis (see (1)). Assuming the receiver layout shown in Figure 1, following *Briggs and Golley* [1968] and using (9), one gets

$$\begin{aligned} \Phi_{21} = \Phi_1 - \Phi_2 &= \frac{2\pi}{\lambda} y_0 \sin \alpha_2 = \frac{\omega}{V'_2} y_0 \sin \alpha_2 \\ &= \Phi(\Delta x_{21}, \omega) = \omega(g/c)y_0 \end{aligned} \quad (10)$$

$$\begin{aligned} \Phi_{23} = \Phi_3 - \Phi_2 &= \frac{2\pi}{\lambda} x_0 \cos \alpha_2 = \frac{\omega}{V'_2} x_0 \cos \alpha_2 \\ &= \Phi(\Delta x_{23}, \omega) = \omega(f/c)x_0 \end{aligned} \quad (11)$$

where λ is the scale size associated with the Fourier component of the diffraction pattern whose angular frequency is ω (so that $\lambda\omega = 2\pi V'_2$). From the above equation, it can be seen that the velocity defined by

$$\begin{aligned} V'_2 &= \omega[(\Phi_{21}/y_0)^2 + (\Phi_{23}/x_0)^2]^{-1/2} \\ \tan \alpha_2 &= (\Phi_{21}x_0)/(\Phi_{23}y_0) \end{aligned} \quad (12)$$

in *Briggs and Golley's* dispersion analysis can be expressed, in terms of the parameters of the correlation analysis, as

$$V'_2 = c(f^2 + g^2)^{-1/2} \quad \tan \alpha_2 = g/f \quad (13)$$

That is, the velocity V'_2 of the dispersion analysis

can be interpreted as an apparent velocity of the correlation analysis (labeling as "apparent" any velocity obtained from the coefficients a, b, c, f, g , and h which differs from the true drift velocity). It should be observed that V'_2 is not equal to other apparent velocities defined in the literature. For example, it can be shown that the apparent velocity V'_1 , defined by *Briggs et al.* [1950], *Briggs* [1968a] and *Kent and Koster* [1966], which is aligned with the true velocity V , and for which the relationship $V'_1 V = V^2 + V_c^2$ (V_c is the characteristic velocity) is valid, is characterized by

$$\begin{aligned} V'_1 &= c[(fb - gh)^2 + (ag - fh)^2]^{1/2}/e \\ \tan \alpha_1 &= (fh - ag)/(gh - fb) \end{aligned} \quad (14)$$

where $e = fb - gh + g(ag - fh)$. On the other hand, *Rino and Livingston* [1982] used the apparent velocity V'_3 , whose components are obtained by dividing the distances between receivers by the time delays for maximum cross correlation between the corresponding signals. Using again the receiver layout in Figure 1, it can be shown that

$$V'_3 = (f^2 + g^2)^{1/2}/(fg) \quad \tan \alpha_3 = g/f \quad (15)$$

It should also be noted that the frequency variation of the velocity V'_2 observed by *Briggs and Golley* [1968] cannot be explained in the context of the present theory, as evident from (13). Neither can we explain the slight skewness of the cross-correlation functions of the received signals around their maxima, also observed by the same authors (see (1)). *McGee* [1966] has explained, based on qualitative arguments, that the two observations should be related. *Briggs and Golley* [1968], although admitting that a dispersive motion of the ionosphere could be involved, suggested, again based on qualitative arguments, that a regular variation of the drift velocity along the ray path would be a more likely source for the observations. Recently, *Wernik et al.* [1983] introduced the effects of both regular velocity variations along the ray path and random velocity fluctuations in the ionosphere into a model of the spaced-receiver experiment, considering a geometry typically found at the equator (infinitely elongated irregularities along the geomagnetic field lines assumed to be perpendicular to the lines joining the receivers). Their results clearly show that any of the modeled features would produce frequency-varying velocities and skewed cross-correlation functions, thus confirming the observations and those previous explanations.

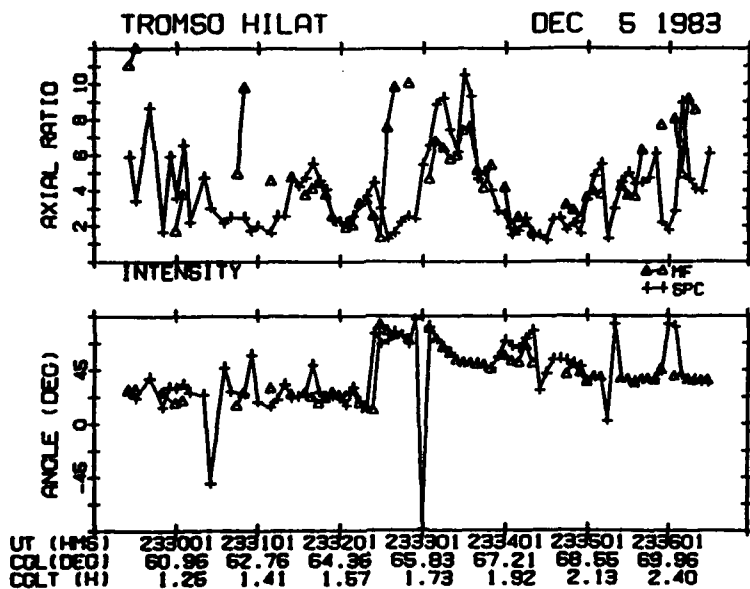


Fig. 2. Axial ratios and orientation angles of the major axes of the anisotropy ellipses of the diffraction pattern, obtained by the spectral (curves SPC, pluses) and the correlation (curves MF, triangles) analyses. Tromsø/Hilat spaced-receiver intensity data recorded on Dec 5, 1983, have been used. The spectral analysis has been restricted to data in the frequency band $1.5 \text{ Hz} < v < 7 \text{ Hz}$. The correlation analysis has employed the modified Fedor algorithm [Fedor, 1967; CFB, this issue].

3. ALGORITHM FOR THE SPECTRAL ANALYSIS OF SPACED-RECEIVER DATA

Let n_r receivers be located at $\mathbf{x}_i = (x_i, y_i)$, $i = 1, 2, \dots, n_r$, on the ground reference plane defined in Figure 2 of the companion paper (CFB). Also, define $\Delta\mathbf{x}_{ij} = (\Delta x_{ij}, \Delta y_{ij}) = \mathbf{x}_j - \mathbf{x}_i$ for all possible combinations of i and j . Further assume that the values of $P_{\phi}(\omega_i)$, $C_{\phi}(\Delta\mathbf{x}_{ij}, \omega_i)$ and $\Phi_{\phi}(\Delta\mathbf{x}_{ij}, \omega_i)$ have been calculated from the received signals at the selected angular frequencies ω_i , $i = 1, 2, \dots, L$ for all possible combinations of i and j . It is not required for the success of the present algorithm that these frequencies be equally spaced.

The values for the parameters f/c and g/c can be calculated using only (9). That is, all available equations of the form

$$\Delta x_{ij}(f/c) + \Delta y_{ij}(g/c) = \Phi_{\phi}(\Delta\mathbf{x}_{ij}, \omega_i)/\omega_i \quad (16)$$

$$i, j = 1, \dots, n_r \quad i = 1, \dots, L$$

can be collected into a $n_r \times 2$ system of linear equations $\mathbf{D}_2 \cdot \mathbf{U}_2 = \mathbf{T}_2$, where $\mathbf{U}_2^T = (f, g)/c$ and the superscript T indicates the transpose of a matrix.

The elements of the matrices $\mathbf{D}_2(n_r \times 2)$ and $\mathbf{T}_2(n_r \times 1)$ are readily inferred from the above equation. A solution for this system of equations can then be found as presented below.

Before calculating the remaining parameters a/c , b/c and h/c , it is necessary to estimate the values of μ and ω_0 . This can be done by minimizing the sum of the squared errors between the measured values $P_{\phi}(\omega_i)$ and those calculated by (7), for all values of i and l . It is not uncommon for the roll-off frequency ω_0 to be much smaller than all the selected frequencies ω_i . When this happens, the dependence of $P_{\phi}(\omega)$ and $C_{\phi}(\Delta\mathbf{x}, \omega)$ on ω_0 can be totally neglected in (7) and (8), reasonably simplifying the estimation of both the spectral index μ and those remaining parameters.

Finally, using the known values for f/c , g/c , μ and ω_0 (when necessary), as well as the fact that $r = F_{\mu}(s) = s^{\mu} K_{\mu}(s)$ is a decreasing function of the argument s (and thus its inverse $s = F_{\mu}^{-1}(r)$ can be found), the values for the parameters a/c , b/c and h/c can be calculated. Inverting (8) to express the value of the argument of the function $F_{\mu}(s)$ in terms of $C_{\phi}(\Delta\mathbf{x}, \omega)$

and substituting expression (2) for the parameter E into the result of this operation, equations of the form

$$\Delta x_{ij}^2(a/c) + 2 \Delta x_{ij} \Delta y_{ij}(h/c) + \Delta y_{ij}^2(b/c) = t_{ij} \quad (17)$$

$$i, j = 1, \dots, n, \quad l = 1, \dots, L$$

where

$$t_{ij} = [\Delta x_{ij}(f/c) + \Delta y_{ij}(g/c)]^2$$

$$+ \{F_p^{-1}[2^{n-1}\Gamma(\mu)C_p(\Delta x_{ij}, \omega_l)]\}^2/(\omega_0^2 + \omega_l^2) \quad (18)$$

can be generated. Alternatively, the right-hand side of (16) can be substituted for the first term (within brackets) in (18). Under the conditions already discussed, ω_0 can be neglected in the same equation.

All the available equations of the form (17) can similarly be collected into a $n_s \times 3$ system of linear equations $D_3 \cdot U_3 = T_3$, where $U_3^T = (a, h, b)/c$ and the elements in the matrix $D_3(n_s \times 3)$ and $T_3(n_s \times 1)$ are easily identified from this result.

The systems of linear equations obtained in this section, both of the form $D \cdot U = T$, generally are overdetermined. In fact, for statistical reasons, it is highly desirable that they be so. Thus they should be solved by the least squares method. Assuming that the observations T are uncorrelated, the following general form is found for the solutions of those systems of equations

$$U = (D^T \cdot D)^{-1} \cdot D^T \cdot T \quad (19)$$

A discussion associated with this last assumption can be found in the companion paper (CFB).

Once the solutions U_2 and U_3 are known, the drift velocity and the anisotropy of the ground diffraction pattern can be easily calculated [Kent and Koster, 1966].

The above algorithm will be applied to a relatively broad frequency band (in the roll-off part of the spectra, so that ω_0 can be neglected). In this case, at most one value of axial ratio and drift velocity, together with their respective orientations, will be obtained from each sample of data.

The same frequency band will also be subdivided and the algorithm then repeatedly applied to each of the individual narrow bands. As a result, curves displaying the frequency variations of the axial ratio, drift velocity and their respective orientations will be obtained from each sample of data.

It is important to note here some advantages of the maximum entropy method (MEM) over the FFT-periodogram technique for the estimation of

spectra [Fougere, 1985] which are very important for the success of the latter application. First, MEM provides smooth spectra, which are free from the artificial fluctuations always present in FFT-periodogram spectra. Further, MEM can calculate power spectral densities over a continuum of frequencies in the band of interest, instead of only at the harmonic frequencies of the inverse of the duration of the available time series. This ensures that a reasonably high and uniform number of auto, coherency and phase spectral values are calculated within each of the narrow frequency bands. See also the discussion of multichannel MEM and the associated references in CFB.

Strictly speaking, the latter use of the algorithm is not consistent with the model from which it has been derived. As one recalls from the previous section and CFB, it resulted from the model's assumptions and its derivation that the coefficients a, b, c, f, g and h should remain constant within the short time interval into which the total record is partitioned for analysis. Ideally, it would then be very important to generalize the previous model to allow for possible frequency variations of these coefficients in a consistent manner. This would probably include the difficult task of evaluating the effects of (1) allowing A, B and C in (5) to become dependent on the scale size of the irregularities in the electron density of the ionosphere, (2) introducing regular velocity gradients along the ray path and random velocity fluctuations in the ionosphere, or (3) a combination of both.

On the other hand, a decision on the usefulness of the model for the "space-frequency" power spectral density represented by (6)-(9) would ultimately be based on its ability to reproduce the observations. It is seen that these expressions display several desirable features: (1) a power law for the auto spectrum; (2) a coherency spectrum which decreases with both the spacings between the receivers and the frequency; (3) a phase spectrum which is a linear function of these variables. The model should thus provide a good fit to the observations, particularly when repeatedly applied to consecutively adjacent narrow frequency bands, with the coefficients a, b, c, f, g, h and μ being held constant only within each of them.

It seems reasonable to expect that, in the limit of small frequency variations of these coefficients, it would still be possible to cast the "space-time" correlation function associated with this relaxed version for the "space-frequency" power spectral density in a very close format to that shown in (1). Consequently, it would also be possible to characterize the ani-

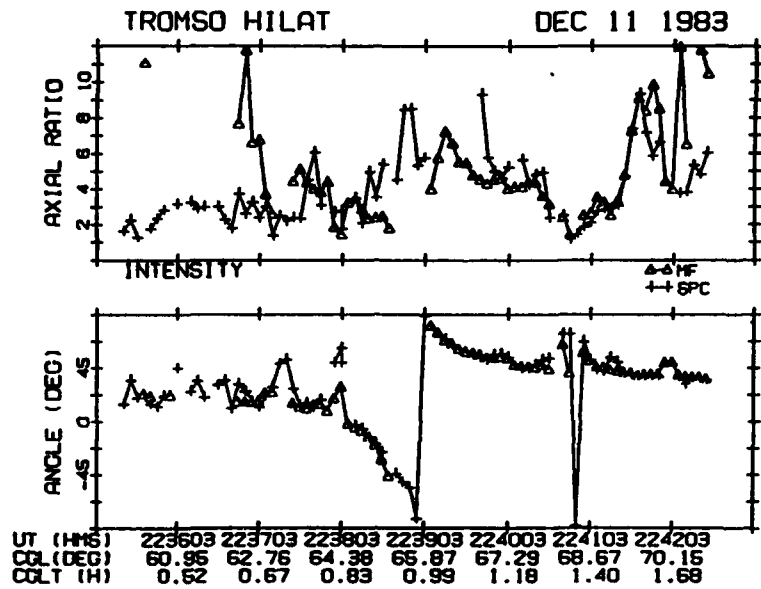


Fig. 3. Axial ratios and orientation angles of the major axes of the anisotropy ellipses of the diffraction pattern, obtained by the spectral (curves SPC, pluses) and the correlation (curves MF, triangles) analyses. Tromsø/Hilat spaced-receiver intensity data recorded on December 11, 1983, have been used. The spectral analysis has been restricted to data in the frequency band $1.5 \text{ Hz} < v < 7 \text{ Hz}$. The correlation analysis has employed the modified Fedor algorithm [Fedor, 1967; CFB, this issue].

sotropy and the drift of the diffraction pattern as before. In this regime, it is then expected that the second way of applying the present algorithm to the data would provide reasonable approximations to actual frequency variations of the axial ratio and drift velocity of the ground diffraction pattern. However, fast frequency variations of these parameters, while still indicating a correct qualitative trend, may not display numerically accurate results.

4. RESULTS OF THE SPECTRAL ANALYSIS

Signals transmitted at 413 MHz by the polar-orbiting Hilat satellite and recorded by three receivers at Tromsø, Norway (69.7°N , 18.9°E), will be employed in the comparison between results of the spaced-receiver analysis by the correlation and the spectral techniques. The receiver layout on the ground and the main features of the data (recorded on December 5, 11, and 12, 1983) have already been presented by CFB, which has also discussed the results of the correlation analysis (axial ratio and orientation of the major axis of the anisotropy ellipse of the diffraction pattern).

The spectral analysis was performed on the same data blocks that were used in the correlation analy-

sis. That is, in the spectral analysis, the same blocks with 10 s of data (sampled at 125 Hz, thus corresponding to 1250 consecutive observations of the signal per channel) have been used. Again, consecutive data blocks have been overlapped by 5 s.

Initially, the spectral analysis has been globally applied to the frequency band limited by 1.5 Hz and 7 Hz. This frequency band is contained by the roll-off part of the spectra, which thus simplifies the estimation of the desired parameters, and also avoids higher frequencies, where the power spectral densities of the received signals are dominated by noise. This frequency band has been divided into 100 constant and adjacent intervals. Next, the auto- and cross spectra have been calculated at each of the frequencies so defined by the maximum entropy method (MEM). The algorithm in the previous section has then been applied to these results as indicated.

The axial ratios and orientations of the major axes of the anisotropy ellipses resulting from the spectral analysis of the intensity spaced-receiver data of December 5 and 11, 1983, are respectively shown in Figures 2 and 3 (curves SPC, labeled with pluses). The angles in the lower panels are measured with respect to the local corrected geomagnetic northward direction, being positive in the NE quadrant. Oc-

casionally observed large jumps in the angles are artificially caused by the existing 180° ambiguity in the orientation of the major axis of the ellipse. The results from the spectral technique will be compared with those yielded by the correlation analysis. With this purpose, calculations using the modified Fedor algorithm, already presented in CFB, are also reproduced in Figures 2 and 3 (curves MF, labeled with triangles).

A good general agreement is observed between the results provided by the two techniques. This agreement is particularly good between the orientations of the major axes and between the axial ratios obtained in the central parts of the two passes, where the elevations of the ray paths are relatively higher. Data with superior quality are obtained in this region, due to the higher average received signal levels and the smaller chance of occurrence of multipath. These examples can thus be accepted as an indication that the spectral analysis and the well-established correlation analysis are generally equivalent.

There is, however, one difference between the results by the two techniques which seems to be significant. That observed around the geometrical enhancement region (2333:15 UT) on December 5, 1983, where the axial ratios obtained by the spectral analysis are, on the average, 35% larger than those calculated by the correlation analysis. This observation supports the main conclusion of the discussion in CFB on the relationship between the results of the spaced-receiver analysis and the antenna spacing. Indeed, the spectral analysis has been applied to a narrower frequency band than that of the correlation analysis (which uses the total available frequency band). This narrower frequency band also is better matched with the "ideal" frequency band for the spaced-receiver measurements observed in Figure 13b of that paper. According to the associated discussion, this condition tends to provide more reliable (and greater, since the *in situ* irregularities are highly field aligned) values of the axial ratio.

It should also be remembered that the present version of the spectral analysis of spaced-receiver data assumes a special functional form to characterize the power spectral density $Q_N(K, \omega)$ of the *in situ* irregularities. On the other hand, the correlation analysis is completely general in this respect. Although the selected form for $Q_N(K, \omega)$ is in good agreement with experimental data, this assumption may in principle also be partially responsible for differences in the results between the two techniques.

The spectral analysis has also been repeatedly applied to very narrow and adjacent frequency bands. One example of frequency variations of the axial ratio and the orientation of the major axis of the anisotropy ellipse resulting from this analysis will be presented with the help of spaced-receiver phase data recorded during the selected Hilat orbit over Tromsø on December 12, 1983. Similarly, consecutive blocks with 10 s of data (overlapped by 5 s), sampled at 125 Hz (thus corresponding to 1250 observations of the phase signal per channel) have been used to calculate the MEM auto- and cross spectra at 175 frequencies (equispaced in their logarithms) in the frequency band limited by 0.72 Hz and 3 Hz. This frequency band has then been divided into seven narrower ones, all containing a common number (25) of those frequencies. The spectral analysis algorithm has then been repeatedly applied to each of the narrow bands to estimate the axial ratio and the orientation corresponding to its central frequency. As a result, two curves showing respectively the frequency dependence (between approximately 0.8 Hz and 2.7 Hz) of these parameters have been obtained from each block of data.

The results corresponding to 7 min of data obtained during the central part of that orbit over Tromsø (between approximately 0018:00 UT and 0025:00 UT) are displayed in Figures 4 and 5. In both, time increases downward, in steps of 5 s between adjacent curves. Each figure thus shows a total of 85 curves. Frequency increases toward the right, in the manner explained above. The curves displaying the frequency variation of the orientation of the major axis have been unwrapped by appropriately adding integer multiples of 360° to the minimum determination of the angles, to avoid both negative values and jumps caused by the 180° ambiguity in this parameter.

It is observed that the time history of the axial ratio obtained by the present technique at the lower frequency (shaded curve at $f = 0.8$ Hz seen in Figure 4) follows very closely that resulting from the correlation analysis, which can be seen in Figure 10 of CFB. In particular, the geometric enhancement of the axial ratio caused by the presence of sheetlike irregularities is observed around 0018:45 UT. A steady increase in the axial ratio due to the transition mentioned in CFB from sheetlike to rodlike structures also is observed after approximately 0022:00 UT. Figure 4 clearly displays smooth frequency variations of the axial ratio for most of the 10-s batches

TRØMSØ HILAT PHASE AXL RATIO DEC 12 1983

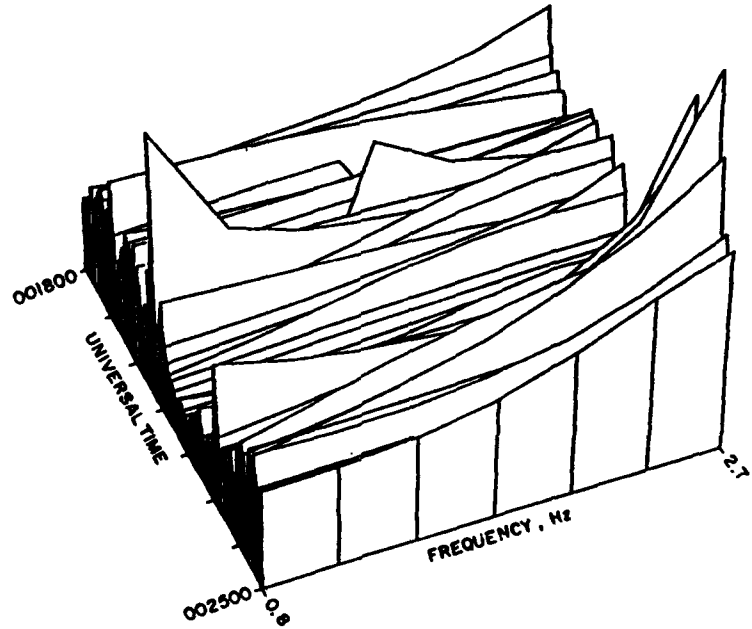


Fig. 4. Frequency dependence of the axial ratio of the diffraction pattern anisotropy ellipse, obtained by repeatedly applying the spectral spaced-receiver algorithm to narrow and adjacent frequency bands. A total of 85 axial ratio frequency curves, each obtained from a block with 10 s of Tromsø/Hilat spaced-receiver phase data recorded on Dec. 12, 1983, are shown. Consecutive data blocks have been overlapped by 5 s. Points along the frequency axis are equally spaced in the logarithm of the frequency; 0.8 and 2.7 are the true end frequencies in hertz.

of data. On the other hand, in Figure 5 the orientation of the major axis of the anisotropy ellipse remains relatively independent of the frequency. These results are analogous to the observations by *Briggs and Golley* [1968], who have also shown smooth frequency variations in the amplitude of the apparent velocity V_2' , while no appreciable change in its direction has been simultaneously detected.

5. CONCLUSION

Through a one-dimensional Fourier transform, the "space-frequency" phase spectra of transionospheric signals received on the ground have been obtained from the basic expression for their "space-time" correlation function. This simple exercise has made it possible to interpret the apparent velocity calculated by the dispersion analysis in terms of the fundamental parameters of the cross-correlation analysis, characterized in (1). This result has been established without any additional restrictions or assumptions.

In particular, it is totally independent of the assumption of sinusoidal waves passing over the receivers [Briggs, 1968b], whose validity is difficult to assess in practice.

By assuming a realistic (power law) functional form for the "wave number-frequency" power spectral density of the F region irregularities, the "space-frequency" auto- and coherency spectra have also been expressed in terms of the same coefficients of (1). It has then been possible to design an algorithm to estimate the anisotropy and the true drift velocity of the ground diffraction pattern, both characterized exactly as in the cross-correlation analysis [Kent and Koster, 1966], directly from the calculated spectra. This result is a generalization of the dispersion analysis.

The algorithm has been applied to Tromsø/Hilat spaced-receiver data in two slightly different modes. In the first, it has been globally applied on a relatively broad frequency band in the roll-off part of the spectra. A good agreement has generally been found

TRØMSØ HILAT PHASE AXL ØRIEN DEC 12 1983

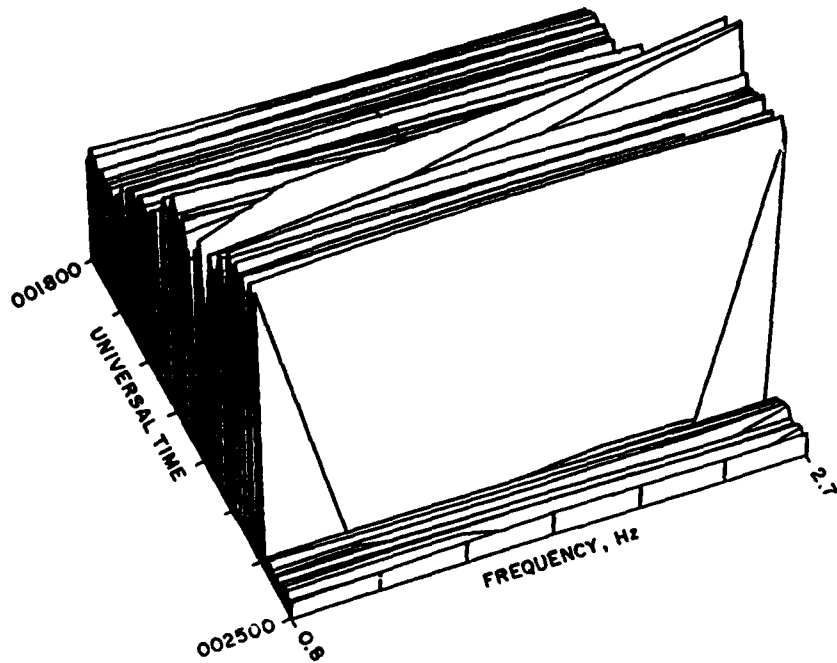


Fig. 5. Frequency dependence of the orientation angle of the major axis of the diffraction pattern anisotropy ellipse, obtained by repeatedly applying the spectral spaced-receiver algorithm to narrow and adjacent frequency bands. A total of 85 orientation angles versus frequency curves, each obtained from a block with 10 s of Tromsø/Hilat spaced-receiver phase data recorded on Dec. 12, 1983, are shown. Consecutive data blocks have been overlapped by 5 s. Points along the frequency axis are equally spaced in the logarithm of the frequency; 0.8 and 2.7 are the true end frequencies in hertz.

between results from this technique and those obtained by the correlation analysis of the same data. A significant difference between the axial ratios calculated by the two techniques has also been observed in the region of local L shell alignment during the orbit on December 5, 1983. The assumption of a special functional form for $Q_N(K, \omega)$ in the development of the cross-spectral analysis, while no equivalent restriction is imposed on the cross-correlation analysis, could be partially responsible for this observation. A more likely explanation for this difference, however, could be the fact that the correlation analysis is applied on the total frequency band of the received signals, while the spectral analysis is applied on a frequency band which is not only limited but also better matched to the "ideal" frequency band for the spaced-receiver measurements defined in CFB. As explained in this reference, the latter situation tends to favor higher axial ratios such as those obtained by spectral analysis in this particular example.

In the second mode, the algorithm has been repeatedly applied on very narrow and adjacent frequency bands, to detect possible frequency variations of the anisotropy of the ground diffraction pattern. Again, Tromsø/Hilat data have been used in the analysis. Smooth variations of the axial ratio with the frequency have been observed, while the orientation of the major axis of the anisotropy ellipse has not experienced any appreciable change with this variable. This result is analogous to the observations by Briggs and Golley [1968], which display frequency variations in the amplitude of the apparent velocity, but not in its direction. Without entirely ruling out a dispersive motion of the ionosphere, they credited these variations to regular (or random) velocity changes along the ray path. Wernik *et al.* [1983], by mathematically modeling the effects of these changes, have confirmed this explanation.

It should be remembered that the model for the "space-time" correlation function of the received sig-

nals represented by (1) assumes constant coefficients for each batch of data selected for analysis. Consequently, a good agreement between the data and the model would be automatically translated into negligible frequency variation of these parameters. It is concluded from Figure 4 that the observed frequency variations of the axial ratio do not confirm the basic hypotheses of the model (for instance, the assumption of constant coefficients). Thus although this model has been very useful in the investigation of primary features of the ground diffraction pattern (such as its anisotropy and drift velocity), it would have to be refined to consider secondary but also important features (such as the frequency variations of its derived parameters) in a more consistent fashion.

Acknowledgments. This work has been performed while E. C. was on a sabbatical leave of absence from CETUC-PUC/RJ, Rio de Janeiro, Brazil. He would like to thank his colleagues and friends from the Physics Research Division, Emmanuel College, and the Ionospheric Effects Branch, Air Force Geophysics Laboratory, for the stimulating scientific environment and the continued demonstrations of hospitality during this period. The discussions within the Hilat scientific community have also been greatly appreciated. The authors thank Sunanda and Santimay Basu for their genuine interest and many valuable suggestions, which led to improvements in the present work. They also wish to acknowledge the essential role of Elizabeth Galligan in the tedious and time-consuming preprocessing of the data. The work at Emmanuel College was supported by AFGL contract F19628-86-K-0038 and by an AFGL laboratory director's fund ILIR 5B01.

REFERENCES

Aarons, J., Global morphology of ionospheric scintillations, *Proc. IEEE*, **70**, 360-378, 1982.

Basu, S., S. Su, Basu, J. LaBelle, E. Kudeki, B. G. Fejer, M. C. Kelley, H. E. Whitney, and A. Bushby, Gigahertz scintillations and spaced receiver drift measurements during Project Condor equatorial F region rocket campaign in Peru, *J. Geophys. Res.*, **91**, 5526-5538, 1986.

Basu, S., S. Basu, E. MacKenzie, and H. E. Whitney, Morphology of phase and intensity scintillations in the auroral oval and polar cap, *Radio Sci.*, **20**, 347-356, 1985.

Briggs, B. H., On the analysis of moving patterns in geophysics. I. Correlation analysis, *J. Atmos. Terr. Phys.*, **30**, 1777-1788, 1968a.

Briggs, B. H., On the analysis of moving patterns in geophysics. II. Dispersion analysis, *J. Atmos. Terr. Phys.*, **30**, 1789-1794, 1968b.

Briggs, B. H., and M. G. Golley, A test for dispersion in F region drifts observed by the radio star scintillation method, *J. Atmos. Terr. Phys.*, **30**, 963-973, 1968.

Briggs, B. H., G. J. Phillips, and D. H. Shinn, The analysis of observations on spaced receivers of the fading of radio signals, *Proc. Phys. Soc. London, Sec. B*, **63**, 106-121, 1950.

Costa, E., P. F. Fougere, and S. Basu, Cross-correlation analysis and interpretation of spaced-receiver measurements, *Radio Sci.*, this issue.

Dyson, P. L., J. P. McClure, and W. B. Hanson, In situ measurements of the spectral characteristics of F region ionospheric irregularities, *J. Geophys. Res.*, **79**, 1497, 1974.

Fedor, L. S., A statistical approach to the determination of three-dimensional ionospheric drifts, *J. Geophys. Res.*, **72**, 5401-5415, 1967.

Fougere, P. F., On the accuracy of spectrum analysis of red noise processes using maximum entropy and periodogram methods: Simulation studies and application to geophysical data, *J. Geophys. Res.*, **90**, 4355-4366, 1985.

Fremouw, E. J., R. L. Leadabrand, R. C. Livingston, M. D. Cousins, C. L. Rino, B. C. Fair, and R. A. Long, Early results from the DNA Wideband satellite experiment: Complex-signal scintillation, *Radio Sci.*, **13**, 167-187, 1978.

Kelley, M. C., K. D. Baker, J. C. Ulwick, C. L. Rino, and M. J. Baron, Simultaneous rocket probe, scintillation, and incoherent scatter radar observations of irregularities in the auroral zone ionosphere, *Radio Sci.*, **15**, 491-505, 1980.

Kelley, M. C., J. F. Vickrey, C. W. Carlson, and R. Torbert, On the origin and spatial extent of high-latitude F region irregularities, *J. Geophys. Res.*, **87**, 4469-4475, 1982.

Kent, G. S., and J. R. Koster, Some studies of nighttime F layer irregularities at the equator using very high frequency signals radiated from earth satellites, *Ann. Geophys.*, **22**, 405-417, 1966.

Keskinen, M. J., and S. L. Ossakow, Theories of high-latitude ionospheric irregularities: A review, *Radio Sci.*, **18**, 1077-1091, 1983.

Livingston, R. C., C. L. Rino, J. Owen, and R. T. Tsunoda, The anisotropy of high-latitude nighttime F region irregularities, *J. Geophys. Res.*, **87**, 10,519-10,526, 1982.

McGee, C. R., On the nature of movements in the ionosphere, *J. Atmos. Terr. Phys.*, **28**, 861-869, 1966.

Moorecroft, D. R., and K. S. Arima, The shape of the F region irregularities which produce satellite scintillations - Evidence for axial asymmetry, *J. Atmos. Terr. Phys.*, **34**, 437-450, 1972.

Rino, C. L., and R. C. Livingston, On the analysis and interpretation of spaced-receiver measurements of transitionospheric radio waves, *Radio Sci.*, **17**, 845-854, 1982.

Wernik, A. W., C. H. Liu, and K. C. Yeh, Modeling of spaced-receiver scintillation measurements, *Radio Sci.*, **18**, 743-764, 1983.

E. Costa, CETUC-PUC RJ, Rua Marquês de São Vicente 225, 22453 Rio de Janeiro RJ, Brazil.

P. F. Fougere, Ionospheric Physics Division, Air Force Geophysics Laboratory, Hanscom Air Force Base, MA 01731.

ATTACHMENT 5

Radio Science, Volume 23, Number 3, Pages 363-378, May-June 1988

Ionospheric constraints on VHF/UHF communications links during solar maximum and minimum periods

Santimay Basu

Air Force Geophysics Laboratory, Hanscom Air Force Base, Massachusetts

E. MacKenzie and Sunanda Basu

Emmanuel College, Boston, Massachusetts

(Received September 24, 1987; revised December 30, 1987; accepted January 17, 1988.)

An extensive VHF/UHF scintillation data base covering the frequency range of VHF to a few gigahertz has been utilized to determine the magnitudes of phase and intensity scintillations and their temporal/spatial structures during the sunspot maximum and minimum periods. The equatorial portion of the study has been based on geostationary satellite observations at Huancayo, a station on the magnetic equator, and at Ascension Island, which is an equatorial anomaly station having an extremely disturbed irregularity environment. The high-latitude part of the study is based on quasi-stationary satellite measurements at a polar cap location (Thule) and two auroral locations (Goose Bay and Tromsø). The Tromsø observations are augmented with the Defense Nuclear Agency HiLat satellite beacon measurements during the solar minimum period. The data indicate a strong solar cycle control of scintillation activity at all locations, resulting in a drastic reduction of the magnitudes and occurrence of scintillations during the current solar minimum period. This pattern is consistent with both a reduction of *F* region ionization density and a reduction of irregularity generation in the solar minimum period. At the magnetic equator the magnitude of scintillations at 1.5 GHz seldom exceeds 3 dB with the percentage occurrence > 2 dB varying from 70% during high sunspot conditions to 30% during low sunspot conditions. At the crest of the equatorial anomaly, on the other hand, during the solar maximum in 1979, fades of 20 dB at 1.5 GHz are observed 30% of the time. At a decreased level of solar activity in 1982, a similar occurrence level is obtained at 1.5 GHz for fade levels of only 5 dB. During the solar minimum period, 1.5-GHz scintillations are virtually absent. Phase scintillation measurements made at Ascension Island indicate that the median value of rms phase deviation is about 5 rad (pr detrend intervals of 100 s). In the auroral region, during the solar maximum period under magnetically disturbed conditions, the median values of scintillation fades and rms phase deviation (82-s detrend) at 250 MHz are observed to be 15 dB and 3 rad, respectively. At Thule, located deep within the polar cap, the median values of scintillation fades and rms phase deviation at 250 MHz attain values as large as 20 dB and 4 rad during the sunspot maximum period. Unlike Ascension Island the scintillation activity at high-latitude stations exhibits a threshold effect and does not decrease until 1983. However, in 1986 with sunspot numbers in the vicinity of 10, fade levels as low as 5 dB at 250 MHz are recorded in the polar cap and auroral stations only 5% of the time. It is noted that at auroral locations, the most prominent feature, namely the existence of magnetic *L* shell-aligned irregularity sheets, is equally evident at both sunspot maximum and minimum.

INTRODUCTION

Satellite communication links in the VHF/UHF range can suffer severe scintillation effects in amplitude and phase due to the presence of irregularities in electron density in the *F* region of the ionosphere. The magnitude of random phase perturbations im-

posed on a transitionospheric communication link depends on the integrated electron density deviation, $\int \Delta N dl$, along the ray path. It may be shown that this parameter is controlled by the irregularity amplitude ($\Delta N/N$) and the background electron density, N , and its distribution in the ionosphere. Satellite in situ measurements have shown that while the irregularity amplitude remains fairly constant the background density in some regions of the globe undergoes a drastic variation with the sunspot cycle. This in turn has a profound effect on the magnitude of intensity

Copyright 1988 by the American Geophysical Union.

Paper number RS0158.
0048-6604/88/00RS-0158\$04.00

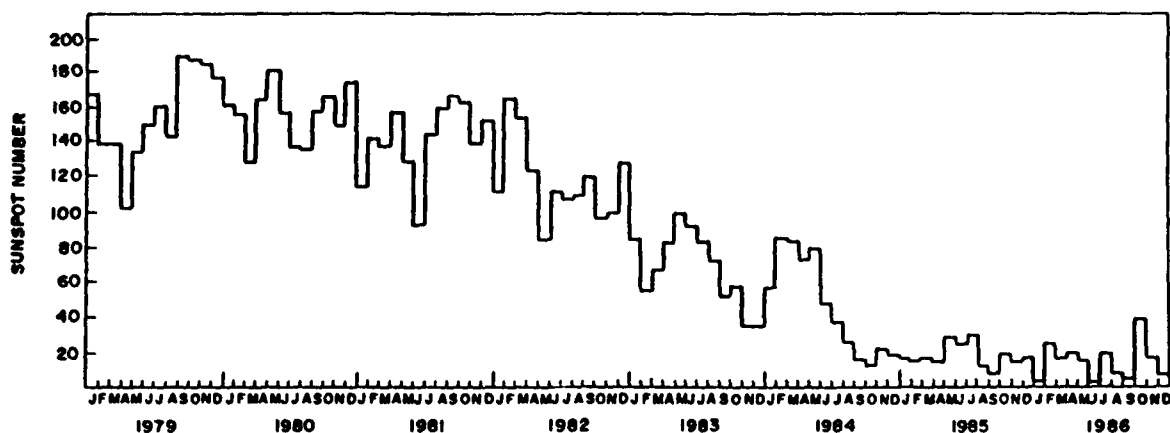


Fig. 1. Variation of monthly mean sunspot number between 1979 and 1986.

and phase scintillations as a function of the sunspot cycle at any point on the globe. Furthermore, the occurrence of irregularities may be reduced with decreasing solar activity, for instance, as a result of the decreased height of the *F* region, and, as such, the percent occurrence of scintillations may decrease with decreasing solar activity. The object of this paper is to describe the observed variation of scintillations as a function of sunspot cycle within the major scintillation-producing regions of the globe using the extensive archive of such data at the Air Force Geophysics Laboratory (AFGL).

RESULTS

We shall present phase and amplitude scintillation data from the solar maximum to minimum period (1979–1986) observed from Huancayo, a station on the magnetic equator, from Ascension Island, an equatorial anomaly station, from Goose Bay and Tromsø, both auroral locations, and from Thule situated deep within the polar cap. Figure 1 shows the nature of variation of the sunspot number between 1979 and 1986 with the maximum value being 190 in August 1979 and the minimum about 2 in June 1986. Table 1 lists positions of stations and ionospheric intersection latitudes (in corrected geomagnetic (CG) system) of the measurements at each station.

Huancayo

The occurrence statistics of 137-MHz scintillations as a function of solar cycle at Huancayo were presented by Aarons [1977]. The occurrence shows a diffuse maximum from October through March with

only a slight decrease seen in December. Scintillations were practically nonexistent during the June solstice for quiet magnetic activity. The occurrence did not vary significantly as a function of solar cycle, the maximum equinoctial occurrence being reduced to 60% occurrence greater than 6 dB in comparison to 80% during sunspot maximum. It was felt that because of saturation effect at 137 MHz, a similar study was necessary at a higher frequency. Su, Basu *et al.* [1980] presented the occurrence statistics of 1.5-GHz scintillations observed at Huancayo during the sunspot minimum period of 1976–1977. The seasonal pattern showed clear equinoctial peaks with 30% occurrence of scintillations greater than 2 dB observed during March and October. Figure 2 shows the corresponding scintillation statistics for the high-sunspot period of 1979–1980. Only the occurrence of scintillations during the vernal equinox was found to increase (from 30 to 60%) in comparison to the low-sunspot case. It is important to note that the magnitude of scintillations was not found to vary significantly as a function of sunspot cycle at the magnetic

TABLE I. Station Locations and Ionospheric Intersection Latitudes

Station	Geographic Location		350-km Intersection CG Latitude
	Latitude	Longitude	
Huancayo	12.0 S	75.3 W	0°
Ascension Island	7.4 S	14.4 W	17°S dip latitude
Goose Bay	53.3 N	60.3 W	64°-69°
Tromsø	69.7 N	18.9 E	66°-69°
Thule	76.5 N	68.7 W	84°-89°

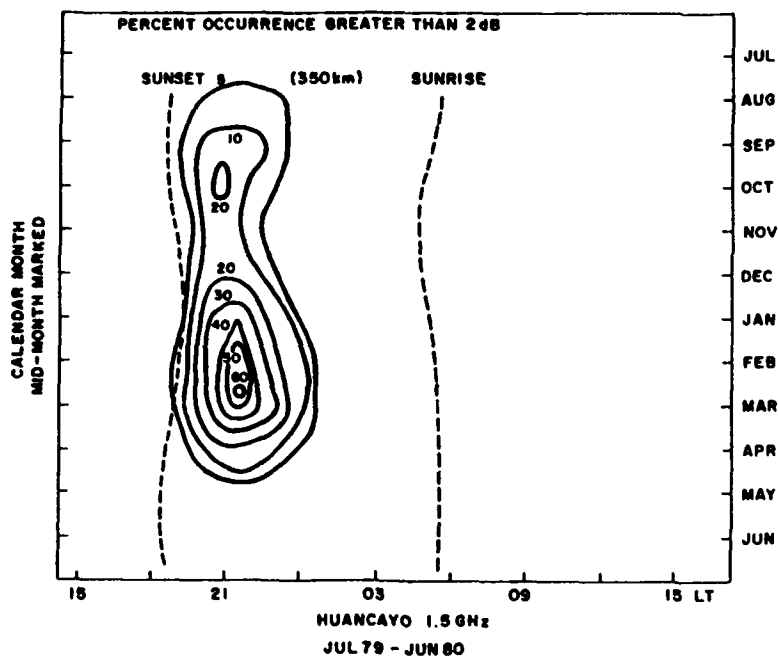


Fig. 2. Percent occurrence of scintillations > 2 dB at 1.5 GHz observed at Huancayo during the solar maximum period of July 1979 through June 1980 for $K_p < 3$.

equator. This is quite contrary to scintillation behavior observed at the equatorial anomaly location to be discussed in the next section.

Ascension Island

It has been shown recently that some of the largest propagation disturbances are observed at this location during sunspot maximum years [Aarons *et al.*, 1981a; Mullen *et al.*, 1985; S. Basu *et al.*, 1987a]. At Ascension Island, continuous amplitude scintillation observations have been performed by the use of 257-MHz and 1.5-GHz transmissions from the Marisat satellite and 244-MHz signal from the Fleetcom satellite. Figure 3a shows an occurrence diagram of 1.5-GHz scintillations in the premidnight period (2000–2400 LT) for the years 1980–1986. While fades as deep as 20 dB at 1.5 GHz are observed 30% of the time in March 1980, fades of only 10-dB magnitude are observed not more than 10% of the time in October 1983. At the lowest level of the sunspot cycle in 1985–1986, there is virtually no occurrence of 1.5-GHz scintillation. To show that even under sunspot maximum conditions, gigahertz scintillation is a serious problem only in the premidnight hours, we present in Figure 3b the corresponding statistics at

Ascension Island for the postmidnight period (0000–0400 LT). It should also be noted that gigahertz scintillations are generally not observed at Ascension Island in the May through August period even under sunspot maximum conditions.

In general, all equatorial stations observe high scintillation activity during the equinoxes, but stations in the American and African sectors record minimum activity during the June solstice, and those in the Pacific sector observe a minimum during the December solstice [Aarons *et al.*, 1980]. Attempts have been made to explain this seasonal-cum-longitudinal pattern of equatorial irregularities in terms of transequatorial neutral wind flows [Miyazawa and Matuura, 1984] and Pedersen conductivity gradients across magnetic flux tubes [Tsunoda, 1985]. In this paper, however, we shall confine our attention to the solar cycle variation of scintillations.

In addition to performing multifrequency amplitude scintillation measurements, a computer-controlled phase-locked receiver (designed by M. D. Cousins of SRI International) was used to measure phase and amplitude scintillations of 244-MHz transmissions of the Fleetcom satellite over a limited period. The phase scintillation statistics at 244 MHz, expressed in terms of rms phase deviation (σ_ϕ),

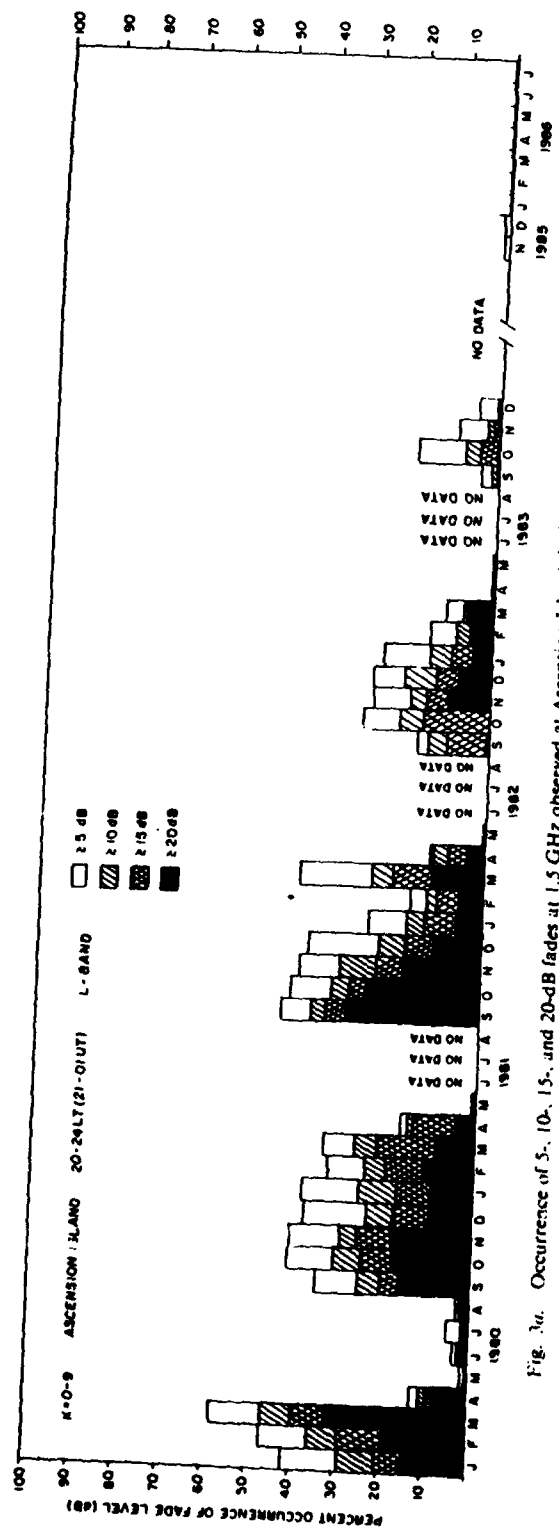


Fig. 3a. Occurrence of 5-, 10-, 15-, and 20-dB fades at 1.5 GHz observed at Ascension Island during 2000-2400 LT (2100-0100 UT) for the period 1980-1986.

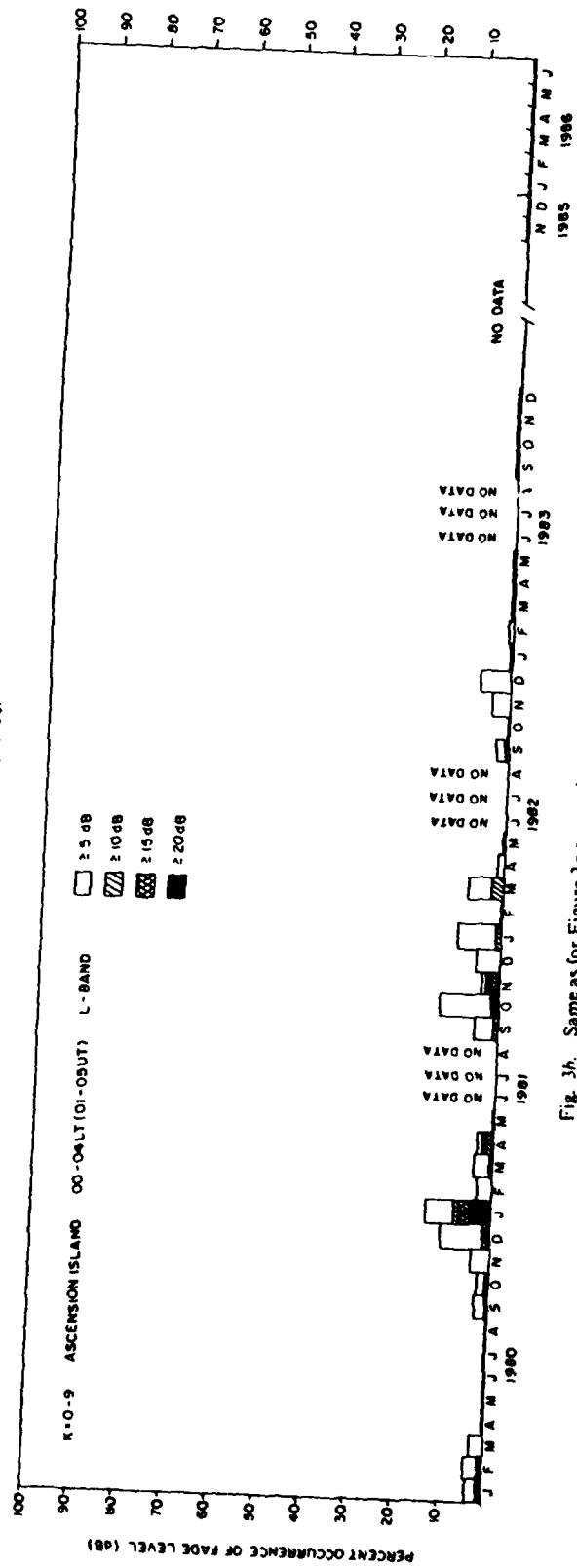


Fig. 3b. Same as for Figure 3a except during 0000-0400 LT (0100-0500 UT).

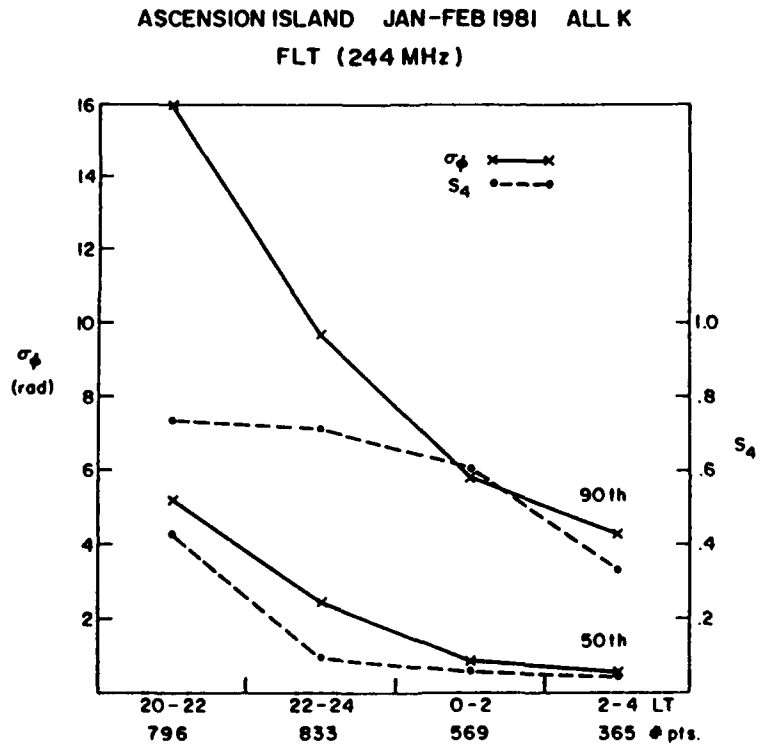


Fig. 4a. The median (50th percentile) and 90th percentile values of phase and intensity scintillations at 244 MHz in terms of four 2-hour blocks of local time (LT) during January–February 1981 at Ascension Island.

during the sunspot maximum period of January–February 1981 are reproduced from S. Basu *et al.* [1987a] in Figure 4a. In the 2000–2200 LT period the median value of σ_ϕ is shown as 5 rad (for 100-s detrend interval), and the corresponding upper decile is obtained as 16 rad. The intensity scintillation index S_4 , defined as the square root of the normalized variance of intensity, is also shown in the figure. The median value of S_4 is about 0.4. In view of the saturation of the receiver encountered at $S_4 \sim 0.7$, the median S_4 is likely to be an underestimate of the actual level of activity. No phase scintillation measurements are available for sunspot minimum conditions.

The other parameters that characterize the structure of scintillations, namely, the decorrelation time and phase spectral strength, were studied for this observing station as well. The decorrelation time has been defined as the time interval that corresponds to the reduction of the autocorrelation coefficient of normalized intensity to 0.5, and the phase spectral strength T_ϕ corresponds to the power spectral density of phase scintillation spectrum at 1 Hz. For intense scintillation events at 244 MHz ($S_4 > 0.6$), Figures 4b, 4c, and 4d show, respectively, the variation of

decorrelation time with phase spectral strength and the percent occurrence of each of these parameters within the period 2000–0200 LT in January–February 1981. Figure 4b shows that the decorrela-

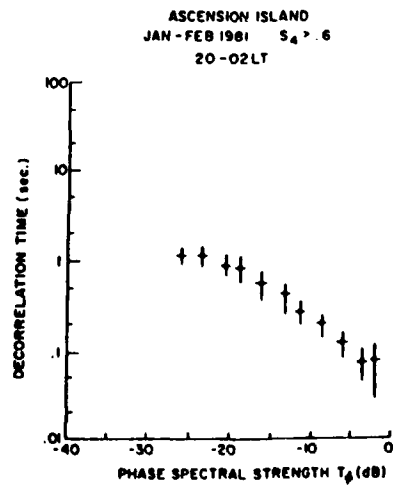


Fig. 4b. Variation of decorrelation time with phase spectral strength at 244 MHz for intense scintillation events ($S_4 > 0.6$) between 2000 and 0200 LT during January–February 1981 at Ascension Island.

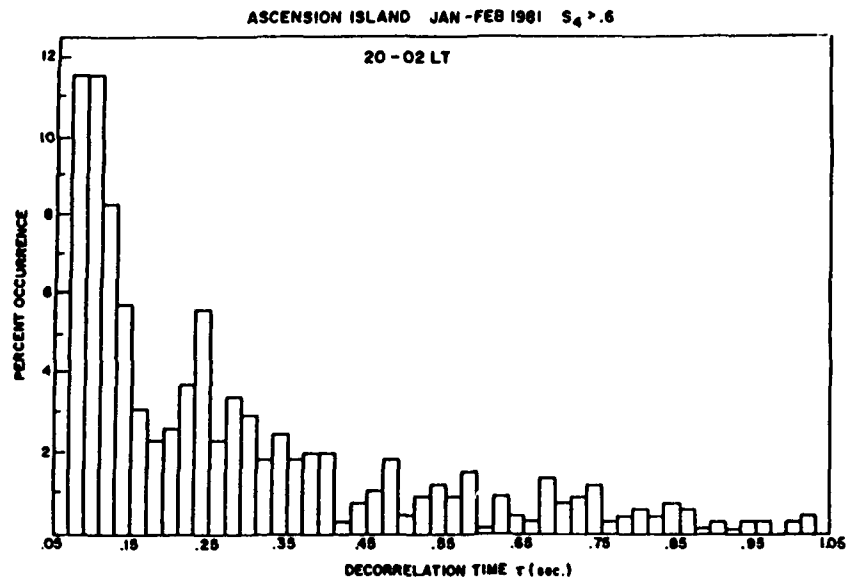


Fig. 4c. Distribution of decorrelation times for the data set shown in Figure 4b.

tion time decreases in a well-ordered manner with increasing phase spectral strength. This behavior is predicted from strong scattering theory and was demonstrated earlier by Rino and Owen [1980]. Fig-

ures 4c and 4d indicate that for this strong scatter population ($S_4 > 0.6$) the most probable value of phase spectral strength is -6 dB and the decorrelation time is about 0.1 s. Since the irregularity drift

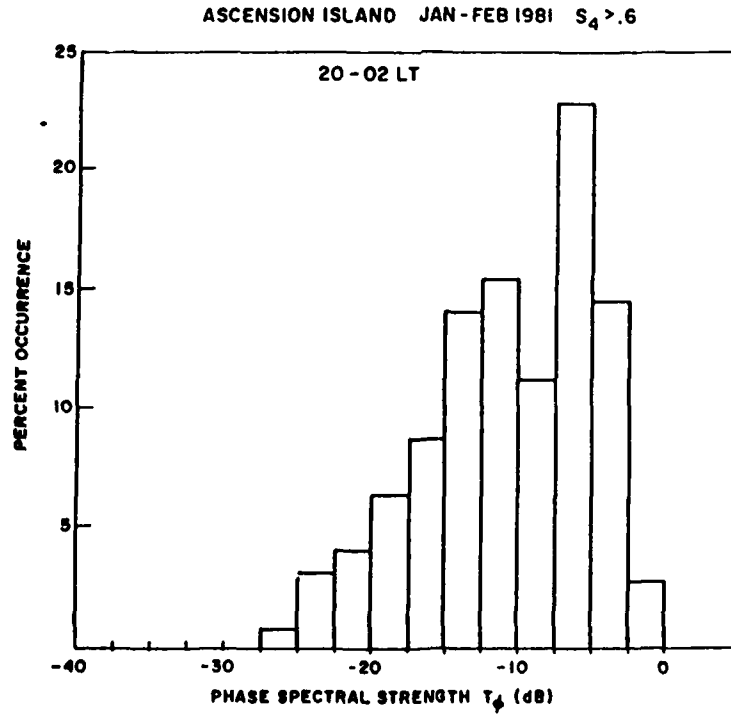


Fig. 4d. Distribution of phase spectral strengths for the data set shown in Figure 4b.

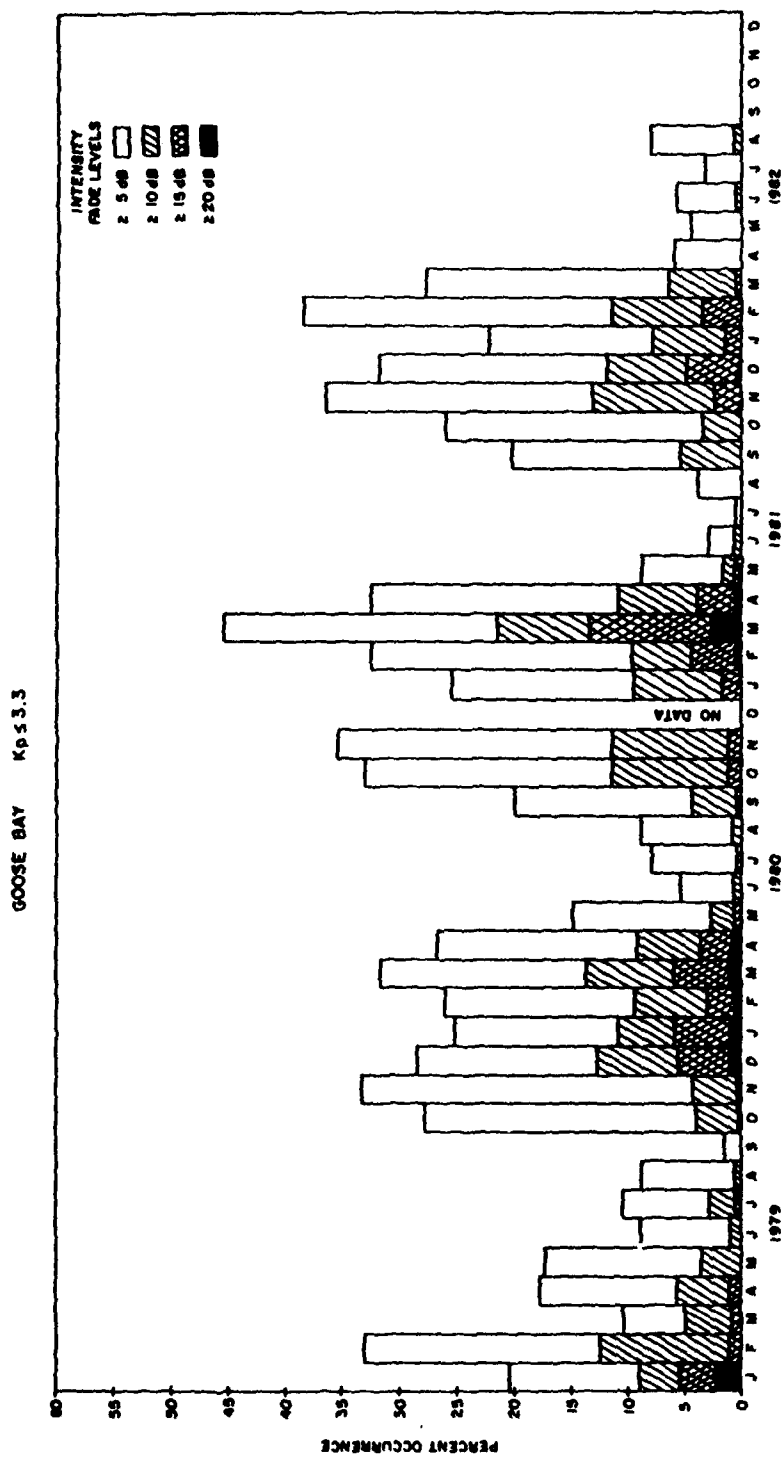


Fig. 5a. Intensity scintillations at 250 MHz observed at Goose Bay for $K_p < 3.3$ under high-sunspot conditions between 1979 and 1982. Note that the apparent seasonal variation may be caused by the latitude variation of the intersection point.

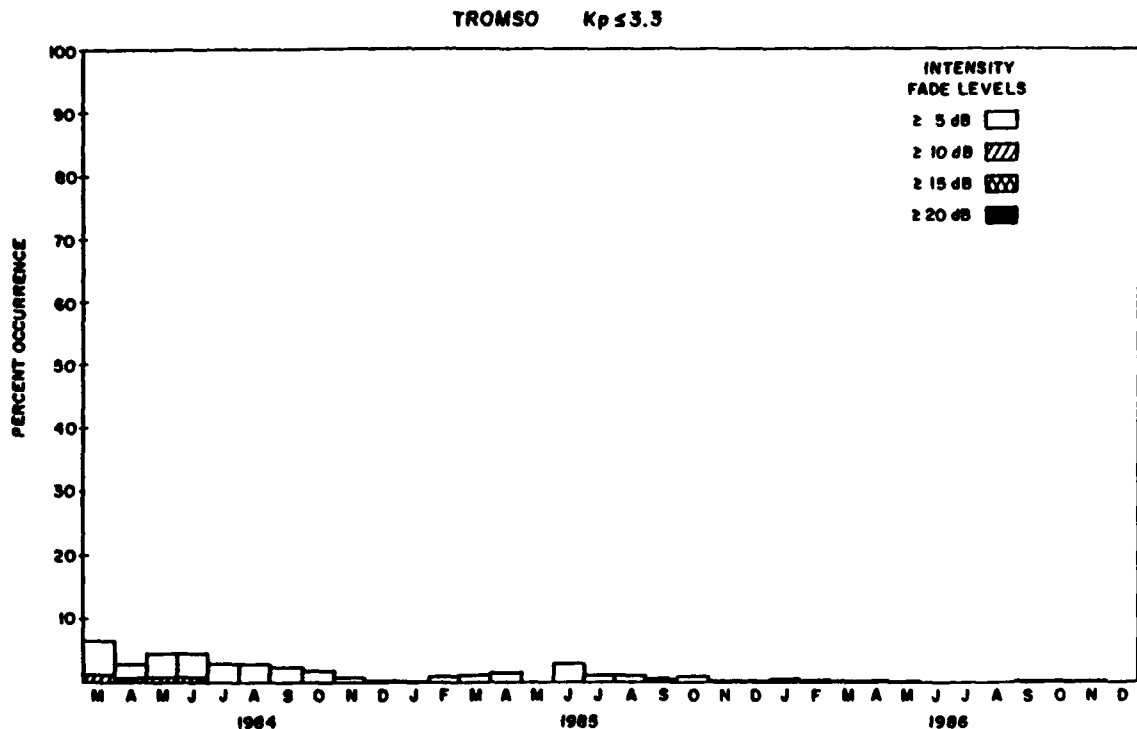


Fig. 5b. Intensity scintillations at 250 MHz observed at Tromsø for $K_p < 3.3$ under low-sunspot conditions between 1984 and 1986.

speed at equatorial locations in the postsunset period ranges between 100 and 200 m s^{-1} , the above decorrelation time corresponds to spatial correlation length of only $10\text{--}20 \text{ m}$.

The effects of strong scattering resulting in decreased spatial correlation lengths are not confined to the VHF (250 MHz) band but extend to the L band as well. At Ascension Island, where the 1.54-GHz transmissions from the Marisat satellite often suffer strong scattering, decorrelation times as small as 0.4 s are obtained in the postsunset period under sunspot maximum conditions [Su, Basu *et al.*, 1983]. For typical irregularity drift speeds in the range of $100\text{--}200 \text{ m/s}$, the spatial correlation lengths at 1.54 GHz may thus be reduced to values as small as $40\text{--}80 \text{ m}$. This is an order of magnitude smaller than the 1 km effective aperture length of typical L band synthetic aperture radar (SAR) systems. Thus this will adversely affect the resolution of the radar system. The above result assumes that the altitude of the SAR system is at least 800 km so that the bulk of the F region ionization lies below the radar and thereby can degrade the system performance.

Goose Bay and Tromsø

We next consider scintillation statistics in the auroral oval. Measurements were available using several polar beacon satellites at 250 MHz from Goose Bay in the North Atlantic sector for sunspot maximum conditions, while data were available from Tromsø in the Scandinavian sector for sunspot minimum conditions. The range of latitude covered for both stations is given in Table 1. We note that both are auroral locations only for nighttime hours between 2200 and 0400 MLT [MacKenzie *et al.*, 1987] with the higher intersection latitudes providing higher probability of scintillations during magnetically quiet conditions ($K_p < 3.3$). The polar beacon satellites used for these measurements also do not provide uniform local time coverage. In addition, different latitude ranges were explored at different times of the year. Thus time periods for which the higher intersection latitudes were sensed around midnight would be favored for higher scintillation occurrence. Unfortunately, there is no easy way of separating these different variables. The occurrence statistics

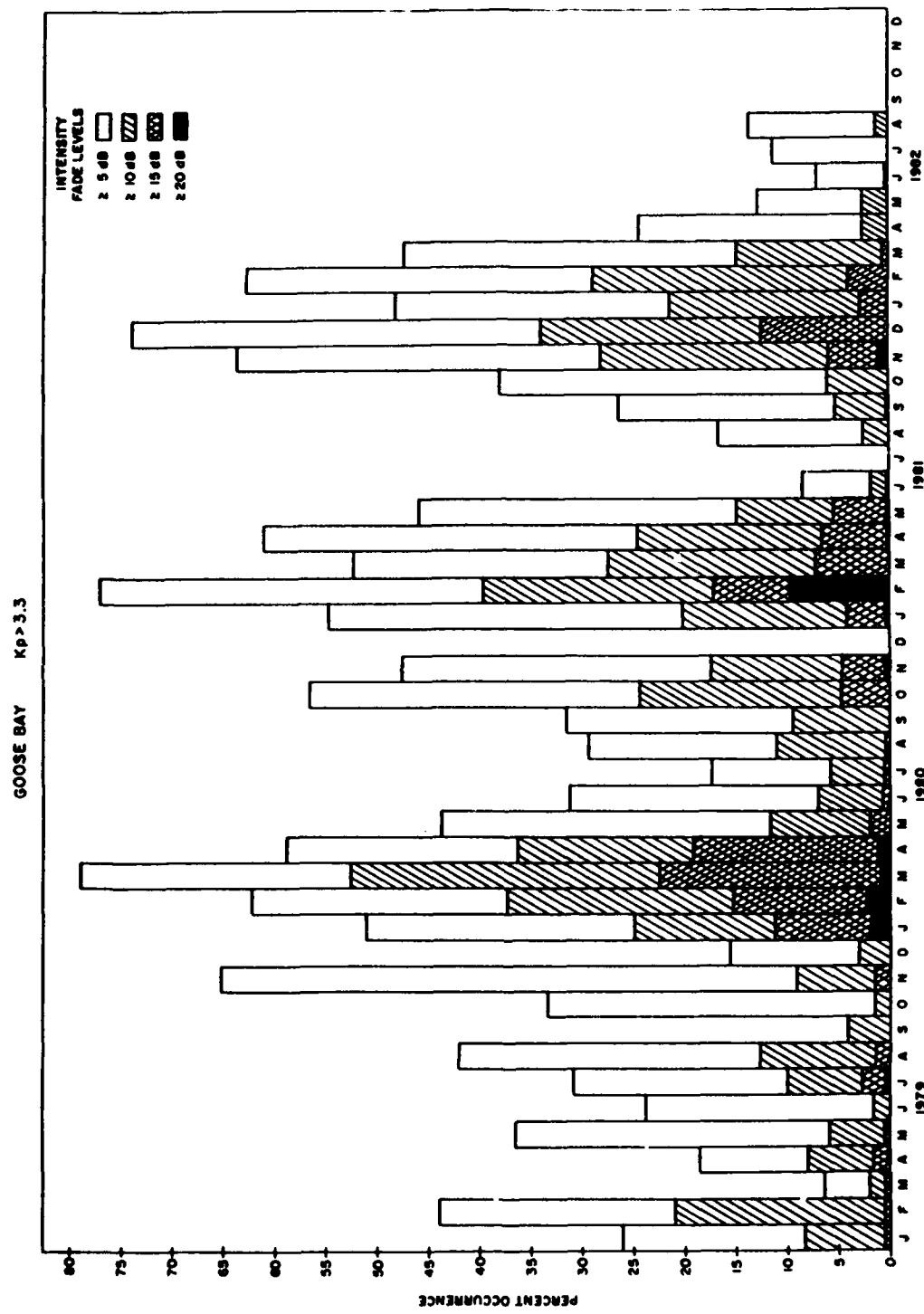


Fig. 5c. Same as Figure 5a except for $K_P > 3.3$.

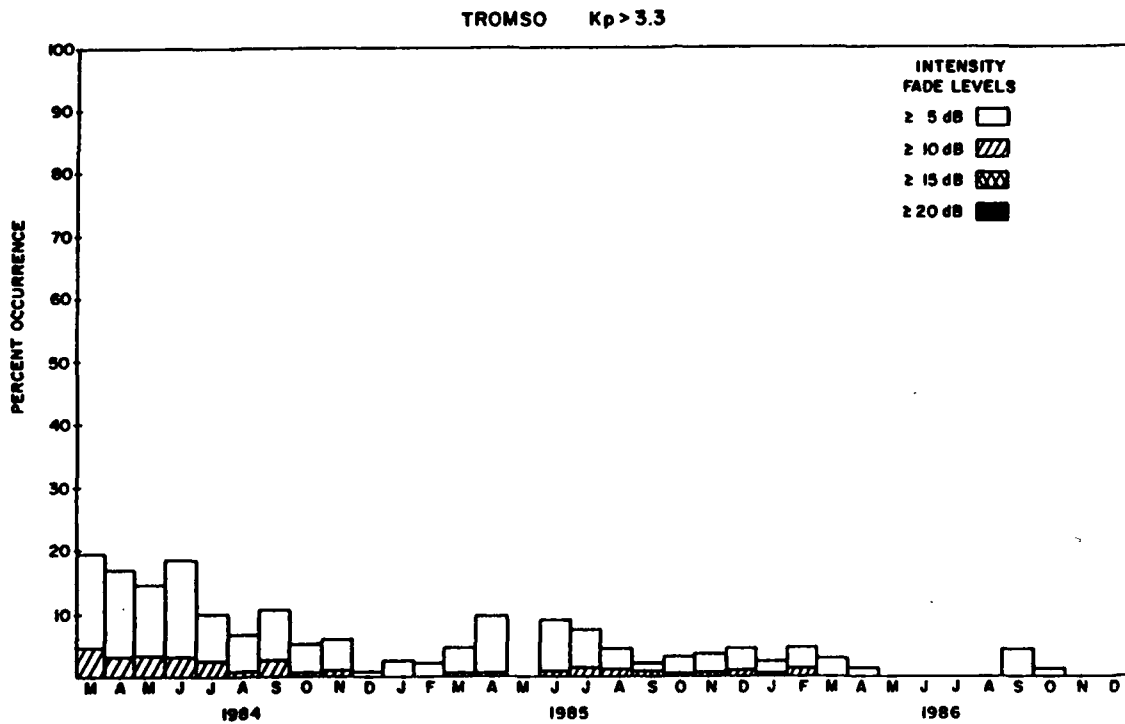


Fig. 5d. Same as Figure 5b except for $K_p > 3.3$.

should be viewed within the framework of these constraints.

Figures 5a and 5b illustrate the drastic variation of intensity scintillations at 250 MHz with sunspot cycle under magnetically quiet conditions ($K_p < 3.3$). As mentioned earlier, the apparent seasonal modulation seen in the Goose Bay data is probably related to the latitude variation of the ionospheric intersection regions in the June solstice in comparison to other seasons. The Tromsø data show extremely low occurrence. The corresponding occurrence characteristics for high magnetic activity are shown in Figures 5c and 5d. Magnetic activity increases scintillation occurrence and magnitude during both solar maximum and minimum periods. Further, the reduction in the apparent seasonal modulation of scintillations at Goose Bay with increasing magnetic activity supports the effect of varying intersection latitude mentioned earlier: It is well known that the scintillation boundary moves equatorward during magnetic disturbances [Su, Basu and Aarons, 1980].

One of the most prominent features of auroral scintillations is the existence of magnetic L shell-aligned irregularity sheets which gives rise to enhanced phase scintillations when the ray path to a

satellite becomes aligned with the local L shell [Fremouw et al., 1977; Rino et al., 1978]. In Figures 6a and 6b we show that the same type of irregularity anisotropy (namely, sheetlike) is present during both sunspot maximum and minimum conditions. Wideband satellite data at 137 MHz obtained at Goose Bay in 1979 are used for Figure 6a [Su, Basu et al., 1981], and the geometrical enhancement is observed in the 63° – 64° invariant latitude bin, while similar data using the HiLat satellite at Tromsø are used for Figure 6b [S. Basu et al., 1987b] and show an enhancement in the 65° – 67° N invariant latitude bin. It should be noted that the higher magnitudes of σ_s observed in the HiLat data result from the use of 30-s detrend intervals in comparison to 10-s used for Wideband data analysis. Since both satellite scan velocities are approximately 3 km s^{-1} , these detrend periods allow phase scintillation computations to be made over 90 km of orbital path for HiLat and only over 30 km for Wideband.

Thule

The occurrence of different levels of intensity scintillation fades at 250 MHz is shown for the period

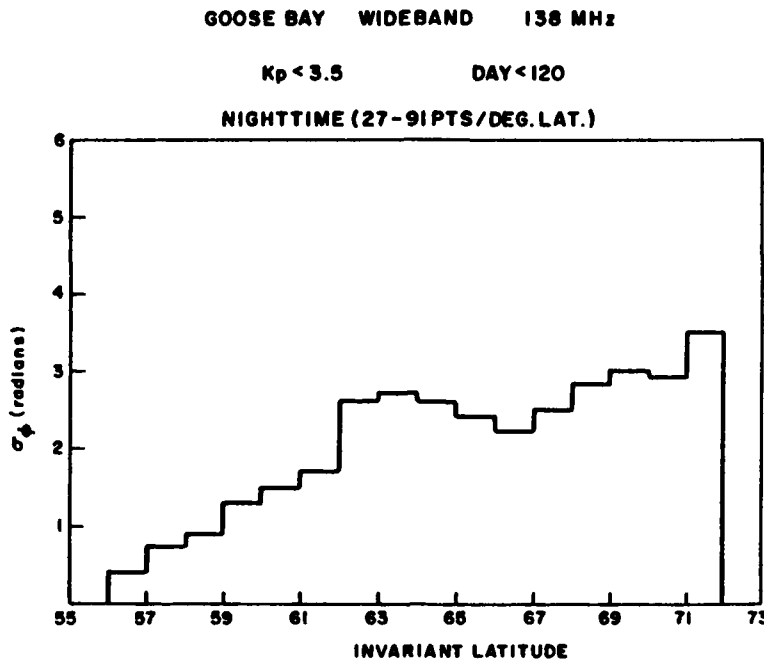


Fig. 6a. Latitude variation of scintillations at 138 MHz observed at Goose Bay during the vernal equinox of 1979 using the Wideband satellite. Note nighttime scintillation enhancement in the 63° - 64° invariant latitude bin caused by sheetlike irregularity anisotropy in the nighttime auroral oval.

1979-1986 in the bottom panel of Figure 7. Because of lack of strong diurnal variation, all 24 hours of observations are included. The drastic variation of occurrence and magnitude of scintillations with sunspot number, shown in the top panel, is evident. It is noted that intensity fades of 20 dB occur $\sim 50\%$ of the time under solar maximum conditions in 1979 and fades as low as 5 dB occur less than 5% of the

time under solar minimum conditions in 1986. It has been discussed earlier by *Su, Basu et al. [1985]* that the reduction in scintillations during the June solstice arises not from a reduction of the background density but rather from a drastic decrease in the irregularity amplitude at kilometer scales, possibly in the presence of underlying *E* region conductivity [*Aarons et al., 1981b; Vickrey and Kelley, 1982; Heelis et al., 1985*].

The phase and intensity scintillation statistics during a sunspot maximum period are reproduced in Figure 8 from *S. Basu et al. [1987a]*. Little diurnal variation is seen, with median values of σ_ϕ at 244 MHz (with 82-s detrend) being 3 rad and the upper decile being 12 rad. It should be noted that in the high-latitude environment large convection velocities are responsible for large σ_ϕ magnitude when a quasi-geostationary satellite is used as a source [*Su, Basu et al., 1985*]. However, in spite of large convection velocities the smallest decorrelation time observed at Thule is approximately 0.3 s in comparison to 0.1 s at Ascension Island, where the scattering strength is much larger. It indicates that higher levels of turbulence at low latitudes decrease the decorrelation time, although the convection velocity does not exceed 200 m s^{-1} . Although phase scintillation measurements

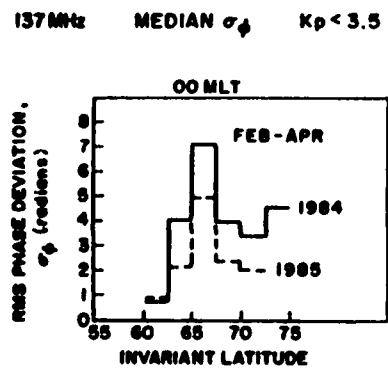


Fig. 6b. Same as in Figure 6a except that the station is Tromsø, the satellite is HiLat, and the years are 1984 and 1985. For Tromsø the geometrical enhancement for sheetlike irregularities occurs in the 65° - 67.5° invariant latitude.

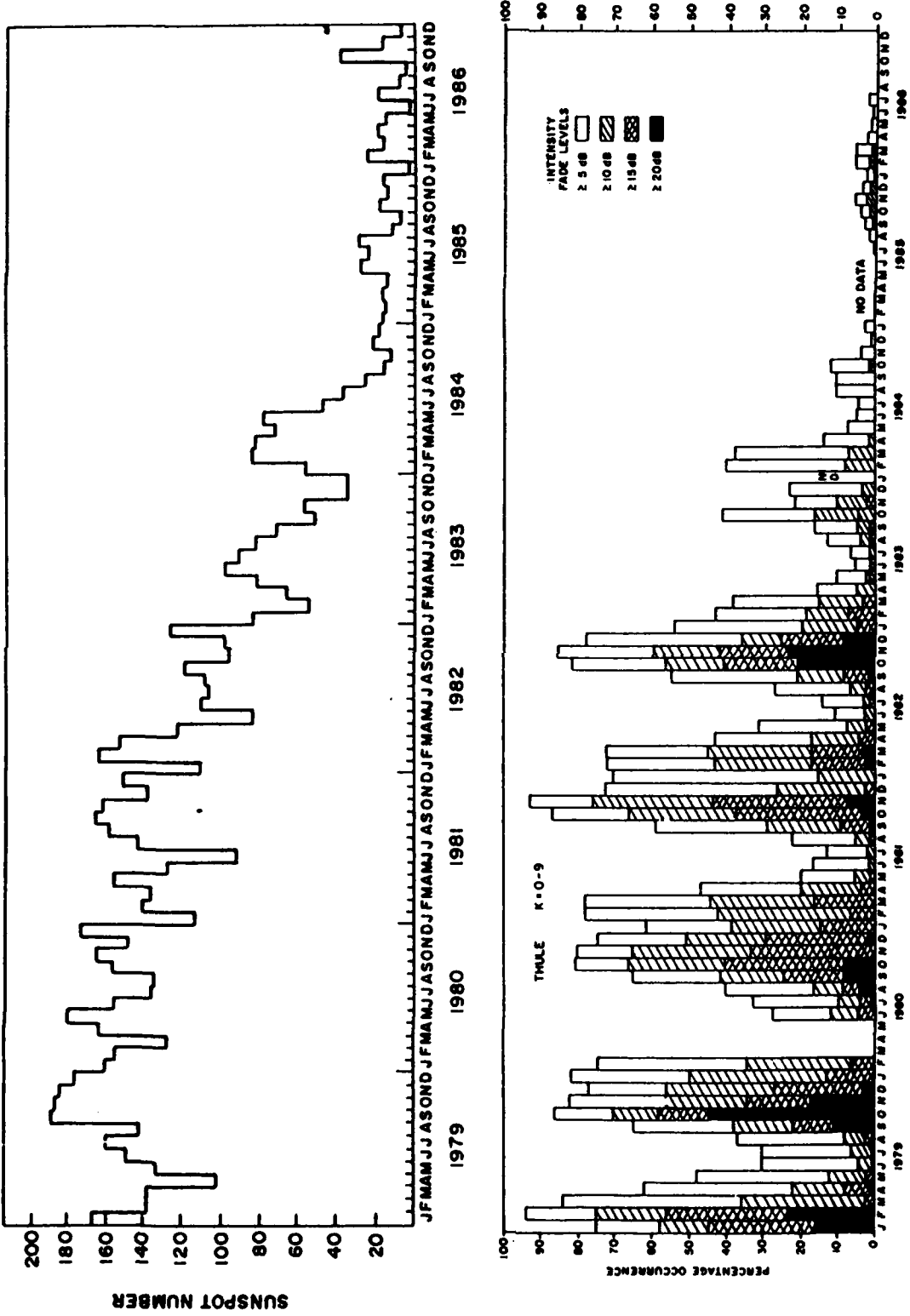


Fig. 7. Occurrence of 5-, 10-, and 20-dB fades at 250 MHz observed at Thule during the period 1979-1986. All local times and all magnetic activity data are included. Figure 1 is repeated in the top panel to emphasize the dependence of scintillation occurrence and magnitude on the sunspot cycle.

were continued into the low-sunspot period, median σ_4 magnitudes hardly ever exceeded 1 rad at 250 MHz, which is the threshold of these measurements, and thus the data are not shown. It should also be mentioned that the Thule measurements at 250 MHz indicate that scintillation activity did not vary much during 1979–1982 in spite of the variation of solar activity during that period. However, scintillations started to decrease rather abruptly with further reduction of solar activity after 1982. It is not clear if there is indeed a threshold level of solar activity above which solar conditions lose their control over irregularity magnitude and their formation. Alternatively, this may be an artifact of saturated scintillation at 250 MHz.

Recently, L band scintillation and total electron content measurements at Thule have been started by the use of global positioning satellites. Very limited data have been published which indicate that ~ 3 -dB fluctuations at L band frequency have been observed at high elevation angles in 1984 [Weber et al., 1986]. These measurements will be useful in the next sunspot maximum period, particularly when 250-MHz scintillation becomes saturated.

SUMMARY

The global occurrence characteristics during sunspot maximum and minimum periods are summarized with the help of the schematic diagrams shown in Figure 9. The left-hand panel of the figure shows the scintillation activity during the sunspot maximum period. The activity level is expressed in terms of actual L band observations at the equator and extrapolations from 250-MHz observations at higher latitudes. The diagram identifies three major regions producing scintillations, namely, the region around the magnetic equator in the postsunset period, the nightside auroral oval and dayside cusp, and the region within the polar cap at all local times. The most disturbed region corresponds to the northern and southern crests of the equatorial anomaly where the magnetic dip is approximately 30° , with more moderate levels of scintillations being observed at the magnetic equator. The generation of the equatorial irregularities in the postsunset hours and the occurrence of a secondary maximum of F region ionization [Anderson and Klobuchar, 1983] at this time combine to produce such enhanced activity in this region. The diagram shows that the gigahertz scintillation activity is much more moderate at the mag-

netic equator, as was determined in the present study and earlier studies [Su, Basu et al., 1980; S. Basu et al., 1986].

The activity level at high latitudes is much more moderate than that at the equator. Among the two high-latitude regions, the polar cap is probably more active than the auroral oval. In the polar cap, blobs of structured plasma convected from the dayside cusp and polar F region arcs generated by particle precipitation have been identified as sources of scintillation activity [Weber et al., 1984; Weber and Buchau, 1981; Su, Basu et al., 1988]. The dayside cusp has also been found to be a seat of significant scintillations [Vickrey et al., 1985]. In the nightside auroral oval the activity level is more moderate than in the polar cap, as indicated in the diagram. In contrast to the magnetic equator, the greater variability of ionospheric drift at high latitudes changes the rms phase deviation and decorrelation times for a given level of intensity scintillation.

The right-hand panel represents the activity level during the sunspot minimum period. A drastic reduction of scintillation activity in all three regions is indicated. The latitudinal extent of equatorial scintillations is also reduced. Near the magnetic equator, scintillation levels of 5 dB at L band become rather uncommon. In the polar cap, 5-dB fade levels at 250 MHz are attained only 10% of the time, whereas at auroral stations scintillation magnitudes at 250 MHz rarely exceed 5-dB levels. At high latitudes, rms phase deviations at 250 MHz do not generally exceed 1 rad, which is the sensitivity of our current receivers.

It is obvious that ionospheric scintillations encountered during the solar maximum period are severe enough to be of concern in the design of radar and communication systems. The drastic reduction of scintillation occurrence at all locations during sunspot minimum is rather intriguing in view of the different instability mechanisms operative at high and low latitudes and thus points to the background density as the major modulating factor. From the point of view of successful scintillation modeling, it is important to determine whether the variation of the background F region ionization density with solar cycle is large enough to explain the observed scintillation behavior or whether it is necessary to postulate variation of irregularity parameters as well. At the equator, where irregularity generation is better understood, it has been shown that the high altitude of the F layer seen during solar maximum years helps the seeding and growth of the Rayleigh-Taylor

THULE JAN-FEB 1982 ALL K
POLAR BEACON 244MHz

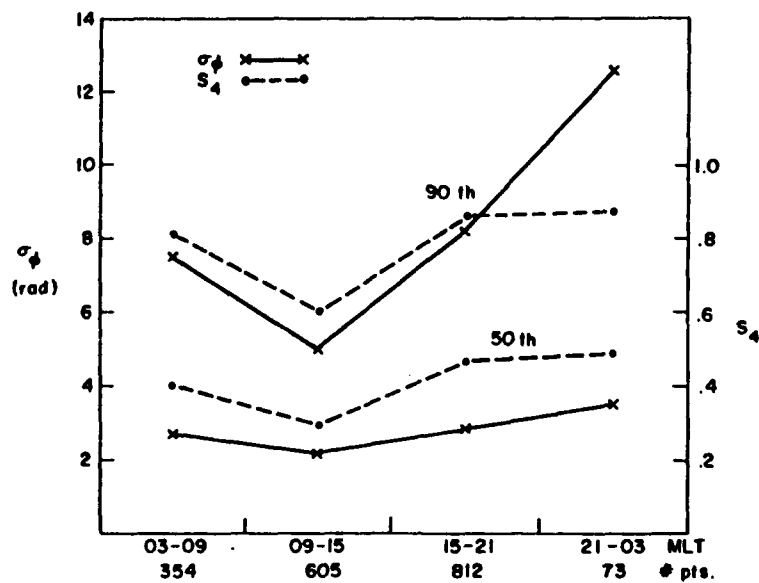


Fig. 8. The median (50th percentile) and 90th percentile values of phase and intensity scintillations at 244 MHz in terms of four 6-hour MLT blocks observed at Thule.

"WORST CASE" FADING DEPTHS AT L-BAND

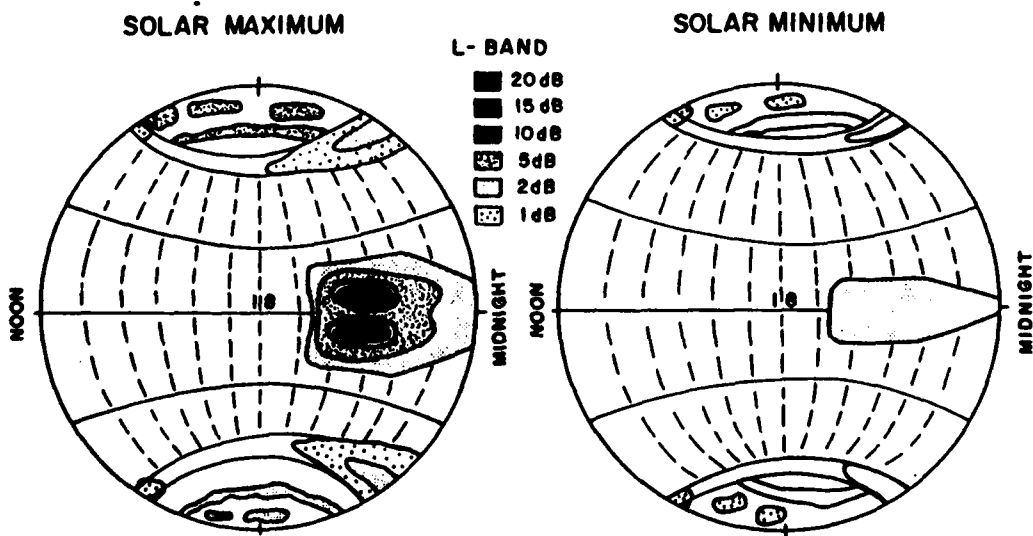


Fig. 9. Global variation of scintillation fades during solar maximum and solar minimum.

instability [Ossakow, 1981] and may explain the increased occurrence of scintillations. It is interesting to note that the semiempirical low-latitude ionospheric model developed by Anderson *et al.* [1987] predicts an order of magnitude variation of background ionization density at the anomaly crest but only a factor of 2 variation at the magnetic equator. The observed variation of scintillation magnitudes as a function of solar cycle agrees well with these predictions. At high latitudes, on the other hand, where a plethora of instabilities may operate [Keskinen and Ossakow, 1983], it is very difficult to determine the extent to which each instability process may be affected by the solar cycle.

Acknowledgments. We thank the Danish Commission for Scientific Research in Greenland for permission to conduct ground experiments at Thule Air Base under Project 23-86. In addition, we thank the Canadian Marconi Company for assistance in obtaining the Goose Bay data. The Tromsø measurements were made with the assistance of personnel at the Tromsø Telemetry Station, while Huancayo data were kindly provided by the Instituto Geofísico del Peru. The work at AFGL was supported in part by Air Force Office of Scientific Research task 2310G9. The work at Emmanuel College was supported by AFGL contract F19628-86-K-0038.

REFERENCES

Aarons, J., Equatorial scintillations: A review, *IEEE Trans. Antennas Propag.*, **AP-25**, 729, 1977.

Aarons, J., J. P. Mullen, J. P. Koster, R. F. DaSilva, J. R. Medeiros, R. T. Medeiros, A. Bushby, J. Pantoja, J. Lanat, and M. R. Paulson, Seasonal and geomagnetic control of equatorial scintillations in two longitudinal sectors, *J. Atmos. Terr. Phys.*, **42**, 861, 1980.

Aarons, J., H. E. Whitney, E. MacKenzie, and S. Basu, Microwave equatorial scintillation intensity during solar maximum, *Radio Sci.*, **16**, 939, 1981a.

Aarons, J., J. P. Mullen, H. Whitney, A. Johnson, and E. Weber, VHF scintillation activity over polar latitudes, *Geophys. Res. Lett.*, **8**, 277, 1981b.

Anderson, D. N., and J. A. Klobuchar, Modeling the total electron content observations above Ascension Island, *J. Geophys. Res.*, **88**, 8020, 1983.

Anderson, D. N., M. Mendillo, and B. Herniter, A semiempirical low-latitude ionospheric model, *Radio Sci.*, **22**, 292, 1987.

Basu, S., Su. Basu, J. LaBelle, E. Kudeki, B. G. Fejer, M. C. Kelley, H. E. Whitney, and A. Bushby, Gigahertz scintillations and spaced receiver drift measurements during Project Condor equatorial F region rocket campaign in Peru, *J. Geophys. Res.*, **91**, 5526, 1986.

Basu, S., E. M. MacKenzie, Su. Basu, E. Costa, P. F. Fougere, H. C. Carlson, Jr., and H. E. Whitney, 250 MHz GHz scintillation parameters in the equatorial, polar and auroral environments, *IEEE J. Selec. Areas Commun.*, **SAC-5**, 102, 1987a.

Basu, S., Su. Basu, E. MacKenzie, and D. Weimer, Ionospheric scintillations and in-situ measurements at an auroral location in the European sector, paper presented at Symposium on Scattering and Propagation in Random Media, Advis. Group for Aerosp. Res. and Dev., Rome, May 1987b.

Basu, Su., and J. Aarons, The morphology of high-latitude VHF scintillation near 70°W, *Radio Sci.*, **15**, 59, 1980.

Basu, Su., S. Basu, J. P. Mullen, and A. Bushby, Long term 1.5 GHz amplitude scintillation measurements at the magnetic equator, *Geophys. Res. Lett.*, **7**, 259, 1980.

Basu, Su., S. Basu, R. C. Livingston, H. E. Whitney, and E. MacKenzie, Comparison of ionospheric scintillation statistics from the North Atlantic and Alaskan sectors of the auroral oval using the Wideband satellite, Rep. AFGL-TR-81-0266, Air Force Geophys. Lab., Hanscom Air Force Base, Mass., 1981.

Basu, Su., S. Basu, J. P. McClure, W. B. Hanson, and H. E. Whitney, High-resolution topside in situ data of electron densities and VHF/GHz scintillations in the equatorial region, *J. Geophys. Res.*, **88**, 403, 1983.

Basu, Su., S. Basu, E. MacKenzie, and H. E. Whitney, Morphology of phase and intensity scintillations in the auroral oval and polar cap, *Radio Sci.*, **20**, 347, 1985.

Basu, Su., S. Basu, E. J. Weber, and W. R. Coley, Case study of polar cap scintillation modeling using DE 2 irregularity measurements at 800 km, *Radio Sci.*, in press, 1988.

Fremouw, E. J., C. L. Rino, R. C. Livingston, and M. D. Cousins, A persistent subauroral scintillation enhancement observed in Alaska, *Geophys. Res. Lett.*, **4**, 539, 1977.

Heelis, R. A., J. F. Vickrey, and N. B. Walker, Electrical coupling effects on the temporal evolution of F layer plasma structure, *J. Geophys. Res.*, **90**, 437, 1985.

Keskinen, M. J., and S. L. Ossakow, Theories of high-latitude ionospheric irregularities: A review, *Radio Sci.*, **18**, 1077, 1983.

MacKenzie, E., S. Basu, and Su. Basu, Ionospheric scintillations/TEC and in-situ density measurements at an auroral location in the European sector, technical report, Air Force Geophys. Lab., Hanscom Air Force Base, Mass., in press, 1987.

Maruyama, T., and N. Matuura, Longitudinal variability of annual changes in activity of equatorial spread F and plasma bubbles, *J. Geophys. Res.*, **89**, 10,903, 1984.

Mullen, J. P., E. MacKenzie, S. Basu, and H. E. Whitney, UHF/GHz scintillation observed at Ascension Island from 1980 through 1982, *Radio Sci.*, **20**, 357, 1985.

Ossakow, S. L., Spread-F theories—A review, *J. Atmos. Terr. Phys.*, **43**, 437, 1981.

Rino, C. L., and J. Owen, The time structure of transionospheric radio wave scintillation, *Radio Sci.*, **15**, 479, 1980.

Rino, C. L., R. C. Livingston, and S. J. Matthews, Evidence for sheet-like auroral ionospheric irregularities, *Geophys. Res. Lett.*, **5**, 1039, 1978.

Tsunoda, R. T., Control of the seasonal and longitudinal occurrence of equatorial scintillations by the longitudinal gradient in integrated E region Pedersen conductivity, *J. Geophys. Res.*, **90**, 447, 1985.

Vickrey, J. F., and M. C. Kelley, The effects of a conducting E layer on classical F region cross-field plasma diffusion, *J. Geophys. Res.*, **87**, 4461, 1982.

Vickrey, J. F., R. C. Livingston, R. T. Tsunoda, C. L. Rino, N. B. Walker, T. M. Dabbs, R. M. Robinson, and R. A. Heelis, The SRI ionospheric plasma structure and dynamics program—1985 results, Def. Nucl. Agency technical report, SRI Int., Menlo Park, Calif., 1985.

Weber, E. J., and J. Buchau, Polar cap F-layer auroras, *Geophys. Res. Lett.*, **8**, 125, 1981.

Weber, E. J., J. Buchau, J. G. Moore, J. R. Sharber, R. C. Livingston, J. D. Willingham, and B. W. Reinisch, F layer ionization patches in the polar cap, *J. Geophys. Res.*, **89**, 1683, 1984.

Weber, E. J., J. A. Klobuchar, J. Buchau, H. C. Carlson, Jr., R. C. Livingston, O. de la Beaujardiere, M. McCready, J. G. Moore,

and G. J. Bishop, Polar cap F layer patches: Structure and dynamics, *J. Geophys. Res.*, **91**, 12,121, 1986.

S. Basu, Air Force Geophysics Laboratory, Hanscom Air Force Base, MA 01731.

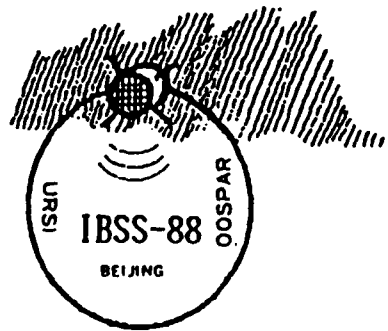
S. Basu and E. MacKenzie, Emmanuel College, Boston, MA 02115.

INVESTIGATION OF THE IONOSPHERE BY MEANS OF BEACON SATELLITE MEASUREMENT

Proceedings of the International
Beacon Satellite Symposium,
April 18-21, 1988 Beijing, China

Edited by Cao Chong

China Research Institute of Radiowave Propagation



International Academic Publishers
(A Pergamon - CNPIEC Joint Venture)

HIGH LATITUDE SCINTILLATIONS

Santimay Basu
Air Force Geophysics Laboratory
Hanscom AFB, MA 01731, USA

Sunanda Basu
Emmanuel College
Boston, MA 02115, USA

ABSTRACT

Recent observations of high latitude phase and amplitude scintillations with the quasi-geostationary polar beacon satellites, high altitude orbiting GPS satellites and the low altitude orbiting HILAT and Polar Bear satellites have contributed greatly to an elucidation of the source regions of F-region irregularities, their evolution and dynamics and their effects on trans-ionospheric propagation links in the VHF/UHF bands. In particular, using the polar beacon satellites which can be tracked for several hours continuously, it was found possible to study for the first time the long-term morphology of phase and amplitude scintillations in the polar cap and relate their structure to the large scale plasma processes. The HILAT satellite observations in the dayside cusp indicate the occurrence of intense VHF scintillations and associated strong HF backscatter. The irregularity configuration in the cusp is found to be rod-like aligned with the geomagnetic field while in the nightside auroral oval magnetic L-shell aligned sheets give rise to large phase scintillations. In the auroral region, in addition to the gradient drift instability associated with plasma 'blobs', intense velocity shears have recently been observed to generate plasma density structures with shallow spectral slopes that have been identified to be sources of strong UHF scintillations and radar backscatter. Whereas the basic irregularity structure is probably preserved through the sunspot cycle, the solar control of the background plasma density is shown to affect greatly the magnitude of scintillations throughout the high latitude region.

INTRODUCTION

The high latitude ionosphere corresponds broadly to the region poleward of the mid-latitude trough and extends as far as the magnetic pole. This region, subdivided into the auroral oval ($\sim 60^{\circ}$ - 75° A, invariant latitude) and the polar cusp and cap ($> 75^{\circ}$ A), is the seat of intense irregularities of electron density that cause phase and amplitude scintillations of signals received from radio stars or satellites and intense backscatter on HF/VHF radars. Tsunoda (1988) has recently presented a comprehensive review of high latitude F-region irregularities. These irregularities in the scale length range of a few kilometers down to meters arise (i) from a structuring of large scale plasma enhancements or blobs through the $E \times B$ gradient drift process in the polar cap and the auroral oval (Weber et al., 1984; Vickrey et al., 1980; Keskinen and Ossakow, 1983); (ii) in regions of soft (few hundred eV) auroral and polar cap particle precipitation (Su, Basu et al., 1983; Weber and Buchau, 1981); and (iii) in velocity shear regions adjacent to inverted-V events by Kelvin-Helmholtz instability process (Su, Basu et al., 1986, 1988a; Keskinen et al., 1988). Co-ordinated incoherent scatter and coherent radars, satellite in-situ, optical/UV imaging and TEC/scintillation measurements have, in recent years, contributed greatly to our understanding of high latitude irregularities and associated plasma processes that give rise to scintillations. In the following sections, we shall discuss the results of

such co-ordinated measurements performed in different regions of the high latitude environment.

RESULTS

We shall illustrate scintillation behavior observed in the polar cap, cusp and nightside auroral oval and attempt to present other co-ordinated observations which provide some insights into the probable generation mechanisms for the irregularities that cause the scintillations.

1. Polar Cap

In recent years the polar cap has been found to be the seat of the largest propagation disturbances in the high latitude environment (Aarons et al., 1981). The scintillations observed in this region are either found to be associated with polar cap arcs, i.e., localized sources within the cap, or with patches of enhanced ionization which drift across the polar cap in an antisunward direction. In the former category, observed under conditions of the interplanetary magnetic field (IMF) $B_z > 0$, the scintillations may be associated with sub-visual F-layer sun-aligned arcs (Weber and Buchau, 1981) or with much brighter E-region polar cap arcs, a special sub-set of which are the theta auroras (Su, Basu et al., 1988b).

It has been shown by Carlson et al. (1984) and by Su, Basu et al. (1988b) that velocity shears are associated with polar cap arcs. Such shears, contiguous to auroral oval arcs, have been found to provide enhanced power at irregularity scale lengths < 1 km (Su, Basu et al., 1988a). This observational result was explained by Keskinen et al. (1988) by invoking the non-linear evolution of the collisional Kelvin-Helmholtz instability as a possible source for the generation of these irregularities associated with sheared plasma flows in the high latitude ionosphere.

Scintillations associated with patches observed during IMF $B_z < 0$ have been studied much more extensively. Weber et al. (1984) diagnosed these plasma density enhancements through optical and ionosonde techniques. Fig. 1 taken from their paper shows an all-sky imaging photometer (ASIP) image at 630 nm of enhanced airglow observed on 22 January 1982 which was caused by the convecting patches of ionization. The numbers on the image correspond to a DE-2 satellite pass that occurred simultaneously. The particle spectrometer data from the satellite was used to prove that the excess ionization observed was not locally produced. Su, Basu et al. (1988c) have further shown that these patches can even be sampled at 800 km as evident from the retarding potential analyzer data from DE-2 depicted in Fig. 2. They also showed that the intense phase and amplitude scintillation depicted in Fig. 3 and caused by the transit of the patch across the ray path to a geostationary satellite (shown by the black dot on Fig. 1) can be modeled with the help of the in-situ data if the F-region peak parameters such as maximum density and scale height are known.

The total electron content (TEC) increase, caused by these patches in the dark polar ionosphere, was estimated using GPS satellites and was found to vary between 10-15 TEC units above a background value of 5 TEC units (Weber et al., 1986). Buchau et al. (1985) have presented evidence for a sunlit sub-cusp ionospheric source for these patches rather than production by precipitating energetic particles. Anderson et al. (1988) have shown by modeling studies that the patches are formed in response to a change in the convection pattern (Heelis et al., 1982) brought about by a sudden change in the cross-tail potential which drives the convection. The small-scale structuring (< 10 km) of these ~ 1000 km patches in the convection field occurs at the steep edges of these enhancements by the $E \times B$ gradient-drift instability mechanism (Chaturvedi and Huba, 1987 and references therein). There is some indication that amplitude scintillations are stronger on the trailing (i.e., $E \times B$ unstable) edge (Weber et al., 1986). However, when the patches are observed in the central polar cap, far from the origin of these enhancements,

it is difficult to distinguish this expected asymmetry between the two edges from either the scintillation or the in-situ technique (Su, Basu et al., 1988c).

Since scintillations are observed in the polar cap irrespective of B_z conditions (i.e., both with sun-aligned arcs, generally observed under quiet magnetic conditions, and convecting patches seen under disturbed magnetic conditions), they show a weak dependence on magnetic activity as monitored by the K_p index. Fig. 4 taken from S. Basu et al. (1988a) shows long-term statistics of 250 MHz scintillations at Thule, a polar cap station, for all K_p as a function of the solar cycle over the period 1979-1986. Due to a lack of strong diurnal variation (S. Basu et al., 1987), all 24 hours of observations are included. The drastic variation of occurrence and magnitude of scintillations with sunspot number, shown in the top panel, is evident. This is interpreted as a reduction in density associated with patches and arcs as a function of the sunspot cycle (Buchau et al., 1985). It has been discussed earlier by Su, Basu et al. (1985) that the reduction in scintillations during the June solstice arises not from a reduction in the background density but rather from a drastic decrease in the irregularity amplitude at km-scales possibly in the presence of underlying E-region conductivity (Aarons et al., 1981; Vickrey and Kelley, 1982; Heelis et al., 1985).

2. Polar Cusp

Satellite in-situ traversals of the dayside polar cusp through the topside F-layer have found this region to be associated with soft electron precipitation, enhanced electron temperature and electron density fluctuations (Curtis et al., 1982). Kelley et al. (1982) presented in-situ rocket measurements of plasma density in the F-region which closely tracked variations in total energy flux associated with precipitating electrons. This would normally lead one to believe that the cusp should be a region of enhanced scintillations as both density and relative density fluctuations are found to be larger. The evidence in the literature is somewhat conflicting, however. Two case studies performed by the AFGL Airborne Ionospheric Observatory (AIO) on January 26, 1979 and January 28, 1984 found low levels of scintillations (approximately 6 dB) at 250 MHz. Two other case studies conducted by Baker et al. (1986) and Basinska et al. (1987) on November 28, 1983 and December 2, 1983, respectively, using the HILAT satellite found saturated VHF and fairly intense UHF scintillations in conjunction with low energy particle precipitation, field aligned currents, and structured velocities. Both groups invoked the current convective instability (Ossakow and Chaturvedi, 1979) as a mechanism for irregularity generation. Of particular interest is the finding of Baker et al. (1986) that a region of east-west extended HF backscatter was found to be co-located with the most intense scintillations and the cleft/cusp related particle precipitation and field aligned currents. Plate 1 of their paper shows the intersection of the HILAT pass (white line) with the radar scattering volume at the time of the most intense scintillations at 1642:05 UT. HF backscatter from the same volume is seen to exceed 25 dB above receiver noise.

3. Nightside Auroral Oval

This is a region of the high latitude ionosphere where evidence has been found for both convected and in-situ generated plasma density enhancements or 'blobs' to be associated with scintillations. Vickrey et al. (1980) were the first to report on convected auroral 'blobs' and scintillations using combined Chatanika radar and 150 MHz transmissions from the Triad satellite. Another more recent case study was conducted by Weber et al. (1985) also using Chatanika radar data and Wideband satellite scintillation data which were received at two fixed ground stations and on the AFGL AIO. In addition, ionospheric structure measured by the radar was compared with remote optical and ionosonde measurements from the AIO and with precipitating electron characteristics measured by a DMSP satellite. From the simultaneous

measurements these authors were able to prove that the plasma density enhancements seen by optical and radar techniques were not locally generated. Fig. 5 shows that the most intense scintillations were associated with the largest plasma density enhancements in the F-region, one associated with the boundary blob (Rino et al., 1983) to the south of the radar and the other near the radar zenith. It further shows that the peak production in the E-region associated with particle precipitation was well to the north of the F-region enhancements and in this case not associated with amplitude scintillations. The auroral blobs structure in the same way as the polar cap patches discussed earlier.

While convecting blobs provide a large fraction of the scintillation events in the nightside auroral oval, scintillations, particularly during substorms, are also found to be associated with intense soft particle precipitation which gives rise to locally produced density gradients and TEC enhancements. One such case was documented by Su, Basu et al. (1983).

In some cases, however, intense scintillations are observed without the presence of well-defined F-region blobs and TEC enhancements. Su, Basu et al. (1986) found that in such cases the scintillations/TEC shown in Fig. 6 are associated with large structured velocity regions as are observed at the edges of auroral arcs. The absence of blobs was established using EISCAT radar measurements, while both EISCAT and STARE provided evidence for velocity shears in the region of scintillations. It is possible that such velocity shears generate irregularities by the collisional Kelvin-Helmholtz process mentioned earlier.

Finally, we would like to report a class of auroral phase scintillation events seen during winter sunspot minimum conditions. One such example of 137 MHz phase scintillations, using the Polar Bear satellite on January 24, 1987 obtained at Sondrestrom Fjord, Greenland, is shown in the top panel of Fig. 7 (S. Basu et al., 1988b). Basically, the phase scintillations (because of the 30s detrend interval of the orbiting satellite with an orbital velocity of 1 km s^{-1} in the E-region) are mirroring TEC structure at tens of km shown in the bottom panel. The TEC structure between 0208:48-0210:48 UT is seen to fall within a band of fairly intense 1-2 Kilo Rayleigh vacuum ultraviolet (VUV) emissions at 135.6 nm located as shown on the upper edge of the diagram. The most intense phase scintillations are co-located with it. It should be noted that the phase scintillation peak at 0211:48 is geometrical in nature and caused by the ray path aligning with magnetic L-shell aligned irregularities (Rino et al., 1978). The magnitude of amplitude scintillation recorded was quite low. The VUV image recorded by Polar Bear will not reproduce well and is therefore not shown. When this pass was recorded at Sondrestrom, the incoherent scatter radar was also operating. Fig. 8 shows an elevation scan in the magnetic N-S plane which is time co-ordinated with the Polar Bear pass. Careful measurements confirmed that the structures between 100-140 km height seen to the south of the station are exactly co-located with the VUV emission feature and the TEC enhancement. Note that the magnitude of the TEC enhancement is approximately 2 TEC units. A layer 40 km thick with uniform density of $5 \times 10^{11} \text{ m}^{-3}$ provides TEC of the right order of magnitude and this is in keeping with the simultaneous radar observations. The density in the F-region is quite low being on the order of $8 \times 10^{10} \text{ m}^{-3}$. Thus with these co-ordinated measurements, we have been able to conclusively prove that the observed TEC enhancements arising from the E-region ionization are due to localized particle precipitation of about 1 keV mean energy which also gives rise to the observed VUV emission features of OI at 135.6 nm. Further, the weak level of amplitude scintillations observed in this case, implies that plasma instabilities which create km-scale irregularities do not have large growth rates in this highly collisional medium. The phase scintillations are probably produced by tens of km-scale irregularities generated directly by the particle precipitation.

SUMMARY

The above sections demonstrate the need for co-ordinated multi-technique measurements if we are to understand the nature of scintillations at high latitudes where a plethora of energy sources exist. Even the E- or F-layer origin of these irregularities is not easily established without the help of other diagnostics. It is obvious that great progress has already been made, particularly, in separating convecting irregularity structures from locally generated ones. Since the tens of km irregularity scales have lifetimes of the order of hours in the dark polar F-region (Vickrey and Kelley, 1982), this makes definitive identification of generation mechanisms even more difficult as irregularities may be found hundreds of km away from their source. With many sophisticated instruments in place and a fair grasp of the problems involved, we should make rapid strides in understanding high latitude scintillations during the upcoming sunspot maximum period.

ACKNOWLEDGMENT

The work at AFGL was supported in part by AFOSR Task 2310C9 and the Defense Nuclear Agency. The work at Emmanuel College was partially supported by AFGL Contract F19628-86-K-0038. The Sondrestrom radar data was made available to us by J.F. Vickrey and C. Valladares.

REFERENCES

Aarons, J., J.P. Mullen, H.E. Whitney, A.L. Johnson, and E.J. Weber, Geophys. Res. Lett., 8, 277, 1981.

Anderson, D.N., J. Buchau, and R.A. Heelis, Origin of density enhancements in the winter polar cap ionosphere, Radio Sci., accepted for publication, 1988.

Baker, K.B., R.A. Greenwald, A.D.M. Walker, P.F. Bythow, L.J. Zanetti, T.A. Potemra, D.A. Hardy, F.J. Rich, and C.L. Rino, J. Geophys. Res., 91, 3130, 1986.

Basinska, E.M., W.J. Burke, Su. Basu, F.J. Rich, and P.F. Fougere, J. Geophys. Res., 92, 3304, 1987.

Basu, S., E. MacKenzie, Su. Basu, E. Costa, P.F. Fougere, H.C. Carlson, and H.E. Whitney, IEEE J. SAC-5, 102, 1987.

Basu, S., E. MacKenzie, and Su. Basu, Radio Sci., Ionospheric constraints on VHF/UHF communications links during solar maximum and minimum periods, Radio Sci., 23, 1988a (in press).

Basu, S., R.W. Eastes, F.P. DelGreco, R.E. Huffman, and Su. Basu, Nightside UV auroral images and VHF/UHF scintillation, Presented at URSI Meeting, Boulder, CO, January, 1988b.

Basu, Su., E. MacKenzie, S. Basu, H.C. Carlson, D.A. Hardy, F.J. Rich, and R.C. Livingston, Radio Sci., 18, 1151, 1983.

Basu, Su., S. Basu, E. MacKenzie, and H.E. Whitney, Radio Sci., 20, 347, 1985.

Basu, Su., S. Basu, C. Senior, D. Weimer, E. Nielsen, and P.F. Fougere, Geophys. Res. Lett., 13, 101, 1986.

Basu, Su., S. Basu, E. MacKenzie, P.F. Fougere, W.R. Coley, N.C. Maynard, J.D. Winnigham, M. Sugiura, W.B. Hanson, and W.R. Hoegy, J. Geophys. Res., 93, 115, 1988a.

Basu, Su., S. Basu, N.C. Maynard, and W.R. Coley, Satellite in-situ measurements of plasma density and electric field structure at high latitudes, Presented at ISRP, Beijing, 1988b.

Basu, Su., S. Basu, E.J. Weber, and W.R. Coley, Case study of polar cap scintillation modeling using DE-2 irregularity measurements at 800 km, Radio Sci., 23, 1988c (in press).

Buchau, J., E.J. Weber, D.N. Anderson, H.C. Carlson, J.G. Moore, B.W. Reinisch, and R.C. Livingston, Radio Sci., 20, 325, 1985.

Carlson, H.C., V.B. Wickwar, E.J. Weber, J. Buchau, J.G. Moore, and W. Whiting, Geophys. Res. Lett., 11, 895, 1984.

Chaturvedi, P.K. and J.D. Huba, J. Geophys. Res., 92, 3357, 1987.

Curtis, S.A., W.R. Hoegy, L.A. Brace, N.C. Maynard, M. Sugiura, and J.D. Winnigham, Geophys. Res. Lett., 9, 997, 1982.

Heelis, R.A., J.K. Lowell, and R.W. Spiro, J. Geophys. Res., 87, 6339, 1982.

Heelis, R.A., J.F. Vickrey, and N.B. Walker, J. Geophys. Res., 90, 437, 1985.

Kelley, H.C., R. Pfaff, K.D. Baker, J.C. Ulwick, R. Livingston, C. Rino, and R. Tsunoda, J. Geophys. Res., 87, 1575, 1982.

Keskinen, M.J. and S.L. Ossakov, J. Geophys. Res., 88, 474, 1983.

Keskinen, M.J., H.C. Mitchell, J.A. Fedder, P. Satyanarayana, S.T. Zalesak, and J.D. Huba, J. Geophys. Res., 93, 137, 1988.

Ossakov, S.L. and P.K. Chaturvedi, Geophys. Res. Lett., 6, 332, 1979.

Rino, C.L., R.C. Livingston, and S.J. Mathews, Geophys. Res. Lett., 5, 1039, 1978.

Rino, C.L., R.C. Livingston, R.T. Tsunoda, R.M. Robinson, J.F. Vickrey, C. Senior, M.D. Cousins, J. Owen, and J.A. Klobuchar, Radio Sci., 18, 1167, 1983.

Tsunoda, R.T., High-latitude F-region irregularities: a review and synthesis, Rev. Geophys. Space Phys., 1988 (in press).

Vickrey, J.F. and H.C. Kelley, J. Geophys. Res., 87, 4461, 1982.

Vickrey, J.F., C.L. Rino, and T.A. Potemra, Geophys. Res. Lett., 7, 789, 1980.

Weber, E.J. and J. Buchau, Geophys. Res. Lett., 8, 125, 1981.

Weber, E.J., J. Buchau, J.G. Moore, J.R. Sharber, R.C. Livingston, J.D. Winnigham, and B.W. Reinisch, J. Geophys. Res., 89, 1683, 1984.

Weber, E.J., R.T. Tsunoda, J. Buchau, R.E. Sheehan, D.J. Strickland, W. Whiting, and J.G. Moore, J. Geophys. Res., 90, 6497, 1985.

Weber, R.J., J.A. Klobuchar, J. Buchau, H.C. Carlson, Jr., R.C. Livingston, O. de la Beaujordiere, M. McCready, J.G. Moore, and G.J. Bishop, J. Geophys. Res., 91, 12, 1986.

6300A ASIP IMAGE

0654 UT

18

06

22 JANUARY 1982
THULE, GREENLAND

Fig. 1. The all-sky imaging photometer image of an ionization patch at Thule.

DE-2 82022 ORBIT # 2550

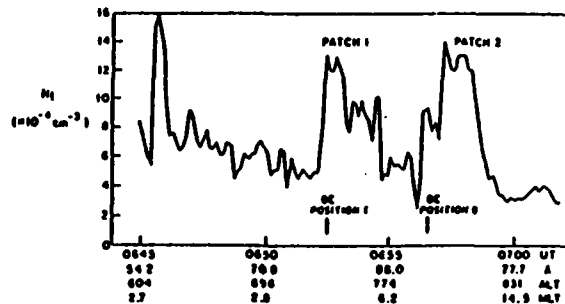


Fig. 2. Two topside ionization patches in the polar cap observed by the DE-2 satellite.

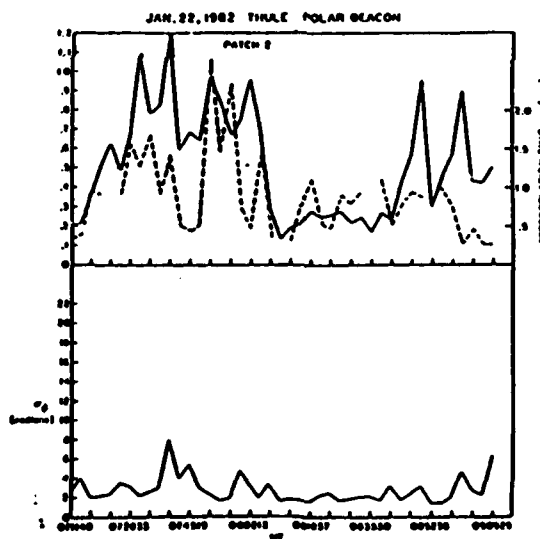


Fig. 3. The intensity scintillation index (S_4), decorrelation time (τ), and phase deviation (σ_ϕ) obtained at 250 MHz during the passage of patch 2 (cf. Fig. 2).

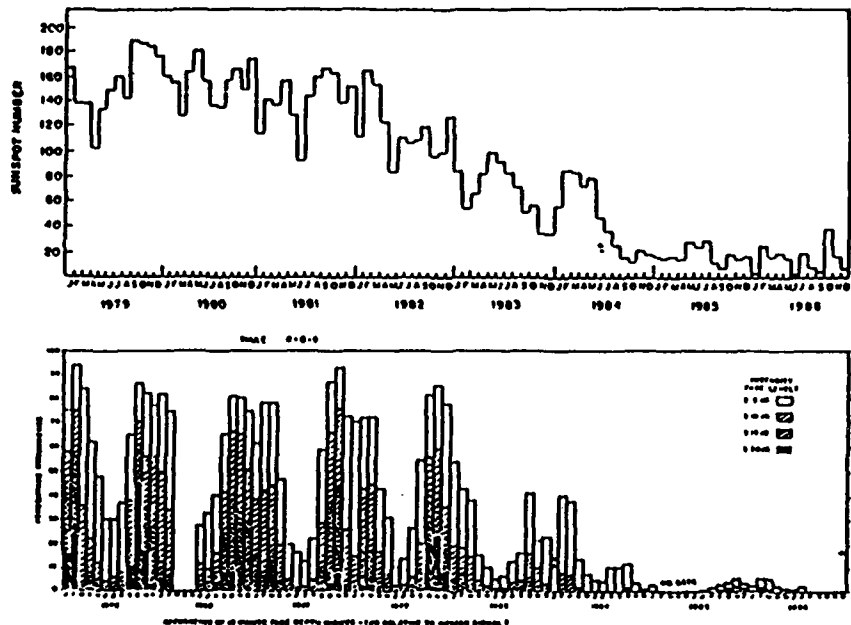


Fig. 4. The variation of sunspot number (top panel) and occurrence at Thule of different intensity fading levels in dB at 250 MHz (bottom panel) during 1979-1986.

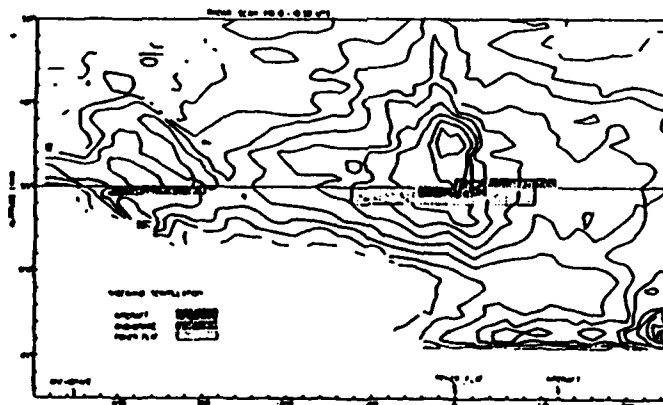


Fig. 5. Contours of ionization density obtained with the Chatanika radar and regions of strong scintillations of Wideband satellite signal.

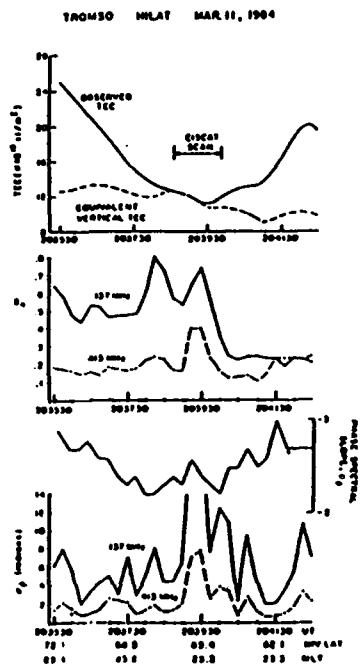


Fig. 6. Illustrates intense scintillations with shallow phase spectral slopes observed in velocity shear regions around 203930 UT without any enhancement of total electron content in the auroral oval.

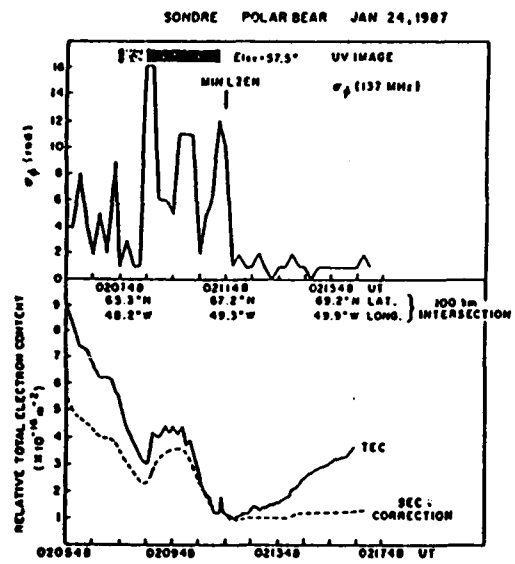


Fig. 7. Detection of strong phase, but marginal intensity, scintillations observed in association with VUV emission and TEC structure.

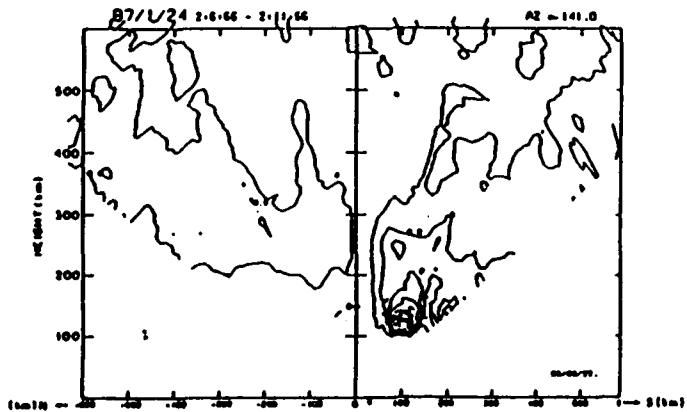


Fig. 8. The elevation scan of Sondrestrom radar identifies a region of enhanced E-region density with the phase scintillation structure in Fig. 7.

Reprinted from Proceedings of Cusp Meeting

SIMULTANEOUS RADAR AND SATELLITE OBSERVATIONS OF THE POLAR CUSP/CLEFT
AT SONDRE STROMFJORD

C.E. Valladares¹, Su. Basu¹, R.J. Niciejewski², and
R.E. Sheehan³

¹Emmanuel College, 400 The Fenway, Boston, MA 02115, USA

²University of Michigan, Ann Arbor, MI 48109, USA

³Boston College, Chestnut Hill, MA 02167, USA

ABSTRACT. On February 9, 1988 a multi-instrument observation of the dayside polar ionosphere was made at Sondre Stromfjord, Greenland as part of a CEDAR high latitude campaign. Our objective was to observe the low altitude signature of the cusp during southward IMF but under fairly quiet ionospheric conditions ($K_p=2$). The HiLat satellite measured in-situ particle precipitation, field-aligned currents and velocity shears in the dayside cusp/cleft, while the VHF beacon on board showed large phase scintillation and saturated intensity scintillation. The phase spectral index was fairly shallow indicating that large power spectral density was present up to scales on the order of 100m. During the spacecraft overflight, the radar was scanning close to the F-region projection of the satellite track. It is the object of this paper to compare the radar measured thermal density, Ti and Te features in the F-region with topside density and velocity structures and particle precipitation characteristics measured in-situ by the satellite at 830 km. The precipitating electron flux measured by HiLat was also input to an ionospheric chemistry model that calculates electron density and temperature profiles for different exospheric temperatures. The modeling results show that most of the features of the radar data may be explained in terms of cleft precipitation, consequent higher exospheric temperatures and enhanced convection.

1. INTRODUCTION

The polar cusp has been defined as the region of very intense and structured particle precipitation with soft magnetosheath-like energy spectra (Heikkila, 1985; Vasylunas, 1985). Typically the average energy of the electrons deposited in the cusp region is below 100 eV (Frank, 1971), and the number flux is on the order of 10^9 - 10^{10} el/cm²-s-ster (Gussenhoven et al., 1985). The location of the low altitude cusp is closely related to the convection pattern which depends on the orientation of the IMF. Potemra et al. (1985) suggested that the velocity reversal and the location of the region 1 current could be used as indicators of the equatorward edge of the cusp. Burch

P. E. Sandholt and A. Egeland (eds.), Electromagnetic Coupling in the Polar Clefts and Caps, 285-298.
© 1989 by Kluwer Academic Publishers.

et al. (1985) pointed out that during southward IMF with By negative, plasma in the pre-noon region convects mostly eastward except for a narrow zone that convects west. This feature was interpreted in terms of a viscous cell. Recently, Bythrow et al. (1988) and Erlandson et al. (1988) have presented evidence that the cusp precipitation region coincides with the region 1 current system, and that the traditional cusp current flows along lines that map to the plasma mantle.

Roble and Rees (1977) developed a numerical model of the high latitude ionosphere to study the response of the plasma parameters when cusp-type or auroral-type electrons are precipitating. They concluded that for soft precipitation and quiet background conditions the F-region electron temperature rises in a few seconds, but plasma density requires a few minutes to build up. Stamnes et al. (1985) pointed out that the solar EUV input may in general contribute substantially to the electron density and temperature in cusp auroras in stations such as Sondrestrom which has a relatively low geographic latitude.

Several efforts have been made earlier to study the polar cusp region at Sondrestrom. Kelly (1985) presented two types of daytime density enhancements observed with the radar. One type has high Te and is associated with region 1 Birkeland currents, and it is located equatorward of the shear reversal (Foster et al., 1985). The other type of Ne increase does not show Te enhancement, instead is related to large plasma flows which transport plasma from lower latitudes.

This paper presents the results of one multi-technique experiment performed at Sondrestrom with the purpose of investigating the following topics: 1) identify the radar signature of the cusp/cleft region in terms of the geophysical parameters measured by the radar, 2) compare the satellite observations at 830 km with the radar measured Ne and Te at F-region altitudes, and 3) determine background conditions for small-scale structuring in the cusp/cleft region. Further, the energy spectra of the precipitating electrons measured in-situ were used as inputs to a model of production rate and ionospheric chemistry, to determine time scales involved in the ionospheric response to the cusp precipitation.

2. OBSERVATIONS

On February 9, 1988 the Sondre Stromfjord radar (66.99°N ; 50.95°W , 74° invariant latitude) was operated in a slow scan mode from 12-15 UT. During the experiment the radar antenna performed elevation scans in the magnetic meridian plane, probing 120 degrees of the sky in 15 minutes. The low scanning speed was selected to provide temperature measurements with small statistical uncertainty and at the same time give adequate latitudinal resolution, 20 km in the F-region. The Hilat satellite crossed the Sondrestrom latitude at 12:55:20 UT. Figure 1 shows the projection of the Hilat track at 350-km altitude, together with the radar coverage at the same altitude. Both, satellite overpass and radar scan, were coordinated to start simultaneously and progress as a north to south motion.

The IMP-8 satellite was in the solar wind on this day. This spacecraft measures the 3 components and the total value of the

FEB. 9, 1988

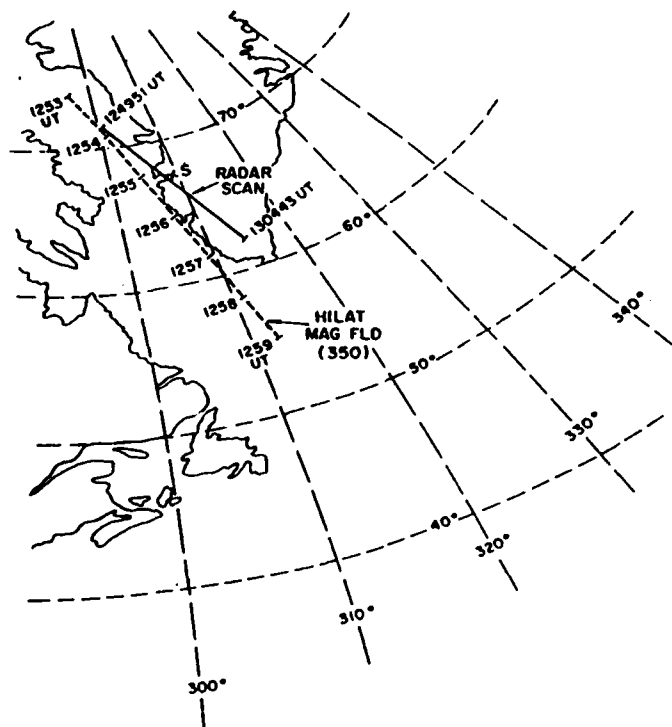


Figure 1. Locations of radar scan and HiLat magnetic field line trace at 350-km altitude for Sondrestrom.

interplanetary magnetic field in the Solar-Magnetospheric coordinate system. During the experiment B_x was positive, the average value was equal to +3 nanoteslas (nT), B_y was negative with a mean value of -2 nT, B_z was mainly negative except for a 15-minute positive excursion from -3 to +1 nT which occurred between 13:10 and 13:25 UT. During the time of the HiLat overpass B_z pointed south. The 3-hour K_p index was 2, the solar sunspot number was 47, and the solar zenith angle (SZA) at Sondrestrom for the time of the measurement was 87° .

2.1. HiLat In-Situ Observations

The HiLat satellite carried both in-situ instrumentation and coherent radio beacons when it was launched in 1983 (Fremouw et al., 1985). The in-situ data will be discussed in this section while the beacon data will be presented in the next section.

Figure 2 shows relevant parameters measured by HiLat during the descending pass of 12:49 UT. Data from 4 instruments on-board HiLat are plotted versus invariant latitude in order to facilitate the comparison with radar data. Panel a shows the number flux measured by the electron flux J sensor (Hardy et al., 1984). The number flux is enhanced almost 2 orders of magnitude between 75.8° and 79° , with respect to the flux level in the polar cap. Panel b is the average energy of the precipitating electrons, as measured by the zenith detector. The mean

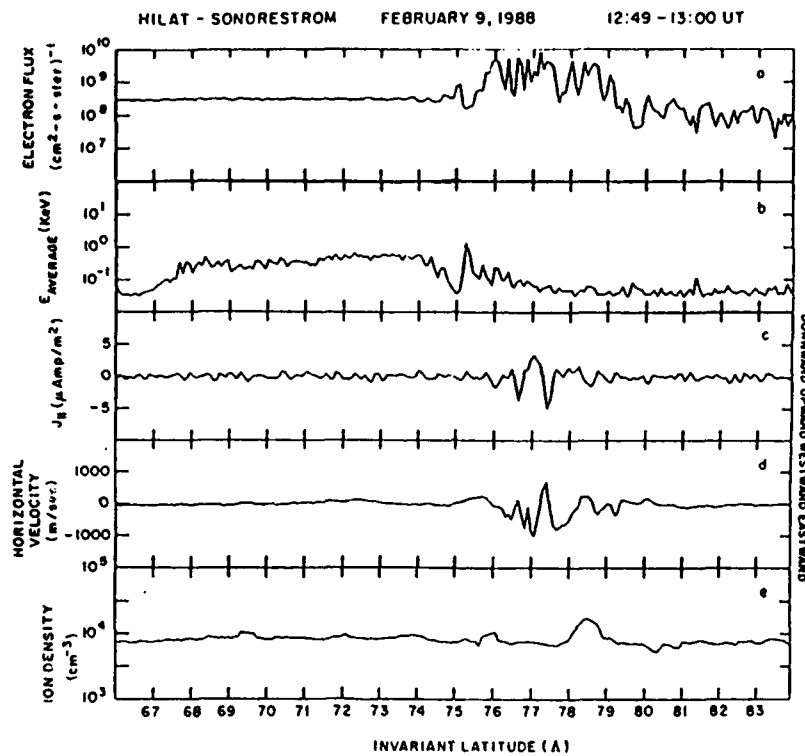


Figure 2. HiLat in-situ data of precipitating electron flux (panel a), average energy of electrons (b), field-aligned current intensity (c), horizontal E-W velocity (d), and ion-density (e) at 830-km altitude.

energy of the electrons is below 100 eV at Λ latitudes greater than 76.5° . The high intensity and softness of the electron precipitation, between 76.5° and $79^\circ\Lambda$ shows that this region represents a classical cusp precipitation (Potemra et al., 1977; Gussenhoven et al., 1985).

The field-aligned current, labeled J_{\parallel} in panel c, was calculated from the eastward component of the magnetic disturbance (Potemra et al., 1984), positive values refer to downward currents. Following the nomenclature used by Bythrow et al. (1988) and very similar to their morning HiLat pass shown in Plate 3, we find an upward directed current which can be identified with the region 2 current with its peak at 76.5° , followed by a downward region 1 current and then an upward traditional cusp current poleward of 77° invariant. The maximum intensity is almost $5 \mu\text{Amp m}^{-2}$ in the cusp.

The crosstrack velocity measured by the IDM on-board HiLat (Rich et al., 1984) is shown in panel d. This velocity is very structured and it is directed primarily eastward between 76° - 79° except for the period between 77.2° and $77.5^\circ\Lambda$, when it turns westward. This small portion of westward velocities seems to be co-located with the cusp current system.

The ion number density measured by the RPA is shown in panel e of Figure 2. N_i is uniform except for the factor of 2 enhancement in the poleward side of the cleft/cusp region, between 78.1° and $78.9^\circ\Lambda$. This density was measured at the satellite altitude (830 km). In a later section, we comment on the implications of this measurement and the N_i

values obtained with the radar.

The RAM velocity from the RPA and the crosstrack velocity measured by the IDM were combined to resolve the plasma velocity vector. The RAM velocity was corrected to compensate for the possible charging of the spacecraft and the uncertainty in the derivation of the RAM velocity ($300-400 \text{ ms}^{-1}$) to provide an agreement with the radar measured drift velocity. Figure 3 shows the flow vector along the satellite trajectory. At invariant latitudes below 75° the plasma velocity is very small as is typical for subauroral latitudes. The invariant latitude range between 76° and 78° is a region with a velocity magnitude almost 1 km and directed northeast. At 77.2° the velocity reverses to a westward convection for about 30 km. This convection pattern is common for B_z southward and B_y negative IMF conditions. Burch et al. (1985) have indicated that limited reversals from east to west then back to east are indicative of the presence of a viscous cell. North of the cusp/cleft region the plasma velocity is eastward and less than 150 ms^{-1} .

HILAT ION DRIFT VELOCITIES

FEBRUARY 9, 1988 1249-1300 UT 1 km/sec —————

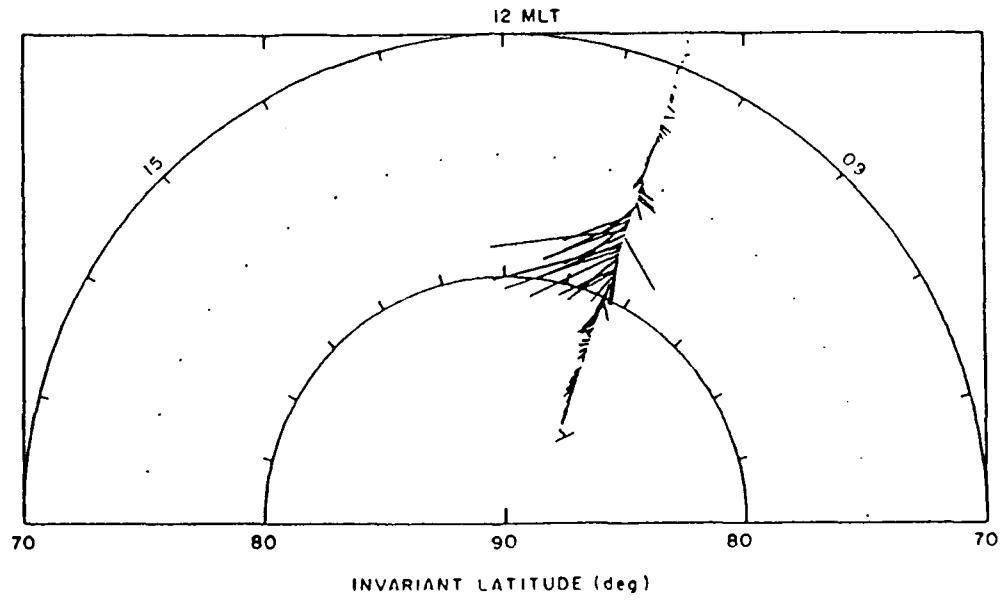


Figure 3. Vector velocities derived by combining the Hilat N-S velocity from the retarding potential analyzer and the E-W velocity measured by the ion-driftmeter.

2.2. Scintillations Using Hilat

Phase and amplitude scintillations are available from the Hilat satellite at 138 and 413 MHz. Total electron content measurements are also available along the slant path between the satellite and the ground station. The F-region of the ionosphere generally introduces the largest perturbation in the signal propagating from the satellite. We

thus show in Figure 4, the 350-km intersection of the ray path from the satellite together with the 350-km HiLat field line track (a part of which was shown in Figure 1) for comparison of the scintillation/TEC behavior in respect to the in-situ data.

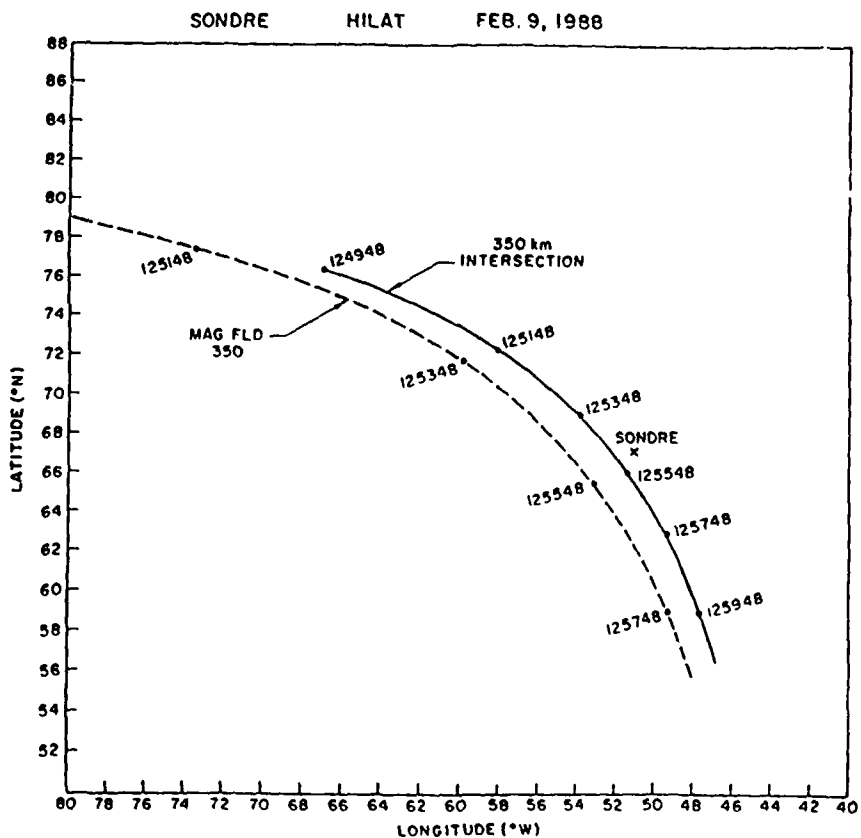


Figure 4. Locations of the ionospheric intersection of the ray path from HiLat and its magnetic field line trace, both referred to 350-km altitude for Sondrestrom.

Figure 5 shows the phase and amplitude scintillations obtained at 137 and 413 MHz from the HiLat satellite. A prominent increase in these parameters is observed between 1251:48-1254:18 UT. In particular, the large amplitude scintillation is noteworthy. The dotted line shows the 137-MHz amplitude scintillation corrected for the effect of the slant path. (The data at elevation angles less than 20° are contaminated by possible multipath effects and hence not considered.) The above time interval corresponds to an invariant latitude interval of 80.2° - 75.8° which encompasses the region where both the largest number flux of precipitated electrons are seen (Panel a of Figure 2) and the largest structured velocities are observed (Figure 3). In addition, the spectral analysis of the phase scintillation data (not shown) yields spectral indices of the order of -2.5. This together with the large magnitude of the phase scintillation index indicates larger power spectral densities at short scales (<1 km) which is consistent with the existence of a relatively high level of amplitude scintillation. The

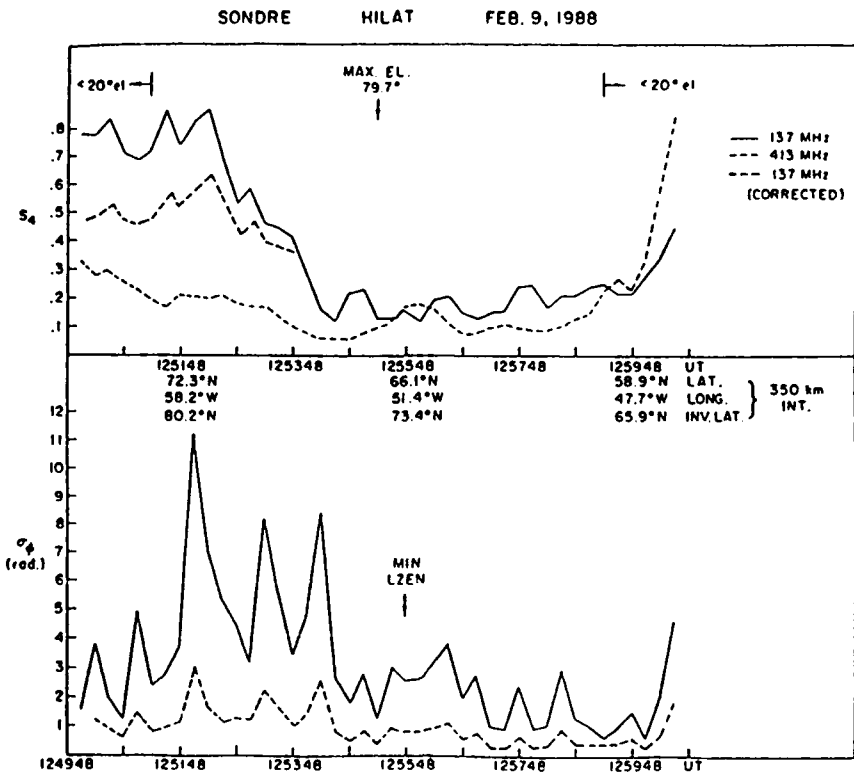


Figure 5. Phase and amplitude scintillations observed by HiLat at 137 and 413 MHz.

position along the orbit of this near-overhead pass where the raypath was aligned with the local magnetic L-shell is indicated as MIN LZEN. Virtually no geometrical enhancement was seen, further confirming the hypothesis that the irregularity region was confined to the cusp/cleft region and did not extend to the overhead location of the station. The equivalent vertical total electron content in the cusp (also not shown) exhibited no significant variations with a value of approximately 3.5×10^{12} el cm $^{-2}$ which is consistent with the integration of the radar profiles in that region.

2.3. Radar Observations

Figure 6 presents the temperature corrected densities for the elevation scan executed simultaneously with the HiLat pass. The maximum number density is 3×10^5 el cm $^{-3}$. This region of high Ni is located in the southern boundary of the radar field of view with the plasma density decreasing linearly for higher values of SZA at positive northern distances. At 150 km north of the radar Ni reaches its lowest value, 1.8×10^5 el cm $^{-3}$. However, at a northern distance of 350 km the density increases to a value of 2.6×10^5 el cm $^{-3}$. Figure 6 shows only a hint of a region of large density while the previous scan, not shown here, and obtained a few minutes earlier, displays better the small region of higher density.

The electron temperature Te and the Te error bars are plotted in

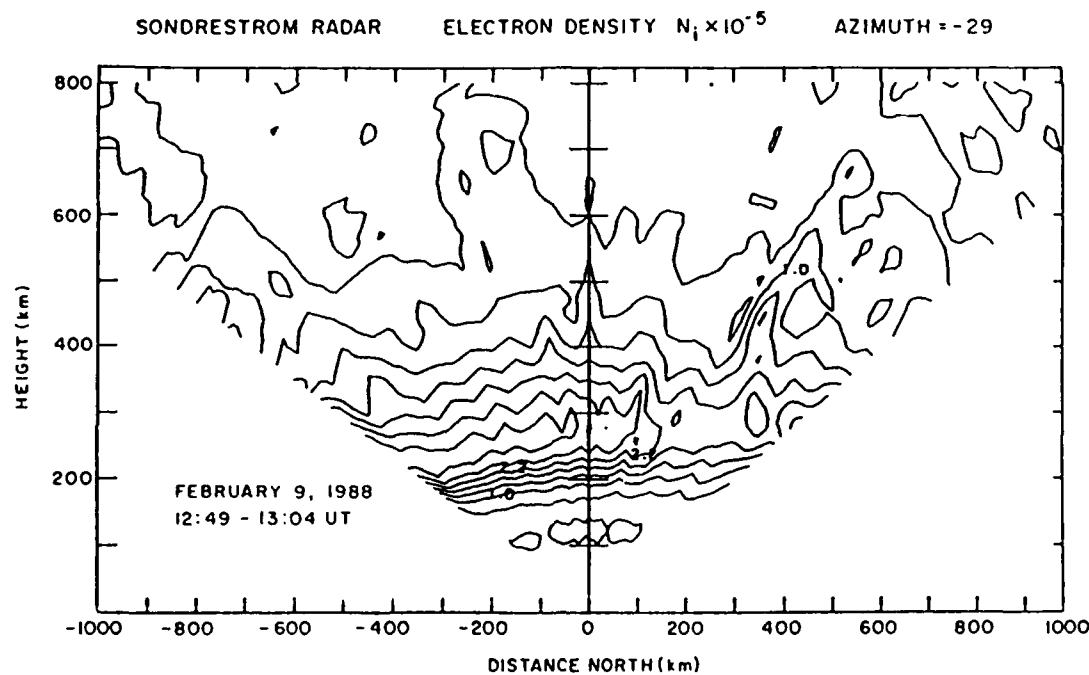


Figure 6. Elevation scan of ionospheric densities made by the Sondrestrom radar between 12:49-13:04 UT on February 9, 1988.

Figure 7. Te slowly increases for larger southern distances from Sondrestrom. This is due to more intense solar illumination at slightly lower SZA. At about 200 km north of the radar site, F-region Te increases from 2200° to 3300° K, probably in response to the precipitation measured by HiLat. The F-region Ti, though not shown here, is also enhanced at 300 km north of the radar. Ti rises significantly from 1000° to 1500° K in that region. The radar data implies that for this day the cusp/cleft region consisted of two well-defined segments: the equatorward side with low Ni and high Te, and the poleward part with high Ni and high Te.

3. MODEL RESULTS

To study the ionospheric response to the flux of soft electrons, we have used a numerical model which starts with the energy spectra of the precipitating electrons measured in-situ by HiLat and then calculates the electron temperature and the density profile of 14 ionospheric species (Strickland et al., 1976; Weber et al., 1985, 1988).

Our 1-dimensional ionospheric chemistry code has 2 distinct parts: part 1 assumes that the incident flux is isotropic at an upper altitude boundary and generates production rate and electron plasma heating profiles; part 2 uses the results from part 1, includes local chemistry, O^+ diffusion, and electron heat conduction. The MSIS 86 model was used to provide the density of the atmospheric neutral constituents.

Figure 8 shows two electron spectra measured by the J-sensor during the HiLat traversal of the cusp/cleft region, both spectra correspond to 4.5 second averages. Model 1 (panel a) was obtained at 1254:30 UT,

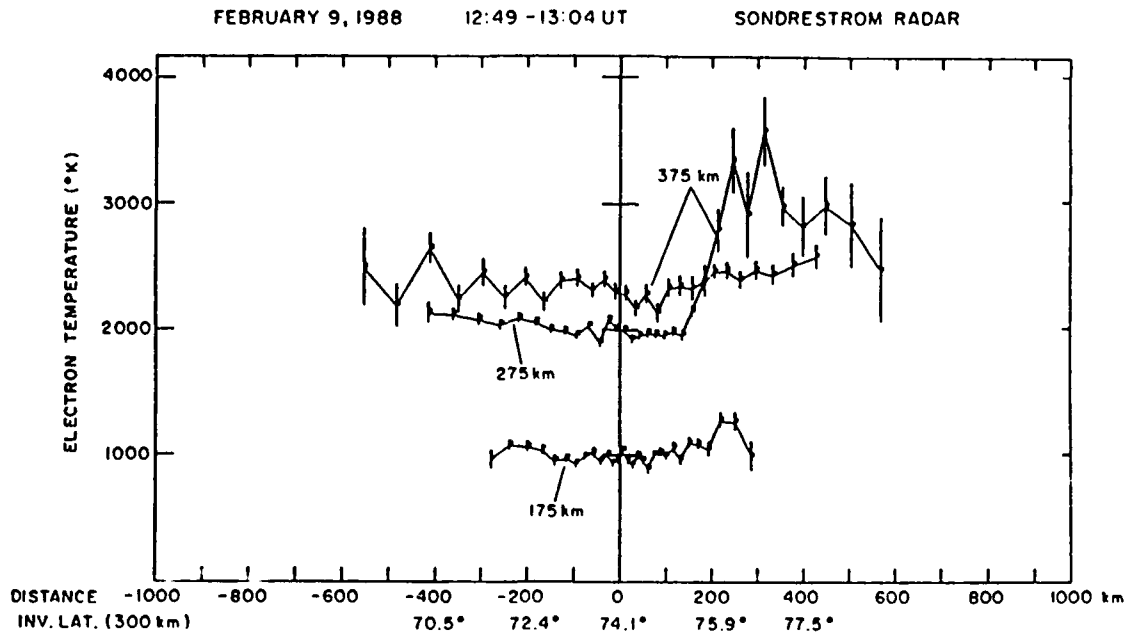


Figure 7. Electron temperatures at 3 altitudes measured by the Sondrestrom radar together with the density measurements shown in Figure 6.

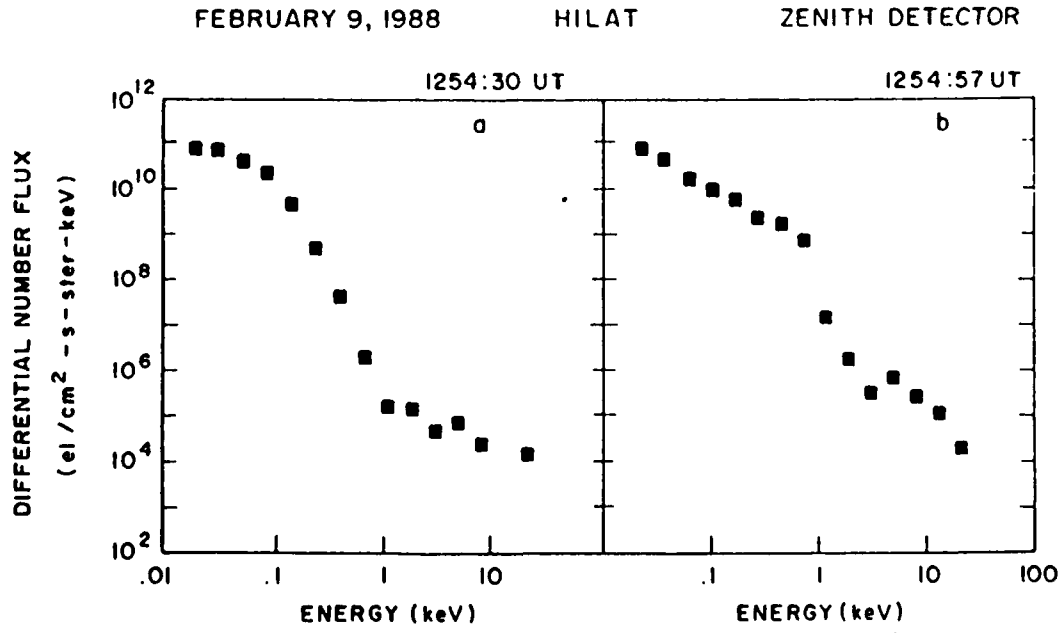


Figure 8. Two spectra of precipitating electrons measured by HiLat. The spectra in panel a was obtained in the cusp proper, while that in panel b was from the cleft region.

corresponding to 77.6 invariant latitude, when the spacecraft was in the cusp region. The energy flux was .32 erg/cm²-s-ster. The spectra of panel a does not show significant acceleration. The spectra of panel b (1254:57 UT, 75.8°A, .76 erg/cm²-s-ster), on the contrary, indicates electrons that have been accelerated to 1 keV. This is considered a typical sub-cusp or cleft electron flux. The cleft spectrum was found to persist for 20s during which the satellite traversed 160 km, whereas the cusp precipitation was observed over a broader region of 240 km.

Figure 9 shows model results using the electron spectra of panel b and two different exospheric temperatures. Each situation starts with the indicated initial electron density profile and then runs as if the flux were precipitating unchanged for 2 minutes. The results indicate that higher exospheric temperature produces increased densities at altitudes greater than 300 km and reduced densities lower down.

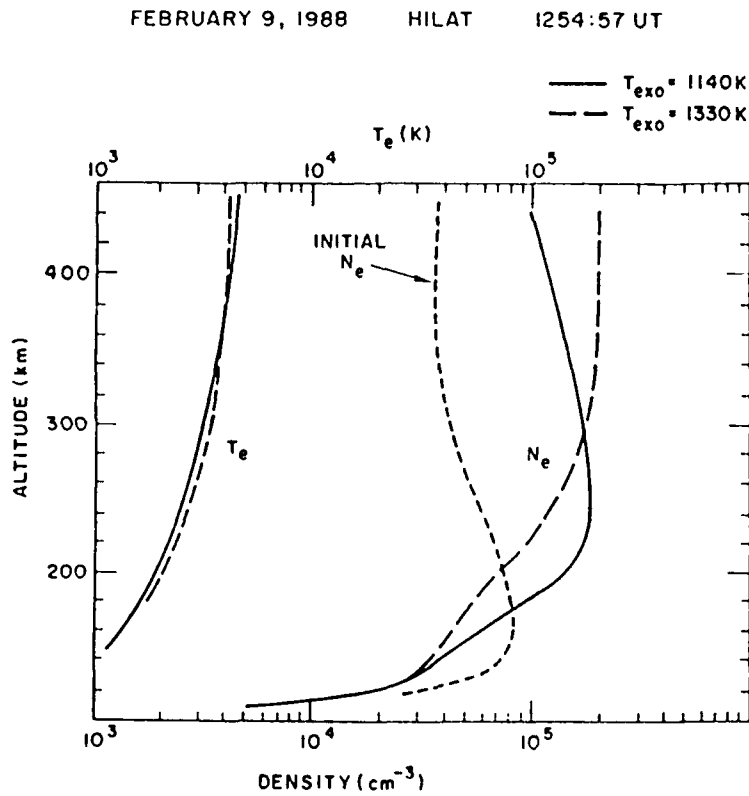


Figure 9. Model results of electron density for electron spectrum shown in Figure 8b. Two different exospheric temperatures are used.

Calculated T_e is less affected by the exospheric temperature variation but is somewhat higher than indicated by the radar measurements. The best agreement with corresponding radar densities is with the model profile for $T_{\text{exo}} = 1140^\circ\text{K}$ which produces a peak density of 2×10^5 at 240 km. Outflowing O^+ ions can also affect the number density profile. We tested this hypothesis employing a range of up- and down-going flows in our model and found that this factor had a relatively small effect on the density, particularly at altitudes below 400 km. While model

results for the more typical cusp spectrum of Figure 8a are not shown, it is important to note that the model had to be run for 5 minutes in order to obtain a peak density of $2 \times 10^5 \text{ cm}^{-3}$. It should also be considered that another source of ionization in the cusp is precipitating ions (Bythrow et al., 1988). However, since HiLat does not measure the ions, we considered electrons only, which will underestimate the total ionization input.

4. DISCUSSION

One of the most significant results of this joint satellite and radar study shows that it is possible to observe a depletion in the pre-noon F-region ionosphere in conjunction with intense particle precipitation (which causes enhanced Te) and rapid eastward convective flows. It seems probable that these rapid eastward flows convect less dense plasma from the downside polar region which is in darkness at this time of the year. The model studies show that steady precipitation over approximately 2 minutes is necessary for the desired density buildup in the ionosphere. Within this time the poleward flow of approximately 1 km s^{-1} will convect plasma more than 1° poleward. Since the cleft-type of precipitation occurred over a region of 160-km latitudinal extent, the convecting plasma was within the precipitation region for the required length of time. The density buildup is seen approximately 1° poleward of the equatorward edge of the cleft precipitation consistent with the model results. The F-region depletion is probably not a result of an exospheric temperature increase alone as the model results indicate that this would probably have caused enhanced densities at the satellite altitude which were not observed in this region. The region poleward of the depletion where an enhancement is observed both in the F-region by the radar and in the topside by the satellite seems to be a consequence of the local particle precipitation, poleward convection of the plasma subjected to more intense precipitation, and the increased Te and Ti which causes an increased scale height of the plasma in the topside.

The small-scale irregularities as diagnosed by the scintillation technique are found in the region of the largest particle fluxes and structured velocities. The same finding was reported by Baker et al. (1986) in a case study at Sondrestrom utilizing data from HiLat and the Goose Bay HF radar. Unfortunately, they did not have support from the incoherent scatter radar there so that they hypothesized a density enhancement in the F-region and the existence of the generalized gradient drift instability based on the satellite precipitation results alone. However, we have shown here that intense precipitation can actually be co-located with a depletion in density in the F-region so that one has to carefully investigate appropriate conditions for the small-scale irregularity generation. With the observed poleward drift, it is only the poleward gradient seen by the radar north of 77° invariant which should be unstable to the gradient drift instability. However, irregularities are observed starting from 75.8° in a region which should be stable to this mechanism. Other case studies done by Basu et al. (1986, 1988) have shown the importance of velocity shears

and field-aligned currents in generating scintillation producing irregularities. We would thus like to suggest one of the transverse-shear driven (Keskinen et al., 1988) or shear-cum-field-aligned current driven modes (Nishikawa et al., 1988) as plausible candidates for the small-scale irregularity generation. Further studies are being planned in the summer and winter polar cusp for more stringent tests of these mechanisms.

Finally, we would like to point out that it has been suggested in the literature that the spectra of the incoherent scatter (IS) signal can be distorted by velocity shears if they are unresolved within the probed volume (Swartz et al., 1988). Field-aligned currents may also alter the returned signal producing asymmetries in the spectra (Foster et al., 1988). In order to determine the level of contamination of our radar measurements we performed a careful examination of the incoherent scatter spectra, looking for deviations from the typical double-humped shape. We found that the anomalies were always smaller than the statistical uncertainties.

ACKNOWLEDGMENTS

We wish to thank F.J. Rich, R.A. Heelis, and D.A. Hardy for making the HiLat in-situ data available to us and for many useful discussions. R.A. Livingston and R.P. Lepping provided, respectively, the HiLat beacon data and the IMP-8 IMF data. The work at Emmanuel College was supported by NSF Grant ATM-8715445 and AFGL Contract F19628-86-K-0038.

REFERENCES

Baker, K.B., Greenwald, R.A., Walker, A.D.M., Bythrow, P.F., Zanetti, L.J., Potemra, T.A., Hardy, D.A., Rich, F.J., and Rino, C.L. (1986) 'A case study of plasma processes in the dayside cleft', *J. Geophys. Res.* 91, 3130.

Basu, S., Basu, S., Senior, C., Weimer, D., Nielsen, E., and Fougere, P.F. (1986) 'Velocity shears and sub-km scale irregularities in the nighttime auroral F-region', *Geophys. Res. Lett.* 13, 101.

Basu, S., Basu, S., MacKenzie, E., Fougere, P.F., Coley, W.R., Maynard, N.C., Winningham, J.D., Sugiura, M., Hanson, W.B., and Hoegy, W.R. (1988) 'Simultaneous density and electric field fluctuation spectra associated with velocity shears in the auroral oval', *J. Geophys. Res.* 93, 115.

Burch, J.L., Reiff, P.H., Menietti, J.D., Heelis, R.A., Hanson, W.B., Shawhan, S.D., Shelley, E.G., Sugiura, M., Weimer, D.R., and Winningham, J.D. (1985) 'IMF By-dependent plasma flow and Birkeland currents in the dayside magnetosphere, 1. Dynamics Explorer observations', *J. Geophys. Res.* 90, 1577.

Bythrow, P.F., Potemra, T.A., Erlandson, R.E., Zanetti, L.J., and Klumpar, D.M. (1988) 'Birkeland currents and charged particles in the high-latitude prenoon region: A new interpretation', *J. Geophys. Res.* 93, 9791.

Erlandson, R.E., Zanetti, L.J., Potemra, T.A., Bythrow, P.F., and Lundin, R. (1988) 'IMF By-dependence of region 1 Birkeland current near noon', *J. Geophys. Res.* 93, 9804.

Foster, J.F., Holt, J.M., Kelly, J.D., and Wickwar, V.B. (1985) 'High-resolution observations of electric fields and F-region plasma parameters in the cleft ionosphere', in J.A. Holtet and A. Egeland (eds.), *The Polar Cusp*, NATO ASI Ser. C; Vol. 145, D. Reidel, Dordrecht, p. 349.

Foster, J.C., del Pozo, C., Groves, K., and St. Maurice, J.-P. (1988) 'Radar observations of the onset of current driven instabilities in the topside ionosphere', *Geophys. Res. Lett.* 15, 160.

Frank, L.A. (1971) 'Plasma in the Earth's polar magnetosphere', *J. Geophys. Res.* 76, 5202.

Fremouw, E.J., Carlson, H.C., Potemra, T.A., Bythrow, P.F., Rino, C.L., Vickrey, J.F., Livingston, R.L., Huffman, R.E., Meng, C.I., Hardy, D.A., Rich, F.J., Heelis, R.A., Hanson, W.B., and Wittwer, L.A. (1985) 'The HiLat satellite mission', *Radio Sci.* 20, 416.

Gussenhoven, M.S., Hardy, D.A., and Carovillano, R.L. (1985) 'Average electron precipitation in the polar cusps, cleft and cap', in J.A. Holtet and A. Egeland (eds.), *The Polar Cusp*, NATO ASI Ser. C; Vol. 145, D. Reidel, Dordrecht, p. 85.

Hardy, D.A., Huber, A., and Pantazis, J.A. (1984) 'The electron flux J sensor for HiLat', *The Johns Hopkins/APL Tech. Digest* 5, 125.

Heikkila, W.J. (1985) 'Definition of the cusp', in J.A. Holtet and A. Egeland (eds.), *The Polar Cusp*, NATO ASI Ser. C; Vol. 145, D. Reidel, Dordrecht, p. 387.

Kelly, J.D. (1985) 'Incoherent-scatter radar observations of the cusp', in J.A. Holtet and A. Egeland (eds.), *The Polar Cusp*, NATO ASI Ser. C; Vol. 145, D. Reidel, Dordrecht, p. 337.

Keskinen, M.J., Mitchell, H.G., Fedder, J.A., Satyanarayana, P., Zalesak, S.T., and Huba, J.D. (1988) 'Nonlinear evolution of the Kelvin-Helmholtz instability in the high-latitude ionosphere', *J. Geophys. Res.* 93, 137.

Nishikawa, K.-I., Ganguli, G., Lee, Y.C., and Palmadesso, P.J. (1988) 'Simulation of electrostatic ion instabilities in the presence of parallel currents and transverse electric fields', *Proceedings of MIT Workshop on Polar Cap Dynamics and High Latitude Ionospheric Turbulence*.

Potemra, T.A. and Zanetti, L.J. (1985) 'Characteristics of large-scale Birkeland currents in the cusp and polar regions', in J.A. Holtet and A. Egeland (eds.), *The Polar Cusp*, NATO ASI Ser. C; Vol. 145, D. Reidel, Dordrecht, p. 203.

Potemra, T.A., Peterson, W.K., Doering, J.P., Bostrom, C.O., McEntire, R.W., and Hoffman, R.A. (1977) 'Low-energy particle observations in the quiet dayside cusp from AE-C and AE-D', *J. Geophys. Res.* 82, 4765.

Potemra, T.A., Bythrow, P.F., Zanetti, L.J., Mobley, F.F., and Scheer, L. (1984) 'The HiLat magnetic field experiment', *The Johns Hopkins/APL Tech. Digest* 5, 120.

Rich, F.J., Heelis, R.A., Hanson, W.B., Anderson, P.B., Holt, B.J., Harmon, L.L., Zuccaro, D.R., Lippincott, C.R., Girouard, D., and Sullivan, W.P. (1984) 'Cold plasma measurement on HiLat', The Johns Hopkins/APL Tech. Digest 5, 114.

Roble, R.G. and Rees, M.H. (1977) 'Time-dependent studies of the aurora: Effects of particle precipitation on the dynamic morphology of ionospheric and atmospheric properties', Planet. Space Sci. 25, 991.

Stamnes, K., Rees, M.H., Emery, B.A., and Roble, R.G. (1985) 'Modelling of cusp auroras: The relative impact of solar EUV radiation and soft electron precipitation', in J.A. Holtet and A. Egeland (eds.), The Polar Cusp, NATO ASI Ser. C; Vol. 145, D. Reidel, Dordrecht, p. 137.

Strickland, D.J., Book, D.L., Coffey, T.P., and Fedder, J.A. (1976) 'Transport equation techniques for the deposition of auroral electrons', J. Geophys. Res. 81, 2755.

Swartz, W.E., Providakes, J.F., Kelley, M.C., and Vickrey, J.F. (1988) 'The effect of strong velocity shears on incoherent scatter spectra: A new interpretation of unusual high latitude spectra', Geophys. Res. Lett. 15, 1341.

Vasyliunas, V.M. (1985) 'Summary', in J.A. Holtet and A. Egeland (eds.), The Polar Cusp, NATO ASI Ser. C; Vol. 145, D. Reidel, Dordrecht, p. 411.

Weber, E.J., Tsunoda, R.T., Buchau, J., Sheehan, R.E., Strickland, D.J., Whiting, W., and Moore, J.G. (1985) 'Coordinated measurements of auroral zone plasma enhancements', J. Geophys. Res. 90, 6497.

Weber, E.J., Kelley, M.C., Ballenthin, J.O., Basu, S., Carlson, H.C., Fleischman, J.R., Hardy, D.A., Maynard, N.C., Pfaff, R.F., Rodriguez, P.A., Sheehan, R.A., and Smiddy, M. (1988) 'Rocket measurements within a polar cap arc: plasma, particle, and electric circuit parameters', J. Geophys. Res., in press.

ATTACHMENT 8

To appear in SPI Conference Proceedings and Reprint Series, Vol. 8 (1989)

COORDINATED OBSERVATIONS OF HIGH LATITUDE IONOSPHERIC TURBULENCE

Santimay Basu

Air Force Geophysics Laboratory, Hanscom AFB, MA 01731

Sunanda Basu and C.E. Valladares

Emmanuel College, Boston, MA 02115

E.J. Weber, J. Buchau, and G.J. Bishop

Air Force Geophysics Laboratory, Hanscom AFB, MA 01731

B.W. Reinisch

University of Lowell, Lowell, MA 01853

ABSTRACT

A coordinated data set comprised of scintillation, ionosonde, incoherent scatter radar and optical measurements obtained on two nights during the CEDAR/WITS campaign of February, 1988 was selected for the study of two distinct classes of high latitude plasma turbulence. Under IMF B_z northward conditions, the polar cap arc detected by the all-sky imaging photometer (ASIP) in this phase of low solar activity (SSN = 40) was found to be associated with a total electron content enhancement of only $2 \times 10^{16} \text{ m}^{-2}$ and weak amplitude scintillations ($S_4 \approx 0.35$) at 250 MHz. The photometer and scintillation measurements indicated that in addition to the dawn to dusk motion of 200 ms^{-1} in the inertial frame, there existed enhanced plasma motion of about 400 ms^{-1} along the arc.

The second data set conforming to IMF B_z southward condition showed the existence of ionization patches in the polar cap and their anti-sunward motion towards the auroral oval. The polar cap patches detected deep within the polar cap with electron contents as large as $10 \times 10^{16} \text{ m}^{-2}$ caused 15 dB scintillations at 250 MHz. These patches detected close to the auroral oval also caused strong scintillations which indicated that the patches get continually structured during their convection through the winter polar cap.

INTRODUCTION

Manifestation of turbulence is so ubiquitous in the high latitude ionosphere that in recent years a great deal of attention has been focused on understanding the various ways in which such turbulence is generated. It is well recognized now that the interplanetary magnetic field (IMF) has a profound influence on the large and small-scale structuring of the high latitude ionosphere. At the present time a rudimentary framework exists in which to organize the large scale structuring (~hundreds of km) in the very high latitude ionosphere-magnetosphere (I-M) system on the basis of the north-south component, namely, B_z of the IMF. Using sensitive all-sky imaging photometers (ASIPs) located deep within the

dark winter polar cap, it has been shown that when IMF B_z is negative, large (~ 1000 km) regions of convecting density enhancement known as patches are observed, whereas, when IMF B_z is positive, sun-aligned arcs are found to populate the polar cap (cf. Fig. 1 of Buchau et al. (1985) [1]). That both patches and arcs are associated with small-scale density and electric field turbulence (\sim kms to m) has been determined by a variety of *in situ* and remote sensing techniques [2]. It should be noted that while sun-aligned arcs in the polar cap are generally observed for B_z north conditions, auroral oval arcs are observed under both polarities of the IMF with the oval arcs being observed more frequently and being associated with larger energy fluxes for B_z south conditions. Taking a very broad overview of the turbulence characteristics associated with patches and arcs, one may state that in the former case the turbulence is caused by an interchange instability process, while in the latter case the turbulence is generated by some combination of particle precipitation, field-aligned currents and sheared plasma flows.

The multi-technique CEDAR/WITS high latitude campaign of February 1988 offered a unique opportunity to further investigate the structuring of patches and arcs. Co-ordinated measurements carried out with the Sondrestrom Incoherent scatter radar, all-sky imagers, orbiting and quasi-stationary satellites and ionosondes allowed us to present a study of these two distinct classes of large scale plasma structures and associated turbulence in the polar cap and auroral oval.

RESULTS

Polar Cap Arc

On February 11, 1988 a prolonged period of northward IMF was obtained between 01-06 UT as illustrated in Fig. 1. We shall show that this period was marked by the occurrence of sun-aligned polar cap arcs [3].

Fig. 2 shows the geometry of measurements with various radio diagnostics. At the ground station in Thule, marked TH (CGL 86°), 1.2 and 1.5 GHz signals from the Global Positioning Satellite (GPS) and 250 MHz transmissions from the Polar Beacon Satellite (PBS) were continuously monitored. The locus of the 350 km intersection point of the raypaths to the PBS and GPS satellites are indicated in the diagram. During this campaign, the AFGL Airborne Ionospheric Observatory was parked at Thule and it was used to perform ionospheric sounding and all sky imaging photometer (ASIP) measurements. The ASIP detected a polar cap arc extended in the noon-midnight direction and drifting towards dusk. Fig. 2 also shows the configuration of the arc (shaded lines) at 0539 UT.

Figs. 3a and b show a sequence of four 6300 Å images recorded at Thule from 0531 to 0557 UT on February 11, 1988.

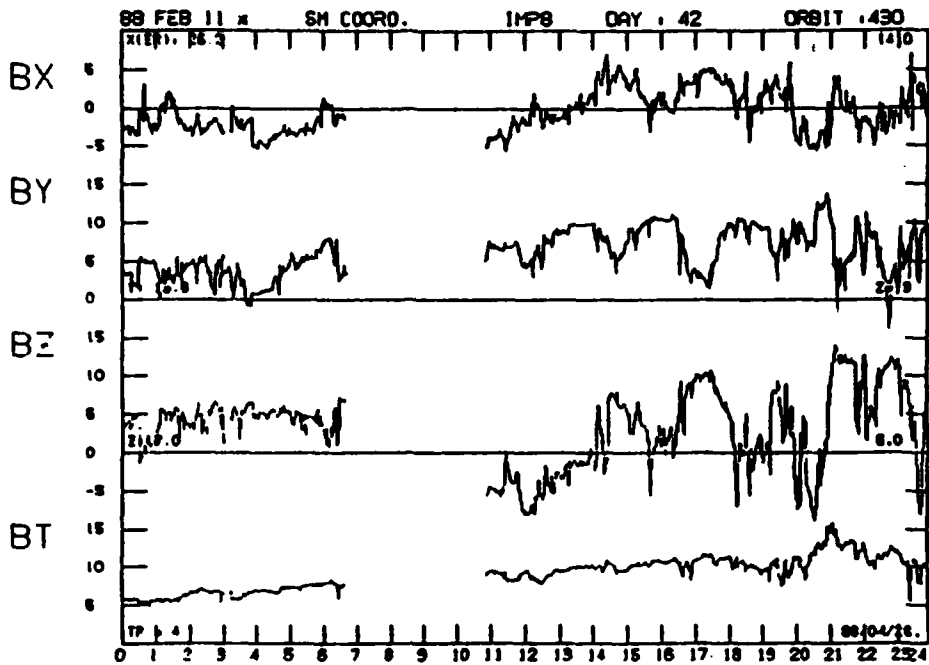


Figure 1. Interplanetary Magnetic Field (IMF) obtained by IMP-8 on February 11, 1988.

The original all-sky lens (180° field of view) images have been transformed to a geographic projection, and the polar cap is displayed as if viewed from above. In order to perform this transformation, an altitude of 250 km was assumed for the 6300 Å emission height. Geographic latitudes from 65° to 80°N are shown at 5° intervals, and geographic longitudes from 30° to 105°W are shown at 15° intervals. Two arcs are visible in the 0531 UT image of Fig. 3a, a faint arc almost through the zenith of Thule and a brighter arc toward the east. Both arcs are nominally aligned in the geographic north-south direction. At this Universal Time this is also the approximate orientation of the CG noon-midnight meridian. By 0539 UT both arcs drifted toward the west, the weaker arc faded, and the brighter arc became even more intense and developed a fold structure. In the 0550 UT image of Fig. 3b, only the brighter, structured arc remained. During the interval 0531-0550 UT, the dawn to dusk (westward) drift speed is derived to be approximately 300-350 m/s in the geographic (co-rotating) frame which is equivalent to 180-230 m/s in the inertial frame. By 0557 UT the arc had drifted even further west, however, the arc faded and was below the ASIP detection threshold after this time. The location of the 350 km sub-ionospheric point from Thule to the Polar Beacon satellite has been indicated in Fig. 2. The

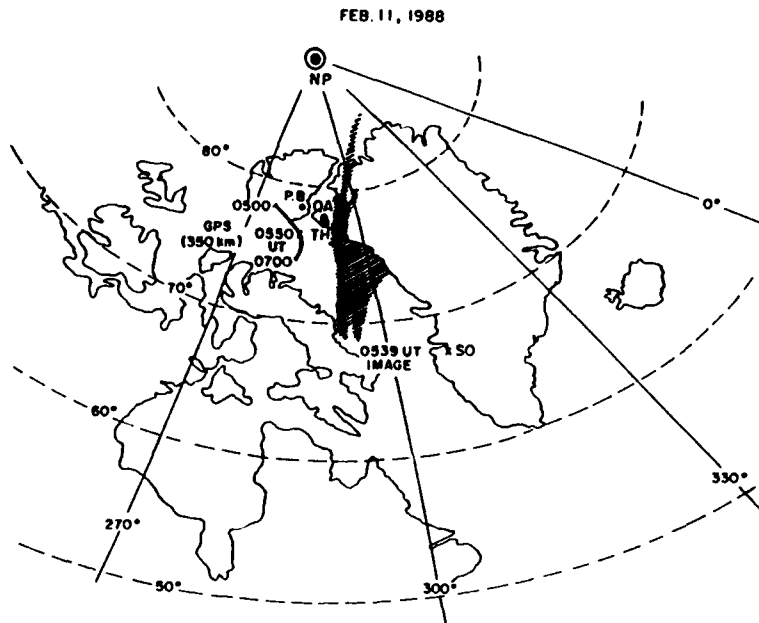


Figure 2. Geometry of observations on February 11, 1988 indicating the ground stations at Thule (TH), Qaanaaq (QA), and Sondre Stromfjord (SO) and the locus of 350 km intersection for the Global Positioning Satellite (GPS) and the Polar Beacon Satellite (PBS) as viewed from Thule. The shaded region represents the polar cap arc at 0539 UT.

arc drifted into the raypath between 0539 and 0550 UT, in good agreement with the onset of scintillation at 0545 UT.

Fig. 4 shows the chart record of amplitude scintillations observed on the 250 MHz link with the PBS. It indicates that the maximum value of 250 MHz scintillations attained was 6.6 dB at about 0550 UT and the duration of the scintillation event did not exceed 12 minutes. Combining with the drift speed of 200 ms^{-1} in the inertial frame, we obtain that the arc associated irregularities occupied a spatial length of 150 km in the dawn to dusk direction.

The signal from the PBS satellite was also received by a computer controlled phase stable receiver which measured both amplitude and phase scintillations. The amplitude scintillation index, S_4 , defined as the standard deviation of amplitude fluctuations normalized to the average signal level, is plotted in Fig. 5. The figure also shows the standard deviation of phase fluctuations (σ_ϕ) computed with a detrend interval of 82 sec. The region of concentrated amplitude and phase fluctuations around 0550 UT which was caused by the arc may be noted. The amplitude scintillation was rather weak ($S_4 = 0.35$) as we also noted from Fig. 4. This implies low values of integrated electron density deviation within the arc.

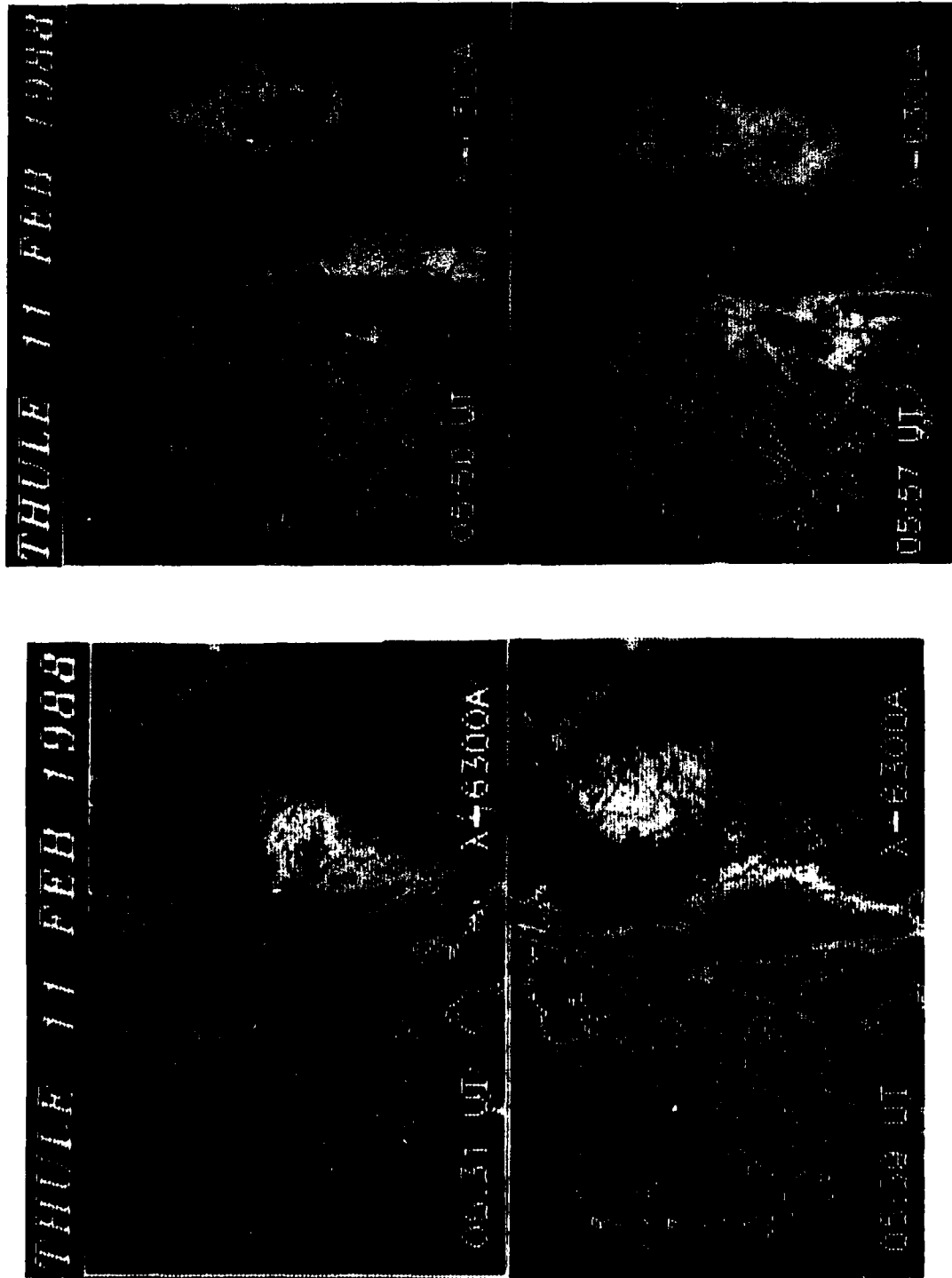


Figure 3. 6300 Å false color ASIP images of a sun-aligned polar cap arc obtained at Thule on Feb 11, 1988.

a. Images at 0531 and 0539 UT . b. Images at 0550 and 0557 UT

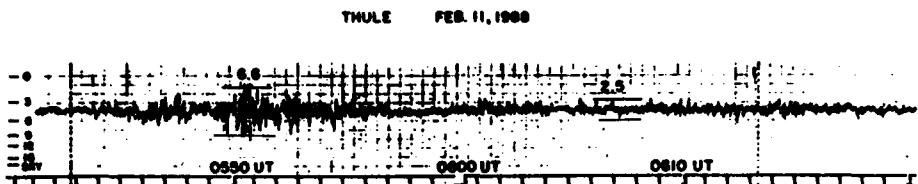


Figure 4. Amplitude scintillations of 250 MHz transmissions from PBS caused by the polar cap arc and recorded at Thule.

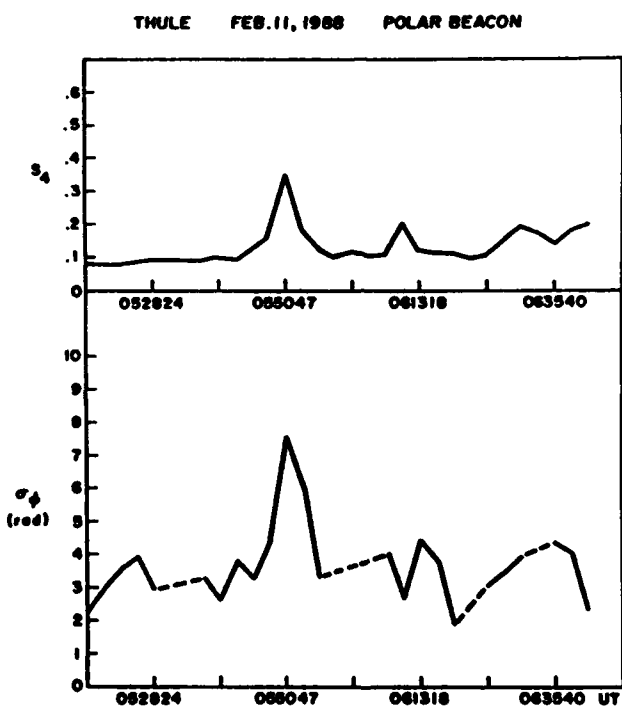
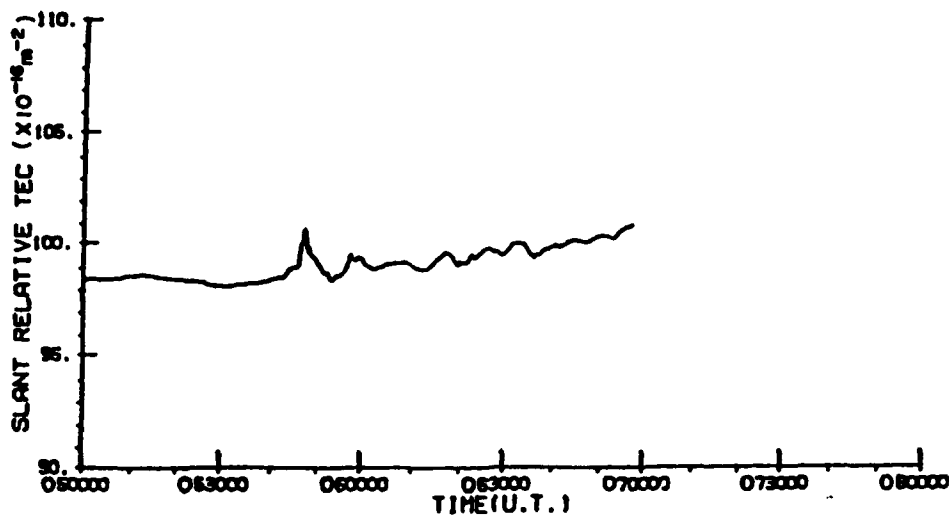


Figure 5. Amplitude and phase scintillation indices S_4 and σ_ϕ for the event in Fig. 4.

The Digisonde 256 (6) at Qaanaaq detected the polar cap arc as an enhanced ionization structure with maximum density of $2.5 \times 10^{11} \text{ m}^{-3}$, a minimum virtual height of about 150 km, and a height of density maximum of ~ 170 km. The neighboring F-region had densities of $5 \times 10^{10} \text{ m}^{-3}$ with $h'F \approx 250$ km and h_{\max} of about 350 km. Fig. 6 shows the relative values of total electron content (TEC) obtained from the GPS satellite by the use of differential doppler measurement. It indicated low values of TEC along a slant ray path through the arc that did not exceed $2 \times 10^{16} \text{ el m}^{-2}$.



FEB 11, 1988
THULE, GREENLAND

Figure 6. Relative total electron content derived from differential Doppler measurements with the GPS satellite. The absolute values are arbitrary.

Compared to $S_4 = 0.35$ the observed phase scintillation magnitude $\sigma_4 = 7$ rad was large. It is known that the magnitude of σ_4 with quasi-stationary satellites may increase in the presence of large plasma drifts [4]. We have shown that in the inertial frame the arc drifted with an average speed of 200 ms^{-1} in the dawn to dusk direction. However, large plasma drifts along the arc [5], which are not detected by the ASIP, may have caused the magnitude of plasma drift perpendicular to the ray path to be large, thereby increasing the σ_4 values. The amplitude scintillation spectra showed considerable broadening indicating the presence of large drift velocities. Figs. 7a and 7b show two samples of amplitude scintillation spectra immediately outside and within the arc with nearly the same values of S_4 . Outside the arc, computations based on Fig. 7a indicate an irregularity drift speed of 100 ms^{-1} across the propagation path. A factor of 5 broadening of the flat portion of the spectra in Fig. 7b suggests drifts within the arc of about 500 ms^{-1} across the propagation path.

Overall, the polar cap arc observed during the sunspot minimum period (SSN = 40) was associated with small enhancement of total electron content and caused weak amplitude scintillations at 250 MHz. The measurements indicated a dawn to dusk motion of the arc at about 200 ms^{-1} but implied, in addition, enhanced plasma flows ($\sim 400 \text{ ms}^{-1}$) along the length of the arc.

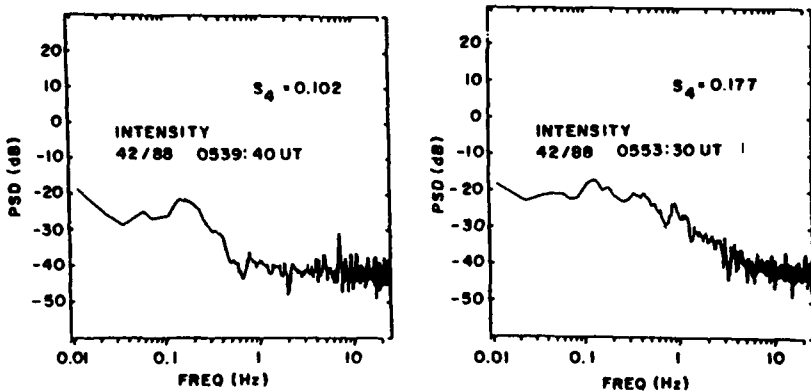


Figure 7. 250 MHz amplitude scintillation spectra (a) prior to and (b) during the encounter of the propagation path with the polar cap arc.

Polar Cap Patches and Auroral Blob

On February 18, 1988, the IMF data were not available for the period of observations. However, a series of polar cap patches were observed on this night which signified that probably IMF B_z southward ($B_z < 0$) conditions had prevailed. In the following paragraphs, we shall discuss the results of our measurements in the polar cap and the auroral oval.

Fig. 8 shows the geometry of the observations. At Thule (TH), the GPS and PBS satellite measurements were performed as explained earlier. During the period under discussion (2100-2300 UT), two PBS satellites were monitored successively as indicated in the diagram. The AFGL aircraft parked at Thule made ASIP and ionosonde measurements. At Qaanaaq (QA), the ASIP and Digisonde [6] measurements were made. The latter provided electron density profiles of the bottomside F-layer and measurements of polar plasma convection [7]. At Sondrestrom (SO), the incoherent scatter radar (ISR) provided east-west (EW) and north-south (NS) scans. The parallels of corrected geomagnetic latitude (CGL) through Sondrestrom are indicated. A transit of the Polar Bear satellite occurred providing scintillation and TEC values. The locus of the intersection of the ray path with 350 km and 100 km altitude, as well as the satellite position mapped down the magnetic field line to 100 km altitude, are indicated.

Fig. 9 shows the isodensity contours in the altitude vs. UT framework as derived from the Digisonde measurements made at QA. Two patches of ionization were detected at ~2200 UT and 2230 UT. The maximum ionization density in the first patch attained a value of $2.5 \times 10^{11} \text{ m}^{-3}$. Following the transit of this patch, background ionization density of $7 \times 10^{10} \text{ m}^{-3}$ prevailed until the second patch moved in at 2230 UT for which

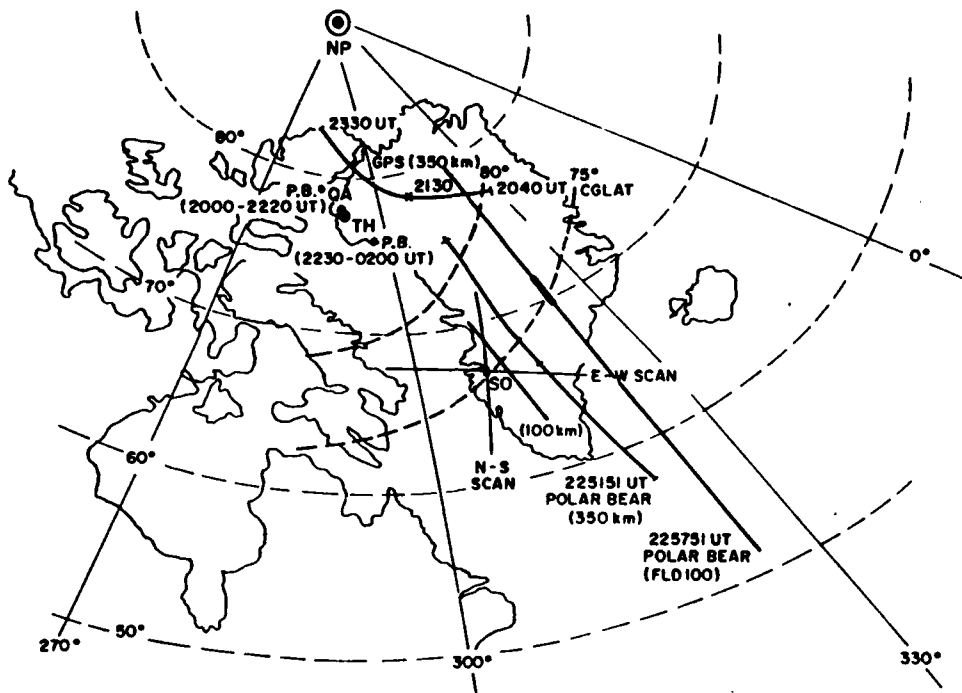


Figure 8. Same as in Fig. 2 except for February 18, 1988. It also shows in dotted lines the corrected geomagnetic latitudes of 75° and 80°, the E-W and N-S scan directions of incoherent scatter radar (ISR) observations at Sondrestrom and the 350 km intersection of the ray path from the Polar Bear Satellite.

a maximum ionization density of $3 \times 10^{11} \text{ m}^{-3}$ was obtained at $\sim 2230 \text{ UT}$. It may be noted that on the leading edge of the patch the isodensity contours are crowded indicating that large scale density gradient existed on this edge. Over the trailing edge of the patch small scale irregularities caused a spread signature on the ionograms as indicated by "scatter only" label. The Digisonde drift measurements with spaced antennas yielded an average anti-sunward drift of 550 ms^{-1} for the ionization patches during the time interval of 2155-2230 UT. For anti-sunward drift, the trailing edges of the patches are expected to be unstable to gradient drift instability in agreement with the observations.

Fig. 10 shows the temporal variation of intensity scintillations observed on 250 MHz transmissions from the PBS satellite. The first scintillation structure around 2220 UT was recorded when the subionospheric (350 km) position of PBS was located to the north and west of Thule. The total duration of the scintillation structure was 21 min. From Fig. 9, we find that the time interval between the peak and the background ionization at the trailing edge of Patch 1, detected by the

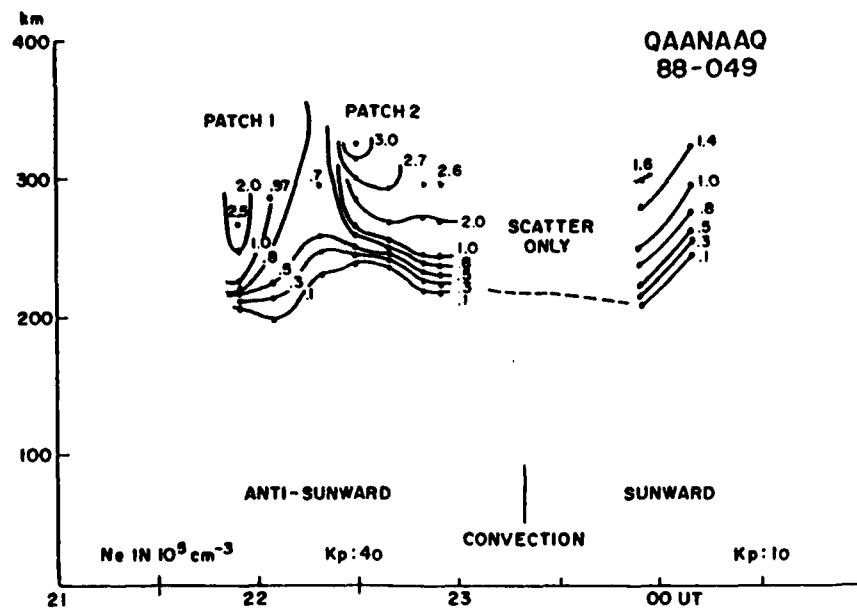


Figure 9. Isodensity contours obtained from digisonde measurements made at Qaanaaq identifying two polar cap patches.

THULE FEB. 18-19, 1988 POLAR BEACON SATELLITE (250 MHz)
INTENSITY SCINTILLATION

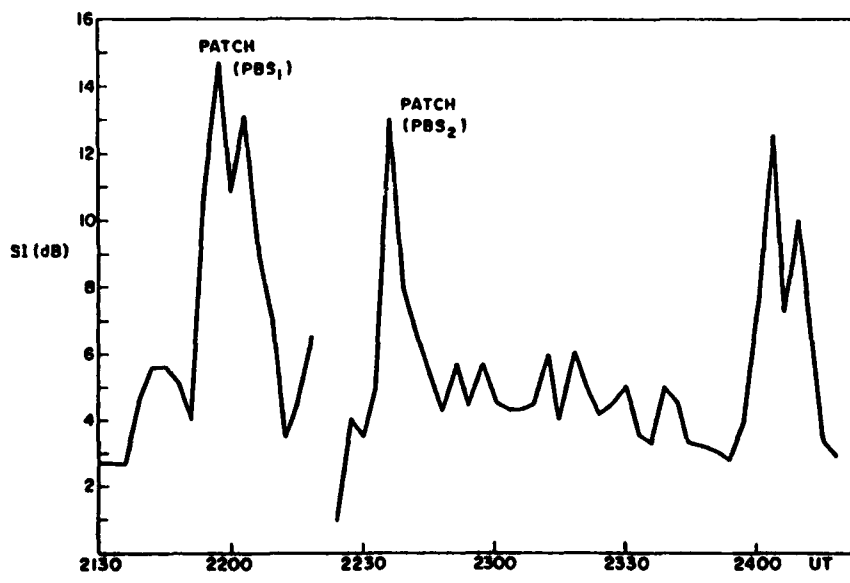


Figure 10. 250 MHz amplitude scintillations in dB obtained from the PBS satellite measurements during the transit of polar cap patches 1 and 2.

Digisonde, was about 23 min. The small difference between the time durations of the scintillation structure and the patch, detected by the Digisonde, may be attributed to the off-zenith location of the satellite measurements. After 2223 UT, scintillation measurements were performed with the PBS satellite at its new position to the south and east of Thule (Fig. 8). Patch 1 had in the meantime been convected past the new satellite position and scintillations caused by Patch 2 were recorded. This structure exhibited a long trailing edge similar to that observed by the Digisonde.

The analysis of differential Doppler measurements made with the 1.2 and 1.5 GHz transmissions from the GPS satellite yielded two clear TEC enhancements at 2205 UT and 2220 UT, marked Patch 1 and Patch 2 in Fig. 11. This is in agreement with the Digisonde observations discussed above. Compared with the brief and weak TEC enhancement ($2 \times 10^{16} \text{ m}^{-2}$) encountered in the polar cap arc and illustrated in Fig. 6, the patches are more extended in altitude with TEC enhancements of 5×10^{16} (Patch 1) and 10×10^{16} (Patch 2) respectively.

THULE, GREENLAND FEB. 18, 1988

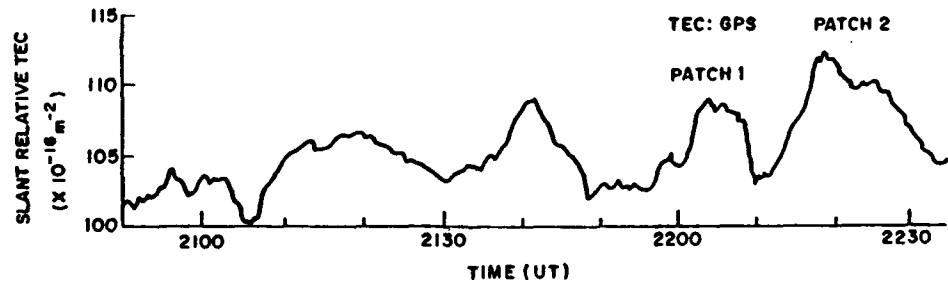


Figure 11. Slant relative TEC obtained from the GPS satellite measurements during the passage of the two patches.

Owing to overcast conditions, no optical measurement could be performed at Thule on this night and therefore, the two-dimensional optical signatures (enhanced 6300 Å) of patches could not be obtained.

We shall now concentrate on the results obtained at Sondrestrom during this time period when measurements at Thule indicated the presence of anti-sunward convecting patches in the polar cap. The incoherent scatter radar (ISR) at Sondrestrom made successive elevation scans at azimuths parallel to and perpendicular to the azimuth of the sun at that local time. Fig. 12 shows the isodensity contours of ionization density in the framework of altitude and distance from Sondrestrom. The results were obtained by making an

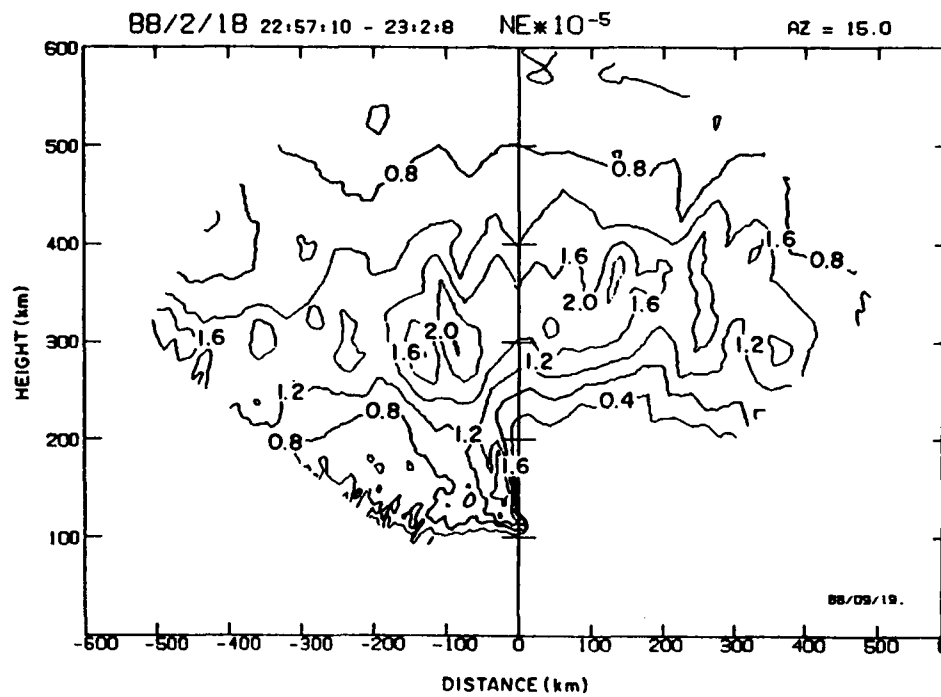


Figure 12. Ionization density contours obtained with an elevation scan of the Sondrestrom ISR at an azimuth of 15°.

elevation scan at an azimuth angle of 15° corresponding to a direction perpendicular to the solar azimuth at this corrected geomagnetic local time. In the figure, positive distances along the abscissa refer to locations to the north of the site. Likewise the negative distances signify southern locations. The orientations of these scans with respect to the geographic and corrected geomagnetic co-ordinates has been indicated earlier in Fig. 8. A study of Figs. 12 and 8 indicates that the poleward edge of the auroral oval moved right overhead of Sondrestrom corresponding to 75° CGL. The scan revealed the presence of an E-region arc immediately to the south of the station. Above the arc, the existence of auroral blobs at F-region heights of 300 km may be noted. To the north of the station density enhancements associated with polar cap patches are obtained. The station provided a sharp demarcation between the auroral oval and the polar cap. During these measurements the sky was clear at Sondrestrom so that ASIP measurements are available. The ASIP images indicated that the polar cap patches were drifting towards the auroral oval [8]. The ISR data indicated that both the patches and the blobs were moving perpendicular to the auroral oval.

Fig. 13 shows the 137 MHz amplitude scintillation index (S_4) and the phase scintillation magnitude (σ_ϕ) recorded at

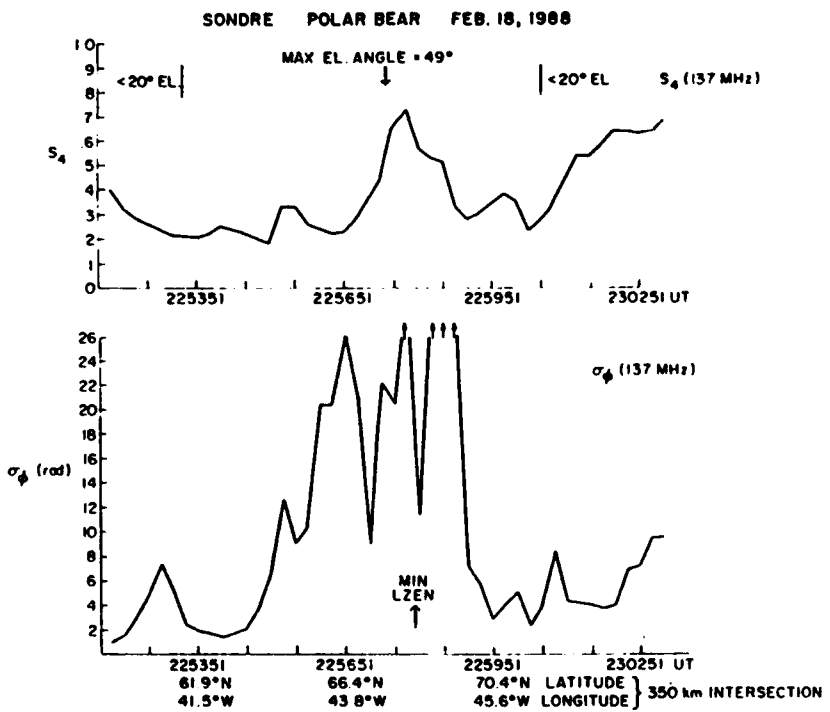


Figure 13. Amplitude scintillation index (S_4) and phase scintillation index (σ_ϕ) obtained from the 137 MHz beacon transmissions from the Polar Bear Satellite.

Sondrestrom when the Polar Bear satellite made its transit over the station. Three prominent phase scintillation structures may be noted, the first two corresponding to the position of the satellite south of 75° CGL and the third one to the north of it. Combining with the radar results discussed above, we may conclude that the first two structures were found within the auroral oval while the third structure was in the polar cap. Further, the first phase scintillation structure was associated with relatively weak amplitude scintillation and small TEC increase, whereas the remaining two corresponded to one pronounced amplitude scintillation event. Fig. 14 shows that the large TEC enhancement was associated with the two phase scintillation events and straddled the poleward edge of the auroral oval. Since such large TEC enhancements are likely to be associated with F-region structures, the second and the third scintillation events appear to be caused respectively by an auroral blob and a polar cap patch. It should be noted that the second scintillation enhancement is partly geometrical in origin, since at this time the ray path became aligned with the local magnetic L-shell. The first phase scintillation structure located inside the auroral oval and associated with negligible amplitude scintillations presumably arises from

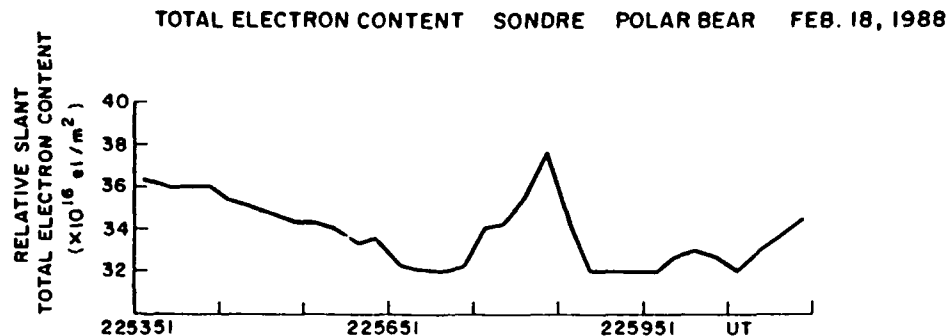


Figure 14. The total electron content (TEC) variations obtained from Polar Bear Satellite observations. The absolute values are arbitrary.

auroral arcs formed by particle precipitation. We have recently encountered such cases which indicate that precipitation induced E-region structures have large scale density variations, but little variations at small scale sizes necessary to cause amplitude scintillations. We should also mention that the UV spectrometer on the Polar Bear satellite registered characteristic auroral emissions at 1304 Å and 1356 Å in the vicinity of 75° CGL.

DISCUSSION

The results of February 11, 1988 indicate that under IMF B_z north conditions polar cap arcs oriented along the noon-midnight meridian drifted from dawn to dusk over the dark winter polar cap. In this phase of the sunspot cycle with the monthly mean sunspot number (SSN) of 40, the background F-region ionization density over the nightside polar cap was only of the order of $7 \times 10^{10} \text{ m}^{-3}$. Within the arc, the electron content enhancements above the background amounted to $2.5 \times 10^{16} \text{ m}^{-2}$. The irregularities within the arc could induce amplitude scintillations at 250 MHz with $S_4 = 0.35$ equivalent to about 7 dB peak to peak fluctuations. In view of the low electron content, it is not possible to account for the observed amplitude scintillations with reasonable estimates of irregularity amplitude, $\Delta N/N$ and 3-dimensional irregularity spectral index, p . For example, with $\Delta N/N = 20\%$ at an outer scale of 20 km, $p = 4$ and irregularity layer thickness of 100 km, $S_4 = 0.09$ at 250 MHz. Consistency between TEC and S_4 values can be obtained if the power law spectral index is reduced to 3. It is quite likely that the irregularity spectral index is steep at long scale-lengths and shallow at short scales. Indeed, in velocity shear regions associated with the arcs, such a decrease in the spectral index of in-situ density irregularities at short scale-lengths has been reported

[9]. Finally, in the case of the arc, a broadening of amplitude scintillation spectra was observed implying that in addition to the dawn to dusk motion of the arc there occurred enhanced plasma motion ($\sim 400 \text{ ms}^{-1}$) along the arc. Such levels of plasma drift arising from sheared plasma flows in the arc also explains why phase scintillation index of 7 radians was obtained in conjunction with relatively small amplitude scintillations.

On February 18 a succession of convecting polar cap patches was observed at Thule and Qaanaaq. Similar patches were also observed at Sondrestrom moving towards the auroral oval. It is interesting to note that in between the patches the background ionization density at Thule was very close to that encountered on the arc day of February 11. But the TEC values in the two patches attained values as large as $5 \times 10^{16} \text{ m}^{-2}$ and $10 \times 10^{16} \text{ m}^{-2}$. It may be noted that during Feb 3-4, 1984, with the monthly mean sunspot number of 85, patches were detected with TEC varying between $10 \times 10^{16} \text{ m}^{-2}$ to $15 \times 10^{16} \text{ m}^{-2}$ above a background level of $5 \times 10^{16} \text{ m}^{-2}$ [10]. Model computations have been made [11] to demonstrate how extended transit of magnetic flux tubes through regions of enhanced solar production located to the south of the cusp can form polar cap patches with enhanced ionization density. Compared to the arc, the TEC values within the patches were higher by a factor of 2 to 4. Amplitude scintillation magnitudes, however, remained within a factor of 2 of that obtained with the arc. This indicates that for the patches we do not need to invoke shallow spectral indices. A detailed study on the spectral indices of scintillations for an arc and a patch can give much insight into the efficiency of generation of short scale irregularities in velocity shear and interchange instabilities.

At Sondrestrom the N-S scan at 2257 UT showed that the poleward edge of the auroral oval occupied a near-overhead position. Auroral arcs were formed at the poleward edge of the auroral oval at altitudes of about 100 km whereas at F-region heights structures with enhanced ionization indicated the presence of auroral blobs. On the poleward portion of the radar scans, polar cap patches were detected. Scintillations with the Polar Bear satellite were obtained as the ray path crossed successively the arc, the blob and the polar cap patch. The ASIP images combined with the radar measurements revealed that both the polar cap patches and the auroral blobs were moving perpendicular to the auroral oval. The presence of irregularities in the polar cap patches prior to their entry indicates that the patches get continually structured as they convect over the polar cap. Future campaigns will focus attention on the convection of patches into the polar cap through the cusp region and their possible exit into the auroral oval.

ACKNOWLEDGMENTS

We wish to thank R.C. Livingston of SRI International and R.E. Eastes of AFGL for making the Sondrestrom Polar Bear satellite beacon and UV imager data available to us. The IMP-8 data were kindly provided by R.W. Lepping. The work at AFGL was supported by Defense Nuclear Agency Project RB00395. The work at Emmanuel College was partially supported by AFGL Contract F19628-86-K-0038 and NSF Grant ATM-8715445. We thank the Danish Commission for Scientific Research in Greenland for permission to conduct ground and aircraft experiments at Thule AB under Projects 28-88 and 30-88.

REFERENCES

- [1] J. Buchau, E.J. Weber, D.N. Anderson, H.C. Carlson, Jr., J.G. Moore, B.W. Reinisch, and R.C. Livingston, *Radio Sci.* **20**, 325 (1985).
- [2] H.C. Carlson, Jr., E.J. Weber, L.P. Block, and Su. Basu, Satellite, airborne, and radar observations of auroral arcs, in Proceedings of the Symposium on Multipoint Measurements of Magnetospheric Processes (COSPAR, Finland, 1988), to appear.
- [3] E.J. Weber and J. Buchau, *Geophys. Res. Lett.* **8**, 125 (1981).
- [4] Su. Basu, E. MacKenzie, S. Basu, H.C. Carlson, D.A. Hardy, F.J. Rich, and R.C. Livingston, *Radio Sci.* **18**, 1151 (1983).
- [5] R.M. Robinson, R.R. Vondrak, and E. Friis-Christensen, *Geophys. Res. Lett.* **14**, 656 (1987).
- [6] K. Bibi and B.W. Reinisch, *Radio Sci.* **13**, 519 (1978).
- [7] J. Buchau, B.W. Reinisch, D.N. Anderson, E.J. Weber, and C. Dozols, *Radio Sci.* **23**, 521 (1988).
- [8] J.H. Doolittle, S.B. Mende, R.M. Robinson, G.R. Swenson, and C.E. Valladares, *Geophys. Res. Lett.* (1989), to be submitted.
- [9] Su. Basu, S. Basu, E. MacKenzie, W.R. Coley, W.B. Hanson, and C.S. Lin, *J. Geophys. Res.* **89**, 5554 (1984).
- [10] E.J. Weber, J.A. Klobuchar, J. Buchau, H.C. Carlson, R.C. Livingston, O. de la Beaujardiere, M. McCready, J.G. Moore, and G.J. Bishop, *J. Geophys. Res.* **91** (1986).
- [11] D.N. Anderson, J. Buchau, and R.A. Heelis, *Radio Sci.* **23**, 513 (1988).

Simultaneous Density and Electric Field Fluctuation Spectra Associated With Velocity Shears in the Auroral Oval

SUNANDA BASU,¹ SANTIMAY BASU,² E. MACKENZIE,³ P. F. FOUGERE,² W. R. COLEY,³ N. C. MAYNARD,³ J. D. WINNINGHAM,⁴ M. SUGIURA,⁵ W. B. HANSON,³ AND W. R. HOEGY⁶

Simultaneous satellite *in situ* measurements of density ($\Delta N/N$) and electric field fluctuation (ΔE) spectra in the high-latitude ionosphere are presented using two orbits of Dynamics Explorer 2 (DE 2) data traversing, respectively, the F region at 350 km altitude and the topside ionosphere at 900 km altitude. The spectral study was primarily confined to large structured velocity regions in the auroral oval. By means of the very complete set of energetic particle, dc and ac electric field, field-aligned current, thermal plasma density, and temperature measurements available from DE 2, we were able to identify two categories of spectra associated with velocity shears irrespective of the height of the satellite. The first category was observed in very intense velocity shear regions of shear frequencies ~ 10 Hz in conjunction with large field-aligned current densities. Under these conditions the spatial spectra of $\Delta N/N$ and ΔE had identical power law indices of -1.8 ± 0.2 between scale lengths of approximately 10 km and 300 m. At scale lengths shorter than 300 m the ΔE spectra steepened to an index of -3 ± 0.5 while the spectral index of $\Delta N/N$ remained close to its original value of approximately -1.8 ± 0.2 , with large power spectral densities observed down to 10 m scale lengths. The second category was observed in more moderate velocity shear regions of shear frequencies ~ 1 Hz in conjunction with weak field-aligned currents. In this case the slopes of the density spectra were essentially unchanged, while the ΔE spectra had a much steeper slope of -3 ± 0.5 between 10 km and a few hundred meters. Other factors identifying the two categories are as follows. The first category of spectra was characterized by the existence of upward flowing ions with conic distributions energized to 30 eV and possibly O⁺ ion cyclotron waves and large electron temperature enhancements. The second category of spectra was associated with wave activity in the 4- to 16-kHz range, most probably O⁺ lower hybrid waves, and occasionally large ion temperature enhancements. The observations of $\Delta N/N$ and ΔE spectral behavior are compared to recent work on two-dimensional plasma turbulence theory and nonlinear simulations of the collisional Kelvin-Helmholtz (KH) instability. In particular, the spectral behavior associated with the moderate velocity shear category agrees well with some recent computations of the spatial power spectra of the KH instability (Keskinen et al., 1988).

INTRODUCTION

Velocity shears in the background convective plasma flow have recently been invoked as a source of subkilometer scale irregularities in the nighttime auroral F region [Basu et al., 1984, 1986]. In the past, particularly at high altitudes (> 2000 km), the S3-3 spacecraft detected very large (~ 0.5 V/m) perpendicular (to B) electric fields with spatial scales as short as kilometers [Mozer et al., 1977]. These authors noted that the intense dc electric fields occurred in regions of extreme plasma turbulence and were generally associated with field-aligned currents. Other spacecraft measurements have also provided evidence for high-latitude electrostatic turbulence [Kelly and Mozer, 1972; Kintner, 1976]. In particular, the Hawkeye measurements of Kintner [1976] showed that velocity field (or electric field) irregularities at short wavelengths (less than a few kilometers) were spatially coincident with velocity field irregularities at wavelengths greater than about 100 km. Further, in the strong shear flow regions the power spectral index of the velocity field in the short-wavelength regime was found to be -2.8 ± 0.3 . Mozer [1971] demonstrated from balloon electric field measurements at long wavelengths (greater than

100 km) that the power spectrum exhibits a power law variation with index -1.6 ± 0.3 . By putting together the long- and short-wavelength measurements, a knee was found in the global power spectrum between 3 and 30 km scale length [Kelly and Kintner, 1978]. As a result of this spectral form, Kelly and Kintner [1978] concluded that there was evidence for the existence of two-dimensional electrostatic turbulence over a large range of scale lengths within the auroral oval.

In a recent review, Kintner and Seyler [1985, p. 125] point out that "the interpretation of Kintner's results would be greatly facilitated by a simultaneous measurement of both the density and electric field fluctuation spectra." These authors also point out that a knowledge of the density and temperature gradients and electron precipitation measurements would help in identifying the source of the observed turbulence: is indeed the two-dimensional turbulence being driven by shear flow, or is it being driven by the current convective process at the longer scales and drift waves at the shorter scales (< 100 m)? At this point, it may be worthwhile to mention that almost all linear theories of plasma instabilities predict stabilization of small scales in the F region in the presence of velocity shears [Guzdar et al., 1982; Huha et al., 1983; Sarvanarayana and Ossakow, 1984] and only recently have nonlinear simulations indicated the generation of small-scale turbulence by means of secondary instabilities growing on the primary waves [Keskinen et al., 1988]. Another possible source of turbulence at the smaller scales could be current-driven ion cyclotron turbulence in the presence of velocity shear.

It is the object of this paper to present a detailed study of simultaneous density and electric field fluctuation spectra over a large scale length range (~ 10 km to 10 m) seen in association with large structured convective plasma flows, field-aligned currents (FAC), and particle precipitation at high lati-

¹ Physics Research Division, Emmanuel College, Boston, Massachusetts.

² Air Force Geophysics Laboratory, Hanscom Air Force Base, Massachusetts.

³ University of Texas at Dallas, Richardson.

⁴ Southwest Research Institute, San Antonio, Texas.

⁵ Geophysical Institute, Kyoto University, Kyoto, Japan.

⁶ NASA Goddard Space Flight Center, Greenbelt, Maryland.

Copyright 1988 by the American Geophysical Union.

Paper number 7A9006.
0148-0227/88/007A-9006\$05.00

The U.S. Government is authorized to reproduce and sell this report. Permission for further reproduction by others must be obtained from the copyright owner.

tudes by using the multiple sensor data on Dynamics Explorer 2 (DE 2). By using the retarding potential analyzer (RPA) it is possible to obtain high-resolution ion (electron) density measurements and study the spectra of these density irregularities. The vector electric field instrument (VEFI) can be utilized to obtain a simultaneous electric field fluctuation spectrum of the dc field while a 20-channel comb filter spectrometer was used to monitor the ac electric fields. The shears in the background flow perpendicular to the orbital track can be measured to a higher resolution (than with the VEFI) by the ion drift meter (IDM) on board. The energetic electron and ion precipitation in the 5-eV to 32-keV range and their pitch angle information can be obtained from the low-altitude plasma instrument (LAPI), while the FAC flowing into or out of the ionosphere can be estimated from the on-board magnetometer (MAG-B). The associated electron and ion temperatures can be obtained from the Langmuir probe and RPA, respectively. To our knowledge, this paper presents with the above data set the most detailed analysis of simultaneous density and electric field fluctuation spectra observed in the high-latitude ionosphere.

We present spectral information and data from the above instruments for two DE 2 orbits traversing the high-latitude ionosphere during which large velocity shears were observed. While it is more common to find larger magnitudes of electric fields at DE 1 altitudes [Weimer *et al.*, 1985], it is by no means unusual to find small-scale (several kilometers) 100 mV m⁻¹ dc electric field fluctuations in DE 2 data obtained at ionosphere altitudes, as will be evident from a study of these two orbits. One of the orbits was through the F peak region (320–450 km), while the other was observed in the topside ionosphere (~900 km). The observations are compared to the results of nonlinear simulations of shear flow driven instabilities and predictions based on two-dimensional turbulence arguments, particularly, as they refer to the Kelvin-Helmholtz (KH) process.

INSTRUMENT DESCRIPTION AND DATA ANALYSIS METHODS

Detailed description of the DE 2 program [Hoffman and Schmerling, 1981] and all the instruments on board was provided in *Space Science Instrumentation* (volume 5, December 1981). We will here indicate the resolutions of the different instruments and their impact on spectral analysis techniques and estimations of various gradient scale lengths.

RPA

The RPA provided us with ion density N_i values at the rate of 64 Hz or approximately every 120 m of flight path [Hanson *et al.*, 1981]. To prevent aliasing, the signals were passed through a three-pole low-pass Bessel filter before being telemetered. These high-resolution density measurements were used in conjunction with the maximum entropy (MEM) technique [see Fougner, 1985] to establish spectral forms of the density irregularities. The ionospheric irregularity measurements were extended to much smaller scale sizes with the help of a comb filter bank. Six filters were employed, each having a bandwidth of a factor of e (2.72); the lowest four frequency ranges and mean scale sizes from which useful data were obtained are reproduced in Table 1, from Hanson *et al.* [1981]. The filters measure the mean irregularity power within their respective bandwidths with about a 45-ms averaging time. Their outputs are sampled every 2 s within a period of 375 ms. By combining the 64-Hz data and the filter outputs, it is possi-

TABLE 1. Comb Filter Bank Characteristics for RPA Density Data

Filter	Frequency Band, Hz	Mean Scale Size, m
1	32–86	125
2	86–233	46.5
3	233–630	17.2
4	630–1700	6.35

ble to study spectral behavior over the scale length range of 10 km to 10 m. The ion temperature T_i is measured approximately once every second by the RPA.

IDM

The IDM measures the horizontal (E-W) and vertical components of ion drift at the rate of 32 Hz or approximately every 240 m along the orbital track [Heelis *et al.*, 1981]. Thus the smallest shear that can be measured by DE 2 in the E-W velocity scale is approximately 0.25 km. Since the largest convection velocities observed are ~ 2.5 km s⁻¹, the largest shear frequencies DE 2 measures are ~ 10 Hz. A complete vector velocity measurement is obtained once per second with the aid of the along-track component of the velocity (the ram component) measured by the RPA.

VEFI

We utilize in this paper the x component of E which is along the spacecraft velocity vector V , and is therefore approximately in the geographic N-S direction. The VEFI used the symmetric double floating probe technique to measure the dc electric field at the rate of 16 Hz [Maynard *et al.*, 1981]. Electric fields generated by the motion of the spacecraft across the magnetic field ($v \times B$) were calculated using a model B and subtracted to obtain the ambient electric field. In the F region the N-S component of the electric field is, of course, responsible for the E-W component of the plasma motion. We used the same MEM spectral technique as was used for the density to study the electric field fluctuation data. In addition, the ac portion of the electric field was monitored by a 20-channel comb filter spectrum analyzer. This spectrometer is divided into three separate filter banks: two eight-channel banks (A and B) covering the range 4–1024 Hz and one four-channel bank (C) covering the range 1–512 kHz. Spectrometer A filters are evenly logarithmically spaced by factors of 2, while spectrometer B contains four narrower channels in addition to four that duplicate channels in spectrometer A. The measurement axes are $\pm 45^\circ$ from the velocity vector. For the data shown in this paper, spectrometer B was assigned to the axis closest to the magnetic field, and A and C were on the axis aligned most nearly perpendicular to the field. At low gain, spectrometers A and B cover the rms range of 5 μ V m⁻¹ to 9.5 mV m⁻¹ while the spectrometer C range is 26 μ V m⁻¹ to 9.5 mV m⁻¹. Table 2 provides frequency ranges covered by spectrometers A, B, and C and the approximate mean scale length if all the fluctuations are considered spatial. Considering the dc and ac data together, we get spectral coverage over the range 10 km to 10 m as was obtained for the densities. For further details regarding the spectrometer the reader is referred to Maynard *et al.* [1981].

LAPI

This instrument contains an array of 15 parabolic electrostatic analyzers to obtain detailed pitch angle distributions

TABLE 2a. Comb Filter Bank Characteristics for VEFI: Spectrometer A

Filter	Bandwidth, Hz	Center Frequency, Hz	Approximate Equivalent λ, m
1	4-8	6	1300
2	8-16	12	650
3	16-32	24	325
4	32-64	48	160
5	64-128	96	80
6	128-256	192	40
7	256-512	384	20
8	512-1024	768	10

of ions and electrons as a function of energy. The mode of operations for these passes provides a 16-point energy spectrum in the energy range 5 eV to 32 keV every second from 16 data channels, but the voltages on the electrostatic analyzers and the set of analyzer outputs sampled are selectable to allow for greater space-time resolution over limited portions of the energy and angular distribution [Winningham *et al.*, 1981]. In this paper we shall display color spectrograms of energy versus time of the precipitating electrons and ions in the range 5 eV to 27 keV, as well as flux versus energy plots of the precipitating electrons at particularly interesting locations in the DE 2 orbit such as in the regions of velocity shears, for instance.

MAG-B

The magnetometer on DE 2 is a triaxial flux gate sensor with a dynamic range of 62,000 nT and a resolution of 1.5 nT [Farthing *et al.*, 1981]. The data to be shown here will be 0.5-s averages of the magnetic field components in geomagnetic coordinates after a model field has been subtracted. Changes in this difference magnetic field can be interpreted as a measurement of field-aligned currents assuming that the FAC extend spatially in the direction orthogonal to this difference (i.e., infinite sheet currents).

LANG

Finally, we use measurements of the electron temperature T_e obtained at 0.5-s intervals using the Langmuir probe [Krehbiel *et al.*, 1981] and compare it to the ion temperature obtained from the RPA at approximately 1-s intervals.

MULTIPLE SENSOR IRREGULARITY DATA FROM DE 2

We present in this section the simultaneously obtained density and electric field fluctuation spectra from two DE 2 passes

TABLE 2b. Comb Filter Bank Characteristics for VEFI: Spectrometer B

Filter	Bandwidth, Hz	Center Frequency, Hz	Approximate Equivalent λ, m
1	4-8	6	1300
2	16-32	12	650
3	45-64	54.5	147
4	64-128	96	80
5	181-256	218.5	37
6	256-361	308.5	26
7	361-512	436.5	18
8	512-1024	768	10

TABLE 2c. Comb Filter Bank Characteristics for VEFI: Spectrometer C

Filter	Bandwidth, kHz
1	1.02-4.09
2	4.09-16
3	16-64
4	128-512

through the high-latitude ionosphere in the presence of intense and moderate velocity shears along with supporting data from the other sensors mentioned in the last section in order to provide an understanding of the background conditions and the sources of free energy that are associated with different types of spectra.

Orbit 4429

This pass traversed the winter southern high-latitude ionosphere from dawn to dusk during a time of moderate magnetic disturbance ($K_p = 4$). Figure 1 shows a projection of the vector velocities measured by the IDM and RPA on a polar plot in an invariant latitude (ILAT)-magnetic local time (MLT) coordinate system. The region between 70° and 80° ILAT in the morning sector shows intense velocity shears with both sunward and antisunward velocities greater than 2 km s^{-1} being observed in close proximity to one another.

To provide an overall perspective of the large-scale density structure that is associated with the velocity structure shown in Figure 1, the LANG data of ion densities N , for the entire dawn-dusk portion of the orbit are shown in the top panel of Figure 2. The bottom panel of electron temperatures T_e provides some information regarding the localized regions of enhanced production (see discussion in the work by Kofman and Wickwar [1984] and Robinson *et al.* [1985] on local heat

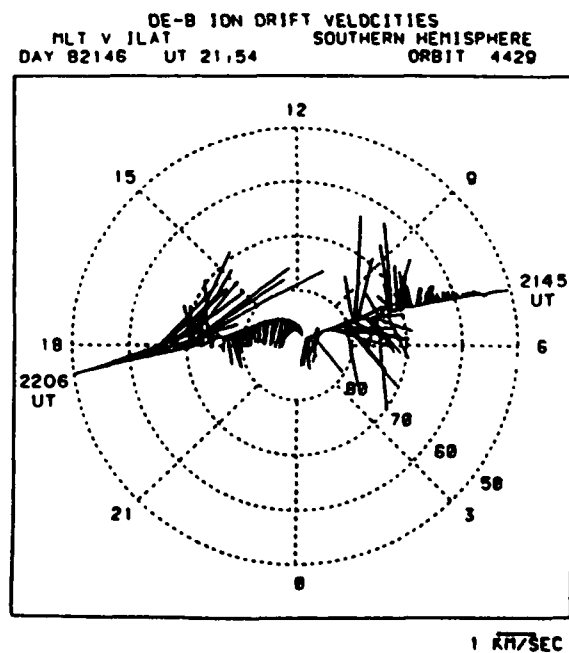


Fig. 1. Vector velocity measurements using IDM and RPA for DE 2 orbit 4429 through the southern high-latitude ionosphere on May 26, 1982, between 2145 and 2206 UT.

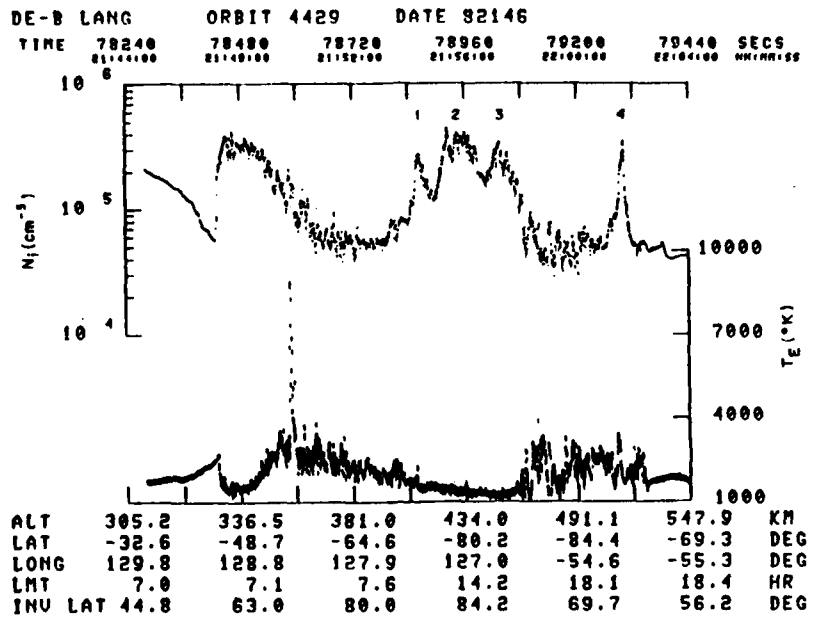


Fig. 2. LANG measurements of ion density N_i and electron temperature T_e observed between 2144 and 2204 UT. Numbers 1-4 represent convecting plasma density enhancements.

production rates and their relationship to enhanced ionization by particle precipitation). Several features are noteworthy. The satellite traverses the F region of the ionosphere, encountering the morning trough region (with its low N_i and elevated T_e characteristics) at approximately 2147 UT at an altitude of 330 km. In the structured velocity region between 2149 and 2154 UT, N_i and T_e are both found to fluctuate with T_e showing a dramatic peak of 9000°K just prior to 2150 UT. The high-resolution data for T_e and ion temperature T_i derived from the RPA near this peak will be shown later in the paper. The gradient in the bulk density observed between 2148 and 2152 UT cannot be accounted for by an altitude effect since the altitude variation is only 50 km, i.e., less than a topside scale height. Thus a large-scale horizontal density gradient also exists with low background densities of $5 \times 10^4 \text{ cm}^{-3}$ being observed in the dark winter polar cap and the larger densities of $4 \times 10^5 \text{ cm}^{-3}$ seen in the auroral oval. Four very clear discrete density structures (marked 1-4) are also observed beyond 2154 UT. Three of them, located in the polar cap with density enhancements of 2-4 over the background associated with low T_e values, are almost certainly patches of ionization convected into the polar cap. Similar patches of ionization drifting in the polar cap during magnetically disturbed times have been reported by Weber *et al.* [1984]. The fourth structure, near the equatorward edge of the evening, auroral oval, is probably the so-called "boundary blob" [Rino *et al.*, 1983; Weber *et al.*, 1985]. Since the object of this current paper is to study density and electric field structure in association with velocity shears, we exclude from the purview of this paper the study of the irregularities associated with the convecting blobs in the polar cap and auroral oval and confine our spectral study to the morningside of the oval between 2146 and 2154 UT, within which the most intense velocity shears were observed.

The LAP1 data for the above period are shown in Plate 1. The top panel shows the electron energy flux between 3 eV

and 27 keV precipitating in the ionosphere at a pitch angle (shown in the third panel) of 45°. The most intense electron precipitation event occurs at 2149:45 UT. The lowest panel, for upflowing ions at a pitch angle of 135°, shows their presence at precisely 2149:45 UT. A careful study of all the pitch angles confirms that these upflowing ions are ion conics which have been energized to 10 eV. The altitude of the satellite at this time is 350 km, and the background thermal plasma density is $\sim 2 \times 10^5 \text{ cm}^{-3}$; hence the ion energization takes place in a collisional medium, as was also observed earlier in rocket flights [Yau *et al.*, 1983]. A very high electron temperature of 9000°K was measured at this time by LANG. Yau *et al.* [1983], however, observed larger ion energization without such an increase in electron temperature. Beyond 2150 UT the electron precipitation is in the nature of intense polar rain.

The integrated total number flux and the energy flux of downward precipitating electrons [Lin and Hoffman, 1982] associated with the electron spectrogram of Plate 1 are shown in the bottom and top panels, respectively, of Figure 3. The ion conic is associated with an electron number flux in excess of $2 \times 10^{10} \text{ cm}^{-2} \text{ s}^{-1}$ and an energy flux of $10 \text{ ergs cm}^{-2} \text{ s}^{-1}$. The middle panel shows that the electron density integrated from 5 eV to 27 keV and 0° to 90° pitch angles is as large as 100 cm^{-3} compared to a local background thermal plasma density of $2 \times 10^3 \text{ cm}^{-3}$.

The energetic fluxes when used in a modified form of the Spiro et al. [1982] formula for Hall and Pedersen conductivities yield the values shown in the two top panels of Figure 4. The modification used five average energies to characterize the precipitating fluxes rather than a single energy as was done by Spiro et al. Between 2149 and 2149:30 UT the modeled Hall conductivity is as large as 40 mhos while the Pedersen conductivity is approximately 15 mhos. Note, however, the presence of very sharp conductivity gradients between 2149:30 and 2150 UT. The ion conic region, in particular, around 2149:45 is associated with very sharp gradients of

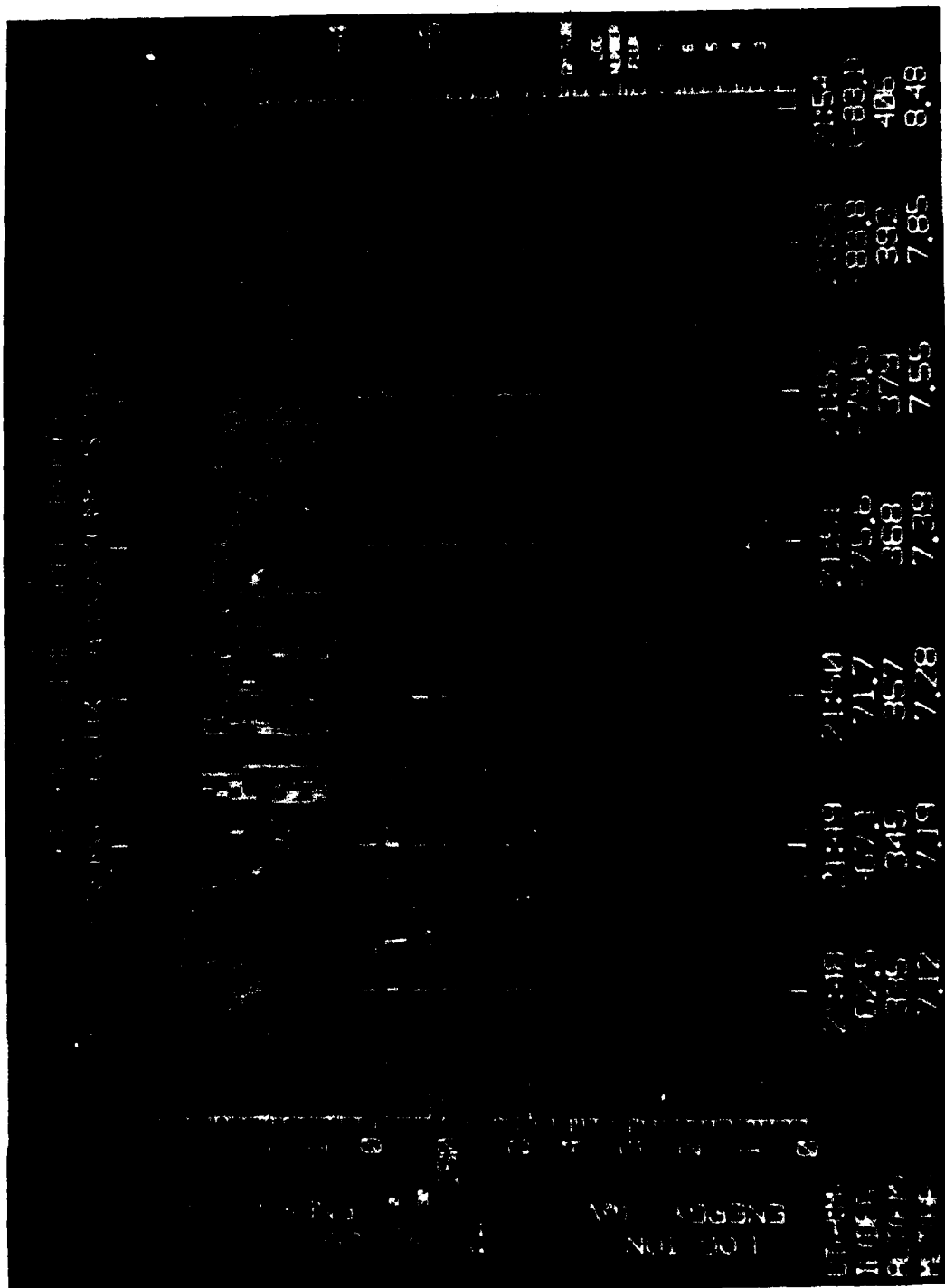


Plate 1. Energetic electron and ion spectrogram and their pitch angle information for the period 2147-2154 UT encompassing the upward flowing ion event at 2149:45 UT.

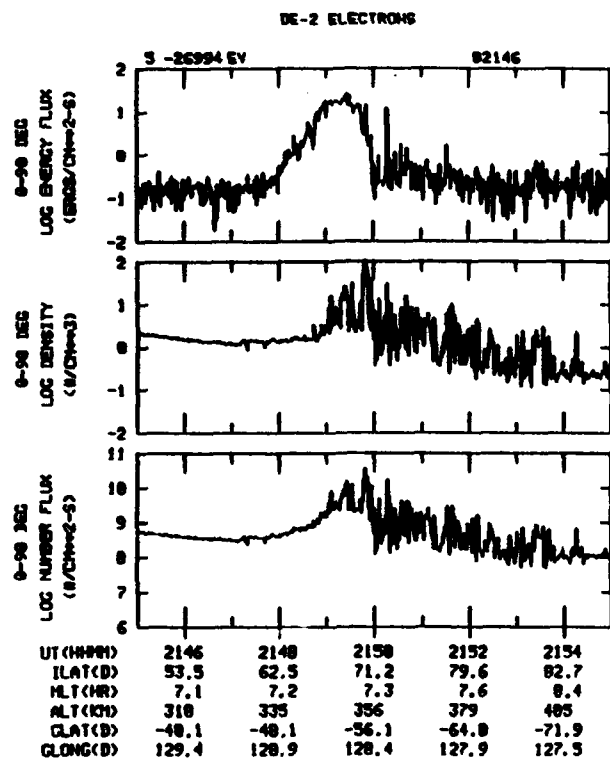


Fig. 3. The total integrated electron number flux (bottom panel), the total integrated electron energy flux (top panel), and the electron densities (middle panel) integrated from 5 eV to 27 keV and from 0° to 90° pitch angles for the spectrogram shown in Plate 1.

both types of conductivities and intense small-scale FAC as shown in the third panel. The magnetometer on board DE 2 shows that narrow intense upward (positive) and downward (negative) FAC as large as $40 \mu\text{A m}^{-2}$ were seen in association with the sharp conductivity gradients between 2149:45 and 2150 UT (third panel of Figure 4). Beyond 2150 UT the conductivities are small, and the associated FAC are small except for peaks of $\pm 20 \mu\text{A m}^{-2}$ near 2150:20 UT. The last panel shows the 32-Hz IDM E-W horizontal drift data (N-S electric field) for 14 s within the high-conductivity gradient and high-FAC region ($> 10 \mu\text{A m}^{-2}$) between 2149:40 and 2149:54 UT and in the low-conductivity and low-FAC region ($\sim 1 \mu\text{A m}^{-2}$) between 2150:20 and 2150:30 UT.

As mentioned earlier, in this paper we wish to present the simultaneously obtained density and electric field spectra observed in regimes characterized by the velocity data of the type shown in the last panel. The shear frequency (highest velocity/shear gradient scale length) in the region around 2149:40 UT is 10 Hz, while that in the region around 2150:20 UT is 1 Hz. In subsequent diagrams we shall show spectra from both regions, identifying the former as S_I for the intense shear category and the latter as S_M for the moderate shear category. For comparison we shall also present a spectrum from a region where little or no velocity shear is seen but which is associated with a high uniform conductivity region such as is seen around 2149 UT in the top panel of Figure 4. This class of spectra will be identified by the symbol S_H to denote the high E region conductivity that is the major characteristic of this class. By reference to the top panel of Figure 3, one notes that there is a uniform energy input in

excess of $10 \text{ ergs cm}^{-2} \text{ s}^{-1}$ over a region 225 km wide (i.e., over 30 s of satellite path) in the S_H region.

In Figure 5 we plot the irregularity amplitude ($\Delta N/N$)_{reg} in the middle panel as a function of position of the satellite between 2146 and 2154 UT. The irregularity amplitude was calculated by using 8 s of RPA data obtained at a 64-Hz sampling rate, and after removal of large-scale trends using a linear detrending algorithm. We also show in the bottom and top panels of Figure 5 the logarithm of the ion concentration data, N_i , obtained from the RPA, and the E-W horizontal drift obtained from the IDM, respectively. There is a region of low irregularity amplitude ($\sim 5\%$) within the high-conductivity (S_H) region between 2149:00 and 2149:30 UT discussed earlier and a series of irregularity amplitude peaks of $\sim 20\%$ in as-

DE-2 ORBIT #4429 MAY 26, 1982

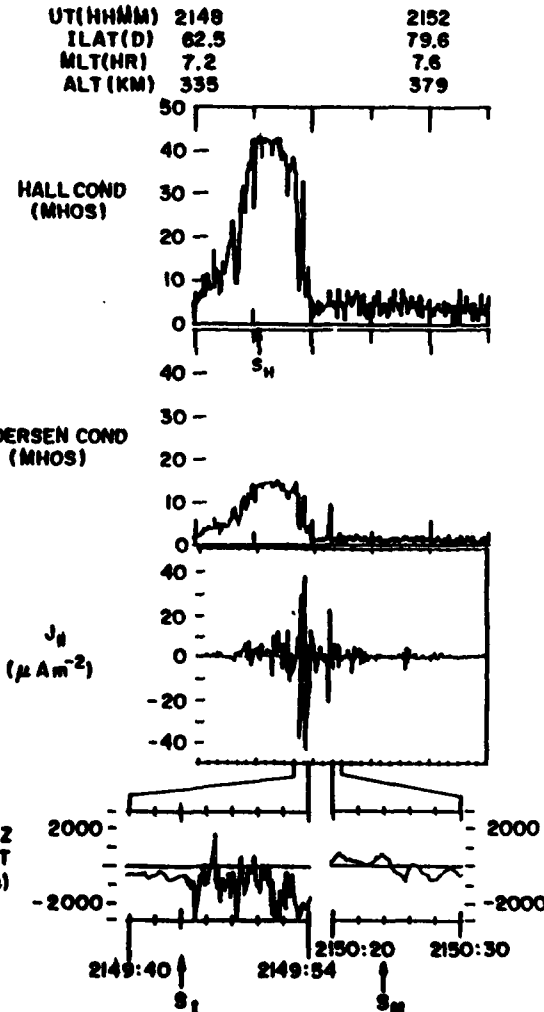


Fig. 4. The Hall and Pedersen conductivities (top two panels) modeled on the basis of the precipitating electron fluxes shown in Plate 1, the small-scale field-aligned current intensities (with upflowing currents shown positive) from the magnetometer (third panel), and the high-resolution E-W ion drifts for two periods in the high field-aligned current intensity region and low field-aligned current intensity region (bottom panel). The three arrows in the top and bottom panels labeled S_H , S_I , and S_M are beginning times for three 8-s periods for which spectral analysis is presented in Figures 6 and 7.

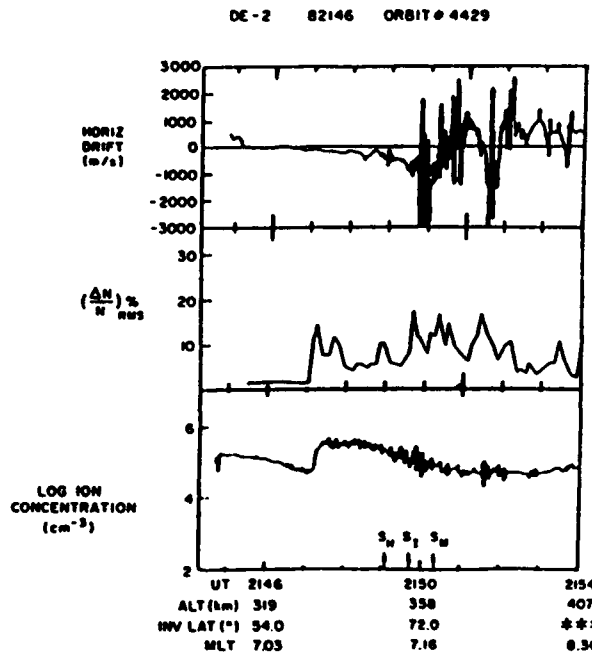


Fig. 5. The E-W ion drifts (top panel), the ion concentrations (bottom panel), and the irregularity amplitude $(\Delta N/N)_{\text{rms}}$ computed over 8-s intervals for the period 2146–2154 UT. S_H , S_I , and S_M have the same meaning as in Figure 4.

sociation with the velocity shears shown in the top panel (small sections of which were shown expanded in the bottom panel of Figure 4).

It should be noted that there is a fairly prominent peak in $\Delta N/N$ between 2147 and 2148 UT which is not related to any structure in the velocity (cf. top panel of Figure 5), but rather to a steep density gradient at the poleward edge of the trough (cf. third panel of Figure 5 and top panel of Figure 2). This $\Delta N/N$ structure could be locally generated by the $E \times B$ gradient drift instability [Keskinen and Ossakow, 1983], but it is in all probability a convected structure since the ram component of the velocity which would drive this instability is also small as seen in Figure 2. We would like to emphasize that the magnitude of $\Delta N/N$ when computed over 8 s of data (64 km of path length) is generally dominated by tens of kilometer scale irregularities, as in a power law environment the power spectral density (psd) increases with scale length. Further, the lifetime of such scales at 350 km in the presence of classical diffusive damping can be many hours in the dark hemisphere [Vickrey and Kelley, 1982]. Thus a 10-km scale irregularity may be convected great distances from its source, and its existence at a particular location does not necessarily give us any indication regarding its generation mechanism. Since the diffusive decay rate is inversely proportional to the square of the scale size, a 100-m irregularity will decay 10⁴ times faster than a 10-km scale. We will therefore present later (in Figure 10) the psd of 125-m and 46.5-m irregularities and show that in such convected structures the psd at these short scale lengths is 1–3 orders of magnitude smaller than in velocity shear regions (which act as sources) even though the $\Delta N/N$ samples computed over 8 s of data are comparable. It is important to note from Figure 3 that between 2147 and 2148 UT the integrated energy flux is low, indicating that enhanced E region

conductivity effect (to be discussed in conjunction with Figure 6) was not responsible for the reduced psd at the short scales.

Spectral Analysis of Orbit 4429

The three regions selected from the morningside of the oval on orbit 4429, S_H , S_I , and S_M , will be utilized to compare simultaneously observed density and electric field fluctuation spectra. The regions can be characterized by high uniform conductivity and negligible velocity shear (S_H); by intense velocity shear and high FAC (S_I); and by medium velocity shear and low FAC (S_M).

It should be noted that in order to study the spectra of density and electric field fluctuations we had to make the assumption that measurements of spatial structure in these quantities made on the satellite are Doppler shifted from zero to the frequency $f = kV_s/2\pi$, where V_s is the satellite velocity. In this paper whenever we refer to wave number k or wavelength $\lambda = 2\pi/k$, it is based upon this hypothesis. In Tables 1 and 2 the conversion from spacecraft-measured frequency to scale length of density and electric field irregularities is performed on this basis. This, of course, assumes "frozen in turbulence." In section 3 of their review, Kintner and Seyler [1985] discuss at length the problems of interpreting time domain satellite measurements for comparison with the findings of fluid turbulence theories which predict power laws in wave number or wavelength space. Actually, the determination of a unique wave number spectrum can be made only in the simple case of zero phase velocity for the process which is giving rise to the irregularities [Fredericks and Coroniti, 1976]. While this assumption may be generally true under most magnetospheric conditions [Temerin, 1978; Sugiura, 1984], the inclusion of neutral winds into the treatment of the KH instability, for instance, yields a finite real frequency, i.e., nonzero phase velocity [Keskinen et al., 1988], which may provide some ambiguity in the interpretation of the observed spectra to be presented.

In Figures 6a and 6b we present the data for three 8-s periods of density fluctuations and their spectra estimated by the maximum entropy method (MEM) technique using 30 filter weights [Fougere, 1985]. The beginning times of the three samples are indicated on the diagram and also identified on the top and bottom panels of Figure 4 (S_H , S_I , S_M). A description of the background conditions for these three spectral types was also given in conjunction with that diagram. The ambient densities and irregularity amplitudes (after removing the linear trend) are shown in the right-hand corner of each sample in Figure 6a. It is important to note that the top two panels have similar average irregularity amplitudes (approximately 20%) and have similar steep gradients and high-frequency structure.

The spectra of these samples shown in Figure 6b have shallow or fairly flat low-frequency behavior and well-defined high-frequency roll-off portions which can be described by power laws in the range 1–10 Hz. Note that the top curve has been shifted upward for clarity and its scale is on the right. The bottom curve is for data obtained in a high-conductivity region (S_H) which shows a slope of -2.4 ± 0.07 for the roll-off portion (determined between the two points on the curve) and a psd at 10 Hz which is approximately 10 dB above the -60-dB noise floor. When we consider the density spectra in the velocity shear regions either associated with or without high FAC (i.e., either S_I or S_M), the spectra seem to be identical, having power law indices of -1.9 ± 0.01 and

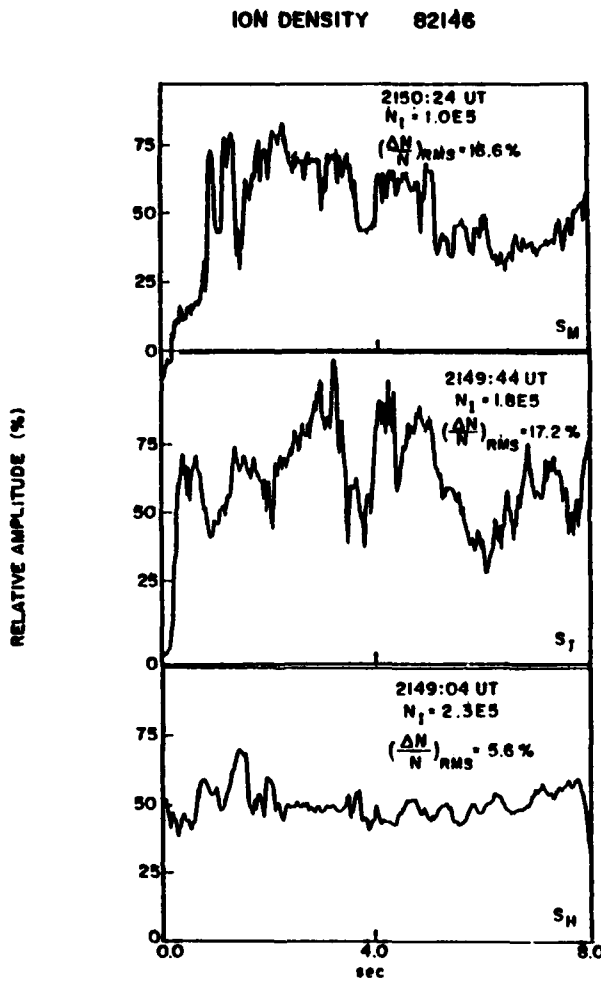


Fig. 6a

Fig. 6. (a) Three 8-s samples of density data for time periods identified in Figure 4 as S_M (bottom panel), S_I (middle panel), and S_H (top panel). (b) Their corresponding maximum entropy spectra. The background ion densities (N_i), irregularity amplitudes $(\Delta N/N)_{RMS}$, and spectral indices are indicated in the respective diagrams.

-2.0 ± 0.02 , respectively, and both having psd of 20 dB above the noise level at 10 Hz. The steeper slope in the high-conductivity region and the shallower slopes and larger psd seen in association with velocity shear are consistent with earlier observations [Basu et al., 1984, 1986].

The corresponding north-south component of the dc electric field data and spectra are shown in Figures 7a and 7b. The electric field structure in the high-conductivity region (S_H) is minimal with $\Delta E = 3 \text{ mV m}^{-1}$ as shown in the bottom panel of Figure 7a. The intense structuring of the field in the high-FAC region (S_I) is evident with $\Delta E = 48 \text{ mV m}^{-1}$. The similarity of the electric field data in Figure 7a and the ion drift data in Figure 4 is expected in the ionospheric F region, as both techniques are valid indicators of the electric field. The third sample taken in a region of low FAC (S_M) shows much less high-frequency structuring than in the previous case, with $\Delta E = 22 \text{ mV m}^{-1}$. The top two panels of Figures 6a and 7a, i.e., the density and electric field waveforms in the N-S direction in the vicinity of the sheared plasma flows, show no visual

correlation with one another, and thus no cross-correlation studies were performed on them.

The MEM spectra of the electric field (using 20 filter weights because of the reduced number of observations in the 8-s interval) are shown in Figure 7b. In view of the 8-Hz Nyquist frequency, the slope fitting is performed in the range 1–5 Hz. In the highly conducting region (S_H) the spectral slope is quite steep, the power law index of the roll-off portion being -3.4 ± 0.02 . The psd at 5 Hz is only 3 dB above the noise floor. A remarkable change of both spectral shape and increased psd at the high-frequency end is evident in the large-FAC region data (S_I). The spectral slope is quite shallow and corresponds to a spectral index -1.6 ± 0.01 . In this case the psd at 5 Hz is 40 dB above the noise floor. Thus there is an enormous amount of power in the dc field fluctuation data down to 1.6 km as compared to that seen in the high-conductivity region. By considering the electrostatic fluctuation data from the comb filter spectrometer we will show below that enhanced power is observed at all scale lengths down to 10 m. The spectral sample obtained in the S_M region has a power law index and psd intermediate between those observed in the S_H and S_I regions. The power law index in this case is -2.8 ± 0.03 , and the psd at 5 Hz is 20 dB above the noise level. There is still a substantial amount of power at fluctuation scales of approximately 1 km but far less than the highly enhanced levels seen in conjunction with very large FAC densities.

Table 3 gives the slopes of the density $(\Delta N/N)$ and electric field (ΔE) spectra in the approximately 10- to 1-km scale length range for the two different kinds of sheared flows encountered in orbit 4429 and also in orbit 1189, which will be discussed later.

It had been our intent to provide a limited statistical study of the two categories of velocity shears represented by the samples S_I and S_M . A close examination of the velocity data showed that for category S_I , the velocity gradient scale lengths varied between 250 and 750 m and the shear frequencies

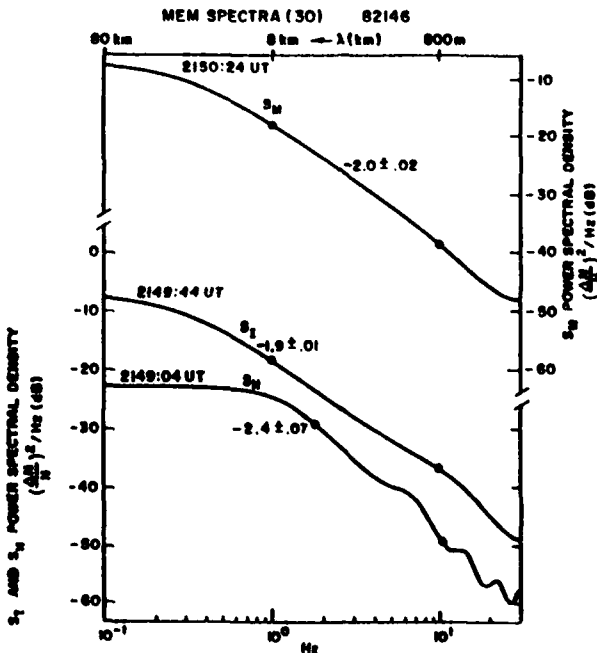


Fig. 6b

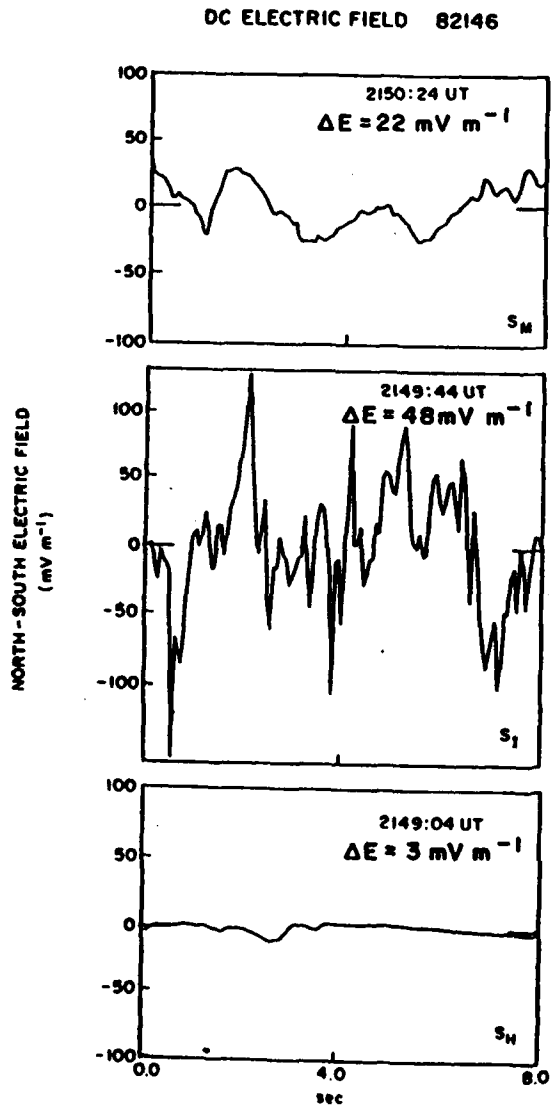


Fig. 7a

Fig. 7. (a) Three 8-s samples of dc electric field data with the corresponding ΔE value. (b) Their maximum entropy spectra. The times are the same as those for Figure 6. Note that the spectrum for 2150:24 UT is shown in the middle panel.

varied between 3 and 7 Hz with some examples of 10 Hz being occasionally observed. The very narrow intense FAC densities of the order of several tens of microamperes per square meter, which are seen in association with the large shear frequencies characteristic of S_1 , occur in such limited regions of space that even a limited statistical study is precluded. We consider this category very important, however, because of the elevated psd that is seen at the small scales of the density and electric field data, which will be presented shortly. This indicates that the high-FAC, large-shear regions provide an intense source for plasma density and electric field irregularities and, although limited in space, they merit a separate category.

The class represented by S_M is characterized by velocity gradient scale lengths of the order of 2–10 km (i.e., an order of magnitude larger than in S_1) and shear frequencies varying between 0.1 and 1 Hz. This category is also associated with much lower small-scale FAC densities of a few microamperes

per square meter. These less extreme background conditions are observed over larger regions of the morning oval and provide an opportunity for a limited statistical study. Figures 8a and 8b provide the results of such a study of the density and electric field spectral slopes (computed as in the above sample cases) observed during the period 2149:52–2154:08 UT. This study provides further substantiation of the results obtained with the case study for category S_M . The density spectral index histogram shows a prominent peak in the range of -1.8 to -2.0 with approximately half of the 24 samples falling in that range. A total of 80% of the density spectral samples have slopes $\leq |2|$. The corresponding histogram for the dc electric field spectral slopes of 31 samples shows a prominent peak in the range -2.5 to -3 with 75% of the population having slopes $> |2.5|$. Certainly, if one were to study the electric field fluctuation spectrum alone near velocity shear regions without the benefit of the other diagnostics available on DE 2, one would most likely conclude that the most probable value of the ΔE spectral slope is close to -3 . This is because the shallow spectral slopes are associated with the high-FAC density regions (category S_1) which are relatively narrow and tend to be averaged out in a statistical study. Thus earlier studies by Kintner [1976] and Kelley and Kintner [1978] quote a value of -2.8 ± 0.3 as the slope of the ΔE spectra in the several-kilometer scale length range.

To extend this spectral study to shorter scale lengths of $\Delta N/N$ and ΔE , we utilize the output of the filter combs on the RPA and VEFI, described earlier, with the various frequencies and corresponding scale lengths listed in Tables 1 and 2. The routine University of Texas at Dallas (UTD) density spectral analysis using the fast Fourier transform (FFT) technique is shown in Figure 9 for S_M , the data for which were shown in the top panel of Figure 6a; the MEM spectrum of the data was shown in the top panel of Figure 6b. In fact the power law index computed from the FFT algorithm over the scale length ranges 5–1 km agrees well with the spectral index derived from the MEM technique computed over 10–1 Hz. However, in addition, the four samplings (denoted by 1–4) in 8 s of the

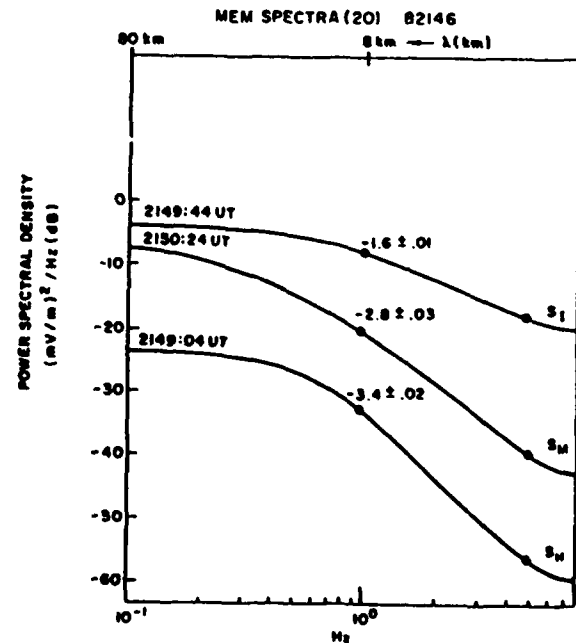


Fig. 7b

TABLE 3. Density and dc Electric Field Fluctuation Spectra Power Law Indices in Velocity Shear Regions ($\lambda \sim 10$ km to 1 km)

	Intense Shear (~10-Hz Frequency)		Moderate Shear (~1-Hz Frequency)	
	$\Delta N/N$	ΔE	$\Delta N/N$	ΔE
Orbit 4429	-1.9 ± 0.01	-1.6 ± 0.01	-2.0 ± 0.02	-2.8 ± 0.03
Orbit 1189	-1.9 ± 0.01	-1.8 ± 0.01	-1.7 ± 0.08	-3.6 ± 0.03

filter outputs have also been added to the FFT spectra (cf. Table 1), and a linear least squares fit is indicated through the points. The power law index of this latter portion is -2.6 . (Note that the psd of the cluster of points at 6.35 m scale length is below 10^{-9} Hz $^{-1}$ and is thus not shown on the diagram.) By reading off the psd of the best fit straight line, for example at the first two clusters of points at 125 m and 46.5 m, respectively, it is possible to determine the power in the density fluctuations at the shorter scales. In Figure 10 we plot the psd at 125 m and 46.5 m observed between 2147 and 2154 UT as read off from the best fit straight line of successive 8-s spectra, an example of which is shown in Figure 9. It is immediately obvious from Figure 10 that the largest psd at both scale lengths are observed in the large structured velocity regions (near S_i and S_M). The psd falls 2-3 orders of magnitude in the high-conductivity region (S_H) around 2149 UT and is also diminished by 1-3 orders within 2147-2148 UT, which, as discussed earlier, is probably a convected structure. Beyond 2151 UT the psd is found to decrease in concert with the reduced structures in the velocity. Since 50-m scale lengths have short lifetimes of the order of a minute [Vickrey and Kelley, 1982], large psd at this scale length most probably indicates that velocity shears in the convective plasma flow provide a source for such irregularities. While a histogram for the spectral slopes of the 125-m to 6-m irregularities within the S_H category is not shown, it is important to note that the slopes are somewhat steeper than those observed for their longer scale length counterparts (Figure 8a), 80% showing values of $>|2.0|$ with a mean value of -2.3 .

Several ac electric field fluctuation (ACE) spectra obtained from spectrometers A, B, and C of VEF1 corresponding fairly closely in time to the dc electric field spectra shown in the top two plots of Figure 7b are presented in Figures 11a and 11b. The ACE spectra in the high-conductivity region corresponding to the bottom plot of Figure 7b have little power above the instrument noise threshold and so are not shown. Figure 11a shows two spectra obtained in the intense shear and large-FAC region (S_i) at 2149:45 and 2149:50 UT. Very large psd, about 5 orders of magnitude larger than the instrument noise threshold, is seen at the three lowest frequencies of both spectra. Since both spectrometer A and B outputs are similar, the description will be given in terms of the frequencies used in spectrometer A. A power law index of -1.8 is seen between 6 and 24 Hz ($\lambda = 1300-325$ m) which agrees well with the index of -1.6 of the dc fluctuation spectra observed at longer scales over the 8-s S_i interval. Beyond 24 Hz there is a noticeable steepening of the spectral slope at both times to a value of -2.6 while the spectrum at 2149:50 also shows an interesting shoulder between 96 and 384 Hz ($\lambda = 80-20$ m). Such a shoulder had been seen earlier in the dayside cusp region by Curtis et al. [1982] at similar altitudes and attributed to O^+ ion cyclotron waves. Because of the existence of the ion cyclotron related shoulders in the ACE spectra, which cause a variability in the measured slopes, it is difficult to list them in a definitive manner as was done for the longer λ range in Table 3. It is also important to note that a steepening between 384 Hz ($\lambda = 20$ m) and 768 Hz ($\lambda = 10$ m) could be partially due to the antenna length of 21 m used in the experiment. It has been

ION DENSITY 82146 ORBIT #4429
2149:52 - 2154:08 UT

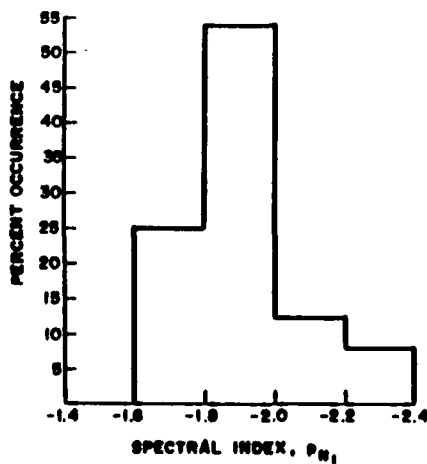


Fig. 8a

ELECTRIC FIELD 82146 ORBIT #4429
2149:52 - 2154:08 UT

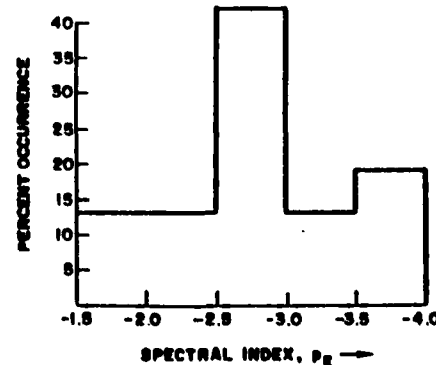


Fig. 8b

Fig. 8. (a) The histograms of spectral indices of density and (b) dc electric field fluctuations for the period 2149:52-2154:08 UT.

DE-2 MAY 26, 1982 ORBIT #4429

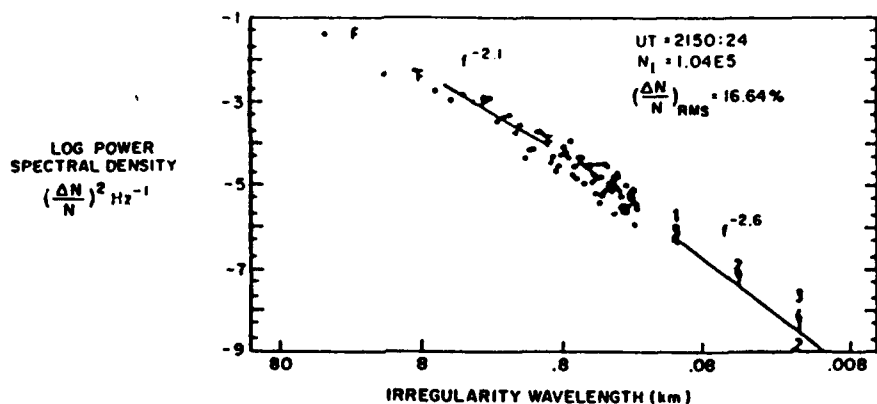


Fig. 9. The FFT spectra for the 8-s density sample shown in the top panel of Figure 6a. The numbers 1-4 at the short scale length end (< 125 m) represent four successive outputs within 8 s from the filter comb listed in Table I. The best fit straight line through the comb filter output is shown. The letters F at the long scale length end indicate a filter output representation of FFT spectra similar to that of the numbers 1-4.

shown earlier that irregularities with a scale length smaller than the antenna length will suffer attenuation by a variable factor depending on the length of the antenna in relation to the scale length being studied [Temerin, 1978].

Wave activity as monitored by the spectrometer C output is minimal, particularly in the O^+ lower hybrid (LH) frequency range of 4–16 kHz. This particular filter output is marked by an arrow on both spectra. It appears that O^+ LH waves are generally weak in the S_{M} regions characterized by high FAC.

In Figure 11b are plotted two ACE spectra obtained at 2150:10 and 2150:30 UT which are associated with the lesser sheared flows and smaller FAC in region S_{M} . Two major differences are noted between these two spectra and those shown in Figure 11a. First, the spectral index at the three lowest frequencies is much steeper, being of the order of -3 , and, second, the wave activity in the O^+ LH frequency range is 2 orders of magnitude more intense. The fact that the spectral index is steeper is consistent with the MEM spectral analysis of the dc data in the S_{M} regime (Figure 7b). It also seems likely that the background conditions that characterize the S_{M} regime, namely, moderate velocity shears and small FAC intensities, are associated with O^+ LH waves.

The two classes of ACE spectra, namely those shown in Figures 11a and 11b, are sufficiently different in their spectral slopes and associated wave behavior to merit further study. One major difference seemed to be in the type of particle precipitation associated with the two different regimes. Figure 12a shows a typical electron energy spectrum obtained at 2149:50 UT in the ion conic region with intense velocity shear and high FAC, while Figure 12b, obtained at 2150:09 UT, is its counterpart in the weaker shear and low-FAC region. In the first case the flux of electrons even at 10 keV is more than an order of magnitude larger than the instrument threshold (shown with the solid line) while in the second, there is no flux at energies > 700 eV. (Note that the two spectra are plotted on two different ordinate scales.) Even at the low energies (~ 100 eV) the number flux is an order of magnitude larger in the ion conic region, and at 10 eV it is 2 orders of magnitude larger. Heelis et al. [1984] have shown that this low-energy component has the characteristics of suprathermal bursts, described earlier by Johnstone and Winterningham [1982], superimposed on the background energetic Maxwellian population.

The second class of particle energy spectrum is similar to intense polar rain with its low average energy. This spectral type is associated with the O^+ LH wave activity. The background energetic population is missing in this case, and the number fluxes are smaller than in the conic region.

The second major difference is in the electron T_e and ion T_i temperature behavior. It was briefly mentioned in connection with Figure 2 that T_e showed a dramatic peak of 9000°K just prior to 2150 UT. In Figure 13 we show the highest-resolution measurements of T_e from LANG and T_i from RPA for a 1-min period commencing at 2149:30 UT. We note that between 2149:46 and 2149:52 UT, T_e/T_i is approximately 2 with T_i being 4000°K and T_e reaching values as high as 9000°K . This is the period of time that the ion conics are observed and the electric field spectra show shallow slopes. The high T_i regions where $T_e/T_i \sim 2$ with T_i varying between 4000° and 5000°K are all associated with steep ACE spectra, but the O^+ LH wave activity is greatly enhanced such as is seen at 2150:10 UT in Figure 11b. However, we wish to point out that $T_i > T_e$ is not a necessary condition for high O^+ LH wave activity to take place. At 2150:30 UT when $T_e > T_i$, O^+ LH waves are still fairly intense. What seems to be more important is the precipitation of electrons with an energy spectrum similar to that shown in Figure 12b.

Orbit 1189

This orbit of the DE 2 satellite traversed the morning sector of the northern auroral oval at 900 km altitude on October 22, 1981, during a magnetically disturbed period ($K_p = 7-$). This orbit was used by Heelis et al. [1984] to study the electrodynamic properties of the ionosphere when a high FAC density of the order of $100 \mu\text{A m}^{-2}$ flows at about 900 km altitude.

Plate 2 shows the LAPI data for this orbit reproduced from Heelis et al. [1984] in a format similar to that of Plate 1 for orbit 4429. In this case the most intense electron precipitation is seen near 2255:30 UT, and it is accompanied by a low-energy (30 eV) ion burst with a pitch angle distribution that is not of a classic conic type but is more consistent with both parallel and perpendicular acceleration of these ionospheric ions. The thermal plasma density in the vicinity of the conical distribution was $5 \times 10^4 \text{ cm}^{-3}$ in this case, a factor of 4

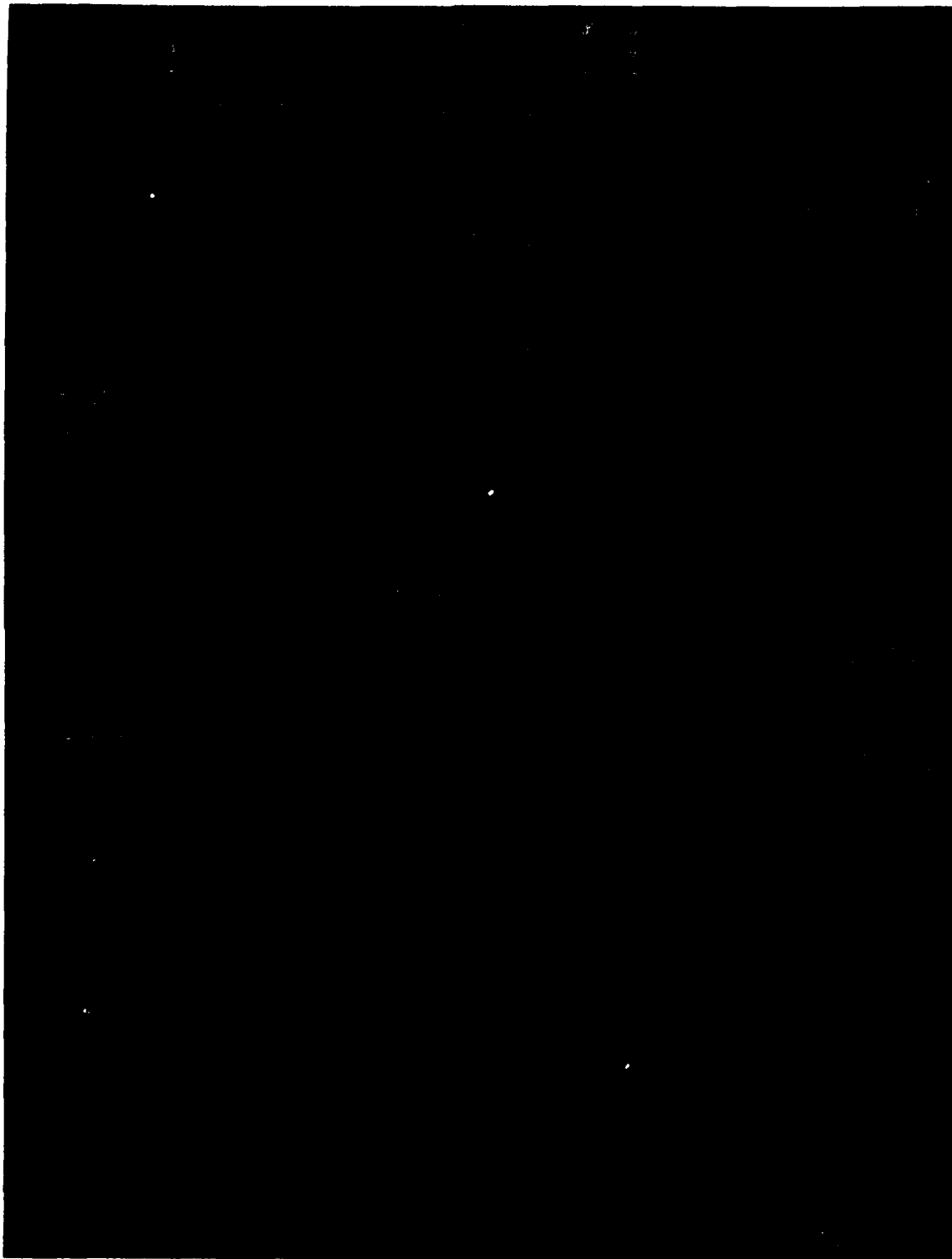


Plate 2. Same as in Plate 1 except for orbit 1189 and the upflowing ion event of 2255:30 UT.

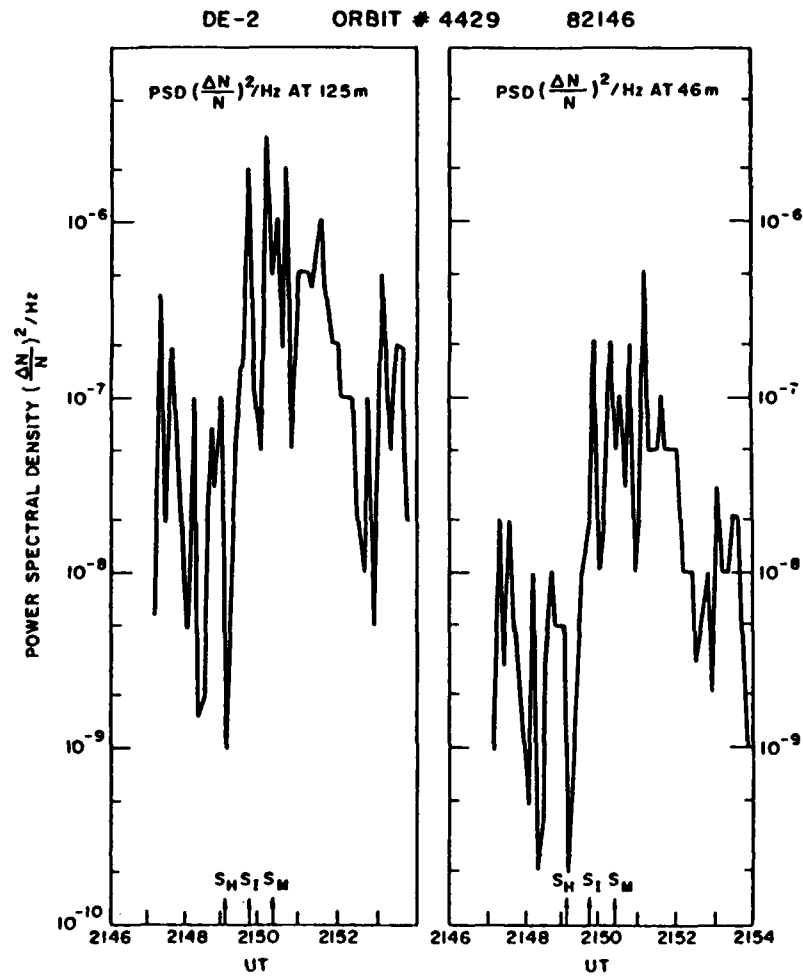


Fig. 10. The power spectral density at 125 m and 46.5 m read off from the best fit straight line such as is shown in Figure 9 for the period 2147-2154 UT. S_H , S_I , and S_M have the same meaning as in Figure 4.

smaller than in orbit 4429, consistent with the higher altitude of orbit 1189.

The ion concentration, three components of the ion drift, and the E-W component of the magnetic field are reproduced from Heelis et al. [1984] in Figure 14 for the period 2250-2258 UT, within which large structured velocities were observed. To these panels we have added a top one, which exhibits the irregularity amplitude $(\Delta N/N)_{\text{rms}}$ over 8 s of data similar to that which was shown in Figure 5. In this case, as in Figure 5, we note a large peak in $\Delta N/N$ at 2251:30 UT which is associated with the poleward edge of the trough but with little velocity structure in the ram direction. In conformity with the earlier case, the psd at short scales is much reduced in this structure, as may be observed from Figure 18, to be presented later. Several large peaks in irregularity amplitude associated with velocity shears are noted beyond 2253 UT with the largest peak being observed in conjunction with the sharpest gradient in the horizontal drift (i.e., N-S electric field). A very sharp gradient is also observed in the ϕ component (i.e., E-W) of MAG-B data which Heelis et al. [1984] estimate to be caused by an upward FAC density of $80 \mu\text{A m}^{-2}$. These authors further note that an upward thermal velocity (negative parallel drift) is observed between 2254 and 2256 with the most intense upward thermal fluxes being observed at the

maximum gradient of ΔB_ϕ at 2255:30 UT. Thus the earlier work of these authors provides a fairly comprehensive description of the background conditions in which our density and electric field spectral characteristics are embedded.

Spectral Analysis of Orbit 1189

We show in Figures 15a and 15b two samples of 8-s high-resolution density data commencing at 2255:24 and 2255:40 UT. By referring to the ΔB_ϕ panel of Figure 14 we note that the first sample is associated with the largest-FAC region (S_I) while the second one is associated with a much smaller gradient and hence a much lower FAC region (S_M). The irregularity amplitude is 14.7% in the first case and 5.2% in the second. However, since high-frequency structure is evident in both, the spectral indices in Figure 15b are virtually identical, both being slightly shallower than -2, as was also observed under similar conditions in orbit 4429.

Figures 16a and 16b show the corresponding electric field data and their spectra. There is a fairly drastic variation observed in the electric field data in Figure 16a, and this is reflected in the corresponding spectra shown in Figure 16b with the high-FAC region (S_I) showing a slope similar to that of the density spectra, while in the small-FAC region (S_M) the electric field spectrum is much steeper than the density spec-

**82146 ORBIT # 4429
DE-2 VEFI AC SPECTRA**

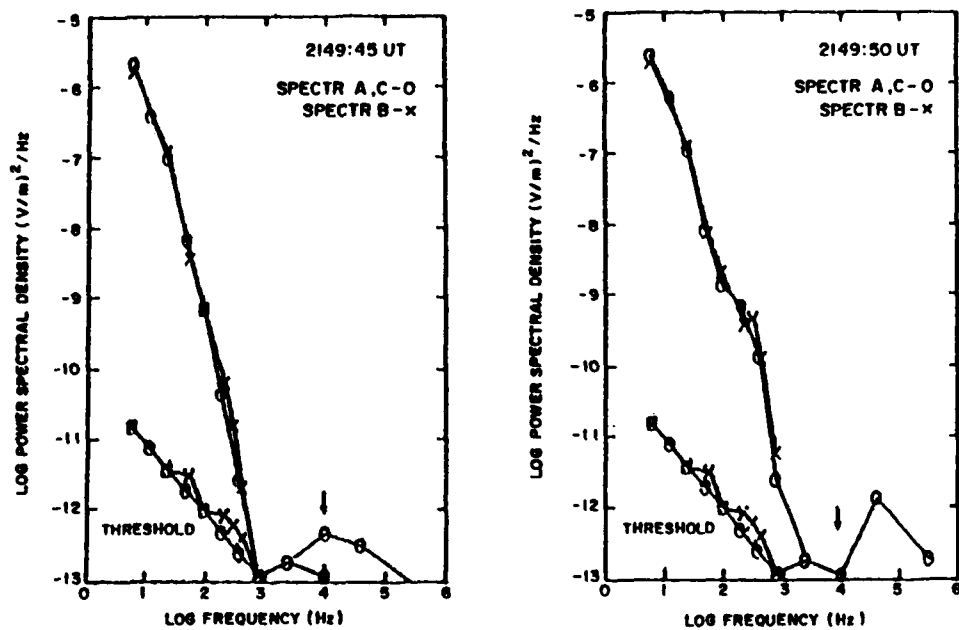


Fig. 11a. Two 1-s ac electric field fluctuation spectra obtained at 2149:45 and 2149:50 UT in the S_i region. The arrows indicate the O^+ lower hybrid wave frequency range. The noise threshold of the instrument is shown.

trum. It is encouraging to note that this basic description of these two classes of $\Delta N/N$ and ΔE spectra is valid for both DE 2 orbits even though the data are obtained from two quite different altitudes, as is evident from Table 3.

A limited statistical study confined only to the S_M regime

(for the reasons outlined in conjunction with orbit 4429) is shown in Figures 11a and 11b for the period covering 2255:32-2258:04 UT. The data again portray a prominent density spectral peak in the -1.8 to -2.0 range with 90% of the samples showing a slope $<|2|$. The electric field spectra

**82146 ORBIT #4429
DE-2 VEFI AC SPECTRA**

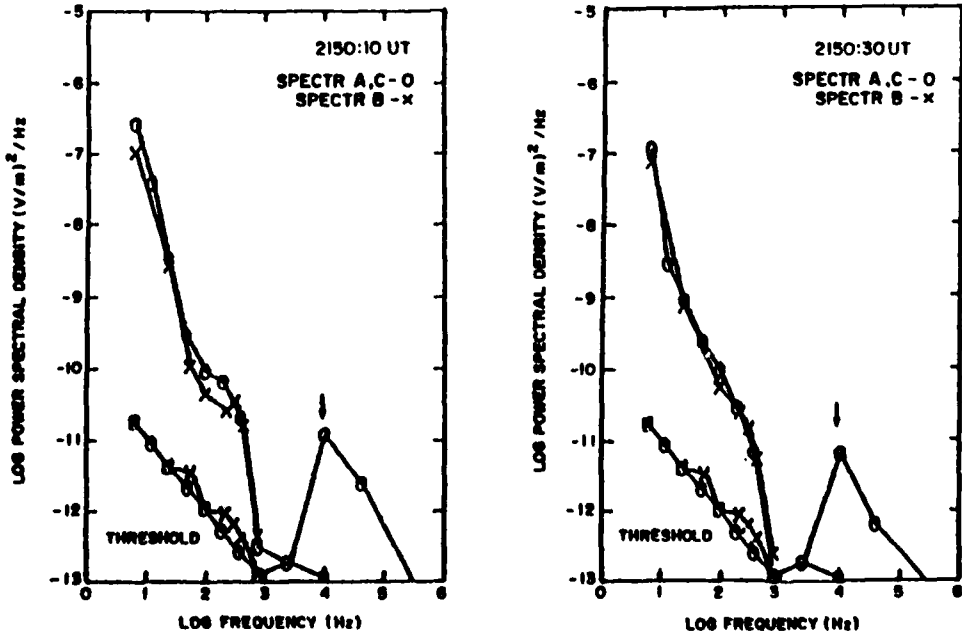


Fig. 11b. Two 1-s ac electric field fluctuation spectra obtained at 2150:10 and 2150:30 UT in the S_M region. The arrows have the same meaning as in Figure 11a.

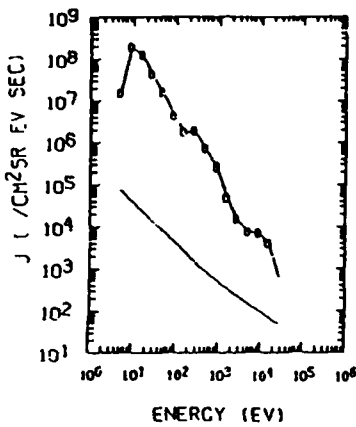
DYNAMICS EXPLORER 2
LOW ALTITUDE PLASMA INSTRUMENT

Fig. 12a

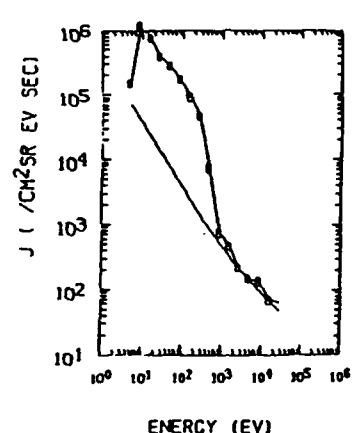
DYNAMICS EXPLORER 2
LOW ALTITUDE PLASMA INSTRUMENT

Fig. 12b

Fig. 12. Energetic electron precipitation spectra at 2149:50 (in the S_I region) and at 2150:09 (in the S_M region). The straight line on the spectra indicates the lowest significant counts in each channel.

clearly show the existence of much steeper slopes than the density, with 75% being $>|3.0|$. Thus even the statistical studies (albeit limited) of $\Delta N/N$ and ΔE spectra in the S_M regime belonging to the two DE 2 orbits agree well with one another, with the higher-altitude orbit showing somewhat steeper ΔE spectral slopes than its lower-altitude counterpart.

To extend the study of spectral behavior to shorter scale lengths for the density, we utilize the UTD spectra and plot, in Figure 18, the filter output at 125 m as a function of time

through the diffuse auroral region up to approximately 2253 UT (cf. Plate 1) where one sees little velocity structure (cf. Figure 14) and into the highly structured velocity region beyond that. We note about 2 orders of magnitude less power at 125 m in the convected structure and diffuse auroral regions as compared to the structured velocity region indicated by S_I and S_M . The psd at 46.5 m exhibits similar behavior and is not shown here.

The ACE fluctuation spectra in the large- and small-FAC

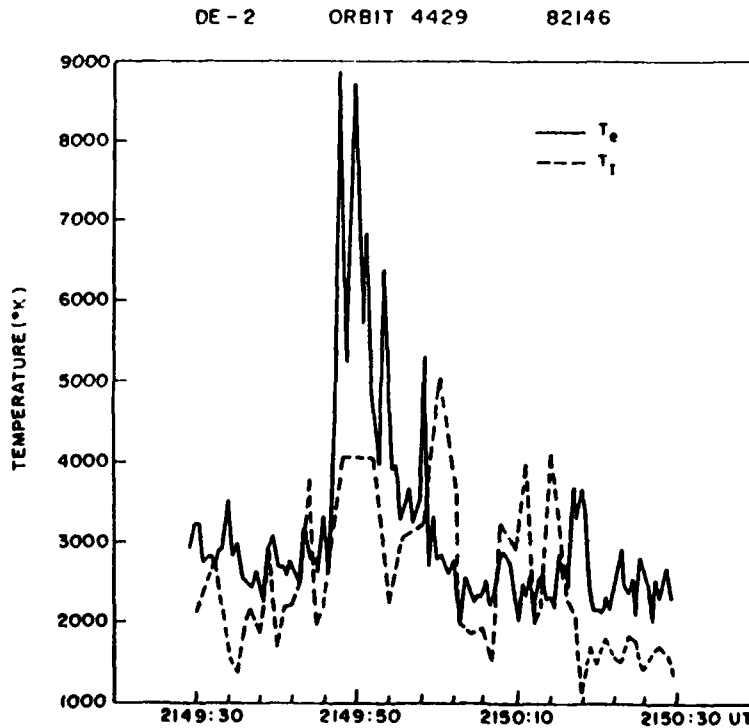


Fig. 13. High-resolution electron (T_e) and ion (T_i) temperatures observed between 2149:30 and 2150:30 UT.

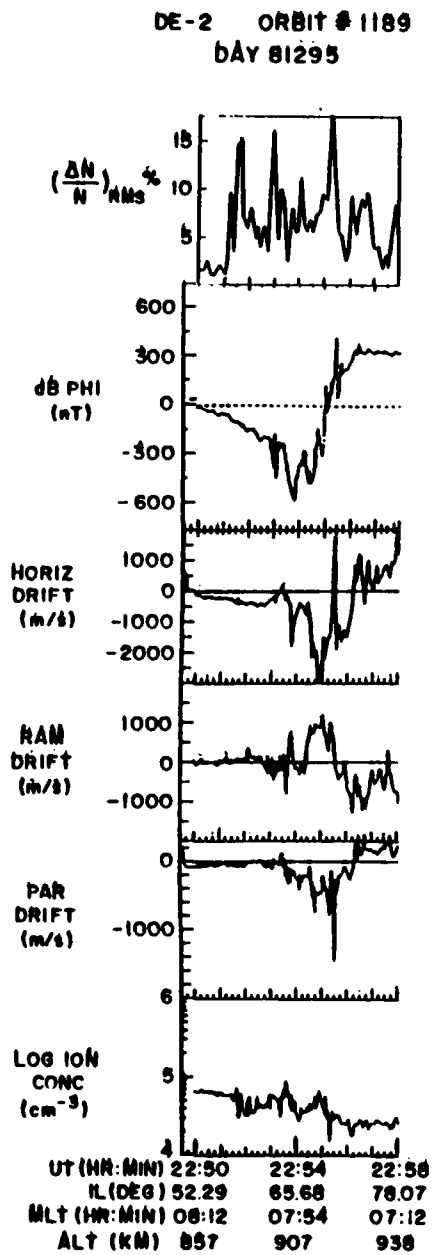


Fig. 14. The ion concentration (bottom panel), three components of ion drift, the magnetometer, and the irregularity amplitude $(\Delta N/N)_{\text{RMS}}$ computed every 8 s for the period 2250-2258 UT.

regions are shown in Figures 19a and 19b. Again a great degree of similarity is seen in their spectral shape when compared with their counterparts for orbit 4429 shown in Figures 11a and 11b. The high-FAC region ACE spectrum of 2255:30 shows a shallow slope at the three lowest frequencies and a flattening in the 48- to 96-Hz range. Heelis et al. [1984] point out that it is possible for the O^+ ion cyclotron wave to be Doppler shifted to such frequencies. Virtually negligible wave activity near the O^+ LH frequency is observed in Figure 19a. In contrast, a much steeper spectrum is observed at the lowest frequencies, and more than an order of magnitude pad enhancement is seen in the O^+ LH wave band at 2255:40 UT.

Again we find a remarkable consistency in the ACE spectral behavior between orbit 4429 and orbit 1189.

The high-resolution T_s and T_i behavior in the interval 2254:40-2255:40 UT is shown in Figure 20. The ACE spec-

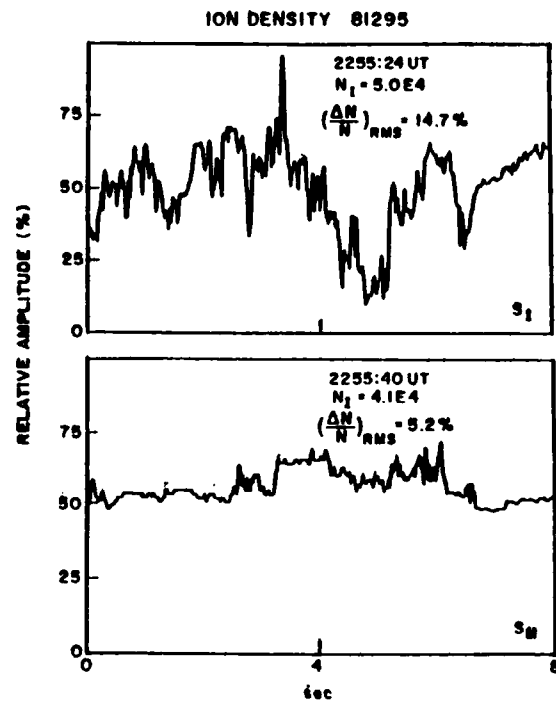


Fig. 15a

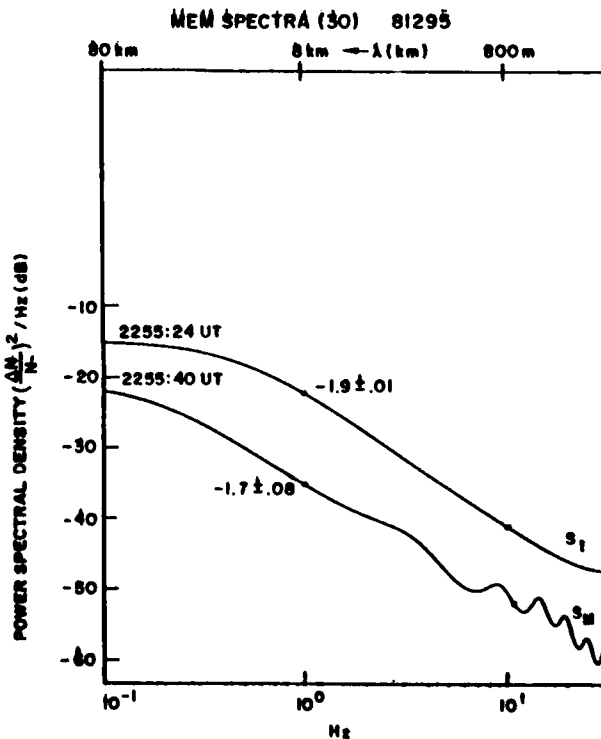


Fig. 15. Two samples of 8-s density data found in the S_I (2255:24) and S_M (2255:40) regions, respectively, of orbit 1189 and their respective maximum entropy spectra.

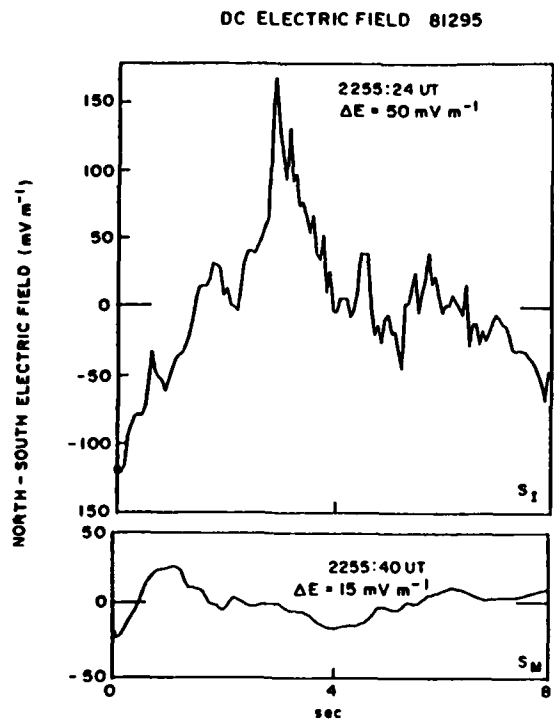


Fig. 16a

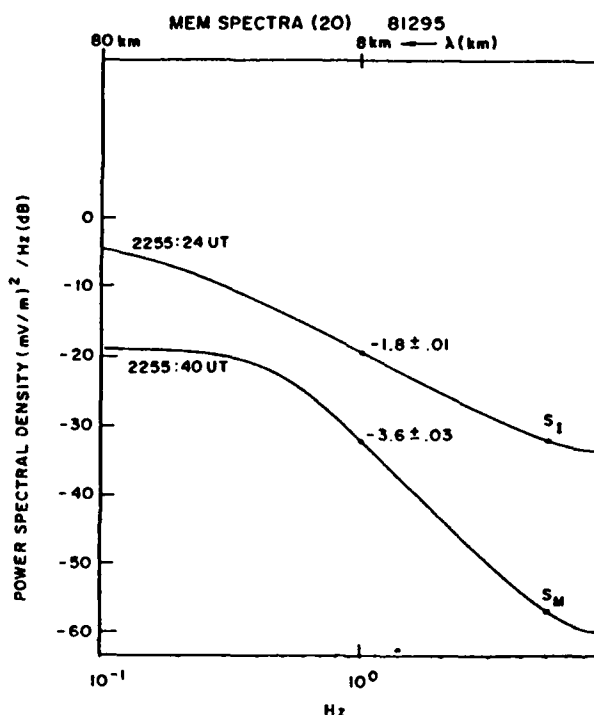


Fig. 16b

Fig. 16. Two samples of 8-s dc electric field data and their maximum entropy spectra. The times are the same as those for Figure 15.

trum at 2255:30 was obtained at a time when the T_e/T_i ratio was as large as 5. At least three instances are visible in Figure 20 where T_e peaks in excess of 8000°K are associated with T_i values below 4000°K. This feature seems to be a characteristic

of only the high-altitude region and is probably due to the lower plasma densities encountered. The ACE spectrum at 2255:40 was obtained when $T_i/T_e \sim 2$, but we wish to add that the O⁺ LH band wave activity is not confined only to high T_i

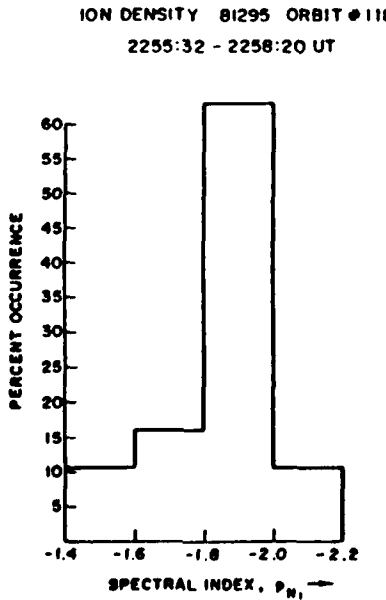


Fig. 17a

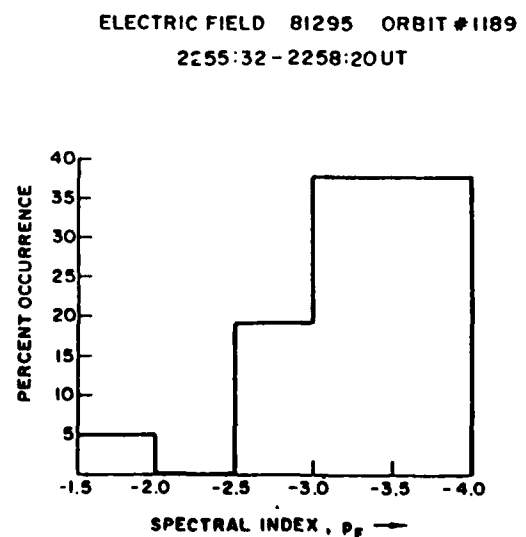


Fig. 17b

Fig. 17. (a) Histograms of spectral indices of density and (b) dc electric field fluctuations for the period 2255:32-2258:20 UT.

DE-2 DAY 81295 ORBIT 1189

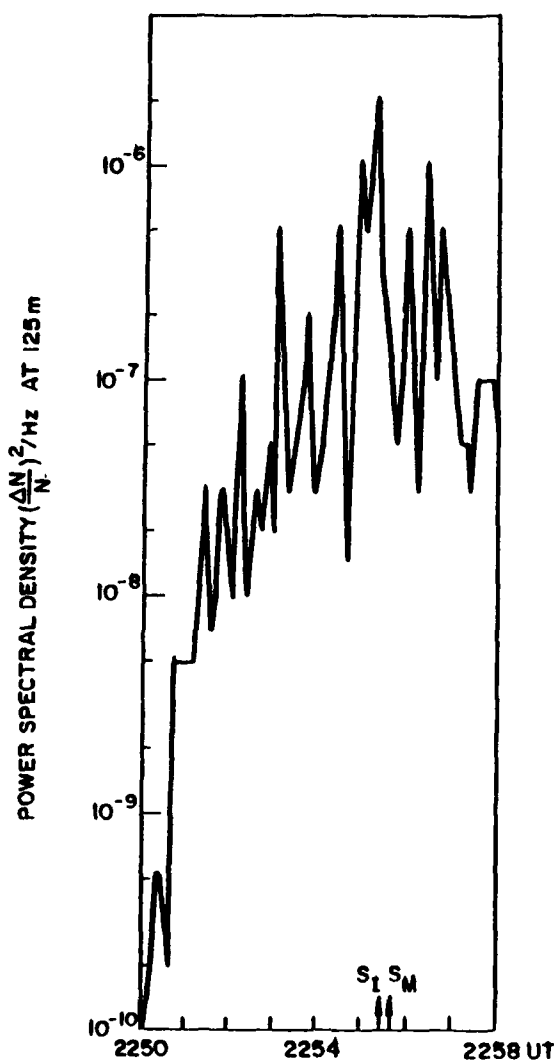


Fig. 18. Power spectral density of 125-m scale length irregularity between 2250 and 2258 UT. S_1 and S_2 have the same meaning as in Figure 16.

regions but seems more related to the nature of the low-energy (~ 100 eV) electron precipitation, as was also seen in orbit 4429.

DISCUSSION

The study of simultaneous density and electric field fluctuation spectra in the vicinity of sheared plasma flows in the auroral oval conducted with two DE 2 orbits at two different altitudes within the F region and the topside ionosphere provides us with two fairly distinctive behavior patterns depending on whether the associated FAC intensities are large or small. The $\Delta N/N$ spectra in both categories were characterized by spectral indices somewhat shallower than [2] with large peaks at short scale lengths down to several tens of meters. The ΔE spectra, on the other hand, were quite different in these two situations. The spectral slopes in intense shear regions (S_1) with large FAC were found to be somewhat shallower than [2] (i.e., similar to $\Delta N/N$ spectra) down to a scale

length of several hundred meters and then steepened considerably to indices of -3 and steeper. The second category of ΔE spectra associated with less extreme background conditions (S_2) had spectral indices of the order of -3 throughout the scale length range from 10 km to 100 m and thus were much steeper than the corresponding density spectra. We present in Figure 21 an idealized representation of the two categories of spectra observed in conjunction with velocity shears in the auroral oval. The observed spectral indices for the $\Delta N/N$ and ΔE spectra covering the ranges -1.8 ± 0.2 and -3 ± 0.5 , respectively, are shown in the diagram. The short scale length ends of the density spectra are shown by dashed lines to indicate uncertainties in spectral indices arising from noise contamination of power spectral estimates and a gap in the frequency coverage between the end of the FFT/MEM spectra and the center frequency of the first filter output, as mentioned earlier.

It is interesting to compare these observational results with predictions of the various fluid plasma models that have been proposed to describe the dynamics of the turbulent ionosphere. Application of standard cascade theory to these models leads to definite relationships between the power spectral indices of simultaneously measured density and electric field fluctuations. Fejer and Kelley [1980] point out that this method of describing turbulent plasmas circumvents the linear instability theory completely and addresses directly the fully developed state as encountered in the present observations. Kintner and Seyler [1985] in their comprehensive review of high-latitude plasma turbulence have provided a framework for this comparison. We refer the reader to their Table 1, listing ΔN and ΔE spectral slopes for different plasma instabilities. It should be noted that spectra of ΔN and $\Delta N/N$ are expected to be the same if $\Delta N/N \ll 1$ as in the present case where the largest value of $\Delta N/N = 0.2$ (C. E. Seyler, private communication, 1986). In the parlance of two-dimensional fluid turbulence the direct cascade region is defined as $k_i \ll k \ll k_d$, and the inverse cascade region as $k_d \ll k \ll k_i$, where k_i represents the wave number at which energy is being injected into the system, k_d the dissipation wave number, and k_d the smallest allowable wave number of the system.

For our S_1 category depicted in Figure 21, if we identify the break scale in the ΔE spectrum occurring at approximately 300 m (approximately the shear gradient scale length) with the scale size at which energy enters the system, then we find reasonable agreement with the predictions of the KH instability in the inverse and direct cascade regimes as listed by Kintner and Seyler [1985]. However, this agreement is probably fortuitous since their analysis does not consider the effects of intense FAC which is a major characteristic of this class of spectra. Further, their analysis treats the density as a passive scalar so that all collisional effects are disregarded.

Recent work by Keskinen et al. [1988] has shown that the inclusion of Pedersen conductivity effects (i.e., ion-neutral collisions) alters the nonlinear evolution of the KH instability in a fundamental way by inhibiting the well-known vortex formation (commonly observed in the collisionless magnetosphere) but leading to the development of anisotropic structures with different power law indices in the two directions perpendicular to the magnetic field. These authors showed that in the near-space environment the important parameter to consider is the ratio $v = \Sigma_p/C_M$, where $\Sigma_p = \int \sigma_p dz$ is the field line integrated Pedersen conductivity and $C_M = \int C_M dz$ is the field line integrated inertial capacitance discussed earlier by Mitchell et al. [1985]. When $\Sigma_p \sim 3.5$ mhos and $C_M \sim 10$ farads, and then $v = 0.35$ Hz, a plausible value in the F region, the simulations show that in the direction of the

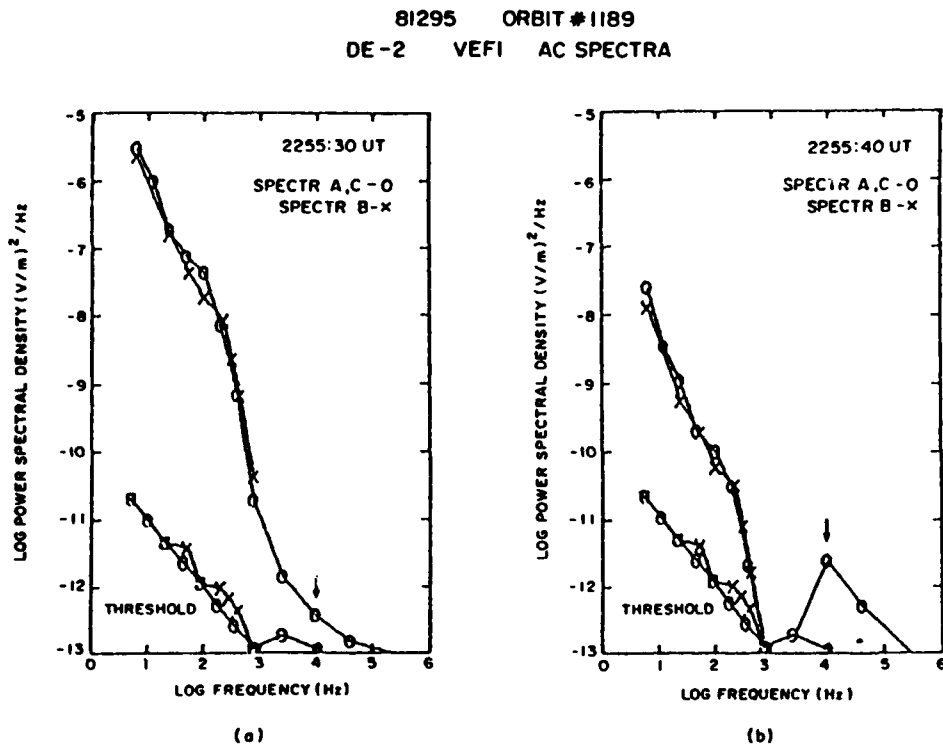


Fig. 19. One-second ac electric field fluctuation spectrum obtained at (a) 2255:30 in the S region and (b) 2255:40 UT in the S_x region. The arrows have the same meaning as in Figure 11.

velocity shear the $\Delta N/N$ spectra yield a power law index of -1.7 ± 0.3 with the corresponding ΔE spectrum yielding an index of -3.3 ± 0.2 [Keskinen et al., 1988, Figures 13 and 14]. These results are in good agreement with our observations for the S_M category. It should be noted that in the Keskinen et al. [1988] study the parameters for their simulation were similar to those of our S_M group, so that the agreement between our observations and their simulations of the collisional KH instability is quite encouraging.

Further, in view of the control of spectral characteristics by the parameter v , which is a ratio of two field line integrated quantities, local values of ion-neutral collision frequencies are not very meaningful parameters in determining the instability regime (collisional or inertial). This is probably reflected in similar spectral characteristics that were observed in the two DE 2 orbits having altitudes of 350 km and 900 km, even though the local values of ion-neutral collision frequencies are quite different at these heights.

We wish to point out that the background conditions associated with the S category are very complex. While we have chosen to emphasize the intense velocity shear and large FAC intensities, it is nevertheless true that it is in this region that one finds the largest precipitating fluxes which produce large T_e enhancements and large conductivity gradients. Thus in addition to velocity shear one expects possible contributions to irregularity generation from the current-driven electrostatic ion cyclotron [Satyanarayana et al., 1985], current convective [Chaturvedi and Ossakow, 1981], and thermal [Lee, 1984] instabilities. The result of these possible multiple sources on irregularity generation is fairly spectacular, with the most sensitive indicator, namely, psd at scales smaller than 125 m,

being orders of magnitude larger than in contiguous regions. Obviously, more work on observations and theory is necessary for a better understanding of the multiple sources and sinks of energy affecting density and electric field fluctuation spectra in such regions.

We have also shown in this paper that in regions of uniform energetic particle precipitation such as the diffuse aurora, which gives rise to fairly uniform E region Pedersen and Hall conductivities, the $\Delta N/N$ and ΔE spectra are both steep with little psd at the small scales even though the irregularity amplitudes at the longer scales may be fairly large, as was also observed by AE-D [Basu et al., 1984]. We believe these spectral slopes are more a consequence of the scale length-dependent lifetimes of the irregularities [Heelis et al., 1985] rather than a reflection of a specific instability process.

One distinct difference seems to be emerging in regard to small-scale irregularities (< 100 m) at high latitudes when they are compared to their counterparts in equatorial spread F . Drift waves seem to play a prominent role in the generation of short-scale irregularities in equatorial spread F . In drift wave turbulence, ΔE spectra follow the same behavior as in the KH case; however, the density is constrained to follow the Boltzmann relation. Thus in the direct cascade regime we have $\Delta N/N$ spectra described by a k^{-3} slope. Such slopes were found with the equatorial Plume and Project Condor rocket campaigns at $\lambda < 100$ m and at altitudes > 300 km [Kelley et al., 1982; LaBelle et al., 1986]. The results of this study show that at high latitudes the ΔE spectrum seems steeper than the $\Delta N/N$ spectrum.

The finding in this paper that the $\Delta N/N$ spectra are either equal in slope to or shallower than ΔE spectra has interesting

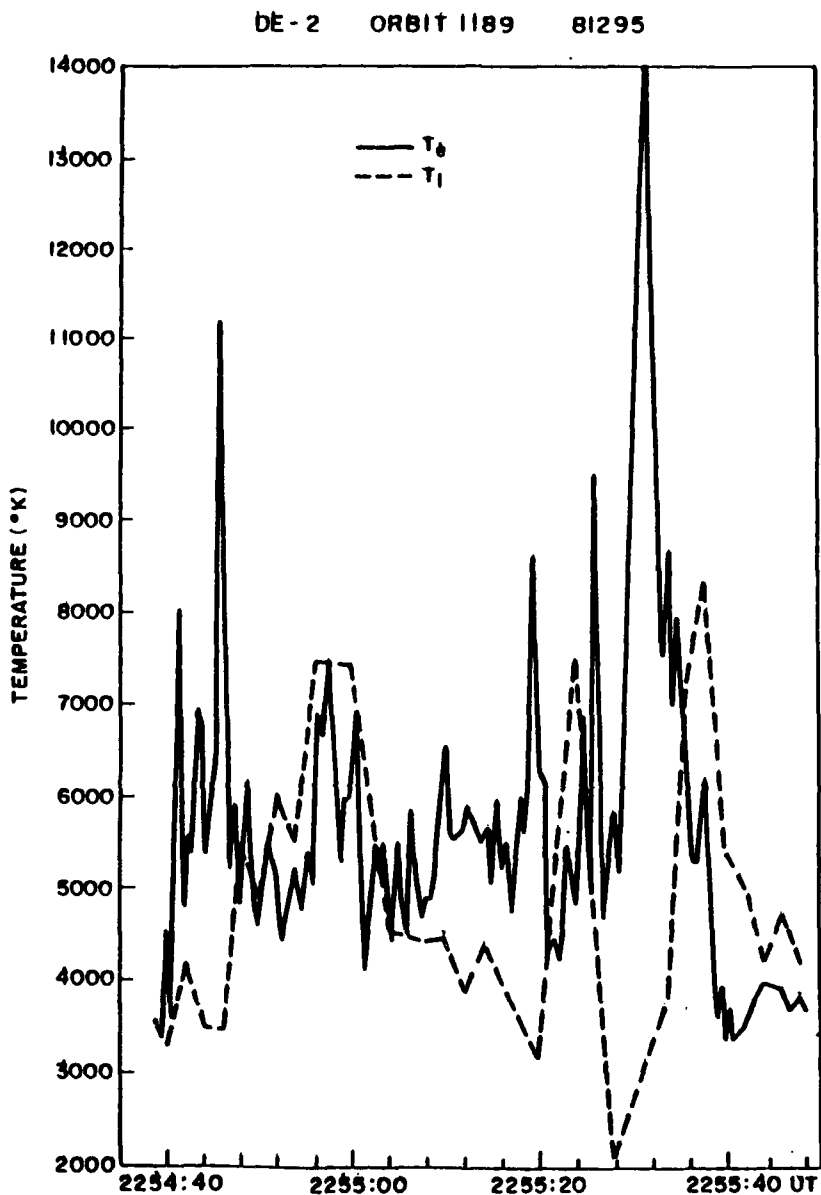


Fig. 20. High-resolution electron (T_e) and ion (T_i) temperatures observed between 2254:40 and 2255:40 UT.

ramifications for the interpretation of scintillation measurements. Scintillation spectra are expected to be influenced by both density and velocity spectra. However, Lotova [1981] pointed out that the scintillation spectrum would actually map the spectrum (either density or velocity) that has the shallower slope. It is thus expected that near velocity shear regions we should be able to deduce the density spectra from scintillation spectral studies as was done in the past [Rufenach, 1974]. Further, Carstens et al. [1985] showed that for the gradient drift instability the $\Delta N/N$ spectrum is also either equal to or shallower than the electric field power spectrum depending on whether the measurements are made in the instability source region or the diffusion regime. Thus the scintillation spectra should generally map the density structure at high latitudes.

While wave activity has been covered in a fairly cursory manner in this paper, we would nevertheless like to point out observed relationships between some recent theories and DE 2 data. For instance, the DE data seems to indicate that ion conics and most probably O^+ ion cyclotron waves are associated with large intensities of FAC while the O^+ LH waves are generally observed in association with precipitating 100-eV electrons in intense polar rain. Thus while we find experimental support for the theory of the current-driven ion cyclotron instability in the bottomside ionosphere [Chaturvedi, 1976; Satyanarayana et al., 1985], we do not seem to find similar experimental verification for the excitation of the O^+ LH instability by longitudinal currents [Satyanarayana and Chaturvedi, 1986]. In this respect, we wish to point out that many of the earlier measurements referred to by these authors

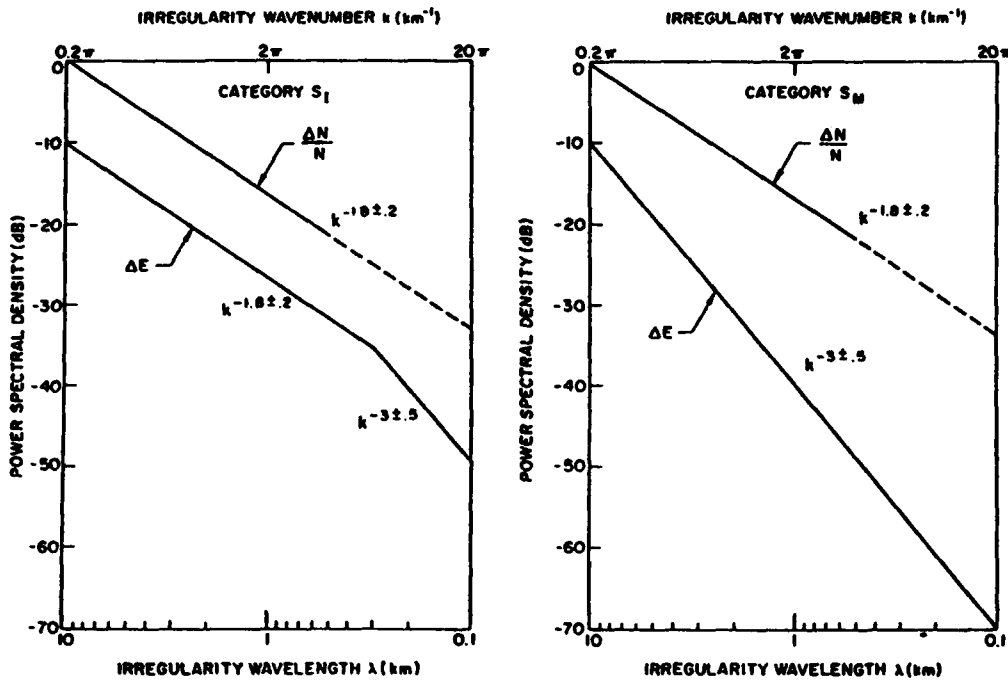


Fig. 21. Idealized representation of the two categories of $\Delta N/N$ and ΔE spectra observed in association with velocity shears in the auroral oval: category S_1 for intense shears (~ 10 Hz), and category S_2 for moderate shears (~ 1 Hz). The $\Delta N/N$ and ΔE spectra have been arbitrarily separated. The short scale length ends of the $\Delta N/N$ spectra are shown dashed because of uncertainty in psd estimates (see text).

did not have as complete a set of particle, field, and current measurements as the present set. For instance, the rocket measurements of Yau *et al.* [1983], which detected low-altitude (400–600 km) ion acceleration events consistent with ion cyclotron wave phenomena did not have a simultaneous measurements of FAC. Thus it is hoped that these DE 2 measurements will provide fairly stringent conditions for testing many of the theories postulated for the generation of irregularities and waves in the high-latitude ionosphere.

Acknowledgments. We wish to thank R. A. Hoffman, the DE project scientist, for his help and interest in the work. R. A. Heelis and L. H. Brace, the principal investigators of the IDM and LANG experiments, made their data readily available for this study. C. S. Lin and B. G. Ledley were also very helpful in providing data from LAPI and MAG-B. We acknowledge useful discussions with C. E. Seyler, P. Satyanarayana, P. K. Chaturvedi, M. J. Keskinen, R. A. Heelis, and C. L. Rino. The work at AFGL was supported in part by AFOSR task 2310G9. The work at Emmanuel College was partially supported by NASA grant NAG5-456 and AFGL contract F19628-86-K-0038. The work at the University of Texas at Dallas was supported by NASA grants NAG5-305 and NAG5-306. The work at Southwest Research Institute was supported by NASA contract NASS-28712, AFGL contract F19628-84-N-0006, and AFOSR contract F49620-85-C-0029. M.S. and N.C.M. gratefully acknowledge support by the Goddard Space Flight Center in the analysis of the electric and magnetic field data. We appreciate the comments of the two referees.

The Editor thanks two referees for their assistance in evaluating this paper.

REFERENCES

Basu, S., S. Basu, E. MacKenzie, W. R. Coley, W. B. Hanson, and C. S. Lin, F region electron density irregularity spectra near auroral acceleration and shear regions, *J. Geophys. Res.*, **89**, 5554, 1984.
 Basu, S., S. Basu, C. Senior, D. Weimer, E. Nielsen, and P. F. Fougerre, Velocity shears and sub-km scale irregularities in the nighttime auroral F-region, *Geophys. Res. Lett.*, **13**, 101, 1986.
 Cenker, J. C., J. J. Berthelier, and C. Beghin, Unstable density gradients in the high-latitude ionosphere, *Radio Sci.*, **20**, 755, 1985.
 Chaturvedi, P. K., Collisional ion cyclotron waves in the auroral ionosphere, *J. Geophys. Res.*, **81**, 6169, 1976.
 Chaturvedi, P. K., and S. L. Ossakow, The current convective instability as applied to the auroral ionosphere, *J. Geophys. Res.*, **86**, 4811, 1981.
 Curtis, S. A., W. R. Hoegy, L. A. Brace, N. C. Maynard, M. Sugiura, and J. D. Winningham, DE-2 cusp observations: Role of plasma instabilities in topside ionospheric heating and density fluctuations, *Geophys. Res. Lett.*, **9**, 997, 1982.
 Farthing, W. H., M. Sugiura, B. G. Ledley, and L. J. Cahill, Jr., Magnetic field observations on DE-A and -B, *Space Sci. Instrum.*, **5**, 551, 1981.
 Fejer, B. G., and M. C. Kelley, Ionospheric irregularities, *Rev. Geophys.*, **18**, 401, 1980.
 Fougerre, P. F., On the accuracy of spectrum analysis of red noise processes using maximum entropy and periodogram methods: Simulation studies and application to geophysical data, *J. Geophys. Res.*, **90**, 4355, 1985.
 Fredricks, R. W., and F. V. Coroniti, Ambiguities in the deduction of rest frame fluctuation spectra from spectra computed in moving frames, *J. Geophys. Res.*, **87**, 5591, 1976.
 Guzdar, P. N., P. Satyanarayana, J. D. Huba, and S. L. Ossakow, Influence of velocity shear on the Rayleigh-Taylor instability, *Geophys. Res. Lett.*, **9**, 547, 1982.
 Hanson, W. B., R. A. Heelis, R. A. Power, C. R. Lippincott, D. R. Zuccaro, B. J. Holt, L. H. Harmon, and S. Sanatani, The retarding potential analyzer for Dynamics Explorer-B, *Space Sci. Instrum.*, **5**, 503, 1981.
 Heelis, R. A., W. B. Hanson, C. R. Lippincott, D. R. Zuccaro, L. H. Harmon, B. J. Holt, J. E. Doherty, and R. A. Power, The ion drift meter for Dynamics Explorer-B, *Space Sci. Instrum.*, **5**, 511, 1981.
 Heelis, R. A., J. D. Winningham, M. Sugiura, and N. C. Maynard, Particle acceleration parallel and perpendicular to the magnetic field observed by DE-2, *J. Geophys. Res.*, **89**, 3893, 1984.
 Heelis, R. A., J. F. Vickrey, and N. B. Walker, Electrical coupling effects on the temporal evolution of F layer plasma structure, *J. Geophys. Res.*, **90**, 437, 1985.
 Hoffman, R. A., and E. R. Schmerling, Dynamics Explorer program: An overview, *Space Sci. Instrum.*, **5**, 345, 1981.
 Huba, J. D., S. L. Ossakow, P. Satyanarayana, and P. N. Guzdar, Linear theory of the E × B instability with an inhomogeneous electric field, *J. Geophys. Res.*, **88**, 425, 1983.

Johnstone, A. D., and J. D. Winnigham, Satellite observations of suprathermal electron bursts, *J. Geophys. Res.*, **87**, 2321, 1982.

Kelley, M. C., and P. M. Kintner, Evidence for two-dimensional inertial turbulence in a cosmic-scale low- β plasma, *Astrophys. J.*, **220**, 339, 1978.

Kelley, M. C., and F. S. Mozer, A satellite survey of vector electric fields in the ionosphere at frequencies of 10 to 500 Hz. I. Isotropic, high-latitude electrostatic emissions, *J. Geophys. Res.*, **77**, 4158, 1972.

Kelley, M. C., R. Pfaff, K. D. Baker, J. C. Ulwick, R. Livingston, C. Rino, and R. Tsunoda, Simultaneous rocket probe and radar measurements of equatorial spread F: Transitional and short wavelength results, *J. Geophys. Res.*, **87**, 1575, 1982.

Keskinen, M. J., and S. L. Ossakow, Theories of high-latitude ionospheric irregularities: A review, *Radio Sci.*, **18**, 1077, 1983.

Keskinen, M. J., H. G. Mitchell, J. A. Fedder, P. Satyanarayana, S. T. Zalesak, and J. D. Huba, Nonlinear evolution of the Kelvin-Helmholtz instability in the high-latitude ionosphere, *J. Geophys. Res.*, **93**, 137, 1988.

Kintner, P. M., Observations of velocity shear driven plasma turbulence, *J. Geophys. Res.*, **81**, 5114, 1976.

Kintner, P. M., and C. E. Seyer, The status of observations and theory of high-latitude ionospheric and magnetospheric plasma turbulence, *Space Sci. Rev.*, **41**, 91, 1985.

Kofman, W., and V. B. Wickwar, Very high electron temperatures in the daytime F region at Sondrestrom, *Geophys. Res. Lett.*, **11**, 919, 1984.

Krebsel, J. P., L. H. Brace, R. F. Thoia, W. H. Pinkus, and R. B. Kaplan, The Dynamics Explorer Langmuir probe instrument, *Space Sci. Instrum.*, **3**, 493, 1981.

LaBelle, J., M. C. Kelley, and C. B. Seyer, An analysis of the role of drift waves in equatorial spread F, *J. Geophys. Res.*, **91**, 5513, 1986.

Lee, M. C., Ohmic dissipation of Pedersen current as the cause of high-latitude F region ionospheric irregularities, *J. Geophys. Res.*, **89**, 7482, 1984.

Lin, C. S., and R. A. Hoffman, Narrow burst of intense electron precipitation fluxes within inverted-V events, *Geophys. Res. Lett.*, **9**, 211, 1982.

Lotova, N. A., Temporal scintillation spectra with allowance for the solar wind velocity distribution: Theory, *Geomagn. Aerov. Engl. Transl.*, **21**, 447, 1981.

Maynard, N. C., E. A. Melecki, and H. F. Burch, Instrumentation for vector electric field measurements from DE-B, *Space Sci. Instrum.*, **5**, 523, 1981.

Mitchell, H. G., J. A. Fedder, M. J. Keskinen, and S. T. Zalesak, A simulation of high-latitude F-layer instabilities in the presence of magnetosphere-ionosphere coupling, *Geophys. Res. Lett.*, **12**, 283, 1985.

Mozer, F. S., Power spectra of the magnetospheric electric field, *J. Geophys. Res.*, **76**, 3651, 1971.

Mozer, F. S., C. W. Carlson, M. K. Hudson, R. B. Torbert, M. Parady, J. Yatton, and M. C. Kelley, Observations of paired electrostatic shocks in the polar magnetosphere, *Phys. Rev. Lett.*, **38**, 292, 1977.

Rino, C. L., R. C. Livingston, R. T. Tsunoda, R. M. Robinson, J. F. Vickrey, C. Sondor, M. D. Cousins, J. Owen, and J. A. Klobuchar, Recent studies of the structure and morphology of auroral zone F region irregularities, *Radio Sci.*, **18**, 1167, 1983.

Robinson, R. M., R. T. Tsunoda, J. F. Vickrey, and L. Guerin, Sources of F region ionization enhancements in the nighttime auroral zone, *J. Geophys. Res.*, **90**, 7533, 1985.

Rufenach, C. L., Wavelength dependence of radio scintillation: Ionosphere and interplanetary irregularities, *J. Geophys. Res.*, **79**, 1362, 1974.

Satyanarayana, P., and P. K. Chaturvedi, Excitation of lower-hybrid instability by longitudinal currents, *Phys. Fluids*, **29**, 336, 1986.

Satyanarayana, P., and S. L. Ossakow, Velocity shear stabilization of the current convective instability, *J. Geophys. Res.*, **89**, 3019, 1984.

Satyanarayana, P., P. K. Chaturvedi, M. J. Keskinen, J. D. Huba, and S. L. Ossakow, Theory of the current-driven ion cyclotron instability in the bottomside ionosphere, *J. Geophys. Res.*, **90**, 12209, 1985.

Spiro, R. W., P. H. Reiff, and L. J. Maher, Jr., Precipitating electron energy flux and auroral zone conductances: An empirical model, *J. Geophys. Res.*, **87**, 8215, 1982.

Sugiura, M., A fundamental magnetosphere-ionosphere coupling model involving field-aligned currents as deduced from DE-2 observations, *Geophys. Res. Lett.*, **11**, 877, 1984.

Temerin, M., The polarization, frequency, and wavelengths of high-latitude turbulence, *J. Geophys. Res.*, **83**, 2609, 1978.

Vickrey, J. F., and M. C. Kelley, The effects of a conducting E layer on classical F region cross-field plasma diffusion, *J. Geophys. Res.*, **87**, 4461, 1982.

Weber, E. J., J. Buchau, J. G. Moore, J. R. Sharber, R. C. Livingston, J. D. Winnigham, and B. W. Reinisch, F layer ionization patches in the polar cap, *J. Geophys. Res.*, **89**, 1683, 1984.

Weber, E. J., R. T. Tsunoda, J. Buchau, R. E. Sheehan, D. J. Strickland, W. Whiting, and J. G. Moore, Coordinated measurements of auroral zone plasma enhancements, *J. Geophys. Res.*, **90**, 6497, 1985.

Weimer, D. R., C. K. Goertz, D. A. Gurnett, N. C. Maynard, and J. L. Burch, Auroral zone electric fields from DE 1 and DE 2 at magnetic conjunctions, *J. Geophys. Res.*, **90**, 7479, 1985.

Winnigham, J. D., J. L. Burch, N. Baker, V. A. Blevins, and R. A. Hoffman, The low altitude plasma instrument (LAPI), *Space Sci. Instrum.*, **3**, 465, 1981.

Yau, A. W., B. A. Whalen, A. G. McNamara, P. J. Kellogg, and W. Bernstein, Particle and wave observations of low-altitude ionospheric ion acceleration events, *J. Geophys. Res.*, **88**, 341, 1983.

S. Basu, P. F. Foujere, and N. C. Maynard, Air Force Geophysics Laboratory, Hanscom Air Force Base, MA 01731.

S. Basu and E. MacKenzie, Emmanuel College, Physics Research Division, 400 The Fenway, Boston, MA 02115.

W. R. Coley and W. B. Hanson, Center for Space Sciences, University of Texas at Dallas, Richardson, TX 75080.

W. R. Hoegy, Code 961, NASA Goddard Space Flight Center, Greenbelt, MD 20771.

M. Sugiura, Geophysical Institute, Kyoto University, Kyoto 606, Japan.

J. D. Winnigham, Southwest Research Institute, Department of Space Sciences, 6220 Culebra Road, P. O. Drawer 28510, San Antonio, TX 78284.

(Received March 13, 1987;
revised August 13, 1987;
accepted September 23, 1987.)

ATTACHMENT 10

To appear in Journal of Geophysical Research, 1990

PLASMA STRUCTURING BY THE GRADIENT-DRIFT INSTABILITY AT HIGH
LATITUDES AND COMPARISON WITH VELOCITY-SHEAR DRIVEN PROCESSES

Sunanda Basu¹, S. Basu², E. MacKenzie¹, W.R. Coley³,
J.R. Sharber⁴, and W.R. Hoegy⁵

¹Emmanuel College

Boston, MA 02115

²Geophysics Laboratory

Hanscom AFB, MA 01731

³University of Texas at Dallas

Richardson, TX 75080

⁴Southwest Research Institute

San Antonio, TX 78284

⁵Goddard Space Flight Center

Greenbelt, MD 20771

Accepted for publication in Journal of Geophysical Research
September, 1989

ABSTRACT

Satellite in-situ measurements made by the Dynamics Explorer-2 (DE-2) satellite were utilized to describe the nature of plasma structuring at high latitudes caused by the gradient-drift instability process. Specifically, by using noon-midnight and dawn-dusk orbits of the DE-2 satellite it was found possible to study the simultaneous density and electric field spectra of convecting large scale (~hundreds of km) plasma density enhancements in the polar cap (known as "patches") in directions parallel and perpendicular to their anti-sunward convection. Distinct differences were noted in the behavior of the ac and dc electric field structure and short scale (<125 m) density irregularities in these two mutually orthogonal directions perpendicular to the geomagnetic field. However, since these two orthogonal directions were not sampled simultaneously, the observed differences cannot be unequivocally related to the direction of convection.

Structured plasma density enhancements in the auroral oval (known as "blobs") were found to have considerable power spectral density at these short scales in the presence of significant Pedersen and Hall conductances in the 10-20 mho range. While density irregularity amplitudes $(\Delta N/N)_{RMS}$ were found to be as large as 15-20 percent using 8-s samples of the DE-2 data, the corresponding dc electric field fluctuation ΔE was found to be less than a few mV m^{-1} for both patches and blobs. This $(\Delta N/N)_{RMS}$ vis-a-vis ΔE behavior for the gradient drift process provided a fairly dramatic contrast with velocity

shear driven processes where the ΔE magnitudes were found to be at least an order of magnitude larger for the same levels of density irregularities. The electric field spectra for the moderate shear category discussed by Basu et al. (1988a) were also found to have a significantly different spectral index as compared to such spectra associated with the gradient drift process. The results of this paper together with those of Basu et al. (1988a) provide fairly conclusive evidence for the existence of at least two generic classes of instabilities operating in the high latitude ionosphere: one driven by large scale density gradients in a homogeneous convection field with respect to the neutrals and the other driven by the structured convection field itself in an ambient ionosphere where density fluctuations are ubiquitous.

1. INTRODUCTION

Recent multi-diagnostic research at high latitudes has identified large scale (\sim hundreds of km) enhanced plasma density regions in the auroral and polar F-region as the seat of large amplitude km-scale irregularities which produce intense scintillation in the VHF/UHF band (Vickrey et al., 1980; Rino et al., 1983; Weber et al., 1984; 1985; 1986; Kersley et al., 1988; Basu et al., 1988b). It is well recognized that such structuring is caused by the gradient drift instability as these discrete regions of density enhancements convect with the background plasma (Chaturvedi and Huba, 1987 and references therein). This interchange-like instability, a plasma analogue of the well-known Rayleigh-Taylor instability which evolves when a heavy fluid is supported against gravity by a lighter fluid, is driven by both a plasma density gradient and an electric field perpendicular to the geomagnetic field. Tsunoda (1988) has presented a very comprehensive review of the experimental and theoretical work related to the generalized gradient-drift instability at high latitudes brought about by a magnetic flux tube interchange process (MFTI). Huba (1989) has also provided an overview of the theoretical and computational techniques that have been applied to study the gradient-drift instability at high latitudes.

The object of this paper is to provide a detailed description of the nature of the density and electric field fluctuations that characterize the 10 to 1 km-scale irregularities associated with such convecting structures. These enhanced density regions have come to be known in the literature as auroral "blobs" (Vickrey et al., 1980) or polar cap "patches" (Weber et al., 1984) depending on their location. While some information is available on the density spectral

characterization of the gradient-drift instability in general (Villain et al., 1986), and of patches, in particular (Basu et al., 1988b), there is, to our knowledge, only one example of simultaneous density and electric field fluctuation spectra of the gradient drift instability published by Cerisier et al. (1985) using data from the ARCAD satellite. On the other hand, a fairly comprehensive description of the density and electric field fluctuation spectra and associated background parameters in the velocity shear region has been provided using DE-2 data by Basu et al. (1988a, hereinafter referred to as Paper I). This, and earlier work (cf. review by Kintner and Seyler (1985) and references therein) stimulated theoretical development of various instabilities in inertial and collisional plasmas driven by shears in flows parallel and perpendicular to the magnetic field (Basu and Coppi, 1988, 1989; Keskinen et al., 1988; Ganguli et al., 1989; Nishikawa et al., 1989).

It is hoped that a similar detailed treatment of the simultaneously obtained density and electric field spectra associated with the gradient drift instability will provide further insights into the process. In particular, at high latitudes where the magnetosphere exerts a strong influence on the underlying ionosphere, it is important to determine whether ion-inertia (associated with collisionless magnetospheric plasmas) or collisional processes are controlling the evolution of the gradient drift instability (Mitchell et al., 1985; Chaturvedi and Huba, 1987). Very recently, the nonlinear evolution of interchange instabilities in the high latitude

ionosphere with scale-size-dependent magnetospheric coupling has been studied using numerical simulation techniques and density and electric field spectra have been computed (Keskinen and Huba, 1989). Ideally one would like to provide experimental results of density and electric field fluctuation spectra in two mutually orthogonal directions perpendicular to the magnetic field which are obtained simultaneously for comparison with the simulation results. Unfortunately, such simultaneous high resolution in-situ data is currently not available in two mutually orthogonal directions. We have thus tried to overcome this handicap by providing limited statistics of density and electric field spectral indices in the direction of plasma convection and perpendicular to that direction, at least, for the case of polar cap patches. It is hoped that such statistical information will provide some clues regarding spectral behavior in these two orthogonal directions. Further, since it is possible to obtain spectra in different directions using numerical simulations of specific instabilities (Keskinen and Ossakow, 1982, 1983; Hassam et al., 1986; Keskinen et al., 1988; Keskinen and Huba, 1989), the experimental data could be useful for comparisons with simulation spectra, which, in turn, could provide some indications regarding occurrence of particular instabilities.

The plan of the paper is to treat in depth the density and electric field fluctuation characteristics of polar cap patches and auroral blobs on two orbits observed by the DE-2 satellite using the retarding potential analyzer, RPA, (Hanson et al.,

1981) and the vector electric field instrument, VEFI, (Maynard et al., 1981) on board. Of these two orbits, one on March 8, 1982 provided a magnetic noon-midnight cut of the northern high latitude ionosphere. In this case the direction of satellite motion along which the density and electric field were being measured was aligned with the anti-sunward drift of the patches observed, so that the spectral characteristics to be presented will pertain to the direction of convection. The second orbit to be discussed provided a dawn-to-dusk cut through southern high latitudes on May 26, 1982. In this case the satellite motion was perpendicular to the anti-sunward drift of the patches. Thus the spectral information pertains to a direction which is orthogonal to the direction of plasma convection. Both these orbits sampled the ionosphere within the F-region at approximately 400 km altitude. However, they exhibited distinct differences, particularly in the statistical behavior of the dc electric field spectra and also in the occurrence of ac electric field turbulence. Several other DE-2 orbits in different local time planes were also studied to determine the consistency of the ac turbulence behavior in polar cap patches. These are discussed in Section 3.

The auroral blobs were usually observed in the region of the return flows, which are either eastward or westward depending on the position of the blob relative to the passage of the Harang discontinuity. Structuring within auroral blobs is discussed in Section 4. Since a satellite with its density monitor provides only a snap-shot of features like polar cap

patches and auroral blobs, we will try to utilize other instruments on DE-2 such as the Langmuir probe, LANG, (Krehbiel et al., 1981) and the low energy plasma instrument, LAPI, (Winningham et al., 1981) to determine the electron temperature and the integrated Hall and Pedersen conductances associated with these plasma density structures to shed some light on their origin and relationship to the background convection.

We also provide in Section 5 a comparison between the magnitude of fluctuations and the spectral characteristics of density and electric field structure associated with the gradient drift instability discussed in this paper and those associated with velocity shear driven processes presented in Paper I. It will be shown that it is rather important to consider both magnitude of perturbations, i.e., saturation amplitudes of these fluctuating quantities, and their spectral characteristics in determining the type of plasma instability. Finally, in Section 6, we attempt to point out similarities and differences of our experimental results with published results of analytical and numerical simulations of interchange instabilities.

2. INSTRUMENT DESCRIPTION AND DATA ANALYSIS METHODS

Detailed description of the DE-2 program (Hoffman and Schmerling, 1981) and all the instruments on board was provided in Space Science Instrumentation (Vol. 5, December, 1981). The resolutions of the different instruments and their impact on spectral analysis results were discussed in Paper I and will not be repeated here.

3. POLAR CAP PATCHES FROM DE-2

We present in this section the simultaneously obtained density and electric field fluctuation spectra from two DE-2 orbits which had well identified discrete patches or plasma density enhancements in the polar cap. While many papers (cited in the Introduction) have appeared on polar cap patches including the comprehensive review by Tsunoda (1988), it is interesting to note that a formal definition of what constitutes a patch has not emerged. There seems to be universal agreement that a patch can vary in size from a few tens to a thousand km, have densities at ionospheric altitudes of at least a factor of 2-3 over the background, occur when the B_z component of the IMF is southward, appear to be produced by solar radiation rather than particle precipitation and have long lifetimes during which the patches drift anti-sunward with velocities on the order of half a km per s. A modeling study conducted by Schunk and Sojka (1987) indicated that the lifetime of a winter patch with a factor of 10 enhancement over the background would be 11 hours, while in summer the lifetime for the same blob would be reduced to 4 hours. While, of course, satellite in-situ data does not provide a time-history of the patches, we identified them on the basis of most of the other characteristics enumerated above. In particular, for our structuring study we chose the two orbits, such that in the first, the satellite motion was parallel to the anti-sunward direction of convection of the patches, while in the second, the satellite motion was perpendicular to the direction of

convection. Data from several other sensors are presented to argue for the non-local source for these density enhancements.

Orbit 3223

This pass traversed the northern high latitude ionosphere two weeks prior to the vernal equinox in 1982 during southward interplanetary magnetic field (IMF) conditions (with $B_z = -3.2$ nT and $B_y = -4.3$ nT between 03-04 UT). The hourly values of B_z had been continuously negative for the six hours prior to the pass, while B_y was negative for a period of about 40 hours. Figure 1 shows a projection of the vector velocities measured by the IDM and RPA on a polar plot in a geographic latitude (GLAT)-solar local time (SLT) coordinate system with ovals of invariant latitude superimposed. There is one region of large velocities in the dayside associated with the cusp/cleft region around 0347 UT while the other is seen in the nightside auroral oval around 0338 UT. The solar zenith angle at the satellite is always large varying from 136° at 0335 UT to 90° at 0347 UT even though the satellite is considered to be sunlit beyond 0341 UT. The velocity vectors observed within the dayside and nightside polar cap are quite well organized with the anti-sunward flow direction coinciding fairly well with the orbital plane of the satellite motion. Thus the density and electric field measurements which are obtained along the satellite orbital plane pertain to those along the direction of convection.

Figure 2 shows the ion density (N_i) and the electron temperature (T_e) measurements obtained by LANG corresponding to the midnight-noon high latitude traversal of the DE-2 satellite shown in Figure 1. The three distinct features marked P_1 , P_2 ,

and P_3 at latitudes $>80^\circ$ invariant having densities in excess of 10^6 cm^{-3} at approximately 400 km altitude are identified as polar cap patches on the basis of the characteristics discussed at the beginning of the Section. It may be noted that these features are fairly 'cold' structures quite dissimilar to the auroral and cusp regions which are associated with large T_e fluctuations. Two auroral blobs denoted B1 and B2 are seen in the nightside auroral oval. Structuring in these blobs will be discussed in a later section.

Figure 3 shows the LAPI data obtained simultaneously by DE-2. The precipitating electron flux at 7.4° pitch angle is shown. It is important to note that Patch 1 is seen to exist entirely in the region of polar rain (Winningham and Heikkila, 1974), whereas Patches 2 and 3 are observed in a region of polar rain augmented by photoelectron fluxes produced below the satellite by scattered UV radiation (Winningham and Gurgiolo, 1982). Weber et al. (1984) showed by modeling studies using the Strickland et al. (1976) electron transport code that such polar rain and photoelectrons cannot account for the enhanced density in the patches. Anderson et al. (1988) have recently shown that such enhanced plasma densities in the dark polar cap could result from extended transit of relevant flux tubes through regions of significant solar production south of the cusp prior to their entry and convection as patches across the polar cap. These authors showed that a viable candidate for creating and organizing these polar cap patches is a time-varying convection pattern. Their modeling studies showed

that the longer the convection pattern change is turned on, the larger the patch region becomes. A possible example of that situation could be Patch 1 in Figure 2, whereas patches more spiky in nature such as Patches 2 and 3 seem to represent a more rapid time variation in the convection pattern.

One of the major points of interest in this paper is the study of the density and electric field fluctuations, namely, $(\Delta N/N)_{RMS}$ and ΔE , associated with the patches as they convect with the background plasma in a generally antisunward direction. In the linear stage of the gradient-drift instability one expects the density perturbation in the N-S direction to be enhanced by a perturbed velocity in the same direction related to an electrostatic field fluctuation in the E-W direction (Keskinen and Ossakow, 1983). However, the patches are probably observed in the non-linear regime when fluctuations in density and electric field develop in both these directions which are orthogonal to the approximately vertical magnetic field. We show in Figure 4a the north-south dc electric field structure from VEFI over the entire high latitude region as also the N-S drift (related to the E-W electric field) obtained from the RPA. (The E-W electric field was not available from DE-2 because of a mechanical problem.) As mentioned in Paper I, while the VEFI data is available with a sampling of 16 Hz, the RPA provides velocities at a 1 Hz rate. Thus only the VEFI data with spatial resolution of approximately 500 m is amenable for spectral analysis which on the basis of a "frozen in turbulence" assumption provides

information regarding the electric field fluctuation structure associated with density structure at scales smaller than 10 km (cf. Pg. 121 of Paper I for a further discussion of this topic).

It was pointed out in the Introduction that the simultaneous $\Delta N/N$ and ΔE spectral analysis for this orbit provides the nature of structuring in a direction which is approximately parallel to the direction of convection in the anti-sunward direction. The velocity in the N-S direction, on the other hand, as mentioned earlier provides some insight into the linear stage of the interchange instability process.

Actually, as is well known (Keskinen and Ossakow, 1983), it is the relative plasma velocity in the neutral rest frame which drives the instability. Unfortunately, the N-S neutral winds which are obtained from the Fabry-Perot Interferometer (FPI) on DE-2 (Hays et al., 1981) were not available for this orbit.

However, to provide some indication regarding the neutral wind behavior we present in Figure 4b both the E-W neutral wind measured by WATS (Spencer et al., 1981) and the E-W plasma drift measured by the IDM (which is, of course, identical to the N-S electric field shown in Figure 4a). In the polar cap the E-W neutral wind and plasma drift are not very different indicating that the polar cap convection has probably been fairly steady in response to the combined southward IMF and the high densities in the patches. It is only in the noon-midnight return flow regions where large differences are seen in the plasma and neutral motion. As a matter of fact, in the auroral

blob region ($50\text{--}55^{\circ}$ geographic latitude) the eastward neutral wind flow is larger than the plasma motion. We will return to a discussion of this point in a later section.

It is quite interesting to note that fairly large amplitude density irregularities were generated, particularly at the edges, of the patches as they convected with a moderate velocity of 250 ms^{-1} through the dayside and into the nightside polar cap. The top panel of Figure 5 represents the irregularity amplitude ($\Delta N/N$)_{RMS} computed over 8s of RPA data of ion densities obtained with a 64 Hz rate over the polar cap region which was identified with the 3 patches shown in Figure 2. The $\Delta N/N$ values (because of the approximately 8-kms^{-1} satellite velocity) provide an idea of plasma structuring over a few tens of km scale. The other 5 panels represent the output of the 5 lowest frequency filters of the ac electric field spectrometer A on DE-2 (cf. Table 2a and its description in Paper I). The filter outputs are obtained once per second with the different filter frequencies covering the sampling range provided by the RPA. By comparing Figures 2 and 5 we find the large patch P_1 has increased $\Delta N/N$ associated with both its leading ($\sim 0341 \text{ UT}$) and trailing ($\sim 0344 \text{ UT}$) edges. In fact, its leading edge seems to be broken up into two parts, one immediately prior to 0341 UT and the other after it, and is probably due to the very large density increase, approximately one order of magnitude, within the patch as compared to the background. The trailing edge of P_1 and the irregularities associated with P_2 and P_3 (because they are each rather narrow)

all coalesce to form a fairly wide irregular region between 0344-0346 UT. The middle portion of P_1 (between 0341:40-0343:40 UT) had low irregularity amplitudes less than 2 percent. A similar situation was found for the patches observed by DE-2 on January 22, 1982 (Basu et al., 1988b).

The ac electrostatic fluctuations associated with the patches are small, being mostly less than 0.1 mVm^{-1} . However, what is rather interesting is that they seem to be confined to the leading and trailing edges of patches as identified on the lowest frequency filter channel on Figure 5. This seems particularly noticeable for the case of patches 2 and 3 where, even though the patches are so narrow, 4 distinct structures are seen which are aligned perfectly with their edges shown in Figure 2, the turbulence within the patches being less than $.01 \text{ mVm}^{-1}$. At this juncture, we wish to point out that several other noon-midnight orbits which show the presence of polar cap patches were examined to determine the nature of the ac turbulence with respect to the patch edges. Orbits such as 3180 on March 5, 1982 and 3201 on March 6, 1982 show the presence of discrete bursts of ac turbulence confined to the patch edges much like that seen in orbit 3223. The magnitude, however, was usually less than 0.1 mVm^{-1} . In contrast, it should be noted that in velocity shear regions, the ac fluctuations reach levels of several mVm^{-1} in the 4-8 Hz range (Heelis et al., 1984 and Paper I). Thus the electrostatic turbulence associated with the density turbulence seems fairly low in the case of convective instabilities.

We are now in a position to study the spectra of the simultaneously obtained density and electric field structure obtained from DE-2 along the direction of convection of the patches. An 8-sec sample of high-resolution density obtained from the RPA starting at 0344:07 UT along the direction of convection together with its spectrum is shown in Figures 6a and b. The corresponding N-S electric field data together with its spectrum is shown in Figures 7a and b. The spectra are computed by using the maximum entropy technique (as discussed in Paper I). Two points are noticeable: first, the electric field fluctuations are very small ($\Delta E = 0.3 \text{ mVm}^{-1}$) and, second, the spectral slopes of $\Delta N/N$ and ΔE between several tens of km to several km are identical. It is important to recognize that because of the power law type of irregularity and electric field spectra, the magnitudes of $\Delta N/N$ and ΔE are dictated primarily by the length of the data sample (8 s for both cases) and the difference in the sampling rates (64 Hz for N and 16 Hz for E) does not produce any significant impact on the magnitude of the fluctuations. In the absence of any information on the nature of the background variation of E and N, a trend line based on a linear least squares fit to the data has been chosen for the determination of $\Delta N/N$ and ΔE . While the detrending process (through its effect on the low-frequency end) may have some bearing on the magnitudes of $\Delta N/N$ and ΔE , its impact on the determination of the spectral indices between two frequencies which avoid both the low and high frequency ends is minimal. In Figures 6b and 7b, for instance, the spectral indices are determined by slope fitting between 0.2 to 0.3 Hz at the low frequency end and 2.0 to 3.0 Hz at the high frequency end (indicated by dots on the spectra).

Figures 8a and b present histograms of the density and electric field spectra of samples between 0339:27-0345:27 UT. Over 80 percent of the samples of both density and electric field fluctuations show spectral slopes between 1.6 to 2.0 with the majority of slopes being within the range 1.8-2.0. Thus one obtains virtually identical spectral behavior of density and electric field fluctuations when both are measured in a direction parallel to the direction of the background plasma convection.

As discussed in Paper I, density fluctuations at several discrete scale lengths between 125m to 6m are available from a set of filters on DE-2. It is thus possible to determine spectral slopes of irregularities < 125 m in scale size. Figure 8c shows the histogram of spectral indices seen at the small scales. The peak of the histogram is seen to lie between 3-3.5, thus indicating that the irregularities have a two-component spectrum much like that seen in equatorial bubbles (Basu et al., 1983; Rino et al., 1981). The long scales > 1 km are described by spectral indices of 1.8 ± 0.2 while the shorter scales < 125 m are best described by spectral indices between 3 to 3.5. It was also found that the even steeper indices seen in the histogram were obtained from the central portion of P_1 where there was little power at short scales. Thus while a break in the spectrum is indicated, it is difficult to specify the scale-length of the break from the DE-2 data because the scale-length coverage is not continuous.

Orbit 4429

This pass traversed the winter southern high-latitude ionosphere from dawn to dusk during a time of moderate magnetic disturbance ($K_p = 4$). The hourly IMF was southward with $B_z = -0.9$ nT and $B_y = -7.4$ nT between 21-22 UT. There was a data gap 6 hours prior to this time. B_y was continuously negative for those 6 hours, while B_z changed sign several times within this period. Figure 9 shows a projection of the vector velocities measured by the IDM and RPA on a polar plot in a geographic latitude (GLAT)-solar local time (SLT) coordinate system with ovals of invariant latitude (ILAT) superimposed. The region between 70° and 80° ILAT in the morning sector shows intense velocity shears with both sunward and anti-sunward velocities greater than 2 kms^{-1} being observed in close proximity to one another. This portion of the orbit was discussed in Paper I. The portion of the orbit of interest here is the region of fairly uniform anti-sunward flows poleward of 70° geographic on the morning side. It should be noted that the dawn-dusk plane of the orbit is orthogonal to the direction of convection in the polar cap. As in orbit 3223, the solar zenith angle value at the satellite was large, varying from 100° at 2148 UT to 112° at 2204 UT.

To provide an overall perspective of the large-scale density structure that is associated with the velocity field shown in Figure 9, the LANG data of ion densities (N_i) and electron temperatures (T_e) for the entire dawn-dusk portion of the orbit are shown in Figure 10. The portion of the orbit

prior to 2154 UT has been described in detail in Paper I. In this section we shall discuss the three discrete density structures marked P_1 , P_2 , and P_3 which have all the characteristics of convecting patches. The bottom panel shows that these are "cold" structures and the LAPI (not shown) provides evidence for polar rain only as was the case for orbit 3223.

It was mentioned earlier that plasma structuring takes place in the neutral rest frame. For this orbit also, the FPI data of the N-S neutral winds were not available. However, the wind and temperature spectrometer, WATS, (Spencer et al., 1981) data of the cross-track neutral winds were available. For the dawn-to-dusk orbit the cross-track neutral wind corresponds to the direction of anti-sunward convection, and therefore, this component of neutral wind is the appropriate one for studying plasma structuring in the linear regime. Figure 11 provides the horizontal E-W winds from WATS and ion drifts from IDM for orbit 4429. The difference between these quantities is very large in the morning and evening auroral ovals as was also the case with orbit 3223. As discussed by Killeen et al. (1985), we note that the ion drifts which respond to magnetospheric energy sources can transfer their energy and momentum to the neutral species on time scales of tens to hundreds of minutes depending on the ion density. Figure 10 shows that the density in the auroral regions is less than 10^5 cm^{-3} , thus requiring hundreds of minutes for the ion-neutral momentum coupling to take place. The neutral thermosphere, therefore, acts as an

integrator, filtering out most of the high frequency structure seen in the ion convection pattern. However, in the polar cap and particularly in the region of the patches where the density is $3 \times 10^5 \text{ cm}^{-3}$, the average value of the IDM drift is 550 ms^{-1} and the WATS wind is 380 ms^{-1} leading to an average differential ion motion in the neutral rest frame of 170 ms^{-1} . The large scale background plasma density gradient perpendicular to the direction of convection is approximately 90-120 km at the edges of the patches. On the assumption that similar density gradients also prevail in the direction of convection, the zero order growth time for the gradient drift instability is on the order of 10 mins. Since the large scale density gradients, particularly in the absence of an underlying E-region, have lifetimes long compared to 10 mins (Vickrey and Kelley, 1982), it is expected that the gradient drift instability will have sufficient time to develop as the patches convect with this differential motion or "slip" velocity.

The irregularity amplitude ($\Delta N/N$) computed over 8-s intervals for the region of the patches between 2154-2158 UT and the N-S component of the electric field which is perpendicular to the anti-sunward convection are shown in Figure 12. The spectral analysis of both these parameters will be presented and contrasted with orbit 3223. We note here that the three patches are all narrower than Patch 1, but wider than Patches 2 and 3 of orbit 3223 with irregularity amplitudes of 5-10 percent at the edges. The magnitude of the anti-sunward convection caused by the N-S electric field is larger as

compared to orbit 3223 with the average electric field on the order of 25 mV m^{-1} , which gives rise to the E-W drift of approximately 500 ms^{-1} as was measured by the IDM and presented in Figure 11. The ac electrostatic fluctuations in five different frequency bands are shown in Figure 13 and provide a different signature than that observed for orbit 3223. In the case of orbit 4429 the electrostatic fluctuations are observed throughout the patches and are not restricted to the density gradients at their edges. In the case of orbit 3223 it was found that the electrostatic fluctuations were confined to only the steep gradients at either end of the patch. This was the case even for Patches 2 and 3 which were quite narrow, but yet two very discrete turbulence regions were seen perfectly aligned with the density gradients. It is tempting to attribute this difference to the fact that the electrostatic fluctuations are sampled parallel to the background convection in one case (orbit 3223) and perpendicular in the other (orbit 4429). Many other DE-2 orbits such as orbit 2552 (Basu et al., 1988b) and orbit 1174 (Emery et al., 1985) which were in the 09-21 MLT plane, and orbits in the dawn-dusk plane with evidence for patches showed continuous ac turbulence throughout the patches as in orbit 4429. The dc electric field spectra also show distinct differences which will be discussed below.

An 8-s sample of high resolution RPA density fluctuation data from within Patch 2 starting at 2156 UT is shown in Figure 14a with its spectrum in Figure 14b. The corresponding electric field data perpendicular to convection together with

its spectrum is shown in Figures 15a and b. By comparing Figures 14b and 15b we note that the electric field fluctuation spectrum is steeper than the density fluctuation spectrum in the scalelength range of several tens of km to several km. Figures 16a and b present histograms of the density and electric field fluctuation spectral slopes of samples between 2154-2158 UT. While the density spectral slope histogram looks very similar to that for orbit 3223, the electric field slope histogram looks quite different. Approximately half of the samples have slopes similar to the density spectra with a range between 1.6-2.0. The other half forms a long tail in the electric field fluctuation spectral slope distribution with slopes ranging from 2.2-3.4. Thus it seems that, contrary to the case of sampling along the direction of convection, the electric field fluctuation spectrum can take on a variety of forms when sampled in a direction which is perpendicular to the direction of convection.

For comparison with the small scale irregularity behavior shown in Figure 8c, we present the corresponding statistics for orbit 4429 in Figure 16c. The range of variation of the indices obtained from the filter output < 125 m is smaller in this case and the most probable value of the slope is 3.0 ± 0.2 . There is more power present at the shorter scales so the very steep slopes obtained for orbit 3223 are not seen here.

4. AURORAL BLOBS

Discrete density enhancements known as auroral blobs (Vickrey et al., 1980) are seen in both the DE-2 orbits discussed in the last section. Two blobs identified as B1 and B2 in orbit 3223 (cf. Figure 2) and one very prominent blob marked B in orbit 4429 (cf. Figure 10) will be discussed in this section.

The blob marked B1 has little structuring associated with it. It could very well be a sub-auroral blob discussed by Weber et al. (1985) as there is little temperature fluctuation associated with it (cf. bottom panel of Figure 3) and the irregularity amplitudes of constituent 8-s samples are relatively small being on the order of 5 percent. The blob marked B2, on the other hand, provides evidence for much larger amplitude irregularities. It is observed in a region of particle precipitation, consequent temperature fluctuations and enhanced conductivities. The height integrated Pedersen and Hall conductances computed using the empirical relationships developed by Robinson et al. (1987) and the DE-2 LAPI data are shown in Table 1 for four different times. Σ_p and Σ_H were computed using the expressions:

$$\Sigma_p = \frac{40E}{16 + E^2} \Phi_E^4$$

$$\frac{\Sigma_H}{\Sigma_p} = 0.45 (E)^{0.85}$$

where, \bar{E} - average energy in KeV of a Maxwellian distribution,
 Φ_E - energy flux in ergs $\text{cm}^{-2} \text{sec}^{-1}$,

Σ_p, Σ_H - Pedersen and Hall conductances in mhos.

It should be noted that the average energy E is computed for fluxes of electrons above 500 eV energy for reasons outlined by Robinson et al. (1987). Two of the LAPI spectra at 0336:43 and 0336:51 UT for which conductances were computed in Table 1 are shown in Figure 17. They are typical of spectra seen in the diffuse auroral region.

In Figure 18 we show the seven consecutive 8-s samples of detrended density data which comprise Blob 2. A rather remarkable behavior of the density is observed in every panel with the rapid small scale fluctuations occurring along the positive (i.e., upward sloping with time) gradients in plasma density superimposed on a quasi-periodic approximately 20-km scale wave structure. Referring to Figures 1 and 2, we find that along the satellite track a positive poleward gradient exists. The fluctuations are completely absent from the negative gradient side even though these gradients are steeper. A similar example was presented by Tsunoda (1988) in his review based on data from the ISOPROBE experiment on board the AUREOL-3 satellite (Beghin et al., 1982; Cerisier et al., 1985; Villain et al., 1986).

From the vector velocity data for this orbit shown in Figure 1 we find that there is a component of velocity in the equatorward direction associated with the blob which is thus antiparallel to the poleward gradient measured along the satellite track. If we assume that we are sensing the instability in its linear state, then subject to the constraint that a satellite can only measure density gradients along its orbital track, we may conclude that the requirements of the

gradient drift instability are not satisfied. However, if it can be shown that there is a larger magnitude of equatorward neutral wind at this time which would cause the plasma motion in the neutral rest frame to be parallel to the density gradient, then the instability requirements may be fulfilled. Unfortunately, the meridional neutral wind was not available for this orbit. However, the zonal (eastward) neutral wind flow is actually larger than the plasma motion as shown in Figure 4b. If the same is true for the meridional (i.e., equatorward) neutral wind then the conditions for the gradient drift instability will have been satisfied. The electric field fluctuation associated with the large density structures shown in Figure 18 is minimal being less than 1.7 mVm^{-1} . This is consistent with the findings of the polar cap patches as well and seems to be a hallmark of the gradient drift instability.

Another point of interest is the presence of considerable power spectral density in the small scale (\sim several hundred m) fluctuations in the presence of large underlying Pedersen and Hall conductances throughout the blob location. Tsunoda (1988) pointed out that a more quantitative assessment of the effectiveness of the $\vec{E} \times \vec{B}$ instability is to estimate the M value given by

$$M = 1 + \frac{\Sigma_p^c}{\Sigma_p^b}$$

where the superscript c refers to the plasma density enhancement or cloud and superscript b refers to the background plasma. Using Tsunoda's Table 1 and our Table 1 we obtain $\Sigma_p^c \approx 0.5 \text{ mho}$ (for peak density within blob $\sim 0.5 \times 10^6 \text{ cm}^{-3}$) and $\Sigma_p^b \approx 10 \text{ mho}$ from the underlying E region. Thus M is very close to unity and by using Tsunoda's equation (10) taken from

Francis and Perkins (1975) the growth rate for the $\vec{E} \times \vec{B}$ instability tends to zero. However we show in Figure 19 the spectrum of the density sample shown in panel 5 of Figure 18. A two component spectrum is seen as obtained for the polar cap patches with a spectral index of 1.9 for scalelengths between 2 km - 200 m whereas the linear least squares fit to the 4 realizations of the Wideband filter output between 125 m - 6 m provides a spectral index of 2.6. What is also significant is that the median power spectral density (psd) at 125 m is on the order of 10^{-7} in the presence of the large Σ_p and Σ_H listed in Table 1. This psd compares favorably with that observed at 125 m at the edges of polar cap patches which essentially have no underlying conductivity structures. In Figure 19 the 20-km scale of the large scale fluctuations is evident. It is also possible to visualize a break in the spectrum (by extending to longer scales the linear least squares fit to the filter output) at a few hundred m-scale which is noticeable in the smaller scale fluctuations on the positive density gradients seen in Figure 18. By performing spectral analysis of 2-s detrended samples which were confined to the ramps on which the small scale irregularities were observed, this break was found to be at approximately 800 m. Thus we are left with the task of explaining the growth of these F-region irregularities when theory predicts otherwise. An alternative point of view is that these small scale irregularities do not map to the E-region, so that the F-region

irregularities can evolve independently (Kintner and Seyler, 1985).

The blob B observed in orbit 4429 in the dusk sector is located in a region of very large sunward flow. It is interesting to note from the density wave form obtained at the peak of the blob and its spectra shown in Figure 20 that this sample contains much less psd at the shorter scales as compared to the spectra shown in Figure 19 even though the irregularity amplitude at the larger scales is almost identical in both cases. It is tempting to speculate that the blob B2 in the midnight sector seen in orbit 3223 may have just entered the auroral oval from the polar cap whereas the blob in orbit 4429 may have been convecting over long distances through the auroral oval from the midnight to the dusk sector. While obviously satellite in-situ measurements alone can never answer this question conclusively, the experimental observations are at least consistent with the blob modeling studies conducted by Robinson et al. (1985) who postulated the entry of polar cap patches through the Marang discontinuity region and their re-configuration into auroral blobs. Some recent experimental data obtained during a CEDAR High Latitude Plasma Structure (HLPS) campaign tentatively support this concept (Doolittle et al., 1989). This issue, however, remains an open one and will be the focus of much investigation in the current sunspot maximum phase.

5. COMPARISON WITH VELOCITY SHEAR DRIVEN PROCESSES

Having provided a fairly detailed case study of the density and electric field structure caused by gradient-drift driven processes in polar cap patches and auroral blobs, we are in a position to contrast their behavior with velocity shear driven structures discussed in Paper I. The most dramatic difference is seen in the magnitude of ΔE that is associated with $(\Delta N/N)_{RMS}$ of a given magnitude when the density structure is attributed to the gradient drift process as compared to a shear driven process. Figure 21 provides a scatter diagram of $\Delta N/N$ vis-a-vis ΔE as observed in the case studies presented in this paper and in Paper I. The very significant increase in the magnitude of ΔE is obvious for the velocity shear driven events. Note that a change of scale is necessary to accomodate the large ΔE magnitudes seen in Paper I. A straight line fit to the velocity shear driven events provides the following relationship between $\Delta N/N$ and ΔE :

$$\Delta E = 1.8 \frac{\Delta N}{N}$$

while for the gradient drift case the corresponding relationship is as follows:

$$\Delta E = 0.15 \frac{\Delta N}{N}$$

In both the above cases ΔE is expressed in mVm^{-1} . Thus there is at least an order of magnitude larger ΔE associated with density structures created by velocity shear driven processes. If one is interested in the relative electric field perturbations $\Delta E/E$ for comparison with $\Delta N/N$, then the above

relationships can be re-written as follows:

$$\frac{\Delta E}{E} = 4.8 \frac{\Delta N}{N} \quad \text{for velocity shear events}$$

and

$$\frac{\Delta E}{E} = 0.6 \frac{\Delta N}{N} \quad \text{for gradient drift cases.}$$

Again, approximately an order of magnitude increase is seen in the fractional electric field perturbation associated with the velocity shear process when compared with the gradient drift process.

We wish to point out that if the density and electric field perturbations for auroral blobs had been superimposed on Figure 21, the blob related points would cluster around the dashed line which is the best fit for the polar cap patch samples. The blob points were not plotted in the interests of clarity. Thus each instability process seems to follow a distinct clustering in the $(\Delta N/N)$ vs. ΔE relationship as one intuitively expects should be the case.

The second point of difference between these two generic types of instabilities is provided by the electric field spectrum. While the gradient drift processes have electric field spectra showing similar spectral indices as the density spectra, namely, 1.8 ± 0.2 , the shear driven processes generally yield electric field spectra with steeper spectral indices than the density. This was particularly evident in the moderate shear category (S_M) discussed in Paper I where the $\Delta N/N$ spectral index was the same as quoted above while the ΔE spectral index was described by a spectral index of 3.

In the intense shear category (S_I) discussed in Paper I, while the density and electric field spectral indices were

identical over a large scale length range and close to the value seen for the gradient drift case, the magnitude of ΔE for a given magnitude of $\Delta N/N$ was largest even larger than that observed in the S_M case. Thus based on magnitude of perturbations and spectral structure, we believe there are at least two, and possibly several, distinctively different classes of instabilities. While the collisional Kelvin-Helmholtz instability has been postulated as an explanation for the moderate shear category (Keskinen et al., 1988), other mechanisms based on shear flows parallel to the magnetic field (Basu and Coppi, 1988, 1989) and that caused by a combination of field-aligned currents and shears perpendicular to the magnetic field have also been invoked (Ganguli et al., 1989; Nishikawa et al., 1989) to explain the intense shear category. It will be instructive to compute the saturation amplitudes of the density and potential fluctuations predicted from these analyses for comparison with the DE-2 data presented here. Another distinguishing feature is the power at the short scales ~ 100 m which is at least an order of magnitude larger in velocity shear regions when compared to such scales seen at the edges of patches and blobs and two to three orders of magnitude larger than that observed within the central portions of wide patches. Since the power spectral density decays slowly with scalelength in the velocity shear case, the shorter scales have spectral indices that are shallower than those observed for patches. Thus Figure 22 for the velocity shear portion of orbit 4429 discussed in Paper I shows a well-defined peak between 2.6-2.8 for the spectral index of scale sizes < 125 m. This is to be compared to indices in excess of 3 for the patches (cf. Figures 8c and 16c).

6. DISCUSSION

The intent of this paper has been primarily to study the magnitude and spectral characteristics of simultaneous density and electric field fluctuations observed in association with convecting polar cap patches where structuring takes place through the gradient drift instability. We were also able to provide some information regarding these spectral characteristics when the DE-2 satellite obtained one-dimensional cuts parallel and perpendicular to the background plasma convection. For instance, we determined that for polar cap patches when sampled parallel to convection, the spectral slopes of both density and dc electric field spectra were identical with the majority of slopes being within 1.8-2.0. However, when patches were sampled perpendicular to convection, 50 percent of the dc electric field samples showed slopes much steeper than the density with the spectral indices ranging from 2.2-3.4. The ac turbulence was confined to the edges of patches in the former case and was seen throughout the patches in the latter case. While distinct differences were observed in the dc and ac turbulence characteristics in the two directions mentioned above, unfortunately these two perpendicular cuts were not simultaneous. However, since no simultaneous measurements are anticipated in the near future, it was felt that analysis such as presented here would provide some insights into spectral evolution of the gradient-drift instability. Given the non-simultaneous nature of the measurements, an analysis based on a large number of DE-2

orbits would have provided greater statistical reliability but is beyond the scope of this paper.

It has been shown in numerical simulation of the instability (Mitchell et al., 1985) that spectral anisotropy may prevail in the collisional limit of the gradient drift instability whereas more isotropic structures are predicted when magnetospheric coupling is considered. In terms of these simulation results (cf. their Figure 1 for the collisional case) which show the presence of prominent protrusions or "fingers" of enhanced density which grow outward into the low density background, one may think of the DE-2 noon-midnight cut as being mostly aligned along these fingers while the dawn-dusk sampling provides a perpendicular cut across the fingers. This is because in polar cap patches, where all-sky-imaging photometers show near-circular cross-sections (Weber et al., 1984; 1986), density gradients are obtained in all directions and it is the direction of convection that probably dictates the orientation of the fingers. Thus when the cuts are made virtually along or at small angles to the fingers, the turbulence is found to be confined to the edges and identical slopes are found for density and dc electric field spectra. As mentioned in an earlier section many other orbits were examined at various magnetic local time planes away from noon-midnight. It was found that the ac turbulence for a wide range of local times (not just exactly dawn-dusk) was much more distributed all through the fingers across what the simulations show to be their narrow dimension and a population of dc electric field spectra emerged with slopes much steeper than their density counterpart.

Recently, Keskinen and Huba (1989) have introduced scale-size dependent magnetospheric coupling in their numerical simulation of the non-linear evolution of the gradient-drift instability. Their principal finding is that the non-linear evolution can be characterized as neither purely inertial (magnetospheric control) nor purely collisional (ionospheric control). They have also determined the power spectra of density and electric field fluctuations in two mutually orthogonal directions. In Table 2 we present a comparison of their findings and ours based on DE-2 data. We have already pointed out that it was not possible for us to obtain two orthogonal cuts simultaneously. Thus we do not have experimental data for comparison with all their sub-groups. It is interesting to note that a steepening is indicated in their electric field spectra when the cut is perpendicular to the initial density gradient and convection. We find evidence for such behavior when DE-2 was travelling in the dawn-dusk direction which was orthogonal to convection. In our opinion it is necessary to investigate further why such steepening is also indicated in the corresponding density structure in the simulation while no such indication is available from the experimental density data. On the other hand, the agreement is excellent between both density and electric field spectral slopes obtained by simulation techniques and actual data when the cut is made along the direction of convection.

As mentioned in the Introduction, hitherto there was one example of simultaneous density and electric field fluctuation spectra available in the literature for the gradient-drift instability (Cerisier et al., 1985). In that example Cerisier

et al. (1985) found that the density and electric field spectral indices were virtually identical and close to a value of 2. They also provided some arguments to indicate that the electric field spectral index may provide some clues regarding the regime of observations: a spectral index close to 2 would indicate an active instability regime while an index close to 0 would signify a diffusion regime. A value close to 2 was found in the overwhelming majority of cases for electric field structuring in patches when sampled in the direction of convection, while sampling perpendicular to convection provided one ensemble with slopes of 2 and another with slopes steeper than 2 in this study. We did not find any evidence for 0 spectral indices for the electric field fluctuation either in patches or in blobs even when samples were used from the center of Patch 1 in orbit 3223 where irregularity amplitudes were quite low. It is interesting to note that Gershman and Ponyatov (1988) have recently pointed out that in the F-region one expects the spatial power spectra of the electric field and electron density fluctuations to have similar shapes if the ion convection velocity is of the same order as the ion thermal velocity, a condition that is generally satisfied for drift velocities on the order of half a km per s.

Recently, Huba (1989) has shown that for comparing rocket or satellite data with simulations, one may get a very different picture depending on the direction of the one-dimensional cut with respect to the striations. When the satellite path intersects a single striation, which may be the

case when the satellite path is parallel to convection, the density enhancement does not look very structured. However, for paths that cut the striations at large angles, the density looks much more structured. These one-dimensional cuts through the two-dimensional simulation pictures look similar to the DE data sampled in the two orthogonal directions presented here. At this point it is important to recognize that the Patches P_2 and P_3 seen in orbit 3223 caused intense scintillations when they drifted through the ray path of a quasi-geostationary satellite being observed from Thule, Greenland (Basu et al., 1985) which (in addition to Figure 5) indicates that the patches contain granularity at km-scales and smaller.

The second important point we wanted to make in this paper was the magnitude of the density and electric field perturbations associated with the gradient drift process and its comparison with the shear-driven process. We presented evidence that the magnitude of the electric field perturbation was, at least, an order of magnitude larger in velocity shear driven processes when compared to the ones produced by the gradient drift instability. The largest perturbations were observed in the intense shear case presented in Paper I. The intense shear cases, however, had very similar spectral slopes of both density and electric field fluctuations as compared to the gradient drift case. Thus, it is our belief that it is crucial to consider magnitudes of perturbations, as well as spectral shapes, for an unambiguous determination of instability types. Even so there may be more than one

mechanism postulated to explain each observational class. Such is the case for the intense shear category as indicated in the last section. We have in this paper provided magnitudes of the saturation amplitudes of the density and electric field perturbations which may provide further clues for identification of the instabilities involved. We also hope that this discussion has helped in resolving the question raised by Heelis (1988) in a recent review that the intense shear category on the basis of spectral slopes alone is difficult to distinguish from the current convective (Ossakow and Chaturvedi, 1979) or gradient drift instability. The current convective instability has not been given too much attention because field aligned currents are, of course, conspicuous by their absence in polar cap patches, the main topic of discussion in this paper. Thus by considering magnitudes of perturbations and spectral shapes, we have been able to identify, at least, two generic types of instabilities important for producing high latitude plasma structure.

ACKNOWLEDGMENTS

We wish to thank R.A. Hoffman, the DE Project scientist, for his help and interest in this work. W.B. Hanson, N.C. Maynard, R.A. Heelis, J.D. Winningham, L.H. Brace, and N.W. Spencer, the Principal Investigators of the RPA, VEFI, IDM, LAPI, LANG, and WATS experiments, made their data readily available for this study. T.L. Killeen was very helpful in providing the combined data from WATS and IDM. We acknowledge useful discussions with M.J. Keskinen, R.A. Heelis, J.D. Huba, P.K. Chaturvedi, H.C. Carlson, Jr., and N.C. Maynard. We thank P.F. Fougere for the use of his MEM spectral analysis program. The work at Emmanuel College was partially supported by NSF Grant ATM-8715445 and AFGL Contract F19628-86-K-0038. The work at AFGL was supported in part by AFOSR Task 2310G9. The work at the University of Texas at Dallas was supported by NASA Grants NAG5-305 and NAG5-306. The work at Southwest Research Institute was supported by NASA Contract NAS5-28712, AFGL Contract F19628-84-N-0006, and AFOSR Contract F49620-85-C-0029.

REFERENCES

Anderson, D.N., J. Buchau, and R.A. Heelis, Origin of density enhancements in the winter polar cap ionosphere, Radio Sci., 23, 513, 1988.

Basu, B. and B. Coppi, Fluctuations associated with sheared velocity regions near auroral arcs, Geophys. Res. Lett., 15, 417, 1988.

Basu, B. and B. Coppi, Velocity shear and fluctuations in the auroral regions of the ionosphere, J. Geophys. Res., 94, 5316, 1989.

Basu, Su., S. Basu, J.P. McClure, W.B. Hanson, and H.E. Whitney, High-resolution topside in-situ data of electron densities and VHF/GHz scintillations in the equatorial region, J. Geophys. Res., 88, 403, 1983.

Basu, Su., S. Basu, E. MacKenzie, and H.E. Whitney, Morphology of phase and intensity scintillations in the auroral oval and polar cap, Radio Sci., 20, 347, 1985.

Basu, Su., S. Basu, E. MacKenzie, P.F. Fougere, W.R. Coley, N.C. Maynard, J.D. Winningham, M. Sugiura, W.B. Hanson, and W.R. Hoegy, Simultaneous density and electric field fluctuation spectra associated with velocity shears in the auroral oval, J. Geophys. Res., 93, 115, 1988a.

Basu, Su., S. Basu, E.J. Weber, and W.R. Coley, Case study of polar cap scintillation modeling using DE-2 irregularity measurements at 800 km, Radio Sci., 23, 545, 1988b.

Beghin, C., J.F. Karczewski, B. Poirier, R. Debrie, and N. Massewitch, The ARCAD-3 ISOPROBE experiment for high time resolution thermal plasma measurements, Ann. Geophys., 38, 615, 1982.

Cerisier, J.C., J.J. Berthelier, and C. Beghin, Unstable density gradients in the high-latitude ionosphere, Radio Sci., 20, 755, 1985.

Chaturvedi, P.K. and J.D. Huba, The interchange instability in high-latitude plasma blobs, J. Geophys. Res., 92, 3357, 1987.

Doolittle, J.H., S.B. Mende, R.M. Robinson, G.R. Swenson, and C.E. Valladares, Ionospheric convection in the polar cap as seen by optical imaging, Submitted to J. Geophys. Res., 1989.

Emery, B.A., R.G. Roble, E.C. Ridley, T.L. Killeen, M.H. Rees, J.D. Winnigham, G.R. Carignan, P.B. Hays, R.A. Heelis, W.B. Hanson, N.W. Spencer, L.H. Brace, and M. Sugiura, Thermospheric and ionospheric structure of the southern hemisphere polar cap on October 21, 1981 as determined from Dynamics Explorer-2 satellite data, J. Geophys. Res., 90, 6553, 1985.

Francis, S.H. and F.W. Perkins, Determination of striation scale sizes for plasma clouds in the ionosphere, J. Geophys. Res., 80, 3111, 1975.

Ganguli, G., Y.C. Lee, P.J. Palmadesso, and S.L. Ossakow, Ion waves in a collisional magnetoplasma with a field-aligned current and a transverse velocity shear, Proceedings of the 1988 Cambridge Workshop in Theoretical Geoplasma Physics, Polar Cap Dynamics and High Latitude Ionospheric Turbulence, MIT, Cambridge MA, 1989.

Gershman, B.N. and A.A. Ponyatov, Relation between spatial spectra of electron-density fluctuations and the electric field for a gradient-drift instability in the ionosphere, Geomagnetism and Aeronomy, 28, 422, 1988.

Hanson, W.B., R.A. Heelis, R.A. Power, C.R. Lippincott, D.R. Zuccaro, B.J. Holt, L.H. Harmon, and S. Sanatani, The retarding potential analyzer for Dynamics Explorer-B, Space Sci. Instr., 5, 503, 1981.

Hassam, A.B., W. Hall, J.D. Huba, and M.J. Keskinen, Spectral characteristics of interchange turbulence, J. Geophys. Res., 91, 13513, 1986.

Hays, P.B., T.L. Killeen, and B.C. Kennedy, The Fabry-Perot Interferometer on Dynamics Explorer, Space Sci. Instr., 5, 395, 1981.

Heelis, R.A., Studies of ionospheric plasma and electrodynamics and their application to ionosphere-magnetosphere coupling, Rev. Geophys., 26, 317, 1988.

Heelis, R.A., J.D. Winnigham, M. Sugiura, and N.C. Maynard, Particle acceleration parallel and perpendicular to the magnetic field observed by DE-2, J. Geophys. Res., 89, 3893, 1984.

Hoffman, R.A. and E.R. Schmerling, Dynamics Explorer program: an overview, Space Sci. Instr., 5, 345, 1981.

Huba, J.D., Theoretical and simulation methods applied to high latitude ionospheric turbulence, Proceedings of the 1988 Cambridge Workshop in Theoretical Geoplasma Physics, Polar Cap Dynamics and High Latitude Ionospheric Turbulence, MIT, Cambridge MA, 1989.

Kersley, L., F.E. Pryse, and N.S. Whealon, Small-scale irregularities associated with a high-latitude electron density gradient: scintillation and EISCAT observations, J. Atmos. Terr. Phys., 50, 557, 1988.

Keskinen, M.J. and J.D. Huba, Nonlinear evolution of high latitude ionospheric interchange instabilities with scale-size-dependent magnetospheric coupling, Submitted to J. Geophys. Res., 1989.

Keskinen, M.J. and S.L. Ossakow, Nonlinear evolution of convecting plasma enhancements in the auroral ionosphere, I, Long wavelength irregularities, J. Geophys. Res., 87, 144, 1982.

Keskinen, M.J. and S.L. Ossakow, Nonlinear evolution of convecting plasma enhancements in the auroral ionosphere, 2, Small scale irregularities, J. Geophys. Res., 88, 474, 1983.

Keskinen, M.J., H.G. Mitchell, J.A. Fedder, P. Satyanarayana, S.T. Zalesak, and J.D. Huba, Nonlinear evolution of the Kelvin-Helmholtz instability in the high-latitude ionosphere, J. Geophys. Res., 93, 137, 1988.

Killeen, T.L., R.A. Heelis, P.B. Hays, N.W. Spencer, and W.B. Hanson, Neutral motions in the thermosphere for northward interplanetary magnetic field, Geophys. Res. Lett., 12, 159, 1985.

Kintner, P.M. and C.E. Seyler, The status of observations and theory of high latitude ionospheric and magnetospheric plasma turbulence, Space Sci. Res., 41, 91, 1985.

Krehbiel, J.P., L.H. Brace, R.F. Theis, W.H. Pinkus, and R.B. Kaplan, The Dynamics Explorer Langmuir probe instrument, Space Sci. Instr., 5, 493, 1981.

Maynard, N.C., E.A. Bielecki, and H.F. Burdick, Instrumentation for vector electric field measurements from DE-B, Space Sci. Instr., 5, 523, 1981.

Mitchell, H.G., J.A. Fedder, M.J. Keskinen, and S.T. Zalesak, A simulation of high latitude F-layer instabilities in the presence of magnetosphere-ionosphere coupling, Geophys. Res. Lett., 12, 283, 1985.

Nishikawa, K.-I., G. Ganguli, Y.C. Lee, and P. Palmadesso, Simulation of electrostatic ion instabilities in the presence of parallel currents and transverse electric fields, Proceedings of the 1988 Cambridge Workshop in Theoretical Geoplasma Physics, Polar Cap Dynamics and High Latitude Ionospheric Turbulence, MIT, Cambridge MA, 1989.

Ossakow, S.L. and P.K. Chaturvedi, Current convective instability in the diffuse aurora, Geophys. Res. Lett., 6, 332, 1979.

Rino, C.L., R.T. Tsunoda, J. Petriceks, R.C. Livingston, M.C. Kelley, and K.D. Baker, Simultaneous rocket-borne beacon and in-situ measurements of equatorial spread F-intermediate wavelength results, J. Geophys. Res., 86, 2411, 1981.

Rino, C.L., R.C. Livingston, R.T. Tsunoda, R.M. Robinson, J.F. Vickrey, C. Senior, M.D. Cousins, J. Owen, and J.A. Klobuchar, Recent studies of the structure and morphology of auroral zone F region irregularities, Radio Sci., 18, 1167, 1983.

Robinson, R.M., R.T. Tsunoda, J.F. Vickrey, and L. Guerin,
Sources of F region ionization enhancements in the
nighttime auroral zone, J. Geophys. Res., 90, 7533, 1985.

Robinson, R.M., R.R. Vondrak, K. Miller, T. Dabbs, and
D. Hardy, On the calculation of conductances from the flux
and energy of precipitating electrons, J. Geophys. Res.,
92, 2565, 1987.

Schunk, R.W. and J.J. Sojka, A theoretical study of the
lifetime and transport of large ionospheric density
structures, J. Geophys. Res., 92, 12343, 1987.

Spencer, N.W., L.E. Wharton, H.B. Niemann, A.E. Hedin,
G.R. Carignan, and J.C. Maurer, The Dynamics Explorer wind
and temperature spectrometer, Space Sci. Instr., 5, 417,
1981.

Strickland, D.J., D.L. Book, T.P. Coffey, and J.A. Fedder,
Transport equation techniques for the deposition of
auroral electrons, J. Geophys. Res., 81, 2755, 1976.

Tsunoda, R.T., High-latitude F-region irregularities: a review
and synthesis, Revs. Geophys., 26, 719, 1988.

Vickrey, J.F. and M.C. Kelley, The effects of a conducting E
layer on a classical F region cross-field plasma
diffusion, J. Geophys. Res., 87, 4461, 1982.

Vickrey, J.F., C.L. Rino, and T.A. Potemra, Chatanika/TRIAD observations of unstable ionization enhancements in the auroral F region, Geophys. Res. Lett., 7, 789, 1980.

Villain, J.-P., C. Beghin, and C. Manuise, ARCAD3-SAFARI coordinated study of auroral and polar F-region ionospheric irregularities, Ann. Geophys., 4, 61, 1986.

Weber, E.J., J. Buchau, J.G. Moore, J.R. Sharber, R.C. Livingston, J.D. Winningham, and B.W. Reinisch, F layer ionization patches in the polar cap, J. Geophys. Res., 89, 1683, 1984.

Weber, E.J., R.T. Tsunoda, J. Buchau, R.E. Sheehan, D.J. Strickland, W. Whiting, and J.G. Moore, Coordinated measurements of auroral zone plasma enhancements, J. Geophys. Res., 90, 6497, 1985.

Weber, E.J., J.A. Klobuchar, J. Buchau, H.C. Carlson, Jr., R.C. Livingston, O. de la Beaujardiere, M. McCready, J.G. Moore, and G.J. Bishop, Polar cap F layer patches: structure and dynamics, J. Geophys. Res., 91, 12121, 1986.

Winningham, J.D. and C. Gurgiolo, DE-2 photoelectron measurements consistent with a large-scale parallel electric field over the polar cap, Geophys. Res. Lett., 9, 977, 1982.

Winningham, J.D. and W.J. Heikkila, Polar cap auroral electron fluxes observed with ISIS 1, J. Geophys. Res., 79, 949, 1974.

Winningham, J.D., J.L. Burch, N. Eaker, V.A. Blevins, and R.A. Hoffman, The low altitude plasma instrument (LAPI), Space Sci. Instr., 5, 465, 1981.

TABLE 1
DE-2 Orbit 3223 82067

Time (UT)	\bar{E} (keV)	Φ_E (ergs/cm ² s)	Σ_p (mho)	Σ_H (mho)
0336:40	5.38	5.73	11.67	23.05
0336:43	5.31	5.55	11.52	22.47
0336:48	4.12	5.47	11.88	18.53
0336:51	4.42	3.21	9.05	14.98

TABLE 2
Comparison of Spectral Indices for the Interchange Instability

		Numerical Simulation	Experimental
δN	$P(k_x)$	2.2 ± 0.3	1.9 ± 0.1
	$P(k_y)$	1.8 ± 0.3	1.9 ± 0.1
δE_x	$P(k_x)$	2.3 ± 0.3	$1.9 \pm 0.1, 2.3 \pm 0.1$ to 3.3 ± 0.1
	$P(k_y)$	2.1 ± 0.3	---
δE_y	$P(k_x)$	2.2 ± 0.3	---
	$P(k_y)$	1.9 ± 0.3	1.9 ± 0.1
x		Direction perpendicular to initial density gradient for numerical simulation Direction perpendicular to convection for experimental data	

FIGURE CAPTIONS

FIGURE 1. Vector velocity measurements using IDM and RPA for DE-2 orbit 3223 through the northern high latitude ionosphere on March 8, 1982.

FIGURE 2. LANG measurements of ion density (N_i) and electron temperature (T_e) for orbit 3223. Three polar cap patches are denoted by P_1 , P_2 , and P_3 and two auroral blobs by B1 and B2.

FIGURE 3. Energetic electron spectrogram at 7.4° pitch angle for DE-2 orbit 3223.

FIGURE 4a. The N-S horizontal drifts from the RPA and N-S electric field from VEFI for orbit 3223.

FIGURE 4b. The E-W neutral wind and plasma drift from WATS and IDM respectively for orbit 3223.

FIGURE 5. The top panel shows irregularity amplitude ($\Delta N/N$)_{RMS} computed over 8-s sample length associated with polar cap patches. The five bottom panels show data of ac electric field turbulence obtained from VEFI. The ac turbulence associated with the edges of patches P_1 , P_2 and P_3 are indicated on the 4-8 Hz panel.

FIGURE 6. 8-s data of irregularity amplitude ($\Delta N/N$)_{RMS} computed from RPA data for patch P_2 on orbit 3223 and its spectrum by the maximum entropy technique.

FIGURE 7. 8-s data of dc electric field fluctuation for the same period as shown in Figure 6 and its spectrum by the maximum entropy technique.

FIGURE 8a. Histogram of spectral slopes of ($\Delta N/N$)_{RMS} for the patch portion of orbit 3223.

FIGURE 8b. Histogram of spectral slopes of ΔE for the patch portion of orbit 3223.

FIGURE 8c. Histogram of spectral slopes of ($\Delta N/N$)_{RMS} for the patch portion of orbit 3223 computed from Wideband filter data with $\lambda < 125m$.

FIGURE 9. Same as in Figure 1 except for orbit 4429 through the southern high latitude ionosphere.

FIGURE 10. Same as in Figure 2. Three polar cap patches P_1 , P_2 , and P_3 and one auroral blob B are seen.

FIGURE 11. Same as in Figure 4b except for orbit 4429.

FIGURE 12. N-S electric field from VEFI and ($\Delta N/N$)_{RMS} computed over 8-s sample length for patch portion of orbit 4429.

FIGURE 13. Five panels of ac electric field turbulence associated with patch portion of orbit 4429.

FIGURE 14. Same as in Figure 6 but for orbit 4429.

FIGURE 15. Same as in Figure 7 but for orbit 4429.

FIGURE 16a. Same as in Figure 8a except for orbit 4429.

FIGURE 16b. Same as in Figure 8b except for orbit 4429.

FIGURE 16c. Same as in Figure 8c except for orbit 4429.

FIGURE 17. Two spectra of precipitating electrons obtained from LAPI on orbit 3223 when DE-2 was sampling the auroral blob B2.

FIGURE 18. Seven consecutive samples of 8-s detrended data of $(\Delta N/N)_{RMS}$ showing steep edges on one side and irregularities on the other within auroral blob B2 on orbit 3223.

FIGURE 19. Spectrum of one 8-s sample of $(\Delta N/N)_{RMS}$ obtained from blob B2 on orbit 3223.

FIGURE 20. One 8-s sample of detrended data of $(\Delta N/N)_{RMS}$ obtained from blob B of orbit 4429 and its spectrum on the top panel.

FIGURE 21. Scatter plot of $(\Delta N/N)_{RMS}$ and ΔE for patches and velocity shear regions. A distinctly different slope fit is obtained for each category.

FIGURE 22. Same as in Figure 8c except for velocity shear region of orbit 4429.

FIGURE 1

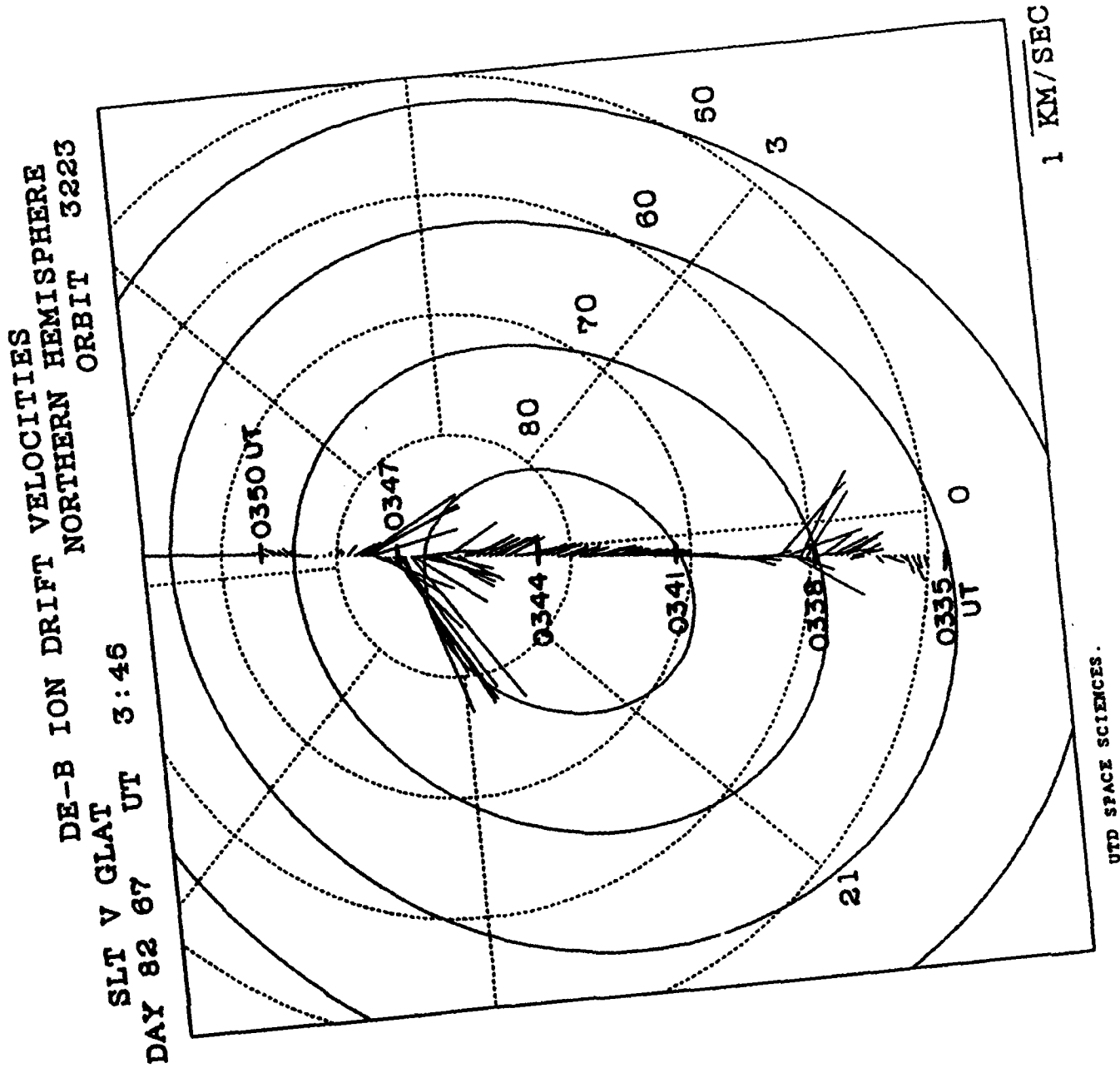
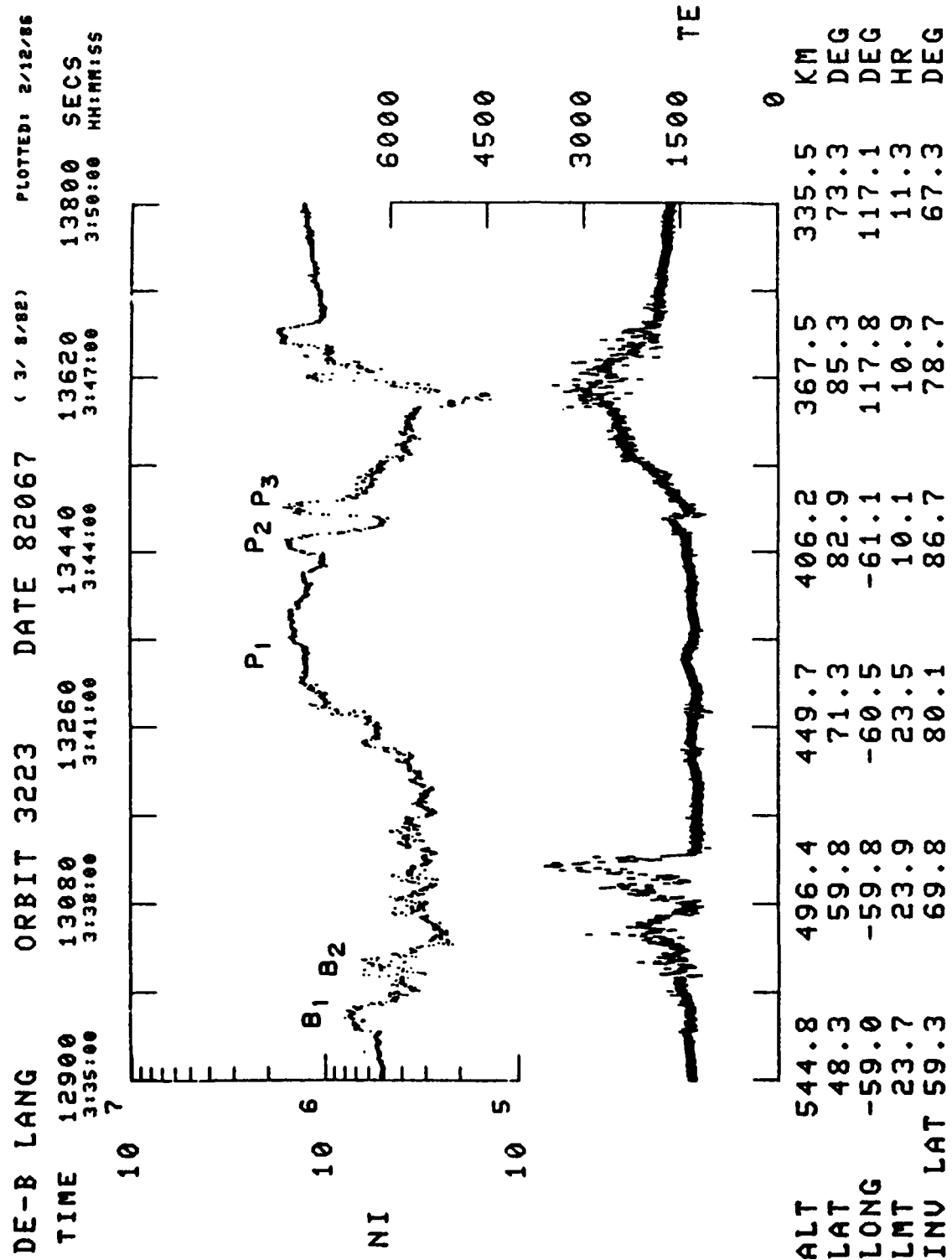


FIGURE 2



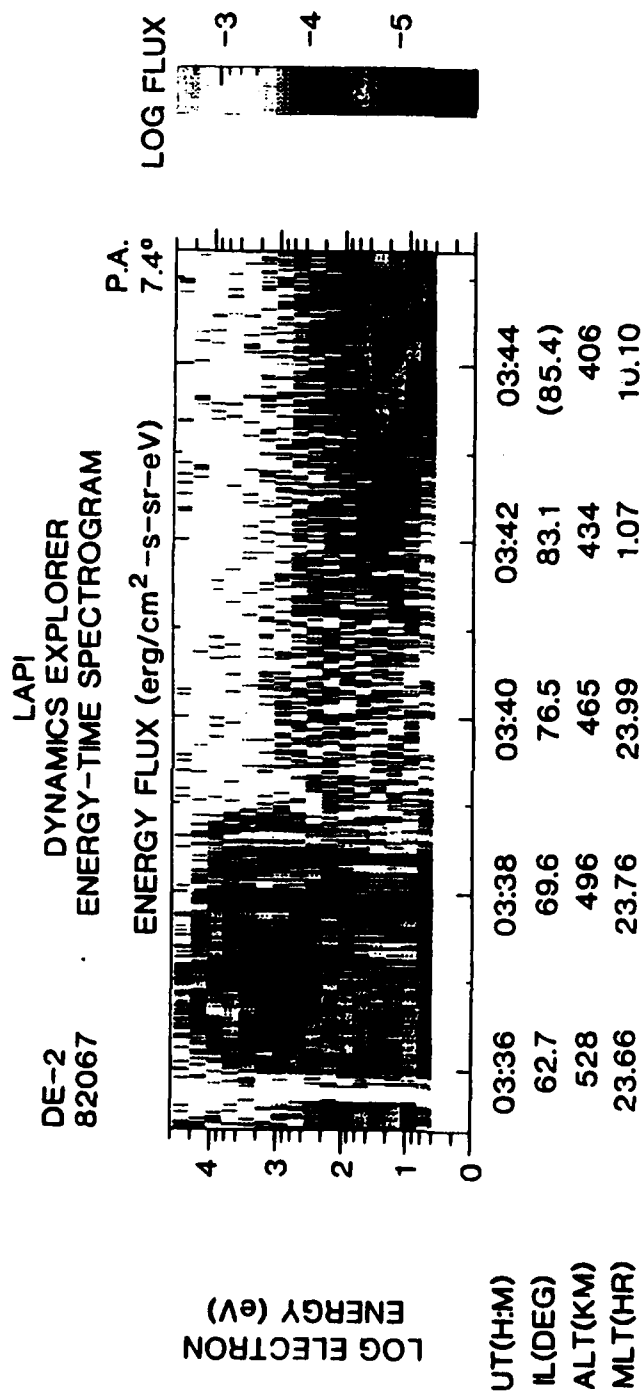


FIGURE 3

DE-2 ORBIT # 3223 82067

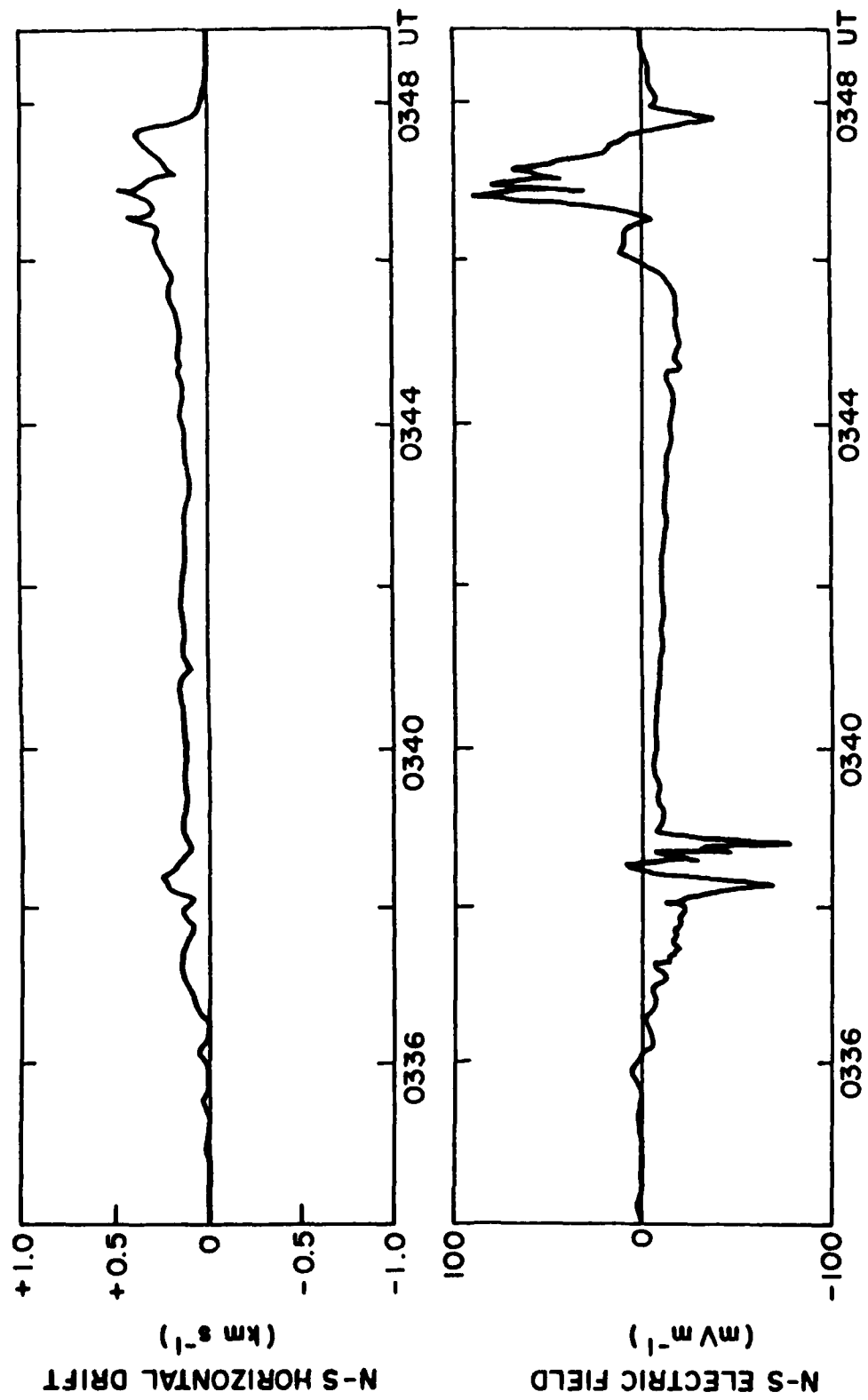


FIGURE 4a

DE-2 WATS / IDM ZONAL ION DRIFT AND NEUTRAL WIND

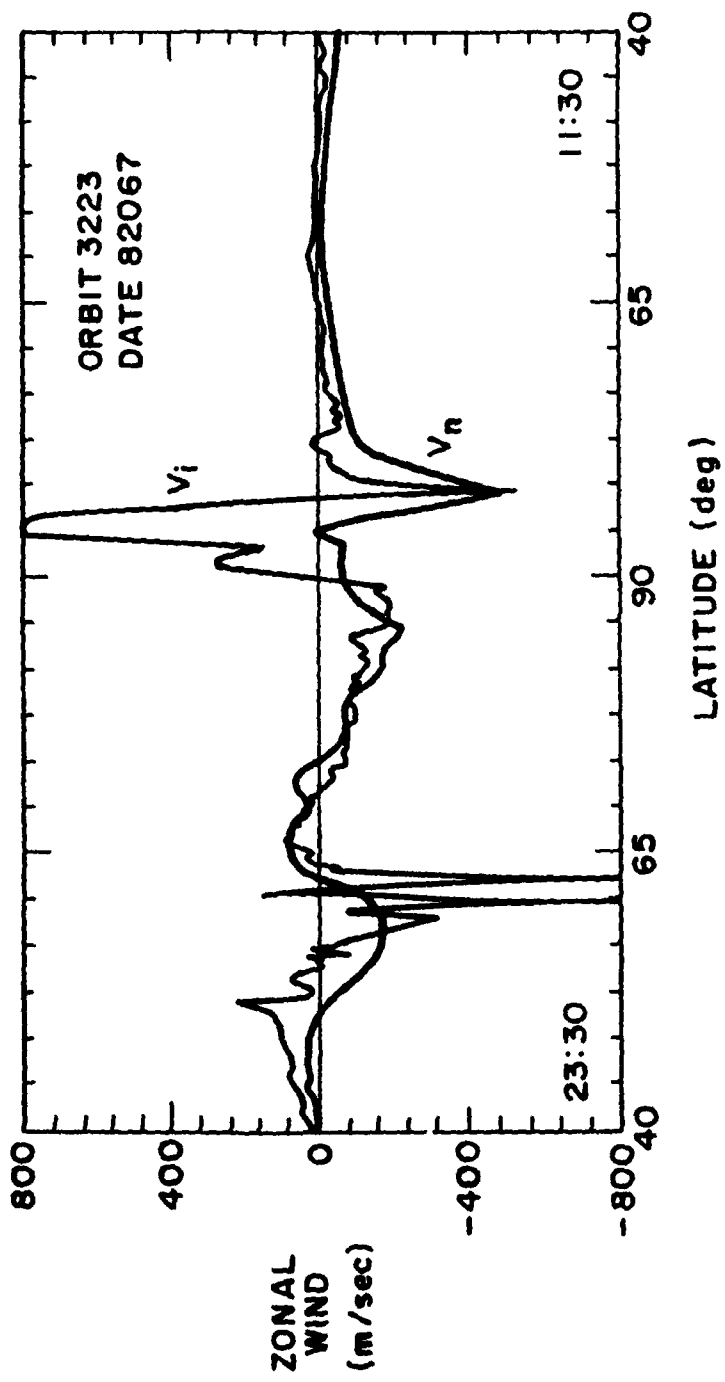


FIGURE 4b

Figure 5

82067

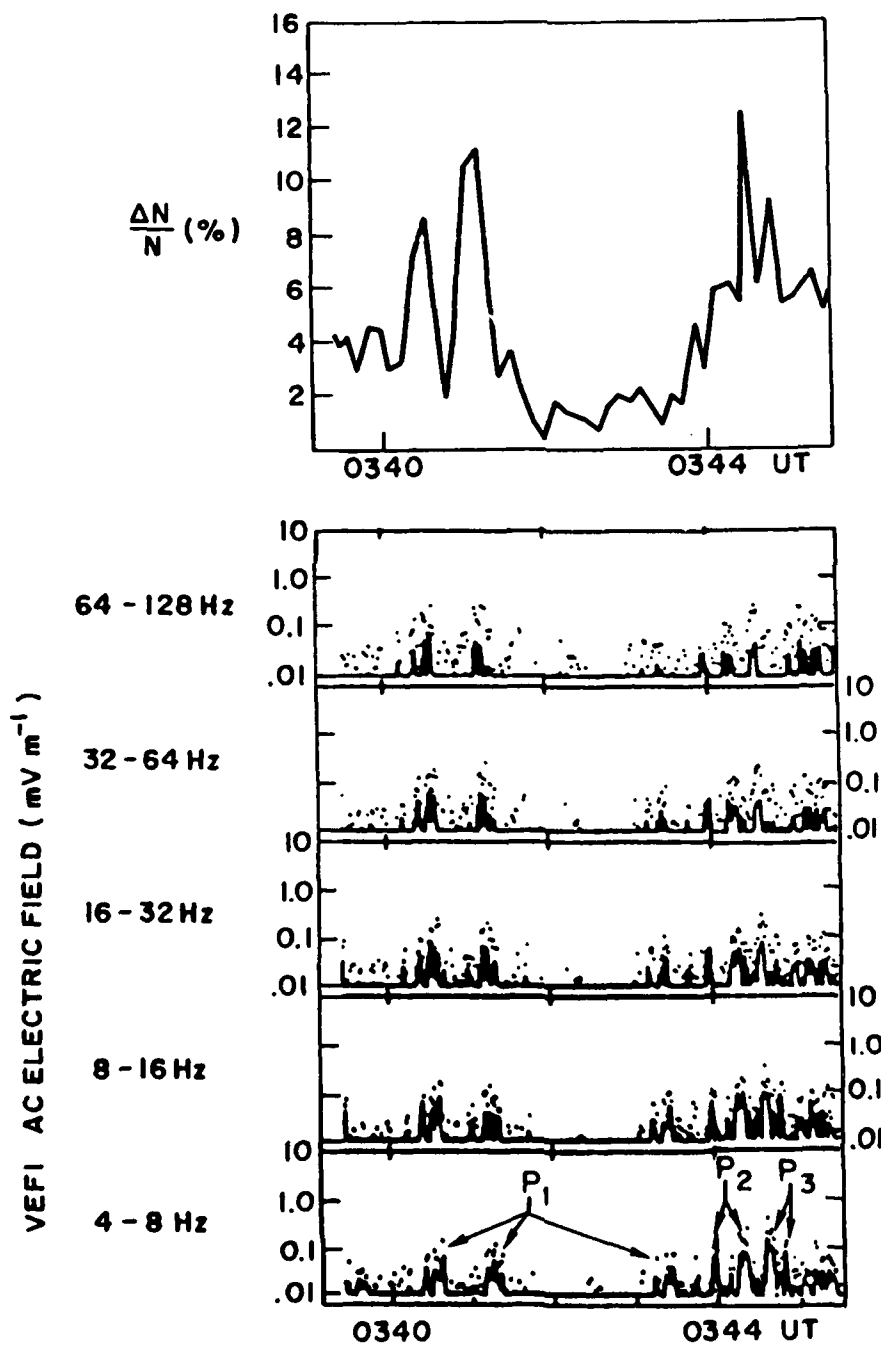


FIGURE 6

ORBIT 3223 82067
ION DENSITY 0344:07 UT

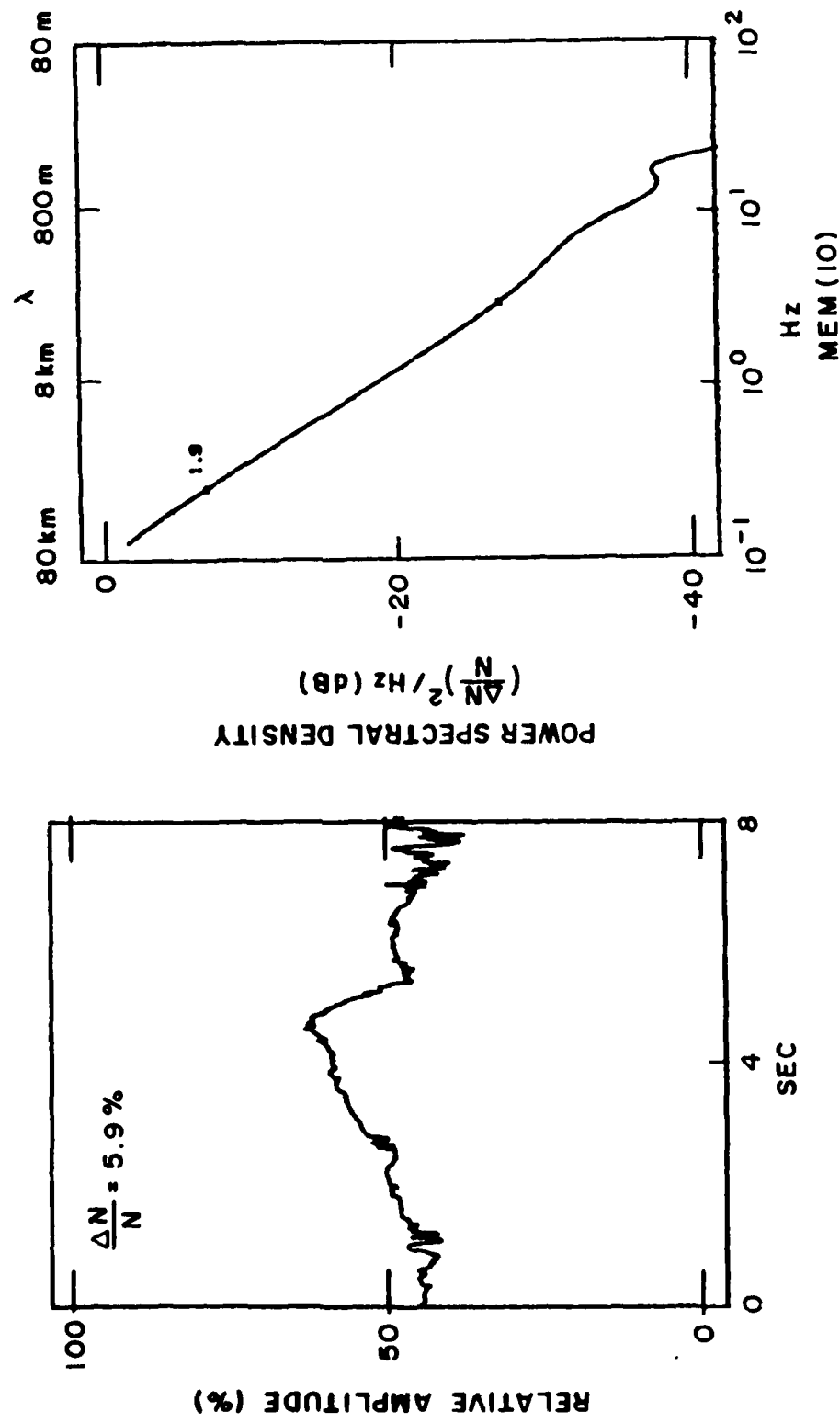


FIGURE 7

ORBIT 3223 82067
N-S ELECTRIC FIELD 0344:07 UT

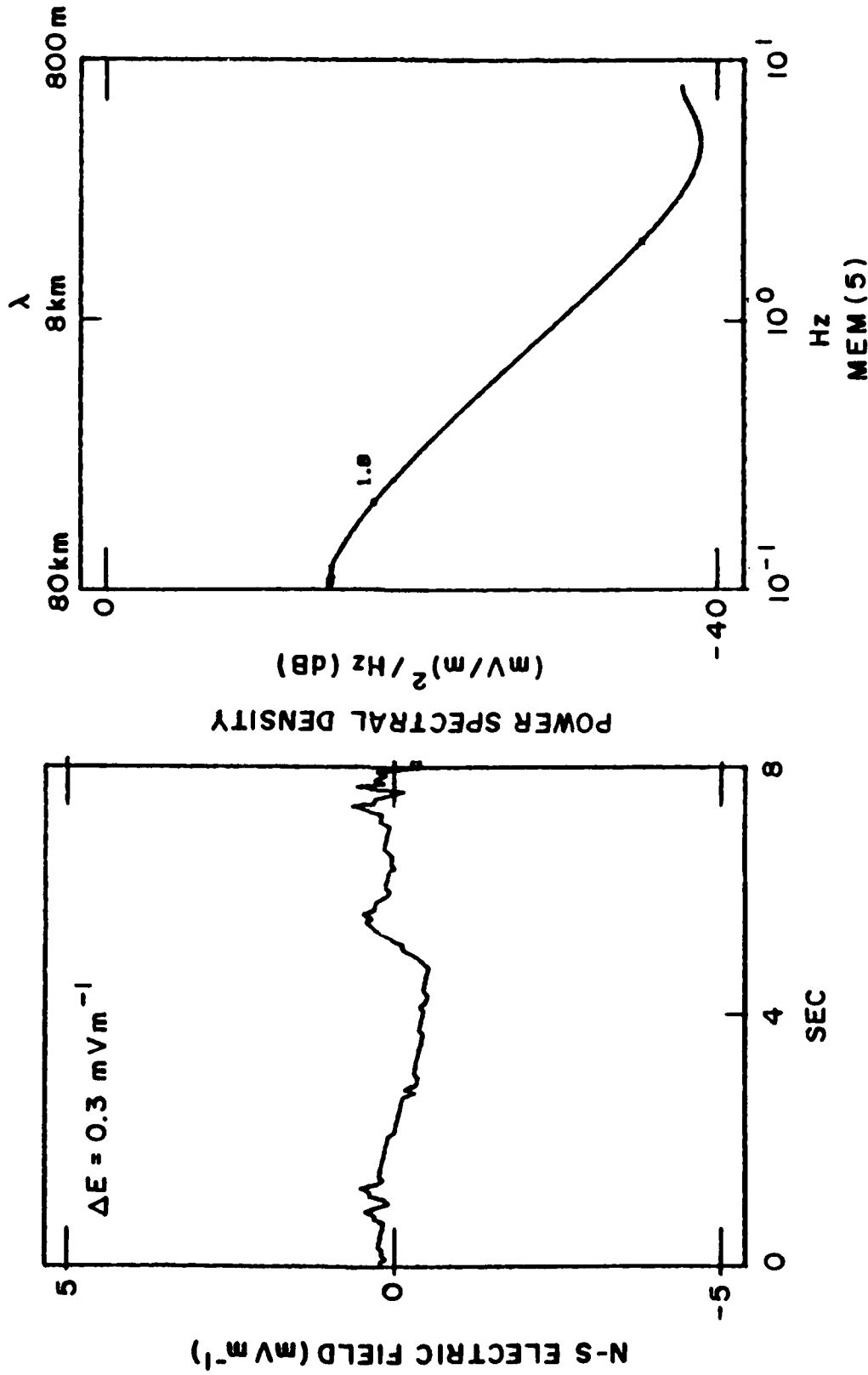


FIGURE 8a

ION DENSITY 82067 DE-2 ORBIT # 32223
0339:27 - 0345:27 UT

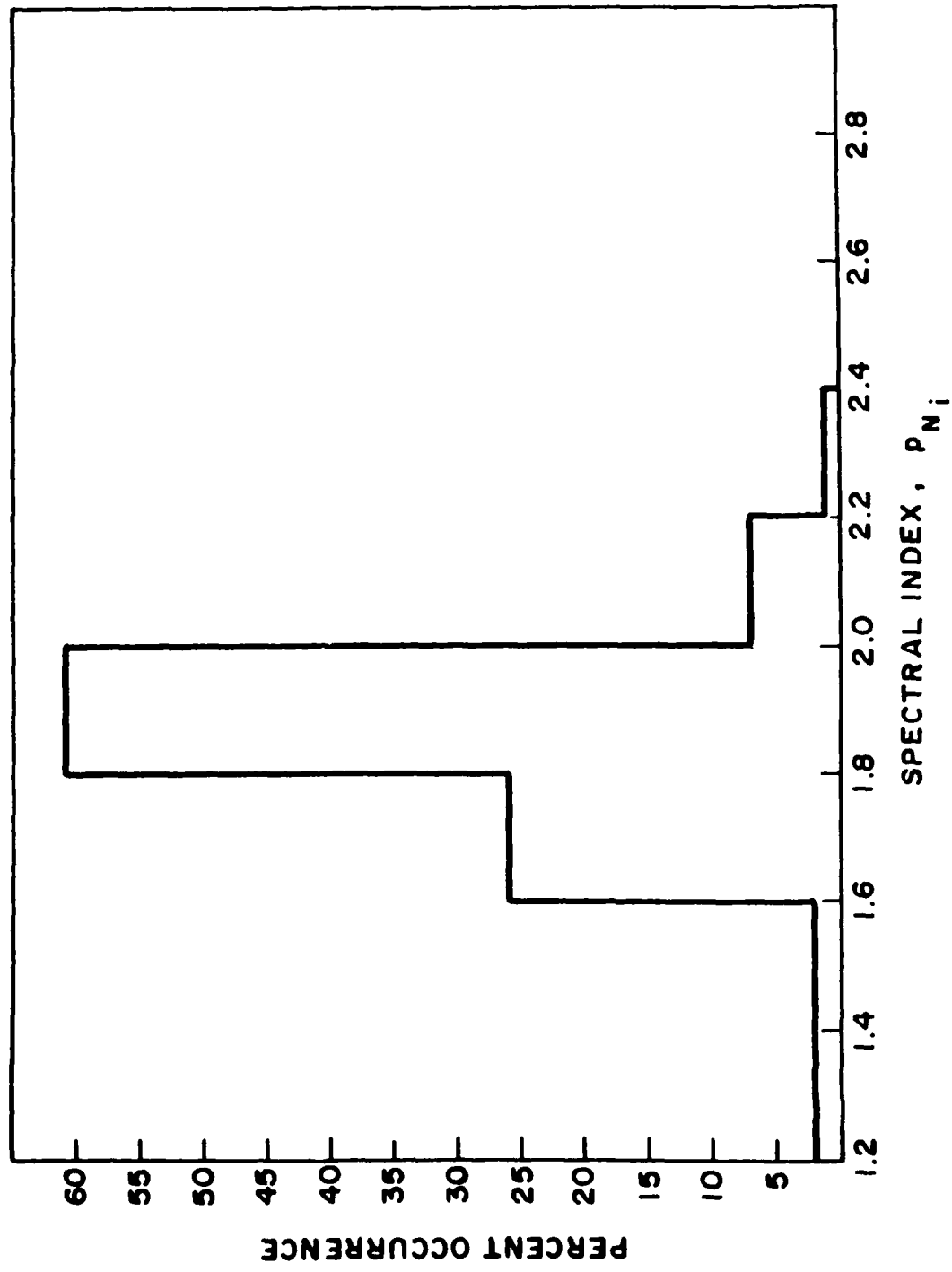


FIGURE 8b
ELECTRIC FIELD 82067 DE-2 ORBIT # 3223
0339:27 - 0345:27 UT

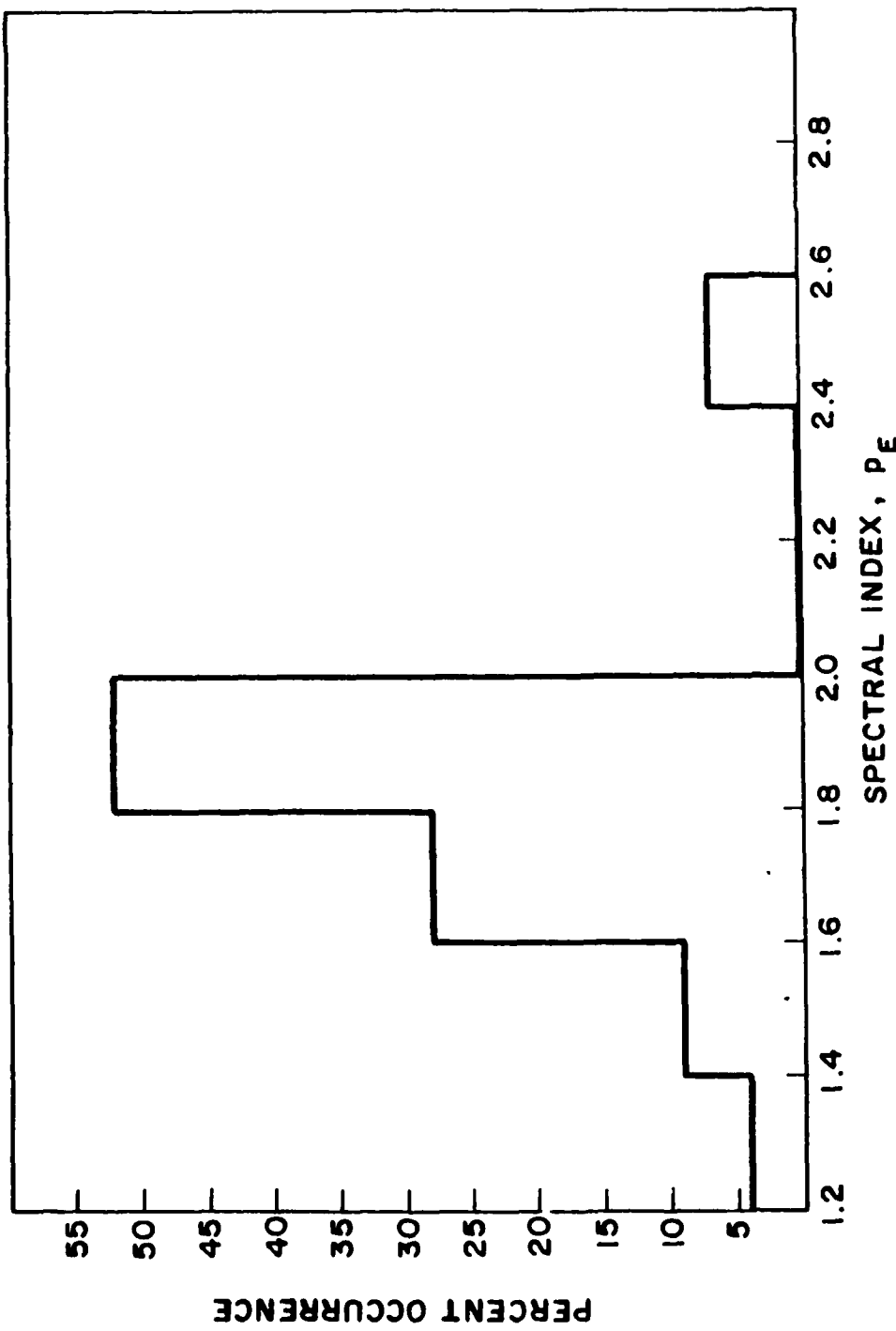


FIGURE 8c

DAY 67, 1982 DE-2 ORBIT 3223
DENSITY SPECTRAL SLOPES ($\lambda < 125$ m)

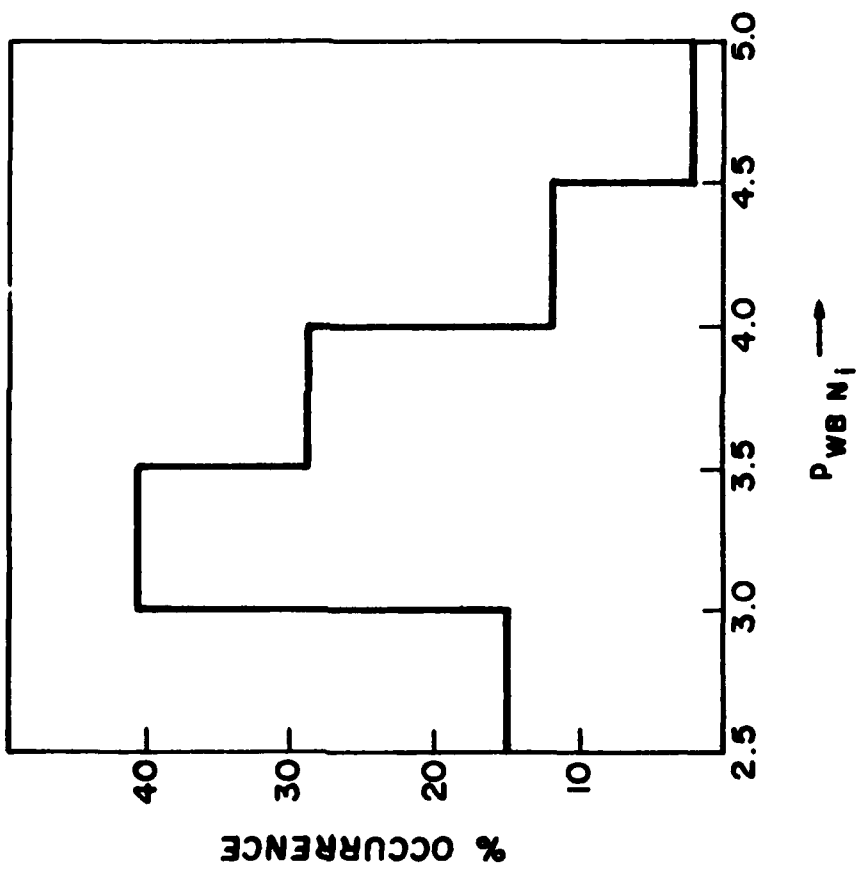
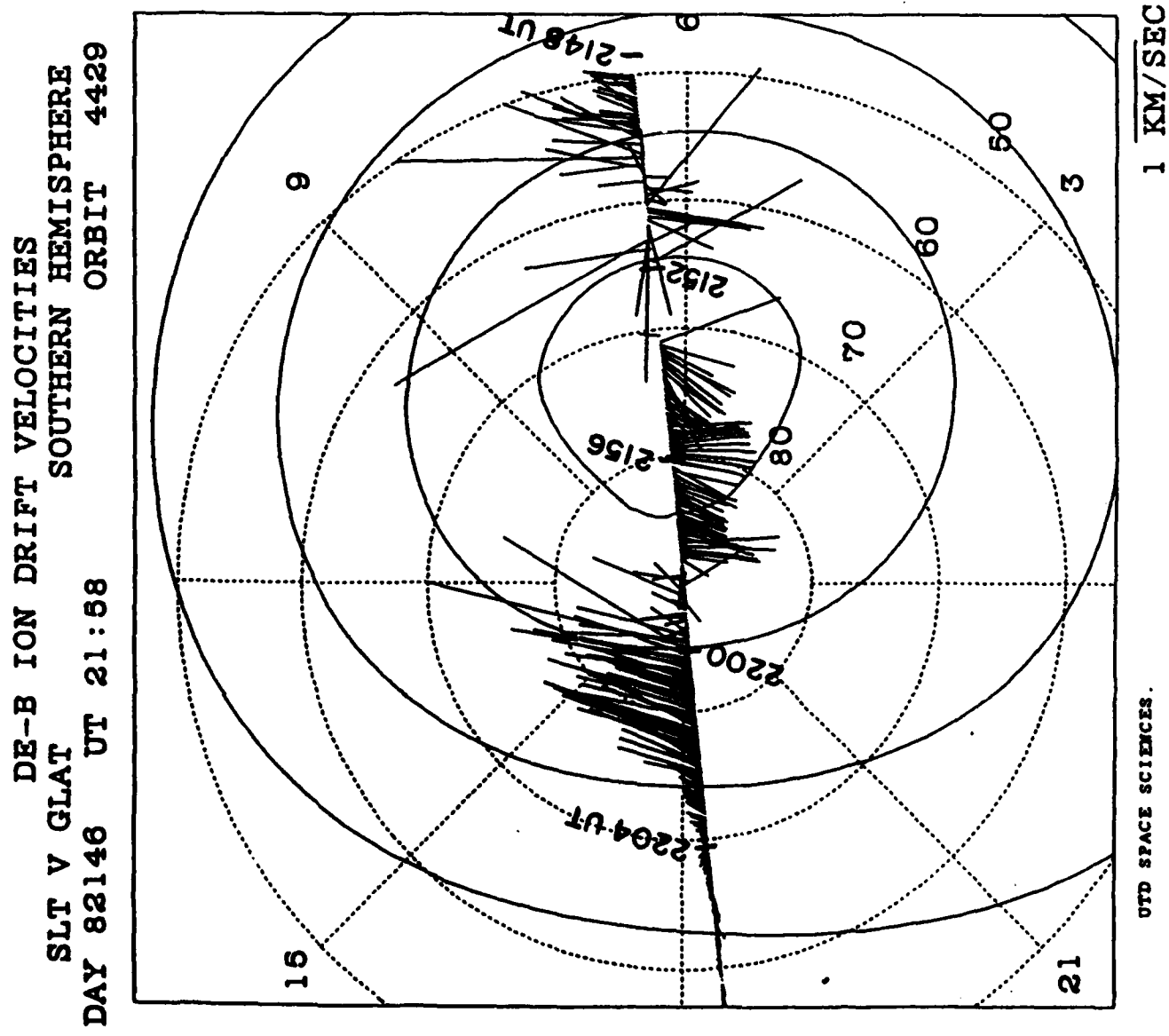


FIGURE 9



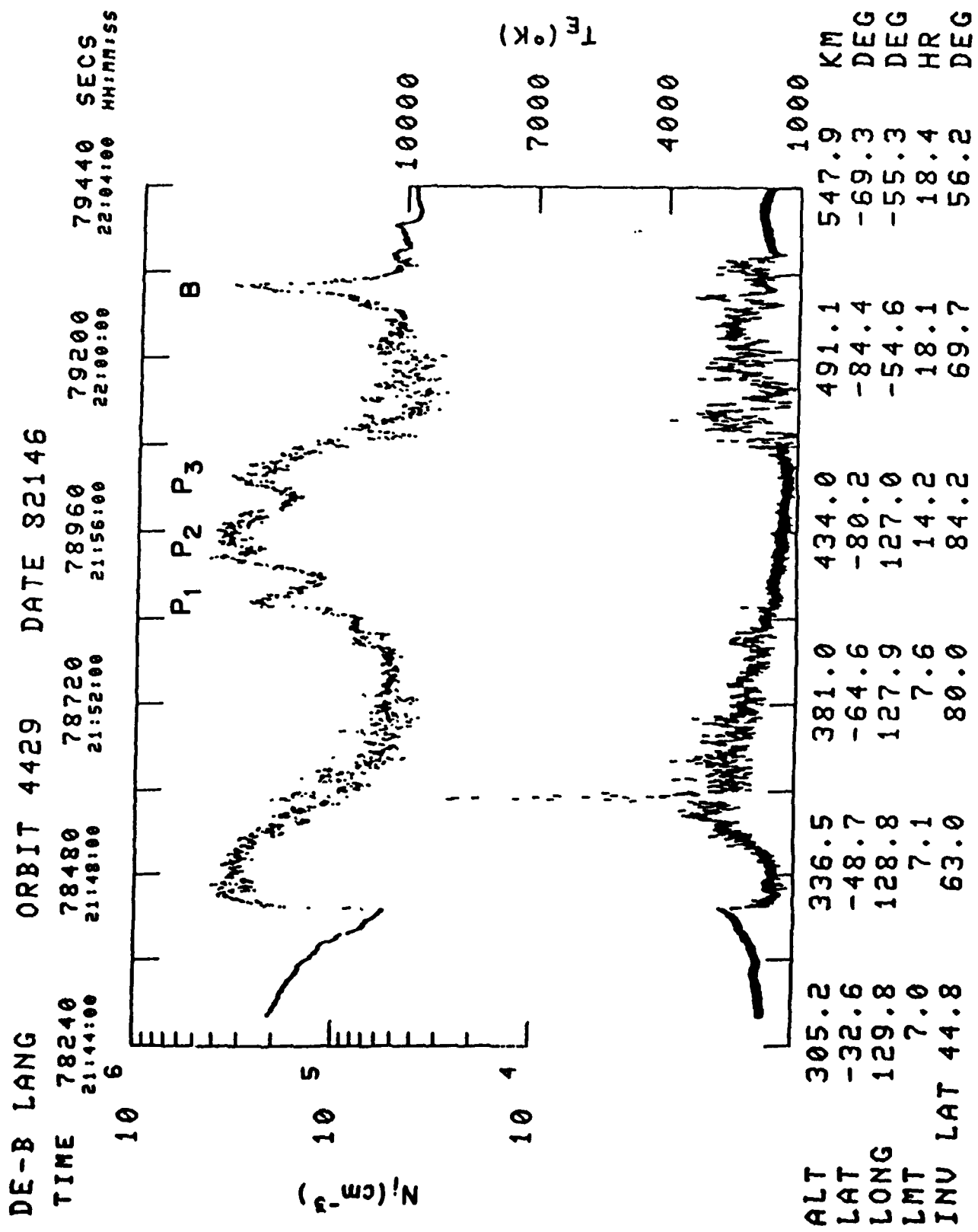


FIGURE 10

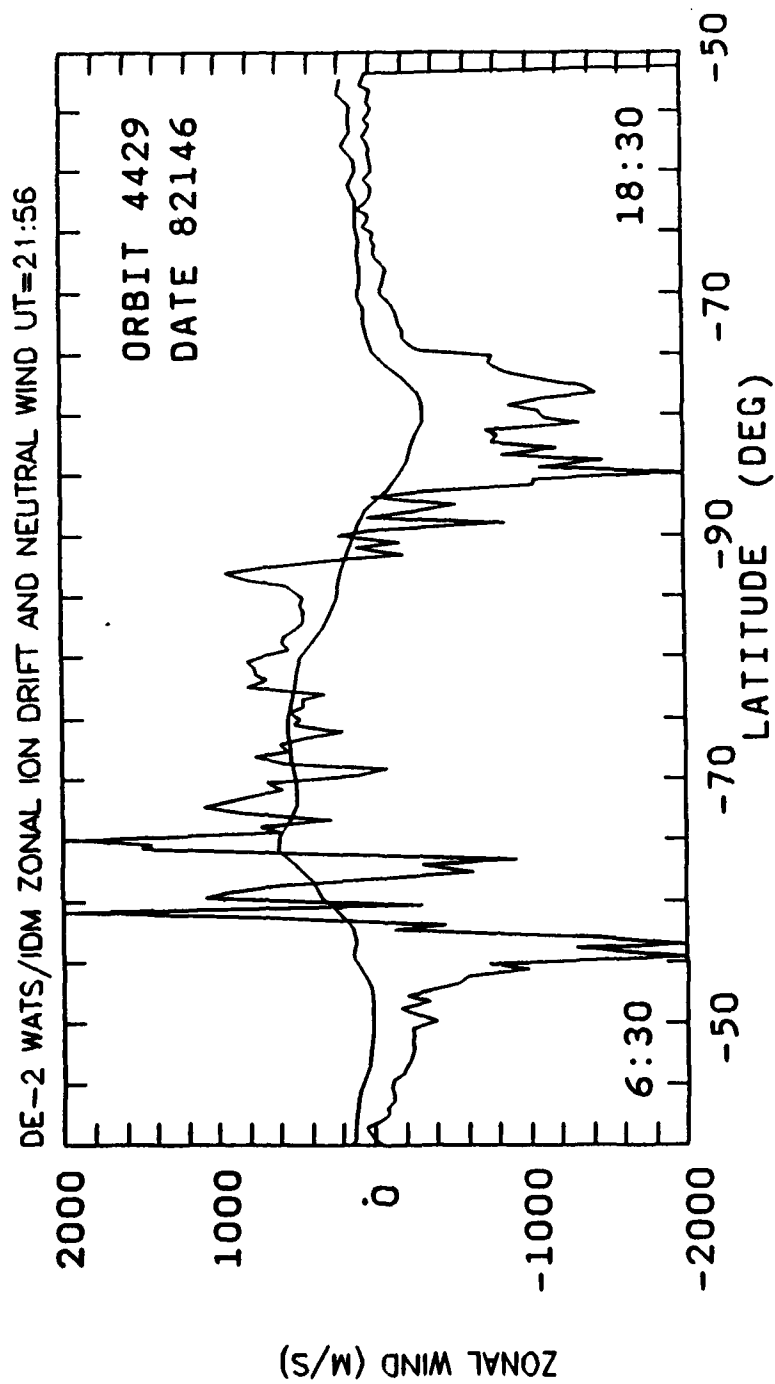
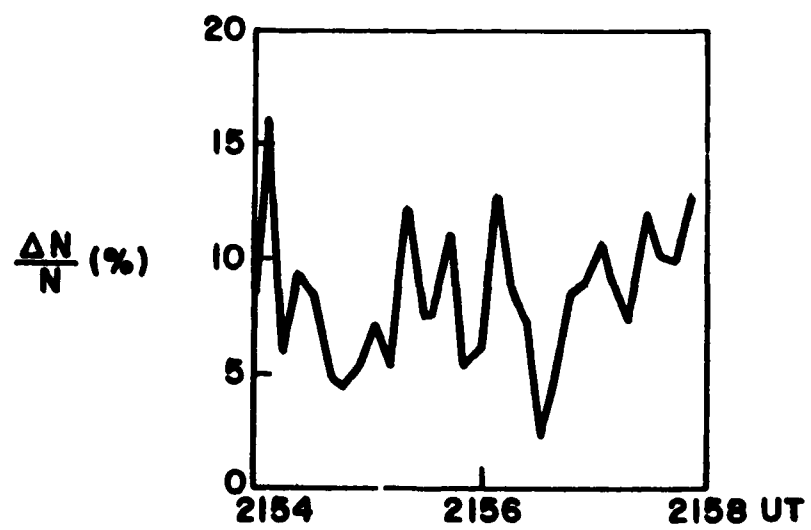
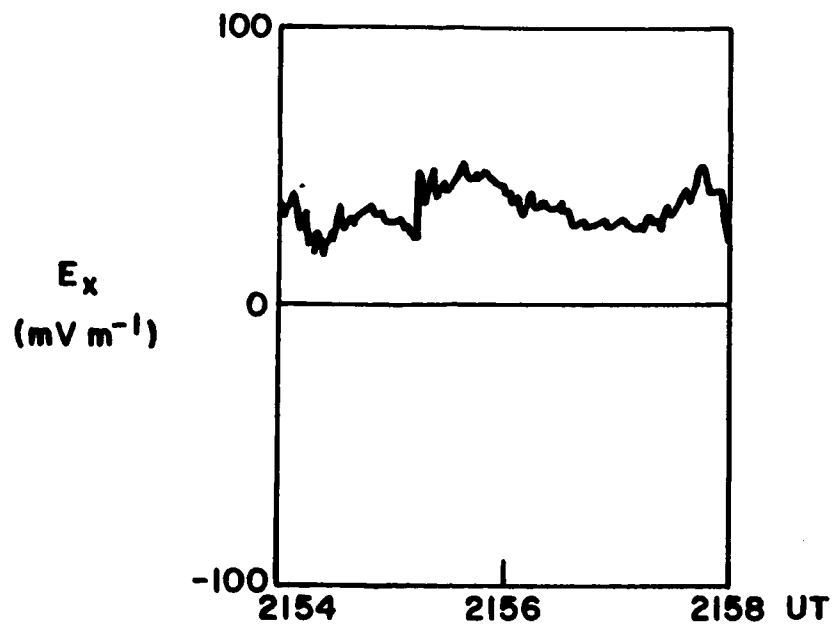


FIGURE 11

FIGURE 12

ORBIT 4429 82146



82146

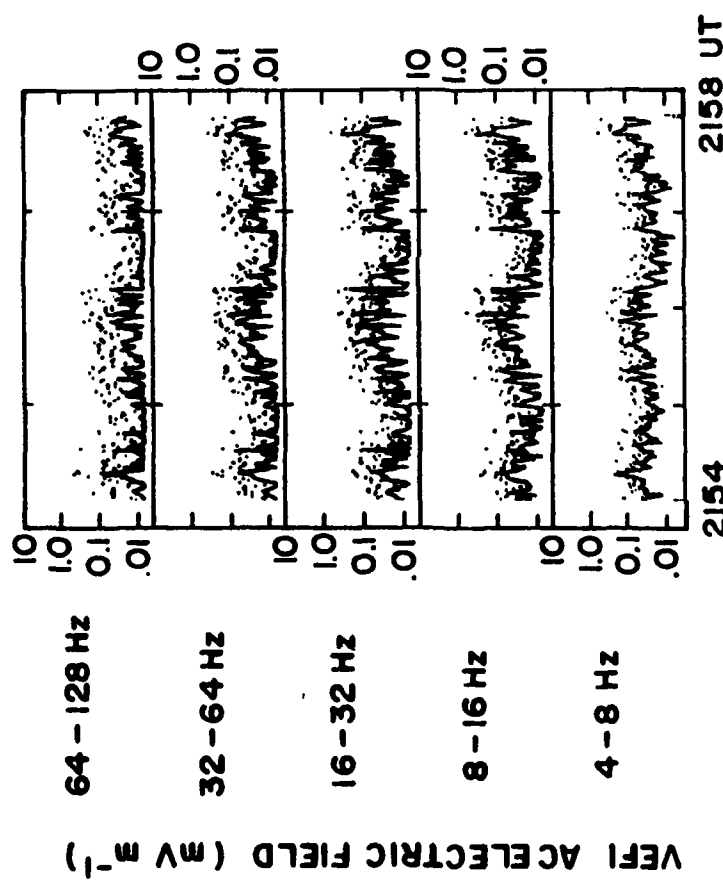


FIGURE 13

ORBIT 4429
ION DENSITY 2156:00 UT
82/46

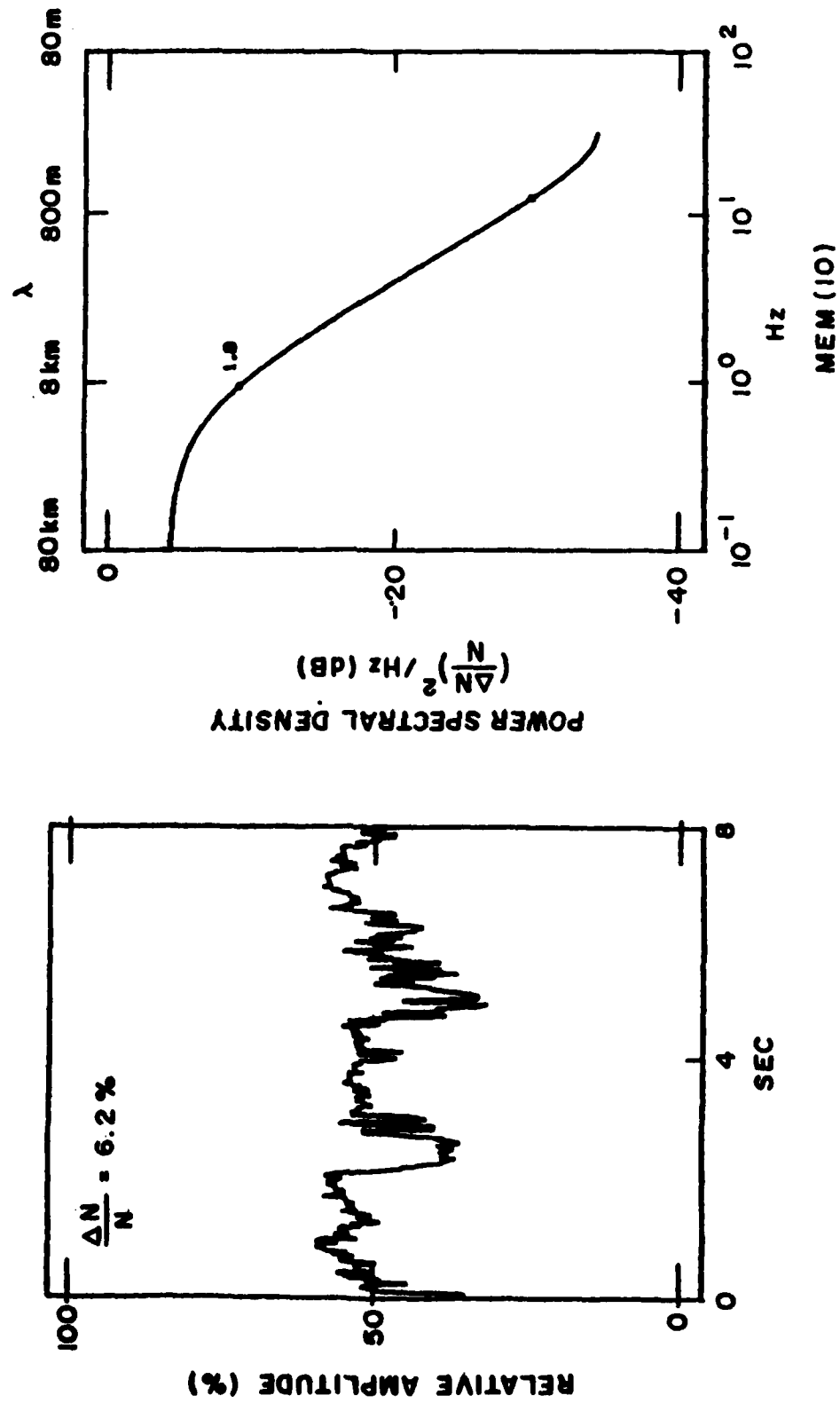
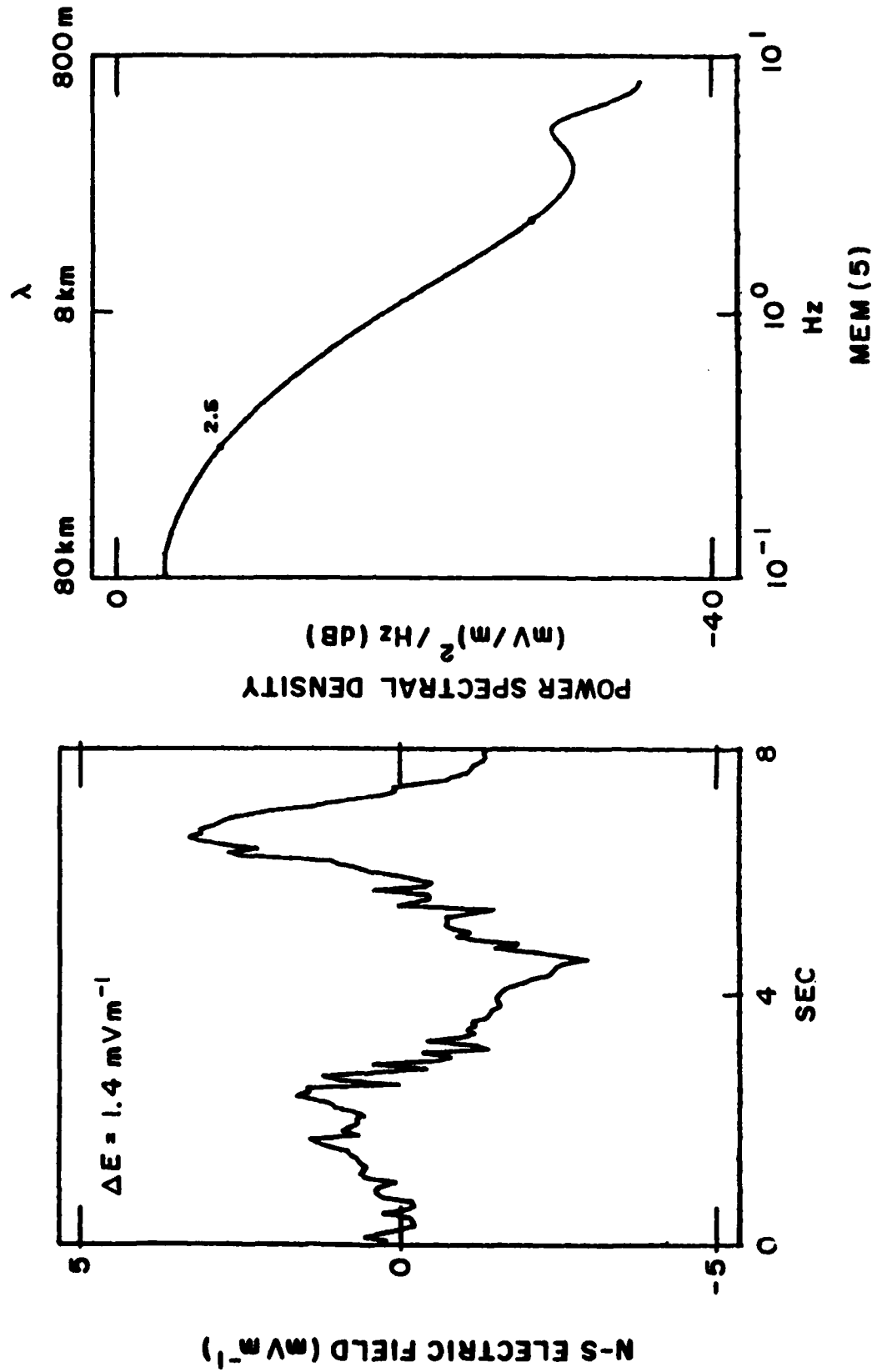


FIGURE 14

ORBIT 4429

N-S ELECTRIC FIELD 2156:00 UT



ION DENSITY 82146 DE-2 ORBIT #4429
2154:00 - 2158:00 UT

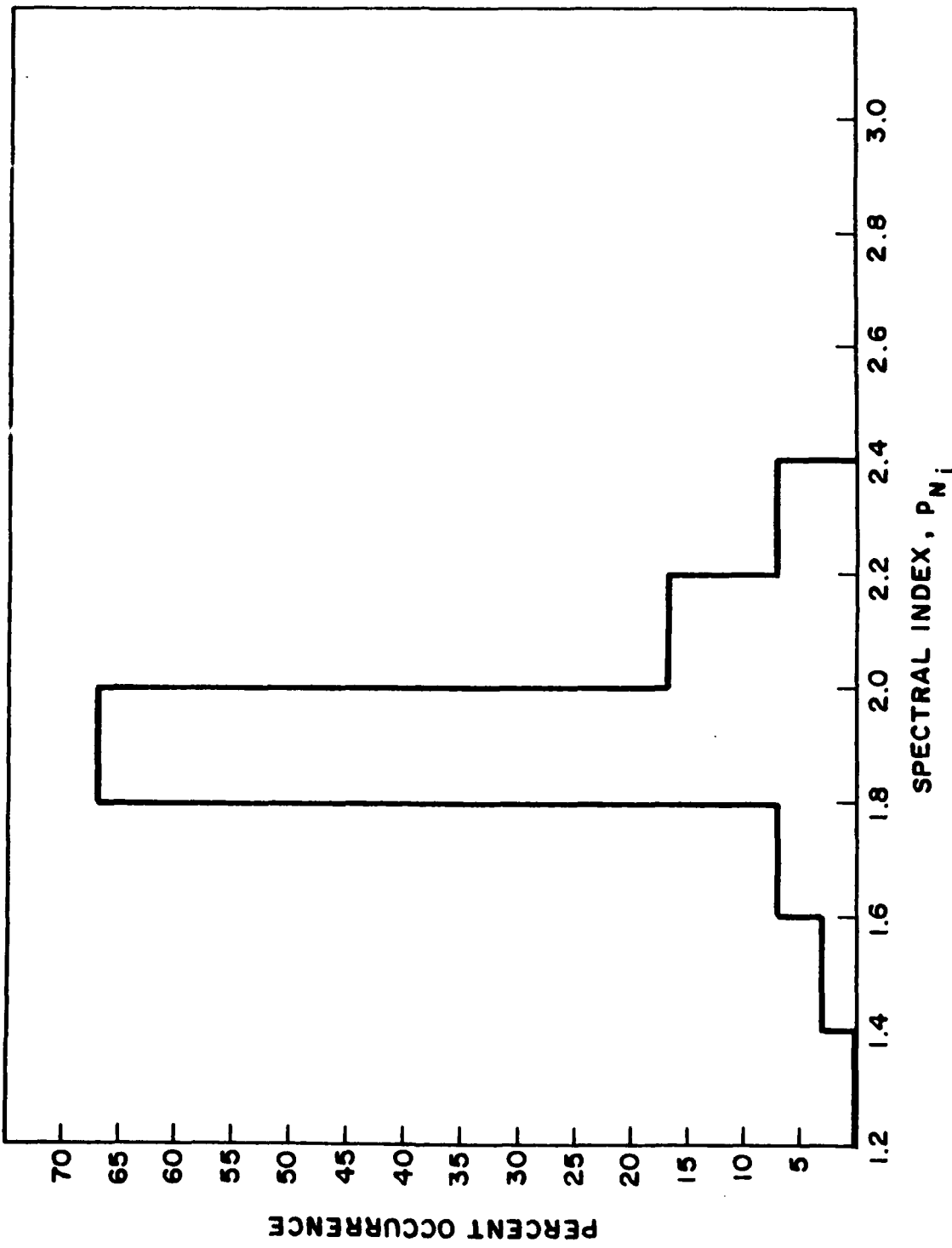


FIGURE 16a

ELECTRIC FIELD 82146 DE-2 ORBIT #4429

2154:00 - 2158:00 UT

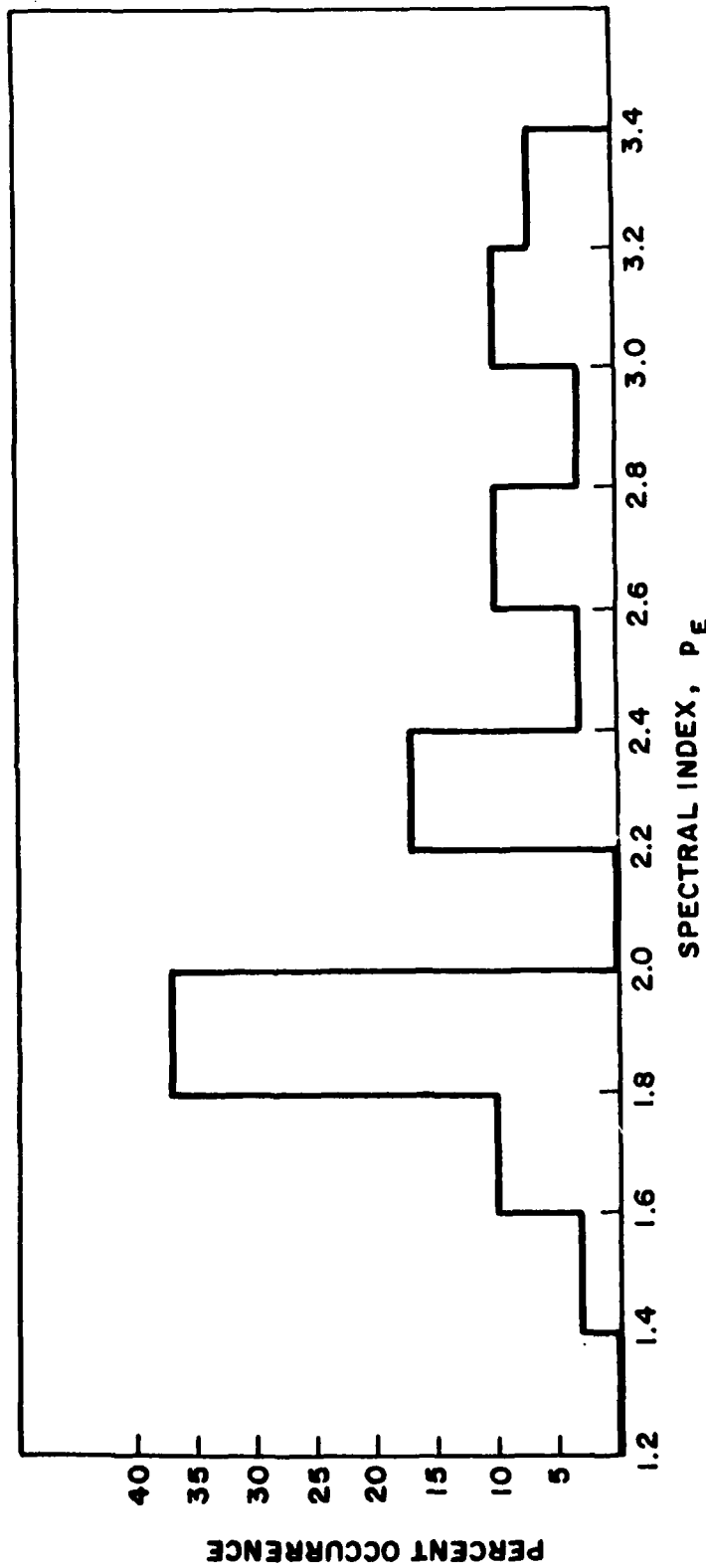


FIGURE 16b

DAY 146, 1982 DE-2 ORBIT 4429

DENSITY SPECTRAL SLOPES ($\lambda < 125\text{m}$)

POLAR CAP PATCHES

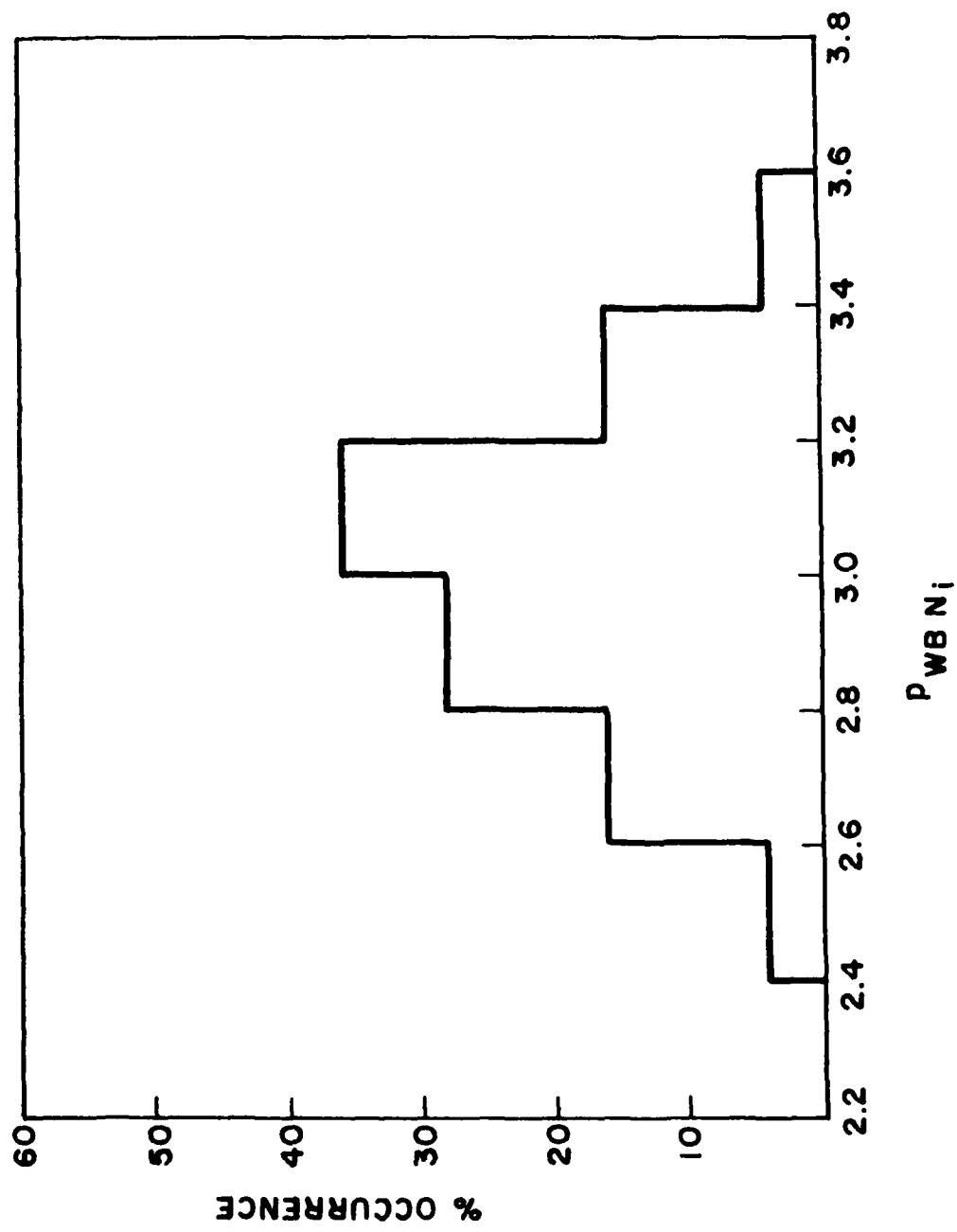


FIGURE 16c

82067 DE-2
LAPI ELECTRONS

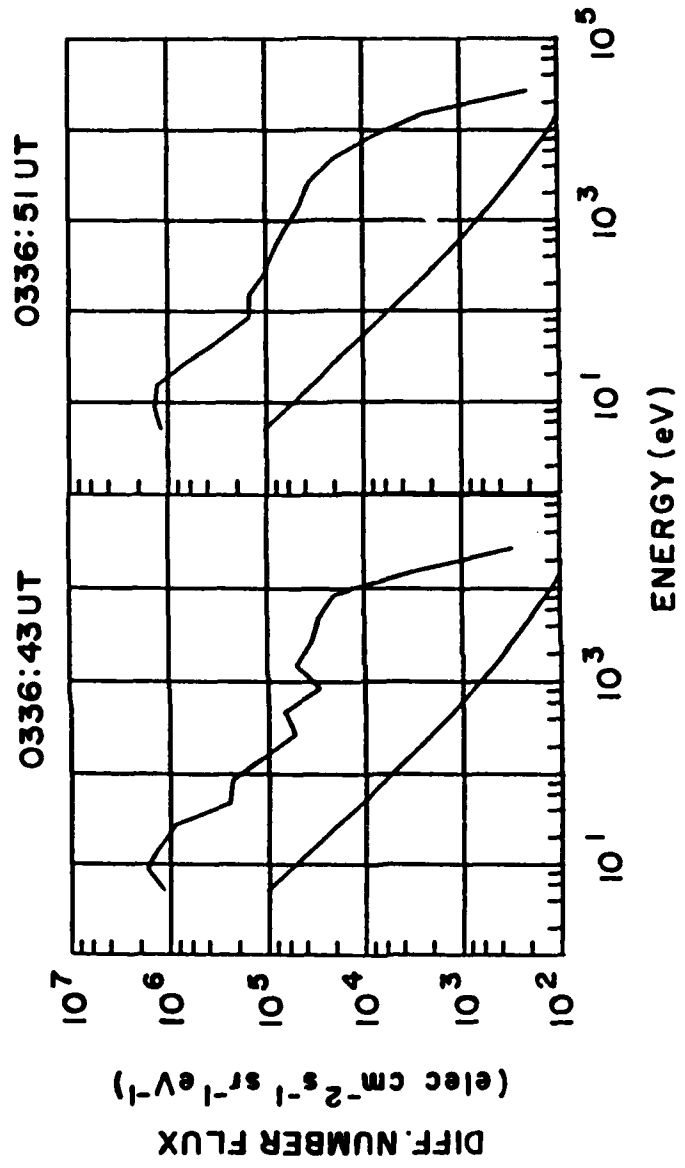


FIGURE 17

82067

ORBIT 3223

AURORAL BLOB

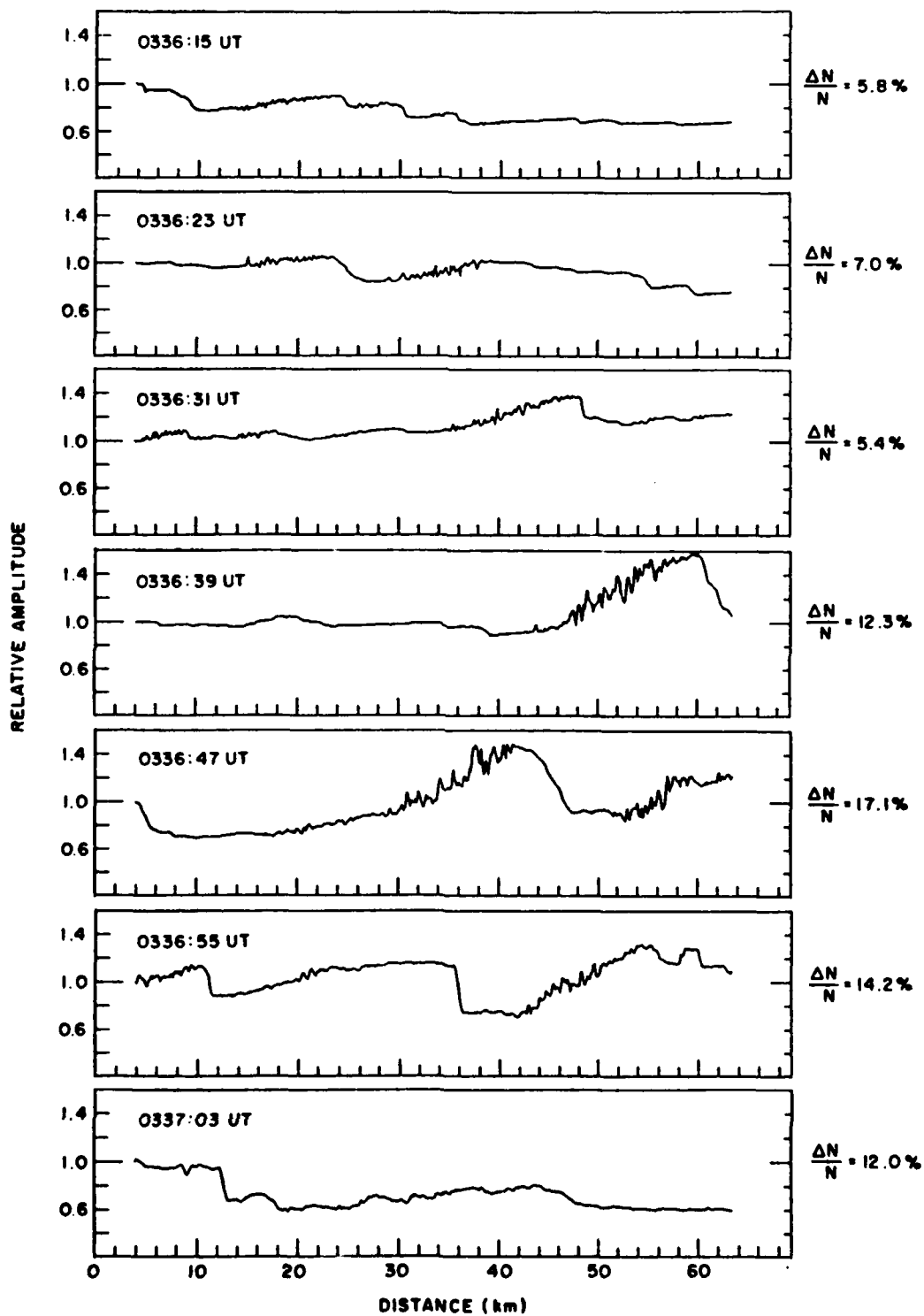


FIGURE 18

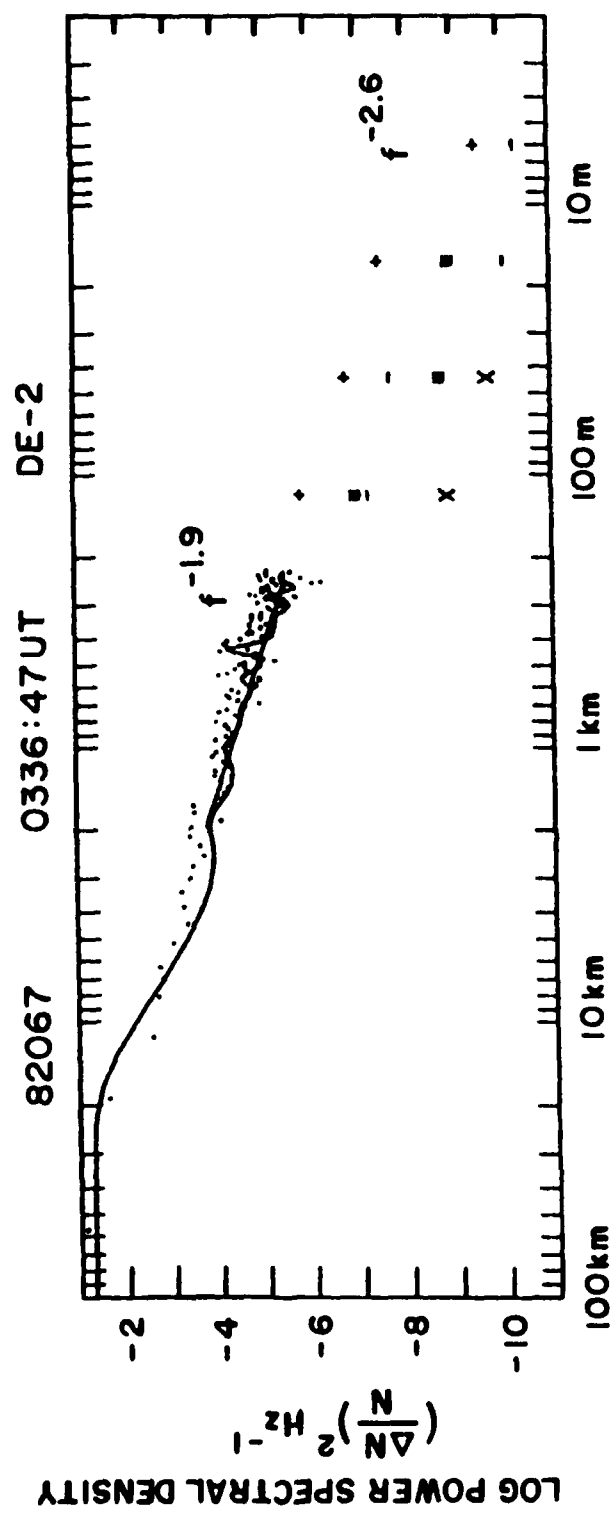


FIGURE 19

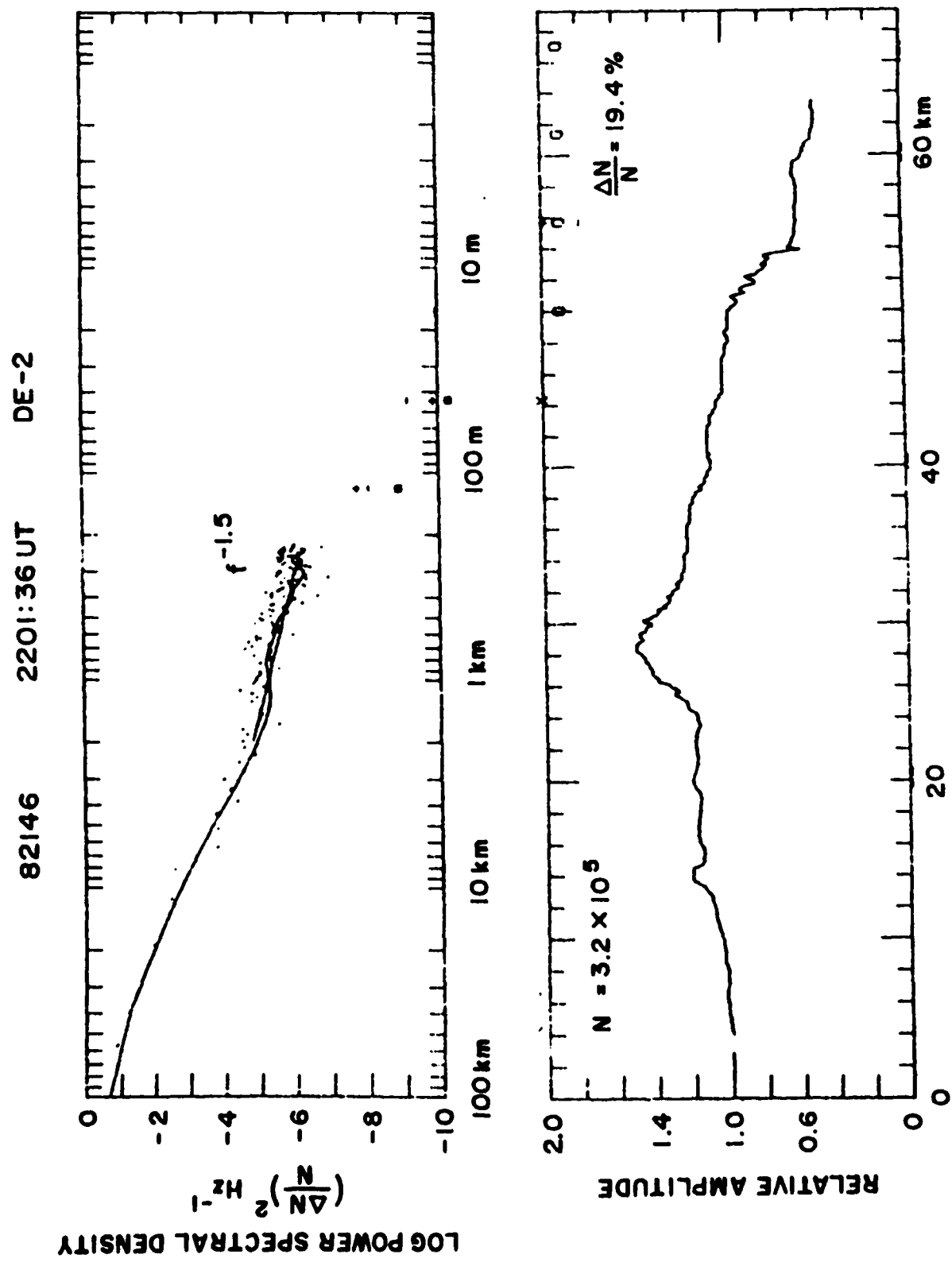


FIGURE 20

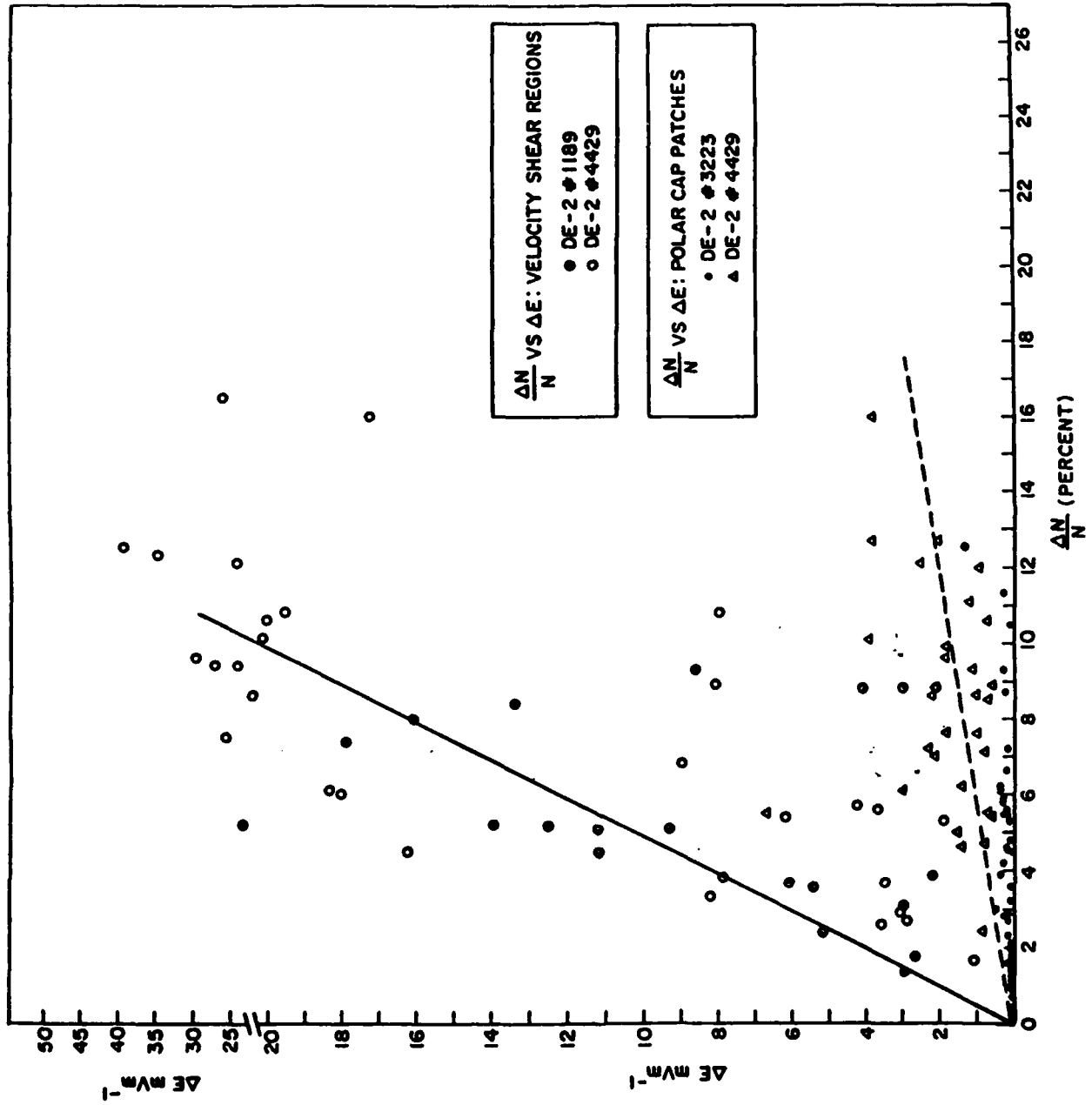


FIGURE 21

DAY 146, 1982 DE-2 ORBIT 4429
DENSITY SPECTRAL SLOPES ($\lambda < 125 \text{ m}$)
VELOCITY SHEAR REGIONS (S_M)

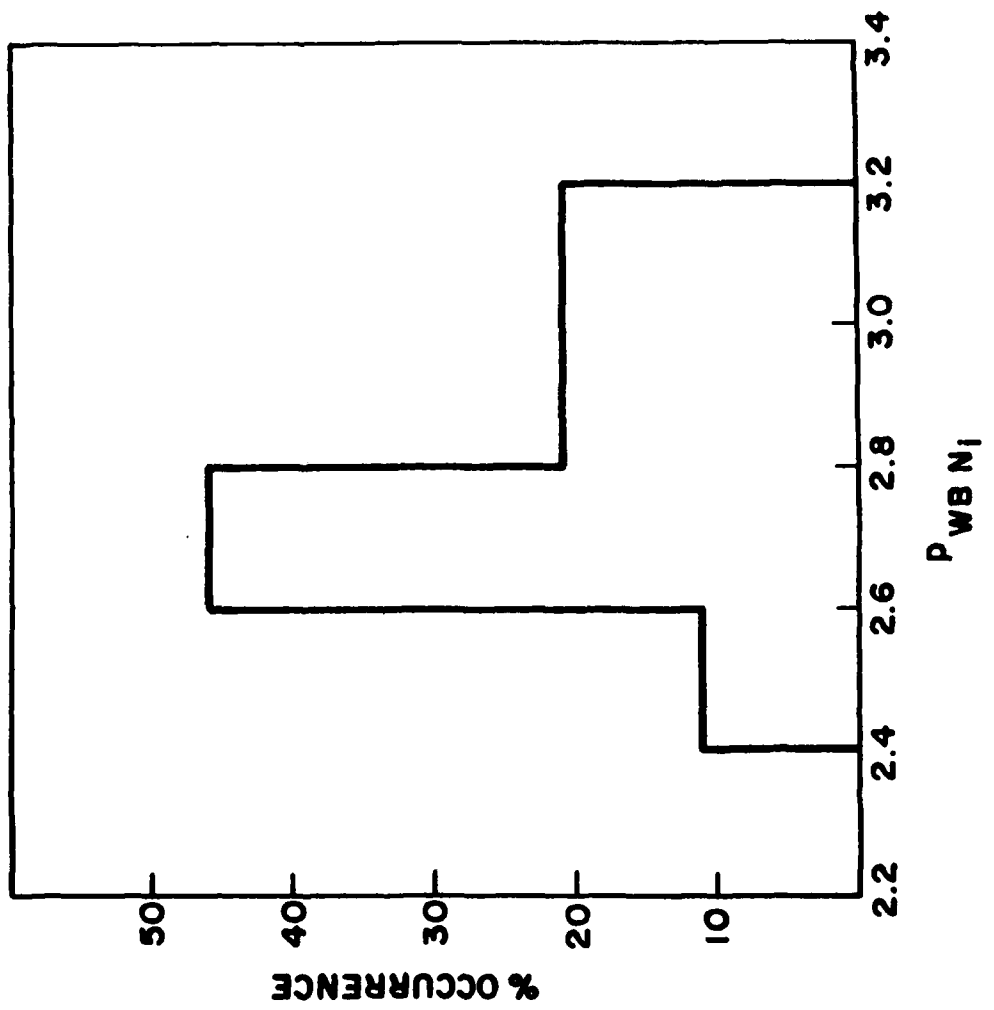


FIGURE 22

ATTACHMENT 11

Daytime Scintillations Induced by High-Power HF Waves at Tromsø, Norway

SANTIMAY BASU,¹ SUNANDA BASU,² P. STUBBE,² H. KOPKA,³ AND J. WAARAMAA¹

During March 1984 the high-power HF heating facility located at Ramfjordmoen (69.6° N, 19.2° E geographic) near Tromsø, Norway, was used to modify the ionospheric F region in the daytime. The intensity and phase scintillations of 250-MHz transmissions from the quasi-stationary polar beacon satellite were measured when the ray path from the observing site to the satellite intercepted the modified ionospheric volume. Narrow band spectral enhancements corresponding to an irregularity scale length of 750 m were detected in the intensity spectra when the radiated HF power developed an estimated power density of about 0.3 mW/m² at the height of reflection. Spectral enhancements at larger scales were not detected in the phase spectra. From the growth and decay of the intensity spectral enhancements during the successive 10-min "on" and 10-min "off" periods of the heater the e -folding growth and decay times of ~ 750 m irregularities were estimated to be on the order of 30 s and 2 min, respectively. The threshold power densities required for the generation of the observed irregularity scale sizes were calculated from the self-focusing instability theory of Cragin et al. (1977) by the use of ionospheric background parameters measured by the EISCAT radar. The theoretical estimates were found to be within a factor of 2 of the HF power densities employed in the experiment. The presence of Fresnel oscillations in the intensity and phase spectra were attributed to a limited irregularity layer thickness less than 50 km. By using the formulations of the thin phase screen theory, it was found that the observed intensity scintillations at 250 MHz correspond to irregularity amplitudes ($\Delta N/N$) of 3% with an outer scale of 1 km.

1. INTRODUCTION

The initial impetus for ionospheric modification by powerful radio waves at HF stems from the work of Ginzburg and Gurevich [1960] and Farley [1963]. Immediately after high-power HF facilities became available at Platteville, Colorado [Ullaut, 1970] and at Arecibo, Puerto Rico [Gordon et al., 1971], not only were the temperature enhancements observed, as predicted by Farley, but a host of unexpected phenomena resulting from the nonlinear interaction of high-power radio waves with the ionospheric plasma were also detected [Carlson and Duncan, 1977; Gurevich, 1978; Fejer, 1979, and references therein]. Among these varied phenomena, electron density variations at ionospheric heights were detected as manifested by artificial spread F on ionograms, radio star and satellite scintillations and enhanced incoherent scatter signals from the perturbed regions [Georges, 1970; Rufenach, 1973; Allen et al., 1974; Thome and Perkins, 1974; Pope and Fritz, 1974; Germansev et al., 1976; Duncan and Behnke, 1978; Erkheimov et al., 1979; Belikovich et al., 1979; Basu et al., 1980, 1983; Frey and Gordon, 1982; Livingston, 1983; Frey et al., 1984]. Later, density variations were measured directly by satellite in situ probes [Farley et al., 1983]. These observations imply that artificial irregularities of electron density covering the scale length range of a few kilometers to tens of meters can be induced in the ionosphere by the action of powerful ground-based HF transmitters. The currently accepted cause of these irregularities is a self-focusing instability in which an initial small plasma density perturbation produces focusing and defocusing of the heating wave in the regions of perturbed density. The focusing in regions of density depletions causes enhanced heating and leads to further depletions. This allows

the perturbations to grow if the effect is large enough to overcome conduction and other dissipation effects. These simple basic ideas form the theme of rather complicated calculations leading to the development of various versions of the theory (Perkins and Valeo [1974], Perkins and Goldman, [1981], Cragin et al. [1977], Gurevich [1978], Kuo and Lee [1983], and Farley et al. [1983] for a critical assessment).

The present paper provides additional observations of the self-focusing effect at the subauroral location of Tromsø, Norway. Results on the magnitudes of intensity scintillations of radio star signals at 933 MHz induced by HF heating at this location have been reported earlier [Frey et al., 1984]. The present results provide information not only on the magnitude of intensity scintillations but phase scintillations as well. Phase scintillation measurements permit a study of irregularity scales at least a decade larger (up to about 10 km) than those causing intensity scintillations. Furthermore, since scintillation magnitudes are larger at the observing frequency of 250 MHz, compared to radio star observations at 933 MHz, power spectral studies of phase and intensity scintillations could be performed. These studies provide information on the detailed structure of electron density fluctuations induced by HF heating. During these measurements, the EISCAT (European incoherent scatter) radar was operated and provided data on the background ionospheric density and temperatures. The EISCAT measurements have been utilized to relate scintillation observations to the existing theories of self-focusing.

In the next section, we describe the observational details related to the geometry of the scintillation measurements, the characteristics of the HF heater at Tromsø and the operation of the receiver used to perform the phase and intensity scintillation measurements. In section 3, we present the characteristics of the irregularity structures induced by HF heating from the magnitude and variation of the phase and intensity scintillation spectra. These results in association with EISCAT radar observations of the background parameters are utilized to obtain numerical estimates of the irregularity amplitude and threshold power density requirements in section 4. A brief summary is provided in section 5.

¹Air Force Geophysics Laboratory, Hanscom Air Force Base, Massachusetts.

²Emmanuel College, Boston, Massachusetts.

³Max Planck Institut für Aeronomie, Katlenburg-Lindau, Federal Republic of Germany.

Copyright 1987 by the American Geophysical Union.

Paper number 7A8936.
0148-0227/87/07A8936\$03.00

The U.S. Government is authorized to reproduce and sell this report. Permission for further reproduction by others must be obtained from the copyright owner.

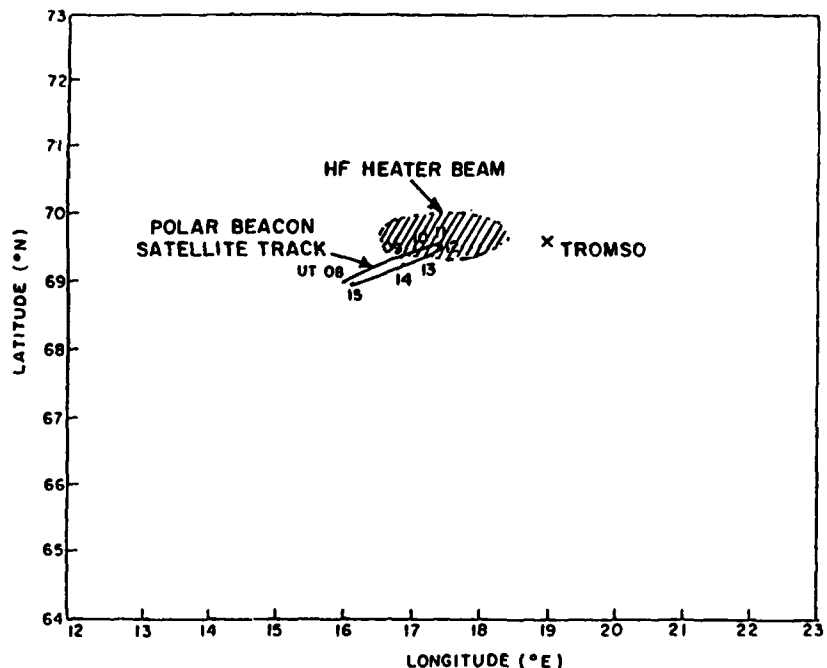


Fig. 1. Geometry of observations indicating the half power beamwidth (shaded region) of the HF heater and the locus of intersection of the ray path from Tromsø to the polar beacon satellite with 250-km ionospheric height. The universal times are marked alongside the subionospheric track.

2. OBSERVATIONS

The heating facility at Rømsjordmoen, near Tromsø, Norway, operated by the Max-Planck Institut für Aeronomie was used to illuminate the ionosphere by high power radio waves [Støkke *et al.*, 1982]. The geographic position of Rømsjordmoen is given by 69.6°N and 19.2°E. The magnetic dip angle of the station is 78° and the *L* value is 6.2. During nighttime, the station coordinates correspond to an auroral location [Su, Basu *et al.*, 1986], but during daytime under magnetically quiet conditions it remains in the subauroral environment. In view of the frequent occurrence of natural irregularities in the nightside auroral oval, the experiments were performed during daytime when controlled perturbations (uncontaminated by natural variations) of the ionosphere could be performed.

The high power HF facility at Ramfjordmoen consists of 12 transmitters each generating a maximum CW power of 125 kW in the frequency range of 2.5–8 MHz. The power is radiated by one of three antenna arrays designed for the frequency intervals of 2.5–4 MHz, 3.85–5.65 MHz and 5.5–8 MHz. In the present experiment, 11 transmitters operating at a frequency of 5.423 MHz and each radiating a power of 90 kW could be employed. The nominal beamwidth of the antenna at the operating frequency was 14.5° so that an effective radiated power level of 218 MW was achieved. This corresponds to an incident power density of 0.34 mW/m² at 225 km altitude. The heater signal of 5.423 MHz was reflected from this altitude during the experiment as indicated by the electron density profile obtained by the EISCAT radar.

The phase coherent signals from the quasi-stationary polar beacon satellite at 250 MHz were received in Tromsø at an elevation angle of 75°. By using phase shifting networks in the heater antenna array system, the heater beam was tilted to the

west to intercept the communication link between the satellite and the ground station in Tromsø.

Figure 1 shows the geometry of the observations indicating the half-power beam area of the heater and the locus of the intersection point of the ray path to the satellite with an ionospheric altitude of 250 km during March 1984. The universal times (UT) marked alongside the subionospheric locus indicate that the satellite signal passed through the heated volume for about 3 hours between 1000 and 1300 UT. The signals from the polar beacon satellite were recorded by a narrow band phase-locked computer controlled receiver. The received signals suffer large free space and ionospheric Doppler and, as such, the satellite updates its frequency at fixed intervals of time (168 s) to assist the ground receivers to acquire the signal. After each satellite frequency update, the receiver acquires phase lock in a finite time and then tracks the signal across the receiver band. Near the band edges, the receiver retunes and repeats tracking. The in-phase and quadrature components of the detected signal, as well as the frequency update information at each retune, are written on a digital tape recorder. From the quadrature components of the signal continuous intensity and phase records between each satellite frequency update are generated later in off-line processing. In general, 82-s blocks of continuous phase and intensity records at intervals of 168 s corresponding to the satellite frequency update intervals are obtained. The 82-s blocks of intensity and the detrended phase records form the basis of signal analysis. Further information on the signal recording and analysis are given by Su, Basu *et al.* (1985).

3. RESULTS

During the experiment on March 1, 1984, the HF heater radiated 5.423 MHz signal with Q mode polarization. The

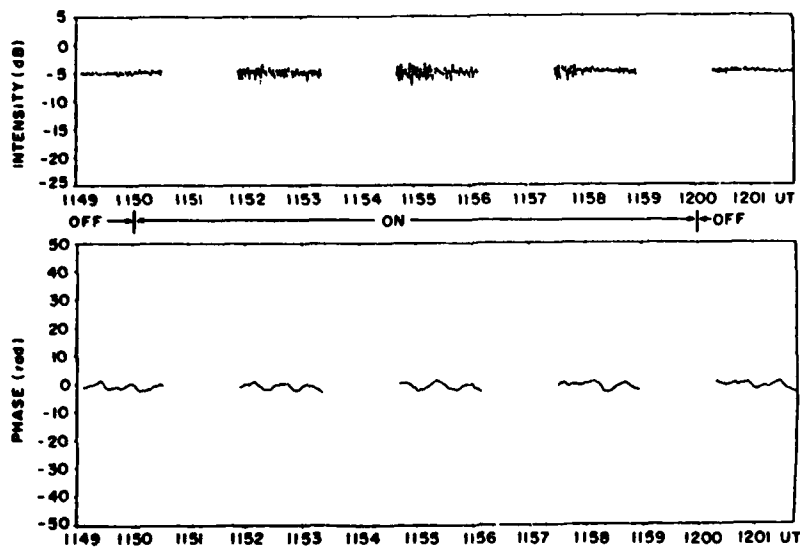
TROMSO MARCH 1, 1984
POLAR BEACON SATELLITE 250 MHz

Fig. 2. The development of (top) intensity and (bottom) phase scintillations of 250-MHz transmissions when the HF heater was turned on. The data segments were acquired over 82 s at intervals of 168 s.

heater frequency (f_h) was less than the critical frequency (f_0) of the ionosphere which was 9 MHz at the time so that over-dense heating ($f_h < f_0$) conditions prevailed. The heater was cycled on for a 10-min period and was followed by a 10-min off period. Approximately three blocks of signals, each of 82-s duration and spaced at intervals of 168 s, were obtained during either the heater on or off periods.

The top and bottom panels of Figure 2 show blocks of intensity and phase records during one heating cycle. The heater was turned on during 1150–1200 UT and remained off for 10 min prior to and after this time interval. From the successive data blocks in the top panel, the development of intensity scintillations may be observed. The growth of small scale phase fluctuations cannot be observed readily from the bottom panel as it is masked by large-scale background phase variations. The growth of phase fluctuations can, however, be noted from the phase spectra to be discussed in the next paragraph.

Figures 3a, 3b, 3c, and 3d illustrate the intensity spectra in the top panel and phase spectra in the bottom panel for 12 successive 82-s segments of signal intensity and phase. The data segments are acquired at intervals of 168 s, and therefore the 12 data segments cover the time period 1149:05 UT to 1221:23 UT. During the above time interval, the HF heater was turned on between 1150 and 1200 UT, turned off during the next 10 min and switched on again between 1210 and 1220 UT. The spectra of each 82-s segment of intensity and phase fluctuations were obtained by using the FFT algorithm incorporating a Blackman-Harris window having a sidelobe level of 78 dB. Each spectrum displays the power spectral density (PSD) in decibels versus the logarithm of frequency (f). Therefore a linear trend of the spectrum signifies a power law dependence of PSD on frequency. Each spectrum displays the day number (day 61, or March 1 in the present case), the central time of the data segment, and some statistical param-

eters. The intensity spectra display the S_4 index signifying the normalized second central moment of intensity [Briggs and Parkin, 1963]. The phase spectra display the root mean square phase deviation in radians (σ_ϕ), the phase spectra strength T in decibels at 1 Hz and the power law spectral indices p_1 and p_2 provided, respectively, by the best fit straight lines to the low-frequency (<0.2 Hz) and the high-frequency (>0.2 Hz) ends of the phase spectrum. By the use of a suitable algorithm, the best fit straight line providing p_2 is constrained to cover the frequency limits of 0.2 Hz and a frequency lower than the noise floor where the spectrum commences to become flat. At the low-frequency end, the best fit straight line covers the frequency range of 0.2 Hz and a frequency that avoids the region of spectral flattening introduced by the detrend filter.

Three frames in Figure 3a and the left-hand frame in Figure 3b constitute a sequence of intensity and phase spectra that cover the period 1150–1200 UT when the HF heater remained on. The left-hand frame in Figure 3a corresponds to a data segment between 1149:05–1150:27 UT, representing one 82-s interval around the central time of 1149:46 UT. Since the heater was turned on at 1150 UT, its effect on the spectrum was caused during the last 27 s of this data interval. A small increase in PSD around 0.2 Hz is discernible in the intensity spectrum shown at the top. The bottom panel of the left-hand frame shows that the phase spectrum registers a plateau at about 0.2 Hz due to an enhancement of PSD at the first Fresnel maximum. Due to the dominance of the low-frequency phase variations, the phase spectra do not always indicate a pronounced structure. However, in some phase spectra, the Fresnel maxima and minima are found to be in antiphase with the oscillations in the intensity spectra as is required by the weak scatter theories of scintillations [Bowhill, 1961]. Such an example will be shown in Figure 4. The next frame of intensity scintillations indicates the developed structure in the intensity spectrum centered at 1152:34 UT. The first two Fresnel

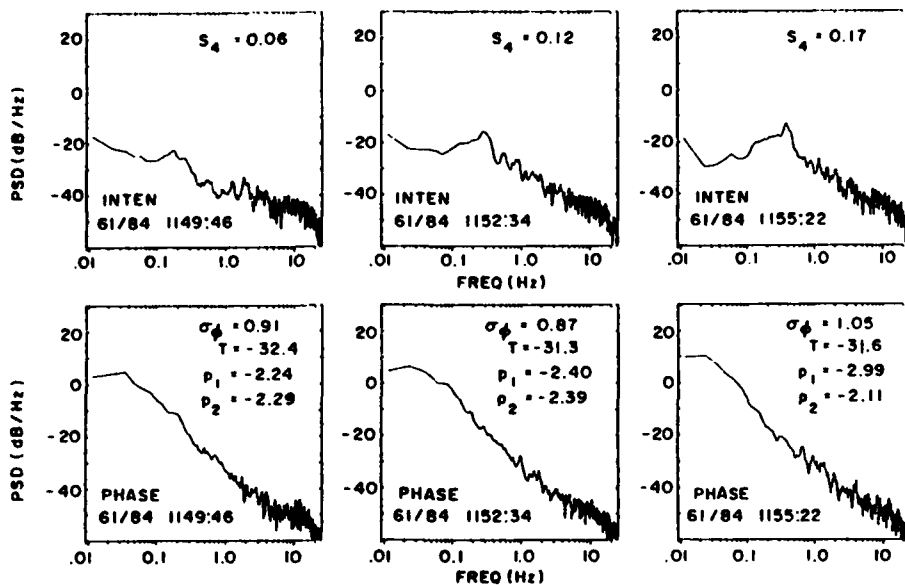


Fig. 3a. The power spectra of (top) intensity and (bottom) phase scintillations of 250-MHz signals from the polar beacon satellite acquired over 82-s data intervals. Each intensity spectra also indicates the S_4 index of scintillation, day number, year and the central time of the data interval. The phase spectra indicate the rms phase deviation, σ_ϕ , spectral strength T at 1 Hz and the spectral indices, p_1 and p_2 at frequencies less than and greater than 0.2 Hz, respectively.

minima at 0.45 and 0.64 Hz are present in the intensity spectrum. The last frame in Figure 3a and the first frame in Figure 3b indicate the developed state of spectral structure further into the on state of the heater with the scintillation index S_4 achieving a maximum value of $S_4 = 0.17$ at 1155:22 UT from a background level so $S_4 \leq 0.05$.

The scale sizes of the irregularities that correspond to the peaks in the intensity scintillation spectra may be estimated if we identify the spectral maximum with the Fresnel dimension. The Fresnel dimension is given by $(2\lambda z)^{1/2}$, where λ (= 1.2 m) is the radio wavelength and z is the distance of the irregu-

larities from the observer. The electron density profile obtained by the EISCAT radar indicated that the HF signal at 5.423 MHz was reflected from a height of 225 km. Assuming that the height of the irregularity layer corresponds to the HF reflection height, the Fresnel dimension is obtained as 735 m. In the spectra discussed above, the growth of PSD could be observed up to frequencies at least a decade higher than the Fresnel maximum. Thus the set of spectra displayed above indicated the growth of irregularity scales in the range of about 750 m to 75 m due to the action of the heater.

The heater was next turned off between 1200 and 1210 UT.

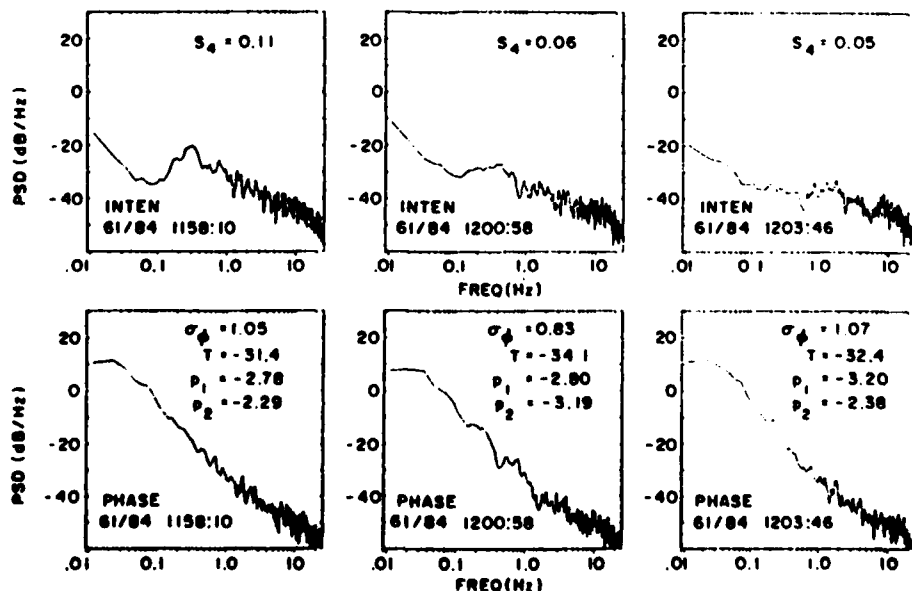


Fig. 3b. Same as Figure 3a between 1158:10 and 1203:46 UT.

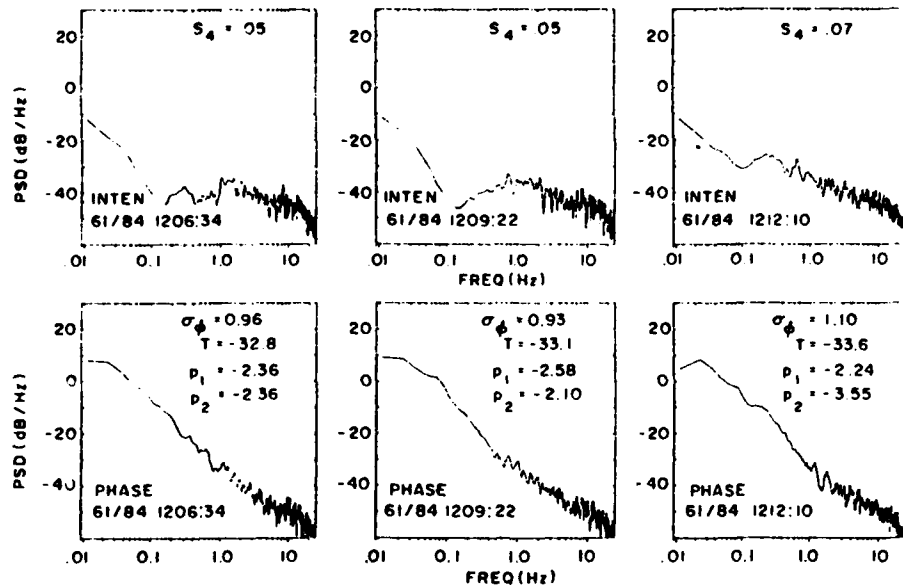


Fig. 3c. Same as Figure 3a between 1206:34 and 1212:10 UT.

The second and third frames in Figure 3b and the first and the second frames in Figure 3c correspond to this off period of the heater. It may be noted that the decay of the spectral structure was not complete in the second frame of Figure 3b which extended to 1.5 min after the heater was switched off. Total decay occurred in the last frame of Figure 3b which covered the period 3–4.5 min after the heater was turned off. The sequence of development and decay of the spectral structures indicate that the growth time of the irregularities with scale sizes ~ 750 m to 75 m is of the order of 30 s, but the decay time is on the order of 2 min.

The heater was next cycled on during the period 1210–1220 UT. The growth of the irregularities in response to the heater may again be observed from the sequence of the intensity and phase spectra displayed in the last frame of Figure 3c and the first two frames in Figure 3d. The spectral structures observed during the first (1150–1200 UT) and the second (1210–1220 UT) on periods of the heater, are found to be remarkably similar even though the magnitude of the S_4 index is smaller. The variability of the heating effect may be related to the off-vertical tilt of the heater beam with the consequent reduction in the interaction between the incident and reflected

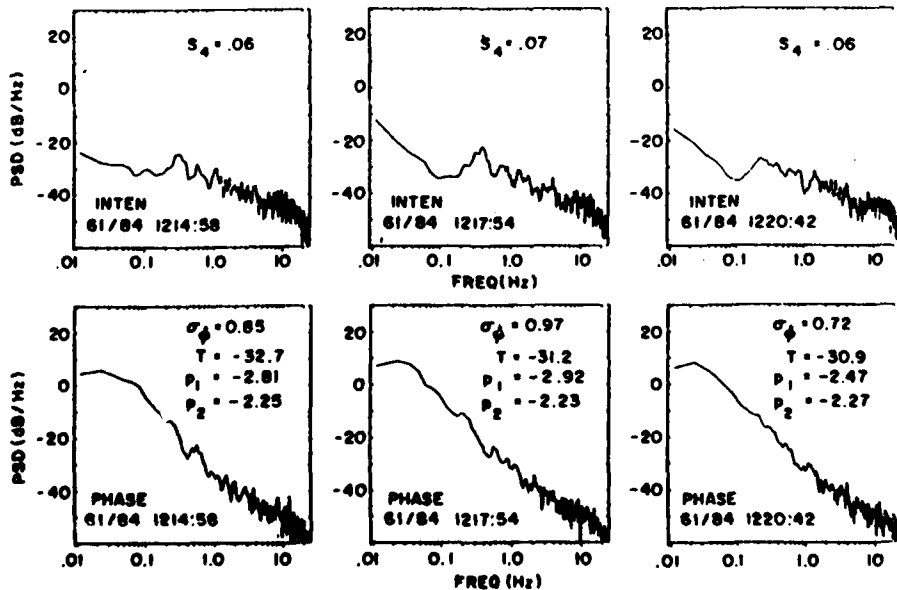


Fig. 3d. Same as Figure 3a between 1214:58 and 1220:42 UT.

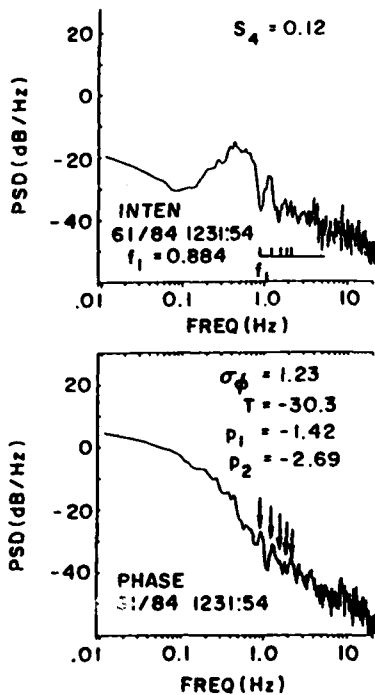


Fig. 4. Illustrates Fresnel oscillations in the (top) intensity and (bottom) phase spectra. Note that the frequencies of the Fresnel minima in the intensity spectrum identified by the scale above the frequency axis in the top panel correspond to the Fresnel maxima in the phase spectrum identified by arrows in the bottom panel.

waves. We also draw attention to the reduction of PSD of the spectral peak by about 5 dB at the end of the first heating cycle at 1158:10 UT (first frame in Figure 3b). This is also evident in Figure 2 where a decrease in the depth of fluctuations is noted near the end of the heating cycle. On many occasions, such a reduction of scintillation magnitude has been observed after a few minutes of continuous heating.

In Figure 4, we focus our attention on Fresnel oscillations observed on the intensity and phase scintillation spectra during the next heating cycle between 1230 and 1240 UT. The first five Fresnel minima in the intensity scintillation spectra have been identified on a scale above the frequency axis and are shown to have frequencies $f_1, 2^{1/2}f_1, 3^{1/2}f_1, 4^{1/2}f_1, 5^{1/2}f_1$, where $f_1 = 0.88$ Hz. The Fresnel oscillations in the phase spectra are shown to be in phase quadrature and maximize at the positions of Fresnel nulls in the intensity spectra. Identifying the first Fresnel minimum ($f_1 = 0.88$ Hz) with the irregularity scale size of $(2z)^{1/2} = 520$ m, the irregularity drift orthogonal to the ray path may be obtained as $V = 0.88 \times 520 = 458$ m/s. At the beginning of the heating cycle, e.g., at 1152:34 UT, the Fresnel minimum was obtained at 0.45 Hz providing an irregularity drift of 234 m/s. Thus the irregularity drift increased considerably during the period of these observations. The presence of Fresnel oscillations in the spectra indicates that the irregularity layer thickness is not large [Basu et al., 1986]. In fact, if the irregularity layer thickness exceeds 50 km, it is found that the Fresnel minima due to the lowermost part of the layer will coincide with the Fresnel maxima due to the topmost part of the layer so that the Fresnel modulations will disappear.

In stating that the irregularity layer thickness is limited, we have implied that the electron density deviation (ΔN) of the irregularities in the scale size range of ~ 750 m to 75 m causing 250-MHz scintillations arises over a narrow range of altitudes, even though it is known that the effects of temperature enhancement and density depletion propagate outwards from the HF reflection height to considerable distances along the magnetic field [Meltz et al., 1974; Mantas et al., 1981]. As such, one expects that the relative irregularity amplitude ($\Delta N/N$) of small scale irregularities causing scintillations would also map out along the magnetic field lines. In this case, however, the electron density deviation, ΔN , obtained as the product of $\Delta N/N$ and electron density N will be controlled by a small altitude interval around the level of maximum ionization density if the distribution is sufficiently skewed with height. In such a configuration, the magnitude of scintillations will be controlled by the maximum ionization density rather than the density at the HF reflection height. Our prior heating experiments at Platteville and Arecibo [Basu et al., 1980, 1983] indicated results to the contrary. We found that when HF heating was performed at an altitude lower than the maximum height of the F layer, the magnitude of scintillations did not change even in the presence of drastic variations of maximum ionization density. This leads us to conclude that even though large-scale density depletions map out along the magnetic field, the short scale irregularities (750 m to 75 m, in the present case) are rather confined in altitude near the HF reflection height [Farley, 1959].

4. NUMERICAL ESTIMATES OF IRREGULARITY PARAMETERS AND COMPARISON WITH THEORY

In the following paragraphs, we shall attempt to obtain estimates of the irregularity amplitudes generated by HF heating from the observed magnitudes of scintillations and also make an order of magnitude comparison of the threshold power densities of HF required to excite the observed scale sizes of the irregularities with that predicted by the existing theories of self-focusing instability. In order to determine the irregularity amplitude, defined as the ratio of the electron density deviation (ΔN) to the background ionization density (N), we utilize the weak scatter theory and make some realistic assumptions. Following Rino [1979], we derive the three-dimensional strength of turbulence (C_s) as

$$C_s = 8\pi^{3/2} q_0^{2r+1} \frac{\Gamma(r+1/2)}{\Gamma(r-1)} (\Delta N)^2 \quad (1)$$

where q_0 is the outer scale wave number, $2r+1$ is the three-dimensional spectral index of the irregularities. We assume that under the action of the heater, striations of kilometer scale sizes are formed [Duncan and Behnke, 1978] and consider that the outer scale wave number is $2\pi \times 10^{-3} \text{ m}^{-1}$. From the observed average slope (p_3) of the phase spectra we obtain $2r = 2.5$. Even though our computations will be based on intensity scintillation magnitudes, the spectral index is derived from the phase spectra as deep Fresnel oscillations in the intensity spectra make it difficult to obtain the intensity spectral index accurately. Substituting the above value of r in (1), we get

$$C_s = 0.89 (\Delta N)^2 \quad (2)$$

Since our observations indicate that the largest S_4 index of intensity scintillation is about 0.2, we use the weak scatter approximation [Rino, 1979] and express the S_4 index as

$$S_4^2 = (r_e \lambda)^2 L \sec \theta C_1 \left(\frac{z \sec \theta}{4\pi} \right)^{v-0.5} \frac{\Gamma[(2.5-v)/2]}{2\sqrt{\pi} \Gamma[(v+0.5)/2] (v-0.5)} \quad (3)$$

where

- r_e the classical electron radius ($= 2.8 \times 10^{-15}$ m);
- λ the radio wavelength of satellite transmissions ($= 1.23$ m);
- L thickness of the irregularity layer;
- θ ionospheric zenith angle;
- z the distance of the irregularity layer from the receiver on the ground;
- \mathcal{J} the geometric factor appropriate for the irregularity anisotropy.

As discussed above, the presence of Fresnel oscillations in the scintillation spectra indicates that the irregularity layer thickness (L) cannot exceed 50 km. We therefore consider $L = 50$ km. The electron density profile obtained by the EISCAT radar and shown in Figure 5 indicates that the scale height of the ionosphere around the reflection height of the heater frequency (f_h) is also about 50 km. For the observing geometry, the ionospheric zenith angle $\theta = 15^\circ$. Substituting these values in (3) we obtain

$$S_4^2 = 2.95 \times 10^{-22} (\Delta N)^2 \mathcal{J} \quad (4)$$

In order to evaluate the geometric factor, we consider that the irregularities are in the form of sheets and aligned with the magnetic meridian [Farley et al., 1983]. The elongation parameters of the sheet along the magnetic field, namely a , are assumed to be equal to 5, and those in a direction transverse to the magnetic field over the magnetic meridian plane are assumed to be $b = 5$. The limiting form of the geometric factor can be expressed as

$$\mathcal{J} = \frac{ab}{\sqrt{A'' C''}} \frac{\Gamma(v)}{\sqrt{\pi} \Gamma(v+0.5)}$$

where the parameters $A'' = 25$ and $C'' = 2.57$ for 5:5:1 sheets [Rino and Fremouw, 1977]. Substituting the appropriate values, the geometric factor for 5:5:1 sheets aligned with the magnetic meridian is obtained as $\mathcal{J} = 0.8571$. Substituting this value in (4), we obtain

$$S_4 = 1.59 \times 10^{-11} (\Delta N)$$

The observations indicate that during the period of heating the S_4 index of intensity scintillations attained a maximum value of 0.17. Thus the electron density deviation $\Delta N = 1.07 \times 10^{10} \text{ m}^{-3}$. Since maximum interaction occurs near the reflection height of the HF signal of frequency $f_{sh} = 5.423 \text{ MHz}$, the background ionization density $N = 6.7 \times 10^4$, $f_{sh} = 3.63 \times 10^{11} \text{ m}^{-3}$. Thus the irregularity amplitude $\Delta N/N = 3.4\%$. It should be mentioned that in view of the observing geometry with respect to the irregularity sheets in the magnetic meridian, scintillations do not get the advantage of irregularity anisotropy. In fact, if the irregularities are considered to be

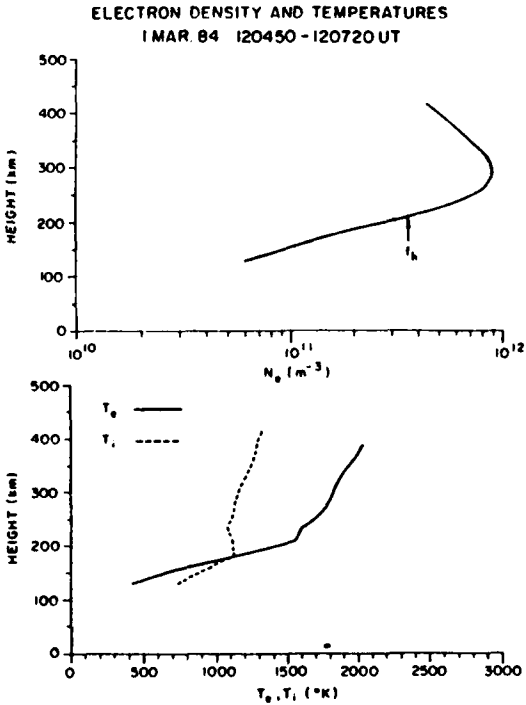


Fig. 5. Illustrates the altitude profiles of (top) electron density, (bottom) electron and ion temperatures obtained by the EISCAT radar. The reflection height of the heater frequency f_h is also indicated in the top panel.

isotropic, the irregularity amplitude is obtained as $\Delta N/N = 2.7\%$, which is slightly smaller than that obtained for the case of sheetlike irregularities in the magnetic meridian.

Next, we attempt to compare the theoretical predictions of threshold power density with the present observations. The intensity scintillation spectra discussed earlier showed that the heater wave excited a dominant spectral structure corresponding to an irregularity wavelength of about 750 m. Since this wavelength coincides with the first Fresnel maximum, the intensity scintillations will not respond to irregularities with scale sizes larger than the above. However, if such large-scale irregularities were indeed excited, their signature would have been obtained in the associated phase spectra. Since the phase spectra do not indicate such a feature, we assume that the dominant irregularity scale size equals 750 m. During the experiment, 11 transmitters could be operated each providing 90 kW of power. Considering the antenna gain, the above configuration yields an effective radiated power of 218 MW which develops a power density of 0.34 mW/m² at the HF reflection level of 225 km. Thus the observations indicated that a dominant irregularity wavelength of 750 m could be generated with HF power density of 0.34 mW/m². We next investigate how well this power level compares with the theoretical predictions of threshold power density for the generation of 750-m irregularities. Farley et al. [1983] carried out such a comparison of their measurements at Arecibo with the self-focusing theories of Cragin et al. [1977] and Perkins and Valeo [1974]. They observed very good agreement between the theory of Cragin et al. and their measurements, but found that the Perkins and Valeo theory predicted much higher levels of threshold power

flux. We have followed Farley et al.'s procedure and calculated the threshold power flux predicted by Cragin et al.'s theory for a dominant scale size of 750 m (wave number $k_1 = 0.0084 \text{ m}^{-1}$) for the conditions of our experiment in Tromsø on March 1, 1984. We had employed an O mode heater wave at a frequency of 5.423 MHz corresponding to a wave number of $k_0 = 0.1136 \text{ m}^{-1}$, which was reflected from 225 km with electron density $N_e = 3.65 \times 10^{11} \text{ m}^{-3}$. At 1203 UT the EISCAT radar provided the electron and ion temperatures as $T_e = 1400^\circ\text{K}$ and $T_i = 1100^\circ\text{K}$, respectively, and the scale height at the reflection point as $H = 50 \times 10^3$. With the above values of ionospheric background parameters we find that the theory of Cragin et al. [1977] predicts a threshold power flux of 0.74 mW/m² for the generation of a dominant scale size of 750 m. Thus the threshold power level predicted by the theory is a factor of 2 higher than the power density of 0.34 mW/m² actually employed in the experiment. In view of the various absorption effects which are difficult to estimate accurately, this factor would be somewhat larger than 2. While this discrepancy may appear to be large, it should be recalled that the threshold power varies as k_1^4 and therefore is very sensitive to the dominant scale length of the irregularities. Owing to this sensitive dependence on the wavenumber, the discrepancy in k_1 for a given threshold power level of 0.34 mW/m² corresponding to our measurements, the dominant scale length of the irregularities to our measurements, the dominant scale length of the irregularities is obtained as 910 m. This value is only 20% larger than the observed scale length of 750 m. Owing to the broad nature of the spectral peak the 20% discrepancy in scale length is within the limits of uncertainty.

In this connection, we should mention that Kuo and Lee [1983] have proposed that an electromagnetic pump wave that has electromagnetic sidebands can give rise to a modulational instability capable of generating both electron density and magnetic field fluctuations. This theory predicts that the threshold power flux for 750 m irregularities is exceedingly low being on the order of 1 $\mu\text{W}/\text{m}^2$. This is 2-3 orders of magnitude lower than the power density employed in most heater experiments. Frey et al. [1984] varied the power density of the heater at Tromsø and observed irregularities in the scale length range of 450 m to 150 m by recording very low levels ($S_4 \sim 0.02$) of radio star scintillations, with heater power densities of 22 $\mu\text{W}/\text{m}^2$. Although they did not have any measurements of background parameters, their contention of disagreement with Cragin et al.'s theory is probably valid. They pointed out that Kuo and Lee's [1983] theory requiring threshold power flux of less than 1 $\mu\text{W}/\text{m}^2$ provide support to their measurements. The estimation of threshold power flux for different scale length of irregularities is important not only from the point of view of instability theories but for possible future active experiments in space as well. In view of the short term dynamic variations often encountered in the high latitude ionosphere, careful measurements of dominant scale lengths as a function of HF power density are necessary. This will certainly be attempted in future experiments of this nature.

5. SUMMARY

We showed that it is possible to excite irregularities in the daytime ionosphere at Tromsø ($L = 6.2$) by the action of high-power HF waves. The dominant scalelength of the artificial

irregularities at 225 km was found to be about 750 m when the heater radiated waves with O mode polarization at 5.4 MHz and developed an estimated power density of 0.3 mW/m² at the reflection height. The magnitude of the intensity scintillation, S_4 , at 250 MHz was about 0.15 and the rms phase deviation computed over 82 s increased by 0.5 radian. This corresponds to an irregularity amplitude of about 3% for an assumed outer scalelength of 1 km. The theoretical [Cragin et al., 1977] predictions of threshold power density was found to be within a factor of 2 of the estimated power density of the heater. Since the estimated power densities are expected to be enhanced by the interaction between the incident and the reflected waves, the theoretical and experimental values are considered to be in fair agreement.

Acknowledgments. We wish to thank H. C. Carlson of the Air Force Geophysics Laboratory for his interest and help in the work. We are indebted to K. Schlegel of the Max-Planck-Institut für Aeronomie for providing the EISCAT radar measurements of the background ionospheric parameters during our experiment. EISCAT is supported by the British SERC, French CNRS, West German MPG, Norwegian NAVF, Swedish NFR, and Finnish SA. The work at Emmanuel College was supported by NSF grant ATM-8413407 and AFGL contract F19628-86-K-0038.

The Editor thanks R. C. Livingston and M. P. Sulzer for their assistance in evaluating this paper.

REFERENCES

- Allen, E. M., G. D. Thome, and P. B. Rao, HF phase array observations of heater-induced spread F, *Radio Sci.*, 9, 905, 1974.
- Basu, S., Su. Basu, A. L. Johnson, J. A. Klobuchar, and C. M. Rush, Preliminary results of scintillation measurements associated with ionospheric heating and possible implications for the solar power satellite, *Geophys. Res. Lett.*, 7, 609, 1980.
- Basu, S., Su. Basu, S. Ganguly, and W. E. Gordon, Coordinated study of subkilometer and 3-m irregularities in the F region generated by high-power HF heating at Arecibo, *J. Geophys. Res.*, 88, 9217, 1983.
- Basu, S., Su. Basu, C. E. Valladares, A. DasGupta, and H. E. Whitney, Scintillations associated with bottomside sinusoidal irregularities in the equatorial F region, *J. Geophys. Res.*, 91, 270, 1986.
- Basu, Su., S. Basu, E. MacKenzie and H. E. Whitney, Morphology of phase and intensity scintillations in the auroral oval and polar cap, *Radio Sci.*, 20, 347, 1985.
- Basu, Su., S. Basu, C. Senior, D. Weimer, E. Nielsen, and P. F. Fougerre, Velocity shears and subkilometer-scale irregularities in the nighttime auroral F region, *Geophys. Res. Lett.*, 13, 101, 1986.
- Belikovich, V. V., E. A. Benedictov, I. W. Berezin, I. A. Dobrushskii, R. A. Razin, A. I. Teplykh, A. V. Tolmacheva, A. M. Tomchinskii, and P. B. Shavin, Scintillation of Cassiopeia A from artificial ionospheric inhomogeneities at 25, 240, and 290 MHz, *Radio Phys. Quantum Electron.*, Engl. Transl., 20, 177, 1979.
- Bowhill, S. A., Statistics of a radio wave diffracted by a random ionosphere, *J. Res. Natl. Bur. Stand. Sect. D*, 65D, 275, 1961.
- Briggs, B. H., and I. A. Parkin, On the variation of radio star and satellite scintillation with zenith angle, *J. Atmos. Terr. Phys.*, 25, 339, 1963.
- Carlson, H. C., and L. M. Duncan, HF excited instabilities in space plasmas, *Radio Sci.*, 12, 1001, 1977.
- Cragin, B. L., J. A. Fejer, and E. Leer, Generation of artificial spread F by a collisionally coupled purely growing parametric instability, *Radio Sci.*, 12, 273, 1977.
- Duncan, L. M., and R. A. Behnke, Observations of self-focusing electromagnetic waves in the ionosphere, *Phys. Rev. Lett.*, 41, 998, 1978.
- Erkhemov, L. M., V. I. Kovalev, A. M. Lerner, E. N. Myaskinov, I. N. Poddelskii, and A. V. Rakhilin, Spectrum of large-scale artificial inhomogeneities in the F layer of the ionosphere, *Radio Phys. Quantum Electron.*, Engl. Transl., 22, 888, 1979.
- Farley, D. T., A theory of electrostatic fields in a horizontally stratified ionosphere subject to a vertical magnetic field, *J. Geophys. Res.*, 64, 1225, 1959.

Farley, D. T., Artificial heating of the electrons in the *F* region of the ionosphere, *J. Geophys. Res.*, **68**, 401, 1963.

Farley, D. T., C. LaHoz, and B. G. Fejer, Studies of the self-focusing instability at Arecibo, *J. Geophys. Res.*, **88**, 2093, 1983.

Fejer, J. A., Ionospheric modification and parametric instabilities, *Rev. Geophys.*, **17**, 135, 1979.

Frey, A., and W. E. Gordon, HF-produced ionospheric electron density irregularities diagnosed by UHF radio star scintillations, *J. Atmos. Terr. Phys.*, **44**, 1101, 1982.

Frey, A., P. Stubbe, and H. Kopka, First experimental evidence of HF-produced electron density irregularities in the polar ionosphere: Diagnosed by UHF radio star scintillations, *Geophys. Res. Lett.*, **11**, 523, 1984.

Georges, T. M., Amplification of ionospheric heating and triggering of "spread *F*" by natural irregularities, *J. Geophys. Res.*, **75**, 6436, 1970.

Getmantsev, G. G., L. M. Erukhimov, E. E. Mityakova, N. A. Mityakov, N. M. Pryktov, V. O. Rapoport, and V. A. Cherepovitskii, Certain results of investigating ionospheric irregularities induced by powerful radio emission using baseground reception of satellite signals, *Radio Phys. Quantum Electron., Engl. Transl.*, **19**, 354, 1976.

Ginzburg, V. L., and A. V. Gurevich, Nonlinear phenomena in a plasma located in an alternating electric field, *Sov. Phys. Usp., Engl. Transl.*, **3**, 115, 1960.

Gordon, W. E., H. C. Carlson, and R. L. Showen, Ionospheric heating at Arecibo: First tests, *J. Geophys. Res.*, **76**, 7808, 1971.

Gurevich, A., *Nonlinear Phenomena in the Ionosphere*, chap. 6.1, Springer-Verlag, New York, 1978.

Kuo, S. P., and M. C. Lee, Earth magnetic field fluctuations produced by filamentation instabilities of electromagnetic heater waves, *Geophys. Res. Lett.*, **10**, 979, 1983.

Livingston, R. C., Heater-generated intermediate-scale irregularities: Spatial distribution and spectral characteristics, *Radio Sci.*, **18**, 253, 1983.

Mantas, G. P., H. C. Carlson, Jr., and C. H. LaHoz, Thermal response of the *F* region ionosphere in artificial modification experiments by HF radio waves, *J. Geophys. Res.*, **86**, 561, 1981.

Meltz, G., L. H. Holway, Jr., and N. M. Tomjanovich, Ionospheric heating by powerful radio waves, *Radio Sci.*, **9**, 885, 1974.

Perkins, F. W., and M. V. Goldman, Self-focusing of radio waves in an underdense ionosphere, *J. Geophys. Res.*, **86**, 600, 1981.

Perkins, F. W., and E. J. Valeo, Thermal self-focusing of electromagnetic waves in plasmas, *Phys. Rev. Lett.*, **32**, 1234, 1974.

Pope, J. H., and R. B. Fritz, Observations of artificially produced scintillations using satellite transmissions, *J. Geophys. Res.*, **79**, 1074, 1974.

Rino, C. L., A power law phase screen model for ionospheric scintillation, I. Weak scatter, *Radio Sci.*, **14**, 1135, 1979.

Rino, C. L., and E. J. Fremouw, The angle dependence of singly scattered wavefields, *J. Atmos. Terr. Phys.*, **39**, 859, 1977.

Rufenach, C. L., Radio scintillation of stellar signals during artificial ionospheric modification, *J. Geophys. Res.*, **78**, 5611, 1973.

Stubbe, P., H. Kopka H. Lauche, M. T. Rietveld, A. Brekke, O. Holt, T. B. Jones, T. Robinson, A. Hedberg, B. Thide, M. Crochet, and H. J. Lotz, Ionospheric modification experiments in northern Scandinavia, *J. Atmos. Terr. Phys.*, **44**, 1025, 1982.

Thome, G. D., and F. W. Perkins, Production of ionospheric striations by self-focusing of intense radio waves, *Phys. Rev. Lett.*, **32**, 1238, 1974.

Utlaut, W. F., Radio-wave modification of the ionosphere: An ionospheric modification experiment using very high power, high frequency transmission, *J. Geophys. Res.*, **75**, 6402, 1970.

S. Basu and J. Waaramaa, Air Force Geophysics Laboratory, Hanscom Air Force Base, MA 01731.
 Su. Basu, Emmanuel College, 400 The Fenway, Boston, MA 02115.
 H. Kopka and P. Stubbe, Max-Planck-Institut für Aeronomie, D-3411 Katlenburg-Lindau, Federal Republic of Germany.

(Received February 11, 1987;
 revised June 17, 1987;
 accepted June 19, 1987.)